T.R.
GEBZE TECHNICAL UNIVERSITY
GRADUATE SCHOOL OF NATURAL AND APPLIED SCIENCES

THE SPECTRAL DECAY PARAMETER K (KAPPA) FOR SUSTAINABLE CITIES IN TURKEY

YEŞİM BİRO
A THESIS SUBMITTED FOR THE DEGREE OF
DOCTOR OF PHILOSOPHY
DEPARTMENT OF CIVIL ENGINEERING
EARTHQUAKE AND STRUCTURAL ENGINEERING
PROGRAMME

GEBZE
2022

T.R.

GEBZE TECHNICAL UNIVERSITY

GRADUATE SCHOOL OF NATURAL AND APPLIED SCIENCES

THE SPECTRAL DECAY PARAMETER K (KAPPA) FOR SUSTAINABLE CITIES IN TURKEY

YEŞİM BİRO

A THESIS SUBMITTED FOR THE DEGREE OF DOCTOR OF PHILOSOPHY

DEPARTMENT OF CIVIL ENGINEERING

EARTHQUAKE AND STRUCTURAL ENGINEERING PROGRAMME

THESIS SUPERVISOR

PROF. DR. BÜLENT AKBAŞ

GEBZE

2022

T.C.
GEBZE TEKNİK ÜNİVERSİTESİ
FEN BİLİMLERİ ENSTİTÜSÜ

TÜRKİYE'DE SÜRDÜRÜLEBİLİR KENTLER İÇİN SPEKTRAL SÖNÜM PARAMETRESİ K (KAPPA)

YEŞİM BİRO

DOKTORA TEZİ
İNŞAT MÜHENDİSLİĞİ ANABİLİM DALI
DEPREM VE YAPI MÜHENİSLİĞİ PROGRAMI

DANIŞMANI
PROF. DR. BÜLENT AKBAŞ

GEBZE
2022

GEBZE TEKNİK ÜNİVERSİTESİ	**DOKTORA JÜRİ ONAY FORMU**

GTÜ Fen Bilimleri Enstitüsü Yönetim Kurulu'nun 23/06/2022 tarih ve 2022/31 sayılı kararıyla oluşturulan jüri tarafından 20/07/2022 tarihinde tez savunma sınavı yapılan Yeşim Biro'nun tez çalışması İnşaat Mühendisliği Anabilim Dalı Deprem ve Yapı Mühendisliği Programında DOKTORA tezi olarak kabul edilmiştir.

JÜRİ

ÜYE (TEZ DANIŞMANI)	: Prof. Dr. Bülent AKBAŞ
ÜYE	: Dr. Öğr. Üyesi Abdullah Can ZÜLFİKAR
ÜYE	: Prof. Dr. Hayrullah KARABULUT
ÜYE	: Dr. Öğr. Üyesi Ahu KÖMEÇ MUTLU
ÜYE	: Prof. Dr. Bilge DORAN

ONAY

Gebze Teknik Üniversitesi Fen Bilimleri Enstitüsü Yönetim Kurulu'nun ...../...../…… tarih ve ……/…..... sayılı kararı.

İMZA/MÜHÜR

SUMMARY

The spectral decay parameter, kappa, is one of the most important parameters in ground motion evaluation and seismic hazard and risk analysis at sites. It can have an impact in terms of 3 to 6 times increased seismic hazard values for high-frequency ground motions depending on the site conditions. In respect to earthquake resistant sustainable cities, this impact is substantial. The parameter is used in many applications to remove path and site effects, to simulate ground motion acceleration, to correct for high frequency attenuation and host-to-target adjustments of ground-motion prediction equations (GMPEs – Ground Motion Models – former attenuation relationships). Multiple approaches were developed for its estimation, which led to inconsistencies and uncertainties. In order to reduce these uncertainties and to improve the reliability of the outcomes being compared, the parameter must be given a consistent representation with its measurements.

The main goal of this PhD thesis is to estimate station based zero epicenter spectral decay parameter at Disaster and Emergency Management Agency (AFAD) strong motion stations with different parametrical restrictions such as distance, magnitude and average shear-wave velocity at 30 meters depth. When not enough data, the broad-band station data from Kandilli Observatory and Earthquake Research Institute (KOERI) is added.

The scope of the PhD thesis is to find answers to what extent can the site-terms of a well-recorded site spatially be extrapolated to nearby sites to calculate the seismic hazard and accordingly seismic risk with less uncertainties for site specific structures and sustainable cities.

Key Words: Spectral Decay Parameter (Kappa), Simulation of Earthquakes, Seismic Hazard, Seismic Risk, Site Specific Host-to-Target Adjustments of GMPEs, Sustainable Cities.

ÖZET

Spektral sönüm parametresi, kappa, kuvvetli yer hareketi ve deprem tehlike ve riski analizlerinde en önemli parametrelerden biridir. Zemin koşullarına bağlı olarak deprem tehlikesi değerlerinde 3 ila 6 kat artış etkisine sebebiyet verebilir. Sürdürülebilir kentler için gerekli depreme dayanıklı yapılar açısından bu etki azımsanamayacak bir ölçektir. Bu parametre bugüne kadar yayılım ve saha etkilerini gidermek, ivme yer hareketi simüle etmek, yüksek frekanslarda sönümlenmeyi düzeltmek ve yer hareketi tahmin denklemlerini (GMPE) veya modelleri (GMM) kaynak-hedefe göre düzeltmek gibi birçok alanda kullanılmaktadır. Geçtiğimiz son yıllarda, kappa tahmini ve deprem tehlike analizi sonuçlarına etkisi üzerine birçok yaklaşım geliştirilmiştir. Tahmin edilen yer hareketi ve tehlike sonuçları üzerindeki büyük etkisi sebebiyle, elde edilecek sonucun belirsizlik ve hata payını düşürmek için, bu parametre hesaplarının sistematik açıdan aynı şekilde hesap edilmesi ve karşılaştırılması önem taşımaktadır.

Bu Doktora Tezinin ana hedefi, kuvvetli yer hareketlerinin kaydedildiği, Acil Durum Yönetimi Başkanlığı (AFAD) Kuvvetli Yer Hareketi gözlem ağına ait istasyonlarının bulunduğu yerde, deprem merkez üssünün sıfır km uzaklıkta olduğu kappa parametresini deprem uzaklığı, büyüklüğü ve 30 metre derinlikteki ortalama makaslama dalga hızı gibi değişik parametreleri kısıtlayarak tahmin etmektir. Yeterli veri bulunmadığı takdirde, Kandilli Rasathanesi ve Deprem Araştırma Enstitüsü'ne (KRDAE) ait geniş band deprem kayıt cihazlarından veri eklenmiştir.

Bu Doktora Tezinin kapsamı, iyi-kaydedilmiş kuvvetli yer hareketlerine sahip bir sahada ve bu sahaya benzer ve yakın zemin parametrelerinin, deprem tehlikesi ve buna bağlı olarak derpem riskinin önemli yapılarda ve sürdürülebilir kentler için hesaplanmasında zemin parametrelerinin ne ölçüde cevap olabildiği hususundadır.

Anahtar Kelimeler: Spektral Sönüm Parametresi (Kappa), Deprem Simülasyonu, Deprem Tehlikesi, Deprem Riski, Zemine Özel Kaynak-Hedef Düzeltmeleri (GMPEs), Sürdürülebilir Kentler.

ACKNOWLEDGEMENTS

I would like to express my deep and sincere gratitude to my supervisor, Prof. Dr. Bülent AKBAŞ, my formal supervisor Prof. Dr. Bilge SİYAHİ GÖKMİRZA for their great support and mentorship during this PhD thesis.

I wish to express my warm and sincere thanks to Prof. Dr. Hayrullah KARABULUT and Dr. Abdullah Can ZÜLFİKAR for their valuable insights and suggestions during our Thesis Progress meetings.

I am truly grateful to our son Bora BİRO for his pure and great encouragement and for what I have learned from this young man and am still learning. I also share my gratitude to my 25 yearlong partner Mehmet Safa Talhan BİRO for his support during my journey of earthquake engineering career and studies. He had not only given many extremely valuable input and new ideas to develop, but he also lifted me up in every step in every possible way during our long journey together.

I am also grateful to my beloved cousin Canan AKMAN MÜFTÜLER for helping me out to discover new insights and mainly that she has been always there for me. I also thank my beloved brother Cüneyt ALPAY and my beloved mother Ender ALPAY, for their encouragement and support along the way.

Finally, I thank my beloved deceased father Kadir ALPAY, for many but mainly his encouragement to become who I am now. I learned the hard work under his wisdom and I wish he would have seen what I have accomplished by now. R.I.P.

TABLE OF CONTENTS

	Page
SUMMARY	v
ÖZET	vi
ACKNOWLEDMENTS	vii
TABLE of CONTENTS	viii
LIST of ABBREVIATIONS and ACRONYMS	x
LIST of FIGURES	xiii
LIST of TABLES	xx
1. INTRODUCTION	1
1.1. Purpose, Contribution and Content of the PhD Thesis	3
2. KAPPA STUDIES and EVALUATION METHODOLOGY	6
2.1. Anderson and Hough Method (Acceleration Spectrum Kappa)	8
2.1.1. Uncertainties Introduced at the Application Phase	9
2.2. Biasi and Smith Method (Displacement Spectrum Kappa)	9
2.2.1. Applicability of the Method	10
2.3. Inconsistency between Application Phases	11
2.3.1. Inconsistency in κ Evaluations	12
2.3.2. Inconsistency in κ_0 Calculations	17
3. UNCERTAINTY REDUCTION TRIALS	19
3.1. Stress Drop and Magnitude Dependency/Independency	20
3.2. Soil Type Dependency and HVSR	21
3.3. Interoperator Variability	27
3.4. Additional Uncertainties	31
4. NEW AUTOMATIC SELECTION PROCEDURE FOR SPECTRAL FLATTENING FREQUENCY (f_x)	33
4.1. The Impact of Fixed f_x Selection	33
4.2. The Impact of Tapering and Filtering	34
4.3. The New Procedure for f_x Selection	38
5. LINEAR FIT versus ROBUST FIT	40
5.1. Linear Regression Fit	40

5.2. Robust Regression Fit 41
6. κ ESTIMATIONS in TURKEY 43
7. NUMERICAL RESULTS 46
7.1. Van Region 51
7.2. Hard Rock AFAD Stations in Turkey 58
7.3. Sivrice-Pütürge Segment of EAF 63
7.3.1. KOERI Results 64
7.3.1.1. Dataset 64
7.3.1.2. Methodology Used 67
7.3.1.3. κ Results 70
7.3.1.4. HVSR Evaluations and Results 86
7.3.1.5. Comparison of κ_0 versus HVSR results and discussion 91
7.3.2. AFAD Results 93
7.3.2.1. Dataset and Methodology 93
7.3.2.2. κ Results 97
7.4. Izmir Region 159
8. CONCLUSION 168

REFERENCES 169
BIOGRAPHY 177
APPENDICES 178

LIST OF ABBREVIATIONS AND ACRONYMS

Abbreviations and Acronyms		**Explanations**
κ	:	Spectral decay parameter
f_x	:	Spectral flattening frequency
κ_0	:	Station based zero epicentral spectral decay parameter
Q ($Q(f)$, Q_0)	:	Seismic quality factor / path attenuation / anelastic attenuation factor
V_{s30}	:	Average shear-wave velocity at 30 meters depth
R_{epi}	:	Epicentral distance
M_w	:	Moment magnitude
S-wave	:	Shear-wave
M	:	Magnitude
κ_{AS}	:	Acceleration spectral decay parameter
κ_{DS}	:	Displacement spectral decay parameter
κ_{BB}	:	Broad band inversion kappa / Broad-band fitting kappa
κ_{RESP}	:	Response spectrum decay parameter
f_c	:	Corner frequency
M_o	:	Seismic moment
R_{hyp}	:	Hypocentral distance
km	:	Kilometer
f_E	:	Spectral amplitude frequency where exponential decay clearly starts
A_0	:	Spectral amplitude
Hz	:	Hertz
f	:	Frequency
M_L	:	Local magnitude
s	:	Second
t^*	:	Attenuation time
f_{max}	:	Cut-off frequency
R^2	:	Correlation coefficient
f_s	:	Significant peak frequencies on HVSR
f_0	:	First peak frequency on HVSR

f_p	:	Highest peak frequency on HVSR
M_s	:	Surface wave magnitude
m/s	:	Meter per second
ms	:	Millisecond
Δf	:	The difference between f_E and f_x
f_{xi}	:	Initial spectral flattening frequency
g/cm^3	:	Gram per centimeter cube
km/s	:	Kilometer per second
κ_H	:	Horizontal spectral decay parameter
κ_{EW}	:	East-West component of spectral decay parameter
κ_{NS}	:	North-South component of spectral decay parameter
T	:	Fundamental natural period
g	:	Acceleration of gravity
κ_V	:	Vertical spectral decay parameter
AFAD	:	Republic of Turkey Ministry of Interior Disaster and Emergency Management Presidency (T.C. İçişleri Bakanlığı Afet ve Acil Durum Yönetimi Başkanlığı)
BC Hydro	:	British Columbia Hydro and Power Authority
CENA	:	Central-Eastern North America
CRMS	:	Cumulative root mean square
EAF	:	East Anatolian Fault
EPRI	:	Electric Power Research Institute
EW	:	East-West component of the earthquake signal
FAS	:	Fourier amplitude spectrum
FFT	:	Fast Fourier transform
GEER	:	Geotechnical Extreme Events Reconnaissance Association
GIT	:	Generalized inversion technique
GMM	:	Ground-motion model
GMPE	:	Ground-motion prediction equation
HVSR	:	Horizontal-to-vertical spectral ratios
KiK-net	:	Japanese Kiban–Kyoshin Seismic-motion Seismograph Network
KOERI	:	Kandilli Observatory and Earthquake Research Institute
KRDAE	:	Kandilli Rasathanesi ve Deprem Araştırma Enstitüsü

NAF	:	North Anatolian Fault
NEHRP	:	National Earthquake Hazards Reduction Program (USA)
NGA	:	Next Generation of Ground-Motion Attenuation Models
NPP	:	Nuclear power plant
NS	:	North-South component of the earthquake signal
PEER	:	Pacific Earthquake Engineering Research
PEGASOS	:	Probabilistic Seismic Hazard Analysis for Swiss Nuclear Power Plant Sites
PGA	:	Peak ground acceleration
PRP	:	PEGASOS Refinement Project
PSA	:	Pseudospectral acceleration
RADIUS	:	Risk Assessment Tools for Diagnosis of Urban Areas against Seismic Disasters
RESOURCE	:	Reference database for Seismic grOund-motion pREdiCtion in Europe
QTS	:	Quasi transfer spectrum
SDEE	:	Soil Dynamics and Earthquake Engineering journal
SESAME	:	Site EffectS assessment using AMbient Excitations
SIGMA	:	Seismic Ground Motion Assessment project
SNR	:	Signal-to-noise ratio
SSR	:	Standard spectral ratios

LIST OF FIGURES

Figure No:		Page
1.1:	Example of *Vs*- and Kappa-correction functions.	2
2.1:	The "ill-defined" kappa region for small earthquakes.	10
2.2:	CRMS of an example recording to pick the S-wave ending.	14
2.3:	Example of the newly developed noise and P- & S-wave selection procedure.	14
3.1:	Correlations between κ and V_{s30}.	22
3.2:	Left: existing data and correlations, all suggesting a downward tendency for hard rock. Right: the alternative asymptotic functional form for correlations of $\kappa_{0,AS}$ with V_{s30}, based on data from EUROSEISTEST (red) and Switzerland (blue), following solely the AS measurement method.	23
3.3:	Comparison of existing Vs_{30}-κ_0 relations.	24
3.4:	Variance of kappa illustrated via error bars.	28
3.5:	New procedure to reduce the interoperator variability.	29
3.6:	SVRC (KOERI) station kappa error bars indicated in red.	30
4.1:	An example of kappa estimations with different choice of $f_E - f_x$ bands for the same signal.	34
4.2:	Comparison of κ fits for raw and tapered signal. (6% difference in κ values in this).	36
4.3:	An example of spectral decay of FAS.	37
4.4:	The effect of low pass filtering to a signal on FAS.	38
4.5:	Example of the newly developed automized f_x pick.	39
4.6:	Example of κ estimation after the newly developed automized f_x pick from Figure 4.5.	39
7.1:	Example parameterization of $Vs - \kappa$ correction functions by fitting a surface to the evaluated correction functions	47
7.2:	Magnitude-distance distribution of strong-motion records in the NGA-West2 database (magnitudes 3 to 7.9).	48
7.3:	Magnitude versus distance coverage of recordings in the NGA-East ground-motion database.	48

7.4:	Example of manually selected f_E and f_x. Here the decay starts at f_E =3 Hz and ends around manually selected f_x =16.29 Hz instead of fixed f_E =2 Hz and f_x =20 Hz.	53
7.5:	Mean horizontal κ trend at Station 6501. Resulting κ_0 is 0.0389 s.	57
7.6:	Vertical κ trend at Station 6501. Resulting κ_0 is 0. 0203 s.	57
7.7:	M_L vs R_{hyp} distribution of selected events at Station 6501.	58
7.8:	Distribution of selected events in terms of R_{hyp} and V_{s30} for AFAD hard rock stations.	60
7.9:	Distribution of evaluated κ_0 values with V_{s30} for AFAD hard rock stations.	62
7.10:	The distribution of selected events with near stations.	66
7.11:	The distribution of selected events with far stations.	67
7.12:	κ evaluation for two components of an event recorded at station ARPR.	68
7.13:	f_E (in blue) and f_x (in orange) distribution with respect to horizontal components' κ's from all events at all stations.	69
7.14:	: The horizontal event kappa, κ_H vs R_{epi} at different magnitude bins via robust multiple linear regression model.	71
7.15:	The horizontal event kappa, κ_H vs R_{epi} at different magnitude bins via robust logarithmic fit model.	72
7.16:	The constrained to overall κ_H vs R_{epi} fit for ARPR station.	73
7.17:	The unconstrained to overall κ_H vs R_{epi} fit for ARPR station.	73
7.18:	The constrained to overall κ_H vs R_{epi} fit for BNGB station.	74
7.19:	The unconstrained to overall κ_H vs R_{epi} fit for BNGB station.	74
7.20:	The constrained to overall κ_H vs R_{epi} fit for DARE station.	75
7.21:	The unconstrained to overall κ_H vs R_{epi} fit for DARE station.	75
7.22:	The constrained to overall κ_H vs R_{epi} fit for DYBB station.	76
7.23:	The unconstrained to overall κ_H vs R_{epi} fit for DYBB station.	76
7.24:	The constrained to overall κ_H vs R_{epi} fit for GAZ station.	77
7.25:	The unconstrained to overall κ_H vs R_{epi} fit for GAZ station.	77
7.26:	The constrained to overall κ_H vs R_{epi} fit for ILIC station.	78
7.27:	The unconstrained to overall κ_H vs R_{epi} fit for ILIC station.	78
7.28:	The constrained to overall κ_H vs R_{epi} fit for SVAN station.	79

7.29: The unconstrained to overall κ_H vs R_{epi} fit for SVAN station. 79
7.30: The constrained to overall κ_H vs R_{epi} fit for URFA station. 80
7.31: The unconstrained to overall κ_H vs R_{epi} fit for URFA station. 80
7.32: The constrained to overall κ_H vs R_{epi} fit for ESGZ station. 81
7.33: The unconstrained to overall κ_H vs R_{epi} fit for ESGZ station. 81
7.34: The constrained to overall κ_H vs R_{epi} fit for ESIJ station. 82
7.35: The unconstrained to overall κ_H vs R_{epi} fit for ESIJ station. 82
7.36: The constrained to overall κ_H vs R_{epi} fit for MDYO station. 83
7.37: The unconstrained to overall κ_H vs R_{epi} fit for MDYO station. 83
7.38: The constrained to overall κ_H vs R_{epi} fit for SVRC station. 84
7.39: The unconstrained to overall κ_H vs R_{epi} fit for SVRC station. 84
7.40: HVSR for 12 KOERI stations. 89
7.41: $HVSR_{FAS}$ of KOERI stations with amplitudes lower than 2.00. 90
7.42: $HVSR_{FAS}$ of KOERI stations with amplitudes higher than 2.00. 90
7.43: $HVSR_{FAS}$ of near site KOERI stations. 92
7.44: The distribution of selected events with selected AFAD stations. 96
7.45: The distribution of selected events with near AFAD stations. 97
7.46: The horizontal event kappa, κ_H vs R_{epi} at different magnitude bins via robust multiple linear regression model. 98
7.47: The horizontal event kappa, κ_H vs R_{epi} at different magnitude bins via robust multiple linear regression model within 100 km. 98
7.48: The constrained to overall κ_H vs R_{epi} fit for Stn0201. 99
7.49: The unconstrained to overall κ_H vs R_{epi} fit for Stn0201. 99
7.50: The constrained to overall κ_H vs R_{epi} fit for Stn0204. 100
7.51: The unconstrained to overall κ_H vs R_{epi} fit for Stn0204. 100
7.52: The constrained to overall κ_H vs R_{epi} fit for Stn0205. 101
7.53: The unconstrained to overall κ_H vs R_{epi} fit for Stn0205. 101
7.54: The constrained to overall κ_H vs R_{epi} fit for Stn0206. 102
7.55: The unconstrained to overall κ_H vs R_{epi} fit for Stn0206. 102
7.56: The constrained to overall κ_H vs R_{epi} fit for Stn0207. 103
7.57: The unconstrained to overall κ_H vs R_{epi} fit for Stn0207. 103
7.58: The constrained to overall κ_H vs R_{epi} fit for Stn0208. 104
7.59: The unconstrained to overall κ_H vs R_{epi} fit for Stn0208. 104

7.60: The constrained to overall κ_H vs R_{epi} fit for Stn0209. 105
7.61: The unconstrained to overall κ_H vs R_{epi} fit for Stn0209. 105
7.62: The constrained to overall κ_H vs R_{epi} fit for Stn0212. 106
7.63: The unconstrained to overall κ_H vs R_{epi} fit for Stn0212. 106
7.64: The constrained to overall κ_H vs R_{epi} fit for Stn0213. 107
7.65: The unconstrained to overall κ_H vs R_{epi} fit for Stn0213. 107
7.66: The constrained to overall κ_H vs R_{epi} fit for Stn1201. 108
7.67: The unconstrained to overall κ_H vs R_{epi} fit for Stn1201. 108
7.68: The constrained to overall κ_H vs R_{epi} fit for Stn1210. 109
7.69. The unconstrained to overall κ_H vs R_{epi} fit for Stn1210. 109
7.70: The constrained to overall κ_H vs R_{epi} fit for Stn2101. 110
7.71: The unconstrained to overall κ_H vs R_{epi} fit for Stn2101. 110
7.72: The constrained to overall κ_H vs R_{epi} fit for Stn2102. 111
7.73: The unconstrained to overall κ_H vs R_{epi} fit for Stn2102. 111
7.74: The constrained to overall κ_H vs R_{epi} fit for Stn2104. 112
7.75: The unconstrained to overall κ_H vs R_{epi} fit for Stn2104. 112
7.76: The constrained to overall κ_H vs R_{epi} fit for Stn2105. 113
7.77: The unconstrained to overall κ_H vs R_{epi} fit for Stn2105. 113
7.78: The constrained to overall κ_H vs R_{epi} fit for Stn2106. 114
7.79: The unconstrained to overall κ_H vs R_{epi} fit for Stn2106. 114
7.80: The constrained to overall κ_H vs R_{epi} fit for Stn2107. 115
7.81: The unconstrained to overall κ_H vs R_{epi} fit for Stn2107. 115
7.82: The constrained to overall κ_H vs R_{epi} fit for Stn2301. 116
7.83: The unconstrained to overall κ_H vs R_{epi} fit for Stn2301. 116
7.84: The constrained to overall κ_H vs R_{epi} fit for Stn2302. 117
7.85: The unconstrained to overall κ_H vs R_{epi} fit for Stn2302. 117
7.86: The constrained to overall κ_H vs R_{epi} fit for Stn2304. 118
7.87: The unconstrained to overall κ_H vs R_{epi} fit for Stn2304. 118
7.88: The constrained to overall κ_H vs R_{epi} fit for Stn2305. 119
7.89: The unconstrained to overall κ_H vs R_{epi} fit for Stn2305. 119
7.90: The constrained to overall κ_H vs R_{epi} fit for Stn2306. 120
7.91: The unconstrained to overall κ_H vs R_{epi} fit for Stn2306. 120
7.92: The constrained to overall κ_H vs R_{epi} fit for Stn2307. 121

7.93: The unconstrained to overall κ_H vs R_{epi} fit for Stn2307. 121
7.94: The constrained to overall κ_H vs R_{epi} fit for Stn2308. 122
7.95: The unconstrained to overall κ_H vs R_{epi} fit for Stn2308. 122
7.96: The constrained to overall κ_H vs R_{epi} fit for Stn2309. 123
7.97: The unconstrained to overall κ_H vs R_{epi} fit for Stn2309. 123
7.98: The constrained to overall κ_H vs R_{epi} fit for Stn2401. 124
7.99: The unconstrained to overall κ_H vs R_{epi} fit for Stn2401. 124
7.100: The constrained to overall κ_H vs R_{epi} fit for Stn2404. 125
7.101: The unconstrained to overall κ_H vs R_{epi} fit for Stn2404. 125
7.102: The constrained to overall κ_H vs R_{epi} fit for Stn2408. 126
7.103: The unconstrained to overall κ_H vs R_{epi} fit for Stn2408. 126
7.104: The constrained to overall κ_H vs R_{epi} fit for Stn2409. 127
7.105: The unconstrained to overall κ_H vs R_{epi} fit for Stn2409. 127
7.106: The constrained to overall κ_H vs R_{epi} fit for Stn2412. 128
7.107: The unconstrained to overall κ_H vs R_{epi} fit for Stn2412. 128
7.108: The constrained to overall κ_H vs R_{epi} fit for Stn2414. 129
7.109: The unconstrained to overall κ_H vs R_{epi} fit for Stn2414. 129
7.110: The constrained to overall κ_H vs R_{epi} fit for Stn2415. 130
7.111: The unconstrained to overall κ_H vs R_{epi} fit for Stn2415. 130
7.112: The constrained to overall κ_H vs R_{epi} fit for Stn2710. 131
7.113: The unconstrained to overall κ_H vs R_{epi} fit for Stn2710. 131
7.114: The constrained to overall κ_H vs R_{epi} fit for Stn2711. 132
7.115: The unconstrained to overall κ_H vs R_{epi} fit for Stn2711. 132
7.116: The constrained to overall κ_H vs R_{epi} fit for Stn4401. 133
7.117: The unconstrained to overall κ_H vs R_{epi} fit for Stn4401. 133
7.118: The constrained to overall κ_H vs R_{epi} fit for Stn4404. 134
7.119: The unconstrained to overall κ_H vs R_{epi} fit for Stn4404. 134
7.120: The constrained to overall κ_H vs R_{epi} fit for Stn4405. 135
7.121: The unconstrained to overall κ_H vs R_{epi} fit for Stn4405. 135
7.122: The constrained to overall κ_H vs R_{epi} fit for Stn4407. 136
7.123: The unconstrained to overall κ_H vs R_{epi} fit for Stn4407. 136
7.124: The constrained to overall κ_H vs R_{epi} fit for Stn4408. 137
7.125: The unconstrained to overall κ_H vs R_{epi} fit for Stn4408. 137

7.126: The constrained to overall κ_H vs R_{epi} fit for Stn4409. 138
7.127: The unconstrained to overall κ_H vs R_{epi} fit for Stn4409. 138
7.128: The constrained to overall κ_H vs R_{epi} fit for Stn4410. 139
7.129: The unconstrained to overall κ_H vs R_{epi} fit for Stn4410. 139
7.130: The constrained to overall κ_H vs R_{epi} fit for Stn4411. 140
7.131: The unconstrained to overall κ_H vs R_{epi} fit for Stn4411. 140
7.132: The constrained to overall κ_H vs R_{epi} fit for Stn4412. 141
7.133: The unconstrained to overall κ_H vs R_{epi} fit for Stn4412. 141
7.134: The constrained to overall κ_H vs R_{epi} fit for Stn4605/4610. 142
7.135: The unconstrained to overall κ_H vs R_{epi} fit for Stn4605/4610. 142
7.136: The constrained to overall κ_H vs R_{epi} fit for Stn4611. 143
7.137: The unconstrained to overall κ_H vs R_{epi} fit for Stn4611. 143
7.138: The constrained to overall κ_H vs R_{epi} fit for Stn4614. 144
7.139: The unconstrained to overall κ_H vs R_{epi} fit for Stn4614. 144
7.140: The constrained to overall κ_H vs R_{epi} fit for Stn4631. 145
7.141: The unconstrained to overall κ_H vs R_{epi} fit for Stn4631. 145
7.142: The constrained to overall κ_H vs R_{epi} fit for Stn4701. 146
7.143: The unconstrained to overall κ_H vs R_{epi} fit for Stn4701. 146
7.144: The constrained to overall κ_H vs R_{epi} fit for Stn5809. 147
7.145: The unconstrained to overall κ_H vs R_{epi} fit for Stn5809. 147
7.146: The constrained to overall κ_H vs R_{epi} fit for Stn5816. 148
7.147: The unconstrained to overall κ_H vs R_{epi} fit for Stn5816. 148
7.148: The constrained to overall κ_H vs R_{epi} fit for Stn6201. 149
7.149: The unconstrained to overall κ_H vs R_{epi} fit for Stn6201. 149
7.150: The constrained to overall κ_H vs R_{epi} fit for Stn6202. 150
7.151: The unconstrained to overall κ_H vs R_{epi} fit for Stn6202. 150
7.152: The constrained to overall κ_H vs R_{epi} fit for Stn6302. 151
7.153: The unconstrained to overall κ_H vs R_{epi} fit for Stn6302. 151
7.154: The constrained to overall κ_H vs R_{epi} fit for Stn6304. 152
7.155: The unconstrained to overall κ_H vs R_{epi} fit for Stn6304. 152
7.156: The horizontal event kappa, κ_H vs R_{epi} up to 100 km at different magnitude bins via robust multiple linear regression model for Stn4404 with V_{s30} = 1380 km/s. 156

7.157: The horizontal event kappa, κ_H vs R_{epi} up to 26 km at different magnitude bins via robust multiple linear regression model for Stn4404 with V_{s30} = 1380 km/s. 157

7.158: κ_0 versus V_{s30} from all AFAD stations that recorded events from Sivrice-Pütürge segment of EAF. 158

7.159: κ_0 versus V_{s30} from near field AFAD stations that recorded events from Sivrice-Pütürge segment of EAF 159

7.160: Locations of the strong ground motion AFAD stations within 100 km epicentral distance. 160

7.161: Pseudo Spectral Acceleration graphs for Bayrakli soil (Station 3513 with V_{s30} = 196 m/s) and rock (Station 3514 with V_{s30} = 836 m/s) stations with respect to 2018 Turkish Seismic Code Design Spectrum. 161

7.162: The weighted average 2014 GMPEs for M_w = 6.6 and M_w = 6.9 with respect to the mainshock recording of 30th October, 2020 Samos earthquake at Station 3514. 162

7.163: Samos region events with $M \geq 3.5$ that are recorded at Station 3514. 164

7.164: Event κ_H values evaluated for the events recorded at Station 3514. 165

7.165: κ_0 value for the new dataset that consists of August 2019 – December 2020 Samos related events is 0.018 s when constrained with the overall κ_H values at Station 3514. 166

LIST OF TABLES

Table No:		**Page**
7.1:	Estimated values of κ_0 for Station 6501 with pre-set Q = 400.	55
7.2:	Estimated values of κ_0 for Station 6501 with pre-set Q = 1200.	56
7.3:	AFAD hard rock stations and κ_0 evaluations.	59
7.4:	The selected event magnitude and the epicentral distance ranges for each KOERI station.	65
7.5:	Station based κ_0 estimations with constrained and unconstrained fit. Constrained fit is favored in the current.	85
7.6:	Station-based $HVSR_{FAS}$ amplitudes and the corresponding peak frequencies.	87
7.7:	The selected event magnitude and the epicentral distance ranges for each AFAD station.	94
7.8:	Station based κ_0 estimations with constrained and unconstrained fit. Constrained fit is favored in the current study.	153
7.9:	Comparison of significant duration, Arias intensity and Housner intensity values for 30th October, 2020 Samos earthquake recorded at Station 3514.	163
7.10:	the κ_H and κ_V values for the new dataset related Samos events at Station 3514.	167

1. INTRODUCTION

For sustainable cities and critical structures which has specific importance that are under the risk of seismic hazard, the ground motion prediction values should represent the seismic risk that would be expected at the location or the region in consideration. For this purpose, either a regional GMPE is established or a transformation from a global GMPE (host) to the target area has to be put in action. In terms of this transformation, lately the biggest challenge is the spectral decay of Fourier amplitude spectrum for especially higher frequencies for the ground motion.

After its first introduction by Anderson and Hough [1984], the spectral decay parameter, kappa (κ), is lately debated in scientific community due to its variations and uncertainties. The main attention was given to the parameter due to its implications on seismic hazard results for Swiss nuclear power plants (NPPs) in PEGASOS (Probabilistic Seismic Hazard Analysis for Swiss Nuclear Power Plant Sites) Refinement Project (PRP). Seismic risk for the low natural period-high natural frequency NPPs and their components, the high frequency related kappa correction of the GMPEs could come up to 6 times the hazard value of the ground motion representation of the Abrahamson and Silva [2008] GMPE. When combined with the de-amplification of a very hard rock site, this effect could drop to half of the hazard value resulting from only the κ correction depending on the site [Biro and Renault, 2012], (Figure 1.1).

The high frequency spectral values are particularly important for low rise, stiff structures and they are usually in high importance category such as dams, NPPs, stadiums, low rise school, municipality, fire department, hospital occupancy structures.

In Earthquake Engineering, κ evaluations influence also mainly the practices of nonlinear structural analysis with representative or simulated earthquakes as well as soil-structure interaction analysis besides the practice of hazard calculations for either seismic codes or for structures that has specific importance. In these evaluations, taking the GMPEs directly as they are formulized for the regions and for the specific structures that sustainability is at high importance, can no longer represent the effective hazard and risk values, especially if the GMPEs show diversity with what is actually recorded in the region.

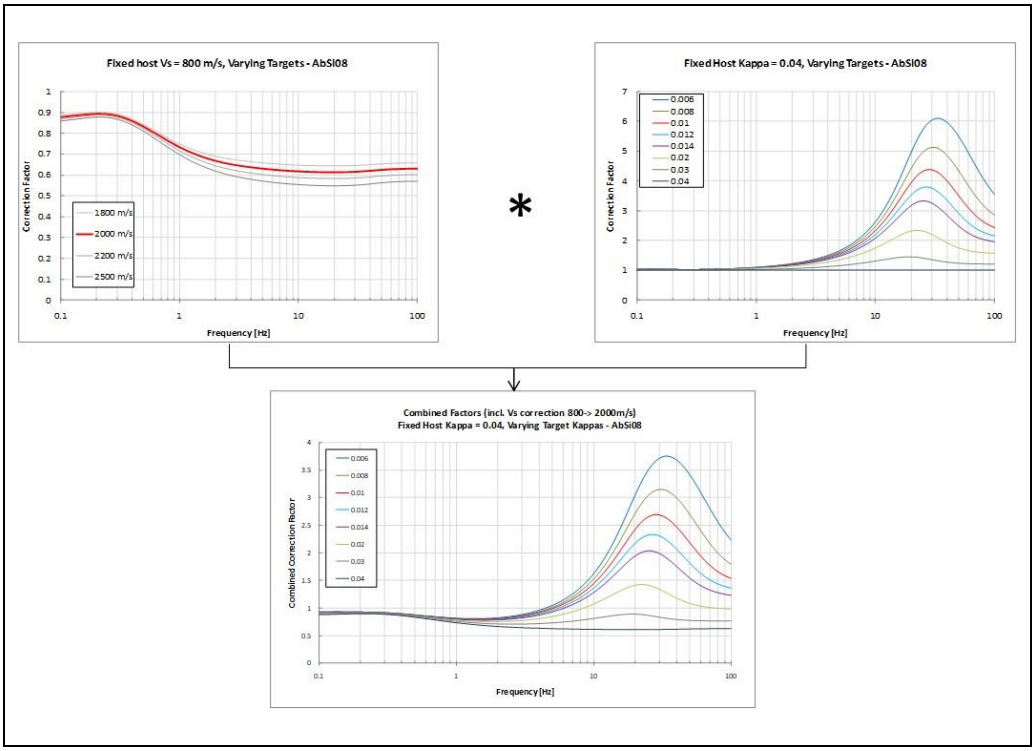


Figure 1.1: Example of V_S- and Kappa-correction functions.

In this PhD thesis, due to its high impact on earthquake hazard and risk, κ calculations for regions in Turkey are evaluated to achieve the goal of sustainability in these regions where the evaluations are carried on.

During these evaluations, an automatic selection procedure for spectral flattening frequency (f_x) is introduced which could help the scientific community to reduce interoperator variability.

It is clear that natural disasters, when not well prepared, impact the economy, social and national wealth of the region that they strike deeply and quite remarkably. For this reason, it is very important to define the hazard and risk as efficient as possible so as to sustain the region for earthquake resistance.

The potential users of the outcome of this PhD thesis would be the scientists who contribute in seismic hazard and risk calculations as well as the earthquake engineers who calculate and/or evaluate earthquake resistant structures.

1.1. Purpose, Contribution and Content of the PhD Thesis

The main objective of this PhD thesis is to evaluate the spectral decay parameter, κ, for selected regions in Turkey where significant amount of earthquake records are available. In this main course, the uncertainty that is associated to the interoperator variability issue which is lately in debate by the scientific community is addressed and a possible solution for it is given by a new automatic procedure to select the spectral flattening frequency, f_x.

After Biro and Renault [2012] presented that the lower the decay of high frequency ground motion amplitudes, the higher the seismic hazard is, the approaches estimating κ was in high interest to be reviewed.

In the creation of and calibration of GMPEs or lately renamed as GMMs (Ground Motion Models) based on stochastic simulations, near-surface attenuation is implicitly considered through a set of station based zero epicentral spectral decay parameter (κ_0) values considered applicable to the region. It is for this reason important to find the applicable values for the region in consideration.

At this moment the seismic hazard maps, including the new Turkish Earthquake Resistant Building Code of 2018, do not adjust the foreign GMPEs for Turkey region. The site characteristics are obtained by site amplification factors given in the code, assuming that the bedrock characteristic of the whole Turkey region is the same as the average of the empirical values of the GMPEs.

For site response applications, which are assumed to be basically controlled by the velocity profile and rock damping characteristics, Laurendeau et. al. [2013] suggested that the integration of site-specific κ_0 effect in empirical model appeared essential to more accurately describe the rock-and-stiff-soil-site function. They indeed also found in their simulations that κ_0 variations produce large ground-motion differences.

The amount of available ground motion data has greatly expanded worldwide during the last years. However, the dependence of the high-frequency ground motion on κ has not yet explicitly been addressed [Web 1].

Previous calculations of κ for the events in Turkey were estimated for mainshock and aftershocks of the important seismic events all together for one average κ_0 and the

effect of the distance of the recordings were not taken into consideration. Instead, all event recordings in all stations that recorded the events were taken into account, regardless how far the events were from the station that recorded them. As κ is controlled by the attenuation along the path and at the site, the path attenuation $Q(f)$ from far field recordings interferes when the event is far away from the station that recorded it. Even though lately new publications and researches on the Turkish data considers each recording site individually, still the far events are included without the correction of the path attenuation $Q(f)$ or with a definition of $Q(f)$ that is derived without taking the site effects such as average shear-wave velocity at 30 meters depth (V_{s30}) profile, site amplification and κ_0 out.

Traditionally κ is treated with the pre-assumption that this parameter is magnitude-independent, but high uncertainty in low magnitude events is observed. Some authors tried to find a correlation between stress drop and not yet found a resolution to reduce this uncertainty. When datasets allowed with decent number of recordings for the evaluations, magnitude dependency is observed in this PhD thesis, like many authors dealing with such datasets are reporting lately worldwide.

Turkish data is very important for the international scientific research and is highly used, but as the evaluation process of κ is not set to a consistent procedure, the outcomes may result with comments and conclusions where there are actually vast uncertainties. Bard et. al [2018] came to a conclusion that host-to-target adjustments of κ for GMPEs are not the best way to get consistent hard rock ground motion prediction via utilizing Bora et. al. [2017] evaluations for Turkey. Bora et. al. [2017] have taken Turkish strong motion data with maximum 200km, Italian with 100km and other strong motion data with 50km epicentral distance (R_{epi}). As discussed before at far epicentral distances the path attenuation $Q(f)$ interferes and needs to be taken out before reaching to a conclusion. The frequency independent Q_0 crustal quality factors are derived in this article instead of a frequency dependent $Q(f)$. As it is mentioned in the article, the estimation of κ_0 is strongly biased upon the assumed Q model. Other authors are also cited who reached similar results with similar data sets which are not well restricted with distance or magnitude.

For all applications of κ_0, multiple approaches were developed for its estimation, which led to inconsistencies and uncertainties in the past. Due to this large impact on ground-motion and seismic hazard, in order to reduce these uncertainties and the

reliability of the outcomes being compared, the parameter should always be given a consistent representation with its measurements [Biro et. al., 2019, 2020, 2021].

The contribution of this PhD thesis will provide a consistent representation of κ and κ_0 for some regions in Turkey, where database allows. For this reason, the common methodology is applied while trying to reduce the uncertainties represented in this thesis. In the explanation of uncertainties, the different outcomes of different scientists, even though using the same methodology to the same database, will be discussed. This interoperator variability could be surpassed with a good definition of which frequency band/range for the same earthquake data should be applied for the spectral linear fit. Due to heavy load of earthquake records in databases, in this PhD thesis, an automatization to select this frequency range is developed and applied to calculate κ. Also, robust fit between epicentral distance, R_{epi}, and κ besides the linear fit is shown for the first time in κ evaluations in Turkey region. The robust fit is also applied to Fourier spectral values while calculating κ to surpass any outlying data in hand.

Both robust fit applications to reach more reasonable resulting κ values, and the new procedure and the automatization technique for spectral flattening frequency, f_x selection presented in this PhD thesis could reduce the uncertainties for this parameter, not only for Turkey but for other regions as well.

2. KAPPA STUDIES and EVALUATION METHODOLOGY

κ basically measures the decay of high frequency ground motion Fourier spectrum amplitudes for each record at one location. κ_0, κ at zero epicentral distance for the same location, then is evaluated from all records, modeled as a function of site and distance by linearly regressing over distance either with path attenuation or quality factor, Q correction (i.e., constrained fit) or without such correction (i.e., unconstrained fit).

The impact of the κ estimation methodology was initially discussed by Biro and Renault [2012] and since then many authors evaluated the estimation methodologies and also tried to understand the uncertainties. In their study, Biro and Renault [2012] have shown the impact of κ correction for specific hard rock sites in Switzerland for hazard evaluations of Nuclear Power Plants. One of the findings in this project was that the lower the decay of high frequency ground motion amplitudes (low κ_0), the higher the seismic hazard was, especially at the higher frequencies up to peak ground acceleration, PGA. The impact could be as three times the spectral acceleration hazard value for very hard rock sites even after the de-amplification effect of soil to hard rock estimations were included to the resulting spectral value.

The same impact was observed by Laurendeau et. al. [2013], while investigating the events between $4.5 \leq M_w \leq 6.9$ recorded at the Japanese stations with V_{s30} ranging from 500 to 1500 m/s (stiff soil to rock sites). The empirical site coefficients obtained and the comparison with the simulated site functions showed in their study that seismic motion on rock and stiff-soil sites does not depend only on V_{s30}, but also on the high frequency attenuation site properties (κ_0). Indeed, the simulations showed that κ_0 variations produce large ground-motion differences in their study.

Due to the high impact on hazard evaluations, it is crucial that κ is evaluated in the light of the latest findings, however there still are discrepancies among the application and evaluation process.

With the realization of the importance of κ parameter, Campbell et.al. [2014] have evaluated the existing κ values without validation that are associated with a reference-rock site condition in central and eastern North America (CENA) in a PEER

report (Pacific Earthquake engineering Research). The probability distribution for the shear-wave (S- wave) site attenuation parameter κ_0, or site κ were evaluated without validation of the existing κ values to see their correlation. Two approaches were used to perform the analyses, first approach fitting response spectral templates to the observed response spectra using simple, usually stochastic, models of the source, path, and site-amplification effects beneath the site and second performing inversions of the observed Fourier amplitude spectra of ground motion using simple stochastic models. The existing κ values from different studies are taken as input data, where some include $M > 2.5$ and up to 200 km R_{epi}. Listing of existing relationships between V_{s30} and κ_0 are given, the Q effects are discussed and recommendations for epistemic uncertainties in reference-rock κ are given in the report. Due to limited number of data, additional studies are recommended to characterize the site attenuation parameter for shear and compression waves as a conclusion.

As indicated in Ktenidou et. al. [2014] there are multiple applications, physical interpretations and measurement methods of κ during the course of time since its first introduction. Different measuring types of measurements were developed for different types of usage purpose, or to be able to reduce the uncertainties.

Later, Ktenidou et. al. [2016a] selected and reviewed four different approaches used for estimating κ in a PEER report and made suggestions on how these approaches could be used, and these are summarized as following:

- κ_{AS} : High-frequency decay of the S-wave Fourier spectrum principle with Anderson and Hough [1984] & Hough and Anderson [1988] methods, where direct measurement on the S-wave Fourier acceleration spectrum above the corner frequency (f_c) where it is theoretically flat in log-log space.

- κ_{DS} : Small magnitude principle with Biasi and Smith [2001] method, where direct measurement on low-frequency part of the Fourier displacement spectrum (much below f_c) where it is theoretically flat.

- κ_{BB} : Inversion of the entire frequency band of the spectrum principle used by Anderson and Humphrey [1991], Humphrey and Anderson [1992], Silva et. al. [1997], Edwards et. al. [2011], where Broadband inversion of the entire

spectrum for source, path and site terms (usually for seismic moment (M_o), f_c and κ_0).

- κ_{RESP} : Peak and shape of the normalized acceleration response spectrum principle suggested by Silva and Darragh [1995] and is used by Silva et. al. [1998], where fitting of stochastically simulated response spectra (where κ is a model input parameter) coupled with site amplification to observed response spectra.

The authors suggested to use hypocentral distances (R_{hyp}) closer than 20 km, depending on the availability of data, and if far field recordings are needed to be added, then $Q(f)$ correction necessity is discussed.

The report also provided preliminary κ_0 estimations for Central-Eastern North America, CENA where the authors mentioned about the inconsistencies between the κ_0 scale factors for analytical modeling and the empirical observations. For this reason, they suggested and planned the EPRI (Electric Power Research Institute) 1993 report [EPRI, 1993] data should be re-evaluated. This attempt is now taking place in the SIGMA-2 Project (2017-ongoing, [Web 1]) under Action 3.1.1. "Ground motion high frequency attenuation proxy (Kappa Project)".

Here in this PhD thesis, the classical approach of Anderson and Hough Method (acceleration spectrum κ) will be discussed, while introducing roughly the displacement spectrum κ as well not to exclude a methodology developed for small magnitude events.

2.1. Anderson and Hough Method (Acceleration Spectrum Kappa)

The measurement of κ was initially done by obtaining linear least squares fit to the logarithm of spectrum of acceleration versus frequency of each recording between f_E, the frequency above which spectral amplitude shape is indistinguishable from exponential decay, and f_x, the frequency where the exponential decay of the acceleration spectrum becomes flat. In this high frequency range, the shape of S-wave acceleration spectrum may be defined by the following [Anderson and Hough, 1984]:

$$A(f) = A_0 e^{-\pi \kappa f} \quad (2.1)$$

where A_0 is the spectral amplitude, f is frequency and κ is the spectral decay parameter.

In their paper, they suggested a linear tendency between κ and R_{epi}, and found relatively smaller values of κ_0 for rock sites than alluvium and consolidated sediments.

After checking the records visually, they mention about the necessity of setting the spectral flattening frequency, f_x at 12-15 Hz instead of 25 Hz in their database, and suggested that *the points at 25 Hz falling above the level consistent with exponential decay may result from the noise of the records* [Anderson and Hough, 1984].

2.1.1. Uncertainties Introduced at the Application Phase

This method has been used widely and mostly in literature of κ evaluations, and many authors have indicated that this approach is better used for relatively large magnitude events. When used for smaller earthquakes, the selection of f_E was focused more than the selection of f_x due to trial of the method applied to the smaller magnitude events at the regions where large magnitude event records are not available, where there is low seismicity, such as Switzerland, eastern USA and eastern Canada, etc.

Here, a danger rises up for these small magnitude events that the record is relatively close to the signal of the noise and a clear definition of flattened portion of the Fourier Amplitude Spectrum (FAS) may no longer be identified as realized in large magnitude event records.

Even for the moderate to large earthquake records, from the same databases, this rather straight forward method could give different resulting κ values if not checked for the f_x. This uncertainty is defined in the concept of "interoperator variability" here in this PhD thesis.

2.2. Biasi and Smith Method (Displacement Spectrum Kappa)

The displacement spectrum kappa assumes the low-frequency displacement spectrum is flat below the corner frequency, f_c measuring the slope of the displacement spectrum for $f << f_c$. It is stated that for small enough earthquakes the frequency range

can match that used in the original kappa method and be applied to larger earthquakes [Biasi and Smith, 2001].

2.2.1. Applicability of the Method

Kilb et. al. [2012] suggested that widely used acceleration spectrum kappa, κ_{AS} are best applied to earthquakes above magnitude 3.5 and the displacement spectrum kappa, κ_{DS} measurements are best applied to earthquakes below magnitude 1.0. Between the as $1.0 \leq M_L < 3.5$ range, kappa results are defined and shown as somehow not well fit by these authors (Figure 2.1). One can also see especially in (a) and (d) that 1.0 < ML region follows the same ill pattern as 1.0 ≤ ML < 3.5 region.

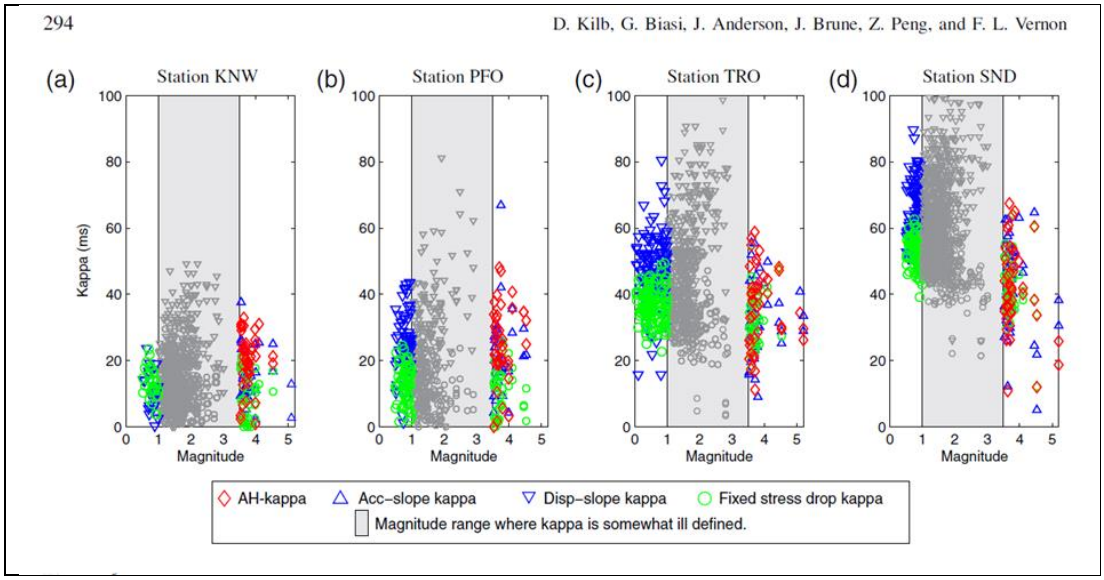


Figure 2.1: The "ill-defined" kappa region for small earthquakes.

The procedure of Anderson and Hough [1984] from acceleration spectrum (κ_{AS}) was also reported to face specific difficulties (e.g., Ktenidou et. al. [2016b], Perron et.al. [2017]) for low to moderate seismic regions while dealing with databases that include $M \geq 1.5$ events.

Using both κ_{AS} and κ_{DS} procedures, Ktenidou et. al. [2016b] evaluated κ for the data combined from different probabilistic seismic hazard project datasets that are from Swiss PRP, European RESOURCE, and Canadian BC Hydro databases for British Columbia. They also evaluated κ for Next Generation of Ground-Motion Attenuation Models (NGA)-West2 and NGA-East database separately. They assigned

a fixed V_{s30} data for NGA-East database, due to the lack of site characterization in that region. They assumed that the κ values can be set as κ_0 at surface of the stations for the events that occurred at distances up to 100 km. For estimating κ_0 at surface, mean Fourier amplitude spectrum, FAS was derived by stacking all recordings per station all together. A fixed frequency band between 15-30 Hz within the mean FAS was used to evaluate and estimate κ_0.

Perron et.al. [2017] tested both κ_{AS} and κ_{DS} procedures for $M \geq 1.5$ events Provence, southeastern France. They showed that the frequency bandwidth, $f_E - f_x$ band, used to define the decay of the Fourier spectrum is important in terms of the uncertainties of estimation of individual kappa values. They introduced a semiautomatic procedure that all of the combinations of the linear regression of this decay in between two initially picked f_E and f_x values with an initially set ± 4 Hz is evaluated, and the best in terms of residuals were picked as final κ_{AS} estimations.

2.3. Inconsistency between Application Phases

In the widely commonly used Anderson and Hough [1984] methodology, while dealing with an earthquake database to evaluate κ parameter from FAS, pre-selected assumptions that are made during the evaluation phase differs from scientist to scientist. Some of the main inconsistencies that can be listed in here are, the selection procedure applied to define the S-wave portion of the signal, the duration of the selected S-wave being restricted to a period of time (i.e. 5 s) or taking the whole S-wave selection of the signal, taking the geometric mean of the east-west and north-south horizontal FAS of the record and evaluate one κ for this mean FAS, the selection of f_E, the assignment of f_x by pre-setting the value, a fixed $f_E - f_x$ selection without checking if each and every recorded earthquake signal FAS really suits, applying different filtering, smoothing and tapering procedures, calculating κ from different approaches rather than applying straight forward the Anderson and Hough [1984] methodology but yet are compared with κ results that are evaluated with Anderson and Hough [1984] method.

Also, during the evaluation phase of κ_0, there are some pre-set assumptions observed in some studies, such as the assumption that κ_0 is magnitude independent,

taking different κ versus R_{epi} tendencies or simply neglecting a tendency, assuming an unconstrained or constrained fit to overall κ values within the R_{epi} to reach κ_0, etc.

Overall uncertainties are encountered due to either some physical parameters related to source, path and site, and due to interoperator variability. These are discussed in the "3. Uncertainty Reduction Trials" section of this PhD thesis after introducing below some examples of the inconsistencies mentioned above.

2.3.1. Inconsistency in κ Evaluations

It is important to first indicate the comparisons made between the κ results of many studies could mislead as if the same procedure is applied as a method to obtain the individual event κ values. These values can be used also during the magnitude dependency/independency, soil type dependency studies as well and yet cannot be identified if they are comparable due to the methodology behind the calculations.

An example can be given from Edwards et. al. [2011], where the authors indicated in their paper that they have used two methods including the Anderson and Hough [1984] Method for their κ evaluations. Due to the low quantity of data available in their dataset for $M > 3.5$ events, they indicated that this method was susceptible to the trade-off between source and site, and rather focused on the attenuation time (t^*) definition in Cornier [1982] indicated in Anderson and Hough [1984] paper. While calculating the t^*, they used a simultaneous broadband inversion of the whole velocity spectrum resolving for corner frequency, f_c, seismic moment, M_o and the κ derived from t^*. Their regression fit to their signals in their dataset were applied to the whole spectrum and the κ outcome was later named as "Broadband Inversion κ, κ_{BB}" by Ktenidou et. al. [2014] and "Broad-band Fitting, κ_{BB}" in Edwards et. al. [2015]. As the low magnitude events are the focus on this study, and lately for all studies with low seismic datasets, the main importance is given to f_E rather than the selection of f_x. During a broad-band fitting of the spectrum of a signal of a low magnitude event including the lower frequencies to the fit causes a higher fit to the higher frequencies of the spectrum and therefore results with a lower value of κ for the higher frequencies where the κ is defined in Anderson and Hough [1984] Method. This even results with negative values of κ as if the seismic wave does not attenuate but rather escalate at high frequencies. This gives an indication as if there is higher risk even from lower

magnitude earthquakes. The danger rises with the assumption of magnitude independency for κ evaluations and applying the same resulting κ values for expected high magnitude earthquakes while evaluating the seismic hazard and risk of the region in hand. As the focus is on f_c, and therefore f_E, for small magnitude events, the noise floor where the spectrum is flattened is missed during these calculations, especially due to the filtering, tapering, and/or smoothing phases while calculating the corner frequency, f_c. This issue will be discussed under the section "4.2. The Impact of Tapering and Filtering" in this PhD thesis.

Later the evaluation results from such as Edwards et. al. [2011] and added datasets, are also used for soil type dependency studies and are compared with other regions regardless of checking if the κ values evaluated are resulting from the same method and same approaches while applying the method. Also, κ_{BB} is suggested by Ktenidou et. al. [2014] for a possible better suit in use for stochastic ground motion simulations, while κ_0 is applied to entire frequency band for those applications. It is forgotten however, that the κ_{BB} is not a homogenous fit to FAS, where this fit focuses mainly a fit first to corner frequency, f_c and low frequencies below f_c. For Turkey, Askan et. al. [2014] validated their simulations using the regional κ_0 values they have evaluated to fit the observed mainshocks. Such validations are necessary for simulations. Analyzing further if the κ_0 fits due to the theoretical Q in depth definition corrects the κ_0 in the simulations in general or not is another wide study, which is not the main focus in this PhD thesis at this moment, as the vast interoperator variability reported since Biro and Renault [2012] first needs to be solved.

If chosen the Anderson and Hough [1984] Method, the selection of the whole signal without selecting the S-wave portion, selection of S-wave, or selecting a portion (duration) of S-wave window of the signal are also commonly in practice and the outcomes of the κ values of these signal portions are compared with each other as if the same procedure is followed. This could still be in an applicable range as the higher frequency content of the FAS of the signal, if taken the whole signal would mainly represent the S-wave portion of the signal. It is suggested here however to select the S-wave window keeping in mind that this window still holds information from P-wave, coda wave and noise, etc. inside.

The best suitable application chosen for this PhD thesis was to select the duration of the S-wave window visually with the help of a procedure developed during the course of the studies. First, the Arias Intensity of the recordings were evaluated and

the 5% of the duration is illustrated as a possible indicator for the S-wave beginning. For the possible S-wave ending, the Cumulative Root Mean Square (CRMS) were calculated and when the decreasing tendency starts in CRMS curve along with time, with the starting instant of the downward trend (Figure 2.2). In this figure, Red line indicates where 5% Arias Intensity is and blue line indicates the bending point of CRMS curve for each component of the earthquake record.

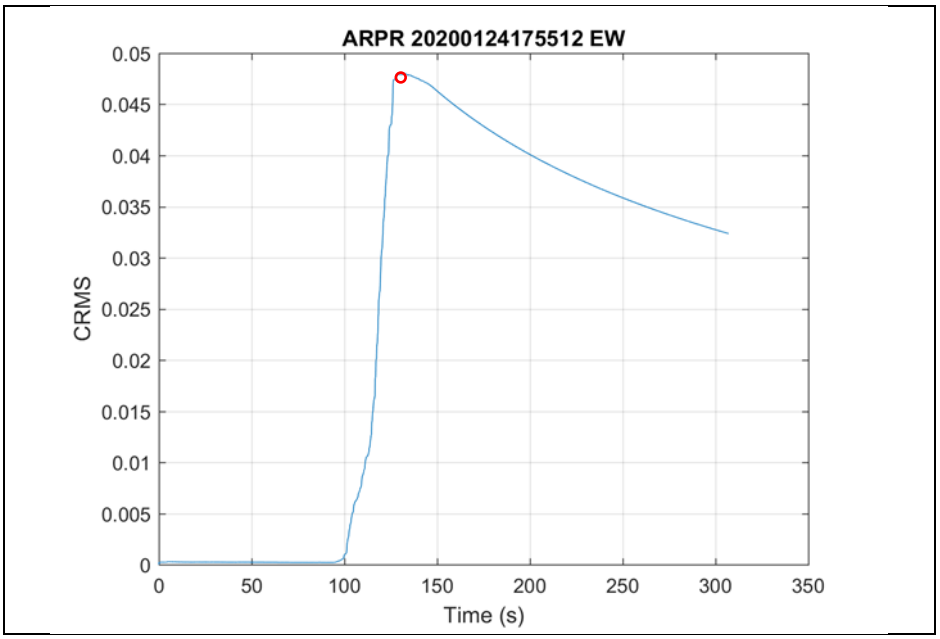


Figure 2.2: CRMS of an example recording to pick the S-wave ending.

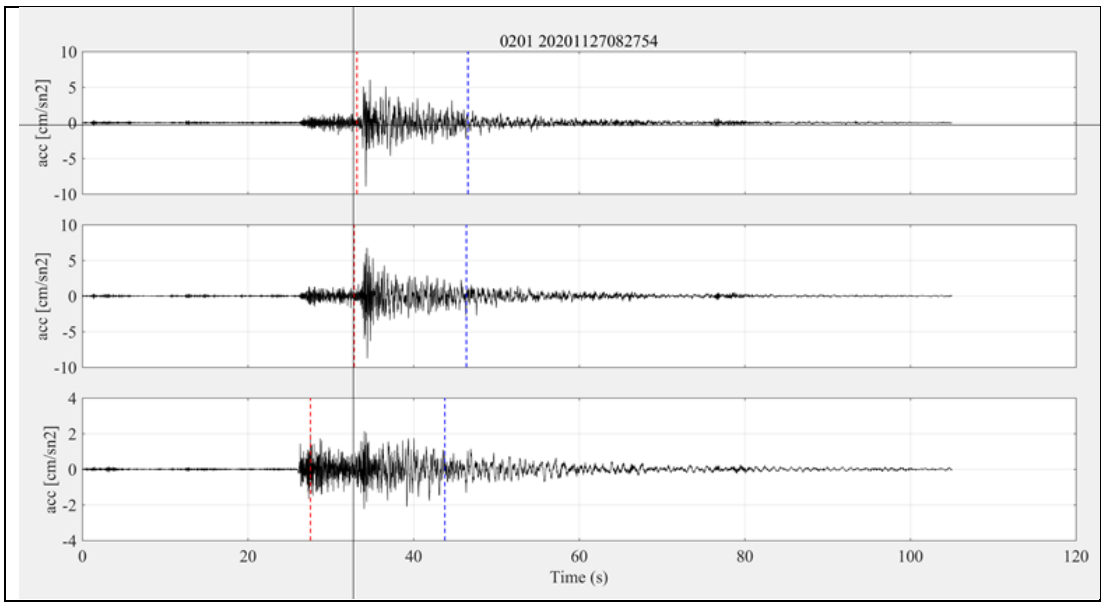


Figure 2.3: Example of the newly developed noise and P- & S-wave selection procedure.

The possible S-wave starting and ending point was illustrated in the same plot for the three components of the records at one screen. A hand selection of noise band as well as P-wave arrival and S-wave band are made from this plot as seen in Figure 2.3.

For calculation phase of this procedure, the S-wave arrival time can be defined as an onset on a curve, describing the buildup energy of an accelerogram with time, that can be represented using the following equation [Husid, 1967]:

$$H_n(t) = \frac{\int_0^t [a(t)]^2 dt}{\int_0^\infty [a(t)]^2 dt} \tag{2.2}$$

where, $a(t)$ is the time-series.

The end instant of the S-wave detecting by using CRMS function can be evaluated using the following equation [McCann and Shah, 1979]:

$$CRMS = \sqrt{\frac{1}{T}\int_0^T \|a(t)\|^2 dt} \tag{2.3}$$

where, $a(t)$ is the time-series, and T represents the computed duration.

As of the selection of f_E, the commonly used criterion is that $f_E > f_c$. The difficulties encountered during the f_c calculation phase for small-moderate earthquakes, the focus is on f_E selection in the literature. The latest approach of assigning $f_E \geq 1.5 * f_c$ value seems like solving this issue for the low-moderate seismic signal records. For large events it is easier to estimate the f_c, as it is a smaller value than the resulting f_c values from small earthquakes. Therefore, even a preset f_E value (i.e., minimum f_E = 2 Hz) could justify to catch the beginning of the FAS decay for calculations to evaluate κ.

In the course of this PhD thesis, the corner frequency, f_c was calculated according to the following procedure [Andrews, 1986]:

$$f_c = \frac{1}{2}\sqrt{\frac{I_V}{I_D}} \tag{2.4}$$

where,

$$I_V = \int_{f_1}^{f_n} V^2(f)df \tag{2.5}$$

where,

$$I_D = \int_{f_1}^{f_n} D^2(f)df \tag{2.6}$$

where $V(f)$and $D(f)$are the velocity and the displacement spectra, respectively.

Not selecting a pertinent frequency band $f_E - f_x$ introduces vast uncertainty to κ evaluations. The selection of f_E is agreed and could be easily achieved in moderate to large magnitude events as mentioned above. The selection of f_x however, is not addressed due to the tapering and filtering applied to the datasets, as these applications could demolish the visually selectable FAS flattened portion. However, this band selection is reported to have high impact on resulting κ values by many authors (i.e., Douglas et. al. [2010], Perron et. al. [2017]). Douglas et. al. [2010] mentions that f_x shows large variations due to varying signal-to-noise ratios and therefore it was not possible to use a constant value for all records since it is time consuming. Many authors deal with the same problematic issue of selecting individually the f_x, and therefore ignore its high influence and take a constant value for f_x. In this PhD thesis, the selection of f_x issue is resolved and the uncertainties of individual resulting κ values have been highly reduced when compared with literature uncertainties reported in related publications. The proposed automated f_x selection procedure in this PhD thesis is believed to help reduce the interoperator uncertainty and take the load off the time-consuming evaluation phase mentioned by Douglas et.al. [2010] by making sure the f_x selection is no longer out of its first meaning: that is the end of the linear downward trend of FAS or when the S-wave spectrum approaches the noise spectrum or the beginning of flattened shape of the FAS.

To be able to identify what is used in the literature related to the topic, these parameters and application procedures are summarized for the literature while they are mentioned so that it can be seen if these are applicable for a comparison with evaluations of this PhD thesis as well as any future study of evaluation of κ.

2.3.2. Inconsistency in κ_0 Evaluations

While comparing the κ_0 results from different studies, it is also important to check if the datasets are consisted of only a limited range of magnitude, distance, etc.

The limitation of maximum distance is important in terms of Q interference. Usually if the database allows, near field events are in value to be able to reduce this interference. To understand the trend in the region under investigation, it would be ideal to have records of different magnitude, and different distances that could give a good correlation. This is not usually the case in the literature due to the paucity of data. The low seismic regions have absence of the large magnitude event records that are close enough to the site under investigation, whereas the high seismic regions could miss the near site records of large magnitude events due to saturation of the recording device of the investigated site. When the datasets cannot provide a correlation on any relation related to the source, path and site, some pre-assumptions are made and should be taken into consideration when comparing the resulting κ_0 values with each other.

For example, in Ktenidou et. al. [2016b] it is assumed that there is no R_{epi} correlation, and the κ versus R_{epi} tendency is flat up to 100 km for estimating κ_0 at surface. Neglecting the κ vs R_{epi} tendency, they then took the mean Fourier amplitude spectrum obtained by stacking all FAS per station only for the range of a fixed $f_E - f_x$ range (15 Hz – 30 Hz) and evaluated one κ out of this mean FAS and called this κ_0 of this station. In their paper the figure for this fit is given only for the FAS between 15 Hz – 30 Hz and cannot provide an essence to see if this preset frequency band is applicable to the dataset or not. The same procedure still is applied in Ktenidou et. al. [2021] while aiming estimation of κ_0 values for rock sites in Central and Eastern North America, CENA. However, in this article the authors have also given illustration of example κ fits to FAS where they flag the records without any visible FAS trend and records with clear down going trend in the FAS, as well as records that exhibit significant near-surface site amplification. They also tried different fixed $f_E - f_x$ ranges

and illustrated in a table. Due to paucity of the new database, κ values with all flags at all distances from all stations are together taken into account for κ_0 estimation.

It is also important to mention if the κ versus R_{epi} fit is constrained or unconstrained during estimation of κ_0 values for a site.

If the dataset of recorded seismic events utilized to estimate κ_0 does not cover a wide range of magnitude, distance and are from different seismic sources with sparse coverage of station locations, defining a regional path attenuation (Q) would not be easy or even at some cases possible if no special Q model is delivered. In such cases, if there are enough near field events recorded at the site under investigation, then κ vs R_{epi} fit may be unconstrained due to lack of Q model and/or estimate and this fit may represent vaguely the path attenuation. This assumption is widely used in scientific community. When there is a possibility to assign a path attenuation estimation for a region with many recordings from many stations, then the κ vs R_{epi} fit for a site can be constrained according to this regional path correction. Such studies with constrained fit however show that the unconstrained fit may give unrealistic κ_0 estimations, especially for sites with databases that consist of far field events. Such case is illustrated in the section "7.3. Sivrice-Pütürge Segment of EAF" under KOERI Results for κ_0 estimation part of this PhD thesis.

3. UNCERTAINTY REDUCTION TRIALS

Due to the variance of the estimated κ values for same region and/or for same site or a similar site with similar soil property, there has been several trials to reduce the uncertainty in those estimations. Even though many authors and scientists report magnitude dependency possibility, due to paucity of the datasets the assumption of magnitude independency is assumed for κ_0 evaluations. When available, for a region with abundant event recordings further studies can be made unless the database includes near as well as far field events with distinguishable uniform path and source information available. This could be done for some regions in Turkey and up to now not yet been attempted. Also, the new AFAD database is not reasonably reachable with such vast amount of event data, as explained under section "7. Numerical Results" of this PhD thesis.

κ_0 estimations are also validated with the soil type dependency, while the parameter shows tendency to lower as a value when soil starts to stiffen. Some κ_0 – V_{s30} correlations are derived at the beginning of last decade but later it was figured out that for very hard rock estimates, either the previous κ evaluations were discovered to be not comparable with each other in terms of different κ estimation methodologies, or that very low κ results are due to paucity of the datasets. As the inconsistencies mentioned in section "2.3. Inconsistencies between Application Phases" are not studied in detail for a large dataset that can deliver a solution to these discrepancies, a good correlation between Some κ_0 – V_{s30} cannot be achieved.

It is also discovered lately that major uncertainties rise from the differences between κ results estimated by different operators/scientists for the same datasets and is named interoperator variability in here. This PhD thesis provides a new automatic procedure to prevent this variability, making it possible to apply it to large datasets.

Some additional uncertainties are newly mentioned and studied in literature and also are addressed here.

3.1. Stress Drop and Magnitude Dependency/Independency

The magnitude dependency tendency is encountered when the magnitude range in the databases used for κ_0 evaluations have enough range of magnitude events to be taken into account. Some scientists tried to explain this phenomenon via stress drop (i.e., Ktenidou et. al. [2017]) but could not conclude with a resolution, some indicates the tendency and yet due to not having enough data for each magnitude bin for the same site and from the same source they continue the evaluations with the assumption of magnitude independency. The possibility that κ is dependent on the magnitude have been strongly mentioned in some research (i.e., Papageorgiou and Aki [1983], Aki [1987], Papageorgiou [1988, 2003], Gariel and Campillo [1989], Wen and Chen [2012], Perron et. al [2017]) and still needs to be studied in detail.

While the uncertainties for estimating κ_0 in terms of maximum usable frequency, low magnitudes were addressed in Ktenidou et. al. [2017] also stress drop issue was discussed, and the large uncertainty in stress drop (corner frequency) for low magnitudes between $1.2 \geq M_L \geq 3.4$ (at 300 km epicentral distance) was reported as not yet being resolved. It is also important to point out that due to instrument responses the maximum usable frequency (f_x) was set to 16 Hz in their study.

Also, while evaluating the site-specific component of κ_0 on the magnitude dependency of within event aleatory variabilities (standard deviations) in ground motion models, Brooks and Douglas [2021] have demonstrated variation in stress drop parameter and found out minimal contribution to magnitude dependency, unlike the site-specific component of κ_0. They concluded that in simulations at least κ_0 was partially responsible for the magnitude dependency captured in the aleatory variability components of some recent GMPEs.

It is also worthwhile to indicate a study in Japan pointing out the seismic moment, M_o dependency while checking two different models for spectral decay. The commonly used worldwide κ model, (κ_{AS}), was compared with commonly used in Japan f_{max} (cut-off frequency) model by Tsurugi et. al. [2020]. They studied high frequency spectral decay characteristics of 105 earthquakes with $3.3 \leq M_w \leq 7.1$ for inland crustal earthquakes in Japan and compared the results from these two models. They concluded that both are applicable for the region they studied to characterize the

high frequency spectral decay. In their study the difference from the common general estimation of κ from each individual event is that the authors estimated κ from average observed spectra obtained from the records, assigning an average distance to the spectra. They also re-estimated κ for individual observed spectra for seven selected big earthquakes from their dataset and compared their results with the average value of κ suggesting the influence of the Q factors used for the analysis was small. While evaluating the κ for individual record, they used the vector summation of the two horizontal components and a frequency range between f_E and 30 Hz. In their findings they summarized that f_{max} in the f_{max} model and the f_E in the κ model tended to be smaller for large earthquakes than moderate and small earthquakes and they concluded that this tendency demonstrated a seismic moment dependency.

In this PhD study the tendency of magnitude dependency could be shown under section "7. Numerical Results" but a definitive magnitude dependent κ_0 evaluation study could not be performed due to the need to include also the smaller magnitude events and a full coverage of near and far field records with a good definition of path characteristics in the dataset. The results presented however are valuable to introduce the magnitude information on κ vs R_{epi} fit representations (section "7.1. Van Region" and section "7.3. Sivrice-Pütürge Segment of EAF" of this PhD thesis) as well as information of a possible magnitude dependency tendency.

3.2. Soil Type Dependency and HVSR

In the last decade there has been an effort to derive $\kappa_0 - V_{s30}$ correlations depending on 1993 EPRI Report very low κ_0 results for hard rock stations. Later the need to recalculate these results were found necessary and is planned to be evaluated under SIGMA-2 Project [Web 1]. Many scientists believed to have such low values at hard rock stations disregarding if the dataset in EPRI results showed good correlation or not for such regions with poor datasets. Latest, Ktenidou et. al. [2021] re-introduces the methodology discussed under section "2.3.1. Inconsistency in κ_0 Evaluations" that they have utilized in Ktenidou et. al. [2016b]. They use this method of stacking all FAS of records from all stations in a low seismic region and reach one κ value *to address the numerous challenges in CENA: a large dataset in a low seismicity stable continental region, with poor magnitude and distance coverage, undesirable*

recording sensor characteristics (low sampling rates leading to poor high-frequency resolution), high uncertainty in the regional stress drop, and lack of site-specific velocity characterization [Ktenidou et. al., 2021]. They also mention that the correlation coefficients (R^2) between 0.04 to 0.07 meaning their dataset gives 4% to 7% fit to their fitting when estimating κ_0 from measurement of each event κ, and therefore they preferred to utilize this stacking methodology instead. The event κ measurement example figures given by Ktenidou et. al. [2021] indicates that the authors preferred fits that does no longer represent the spectral decay and give an example to the inconsistencies mentioned under section "2.3. Inconsistencies between Application Phases" of this PhD thesis.

With such datasets in low seismic regions, there have been attempts to have a correlation between κ_0 and V_{s30} as mentioned above. A comparison of these is given in Biro and Renault [2012] (Figure 3.1). It should be noted that these correlations include the Swiss database and/or different κ estimation methods such as Edwards et. al. [2011] where they have κ_{BB} instead of κ_{AS} as described under section "2.3.1. Inconsistency in κ Evaluations" of this PhD thesis.

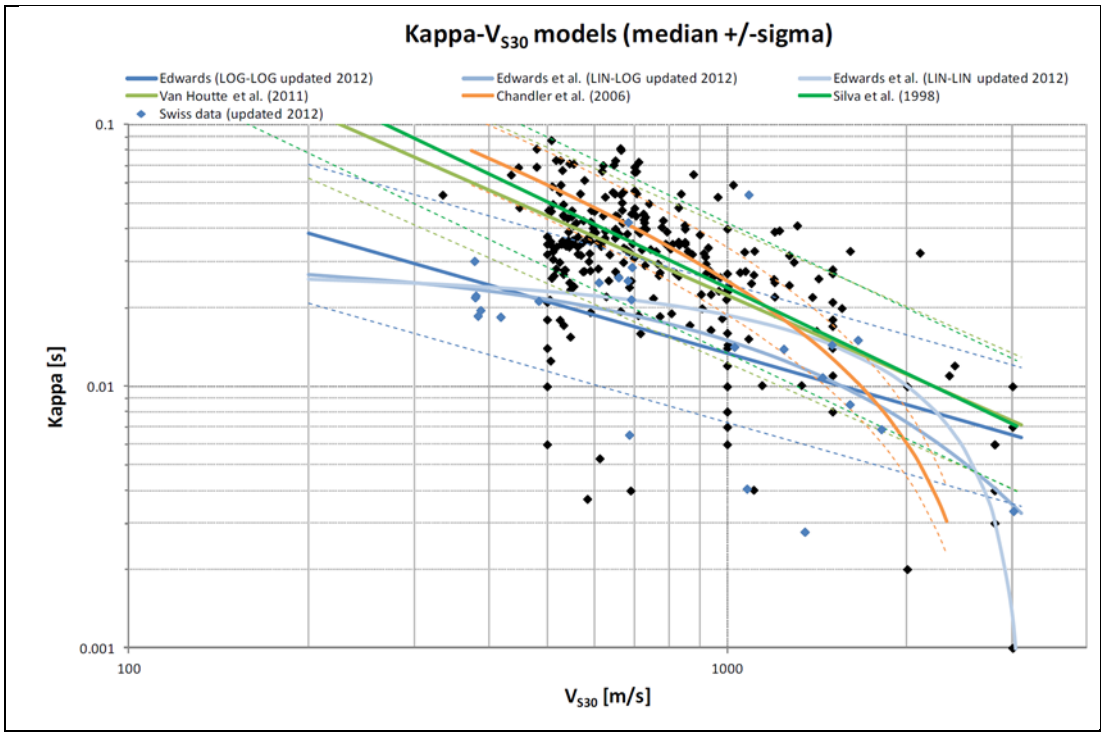


Figure 3.1: Correlations between κ and V_{s30}.

Later, Ktenidou et. al. [2014] reported that *the κ_0 – V_{s30} correlations in literature may not be directly comparable due to the possible difference in methodology used for κ evaluations or the characteristics of different regions*, and explained in detail the differences in the κ estimation methods.

In Ktenidou et. al. [2015] an alternative asymptotic functional form for correlations of $\kappa_{0,AS}$ with V_{s30} is then developed and is illustrated as in Figure 3.2. They propose a flat correlation between κ_0 and V_{s30} after reaching a V_{s30} value depending on the region, however they also indicate the lack of datasets in high V_{s30} regions.

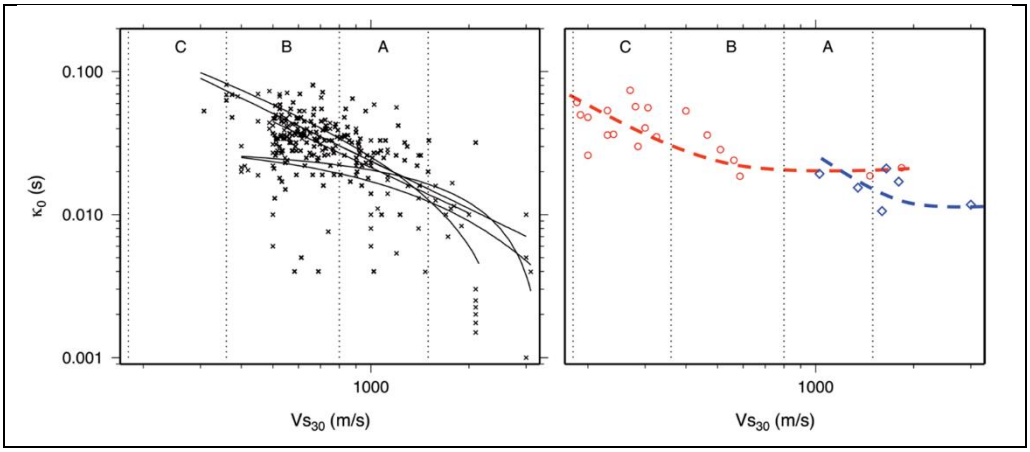


Figure 3.2: Left: existing data and correlations, all suggesting a downward tendency for hard rock. Right: the alternative asymptotic functional form for correlations of $\kappa_{0,AS}$ with V_{s30}, based on data from EUROSEISTEST (red) and Switzerland (blue), following solely the AS measurement method.

In Edwards et.al. [2015] same tendency is provided with some additional models as well as updated correlations as seen in Figure 3.3. The authors have noted that some of the models are extrapolated beyond their maximum used V_{s30} values. This paper is also investigated in terms of tapering and smoothing effects under section "4.2 The Impact of Tapering and Filtering" of this PhD thesis, therefore the estimated κ values and the station based κ_0 values can be biased due to the tapering and smoothing effects. However, these two studies by Ktenidou et. al. [2015] and Edwards et. al [2015] are good to illustrate the fact that for hard rock sites the lowering effect of κ_0 according to V_{s30} could be non or less than thought before. This is also observed in the course of this PhD thesis and is discussed under section "7. Numerical Results".

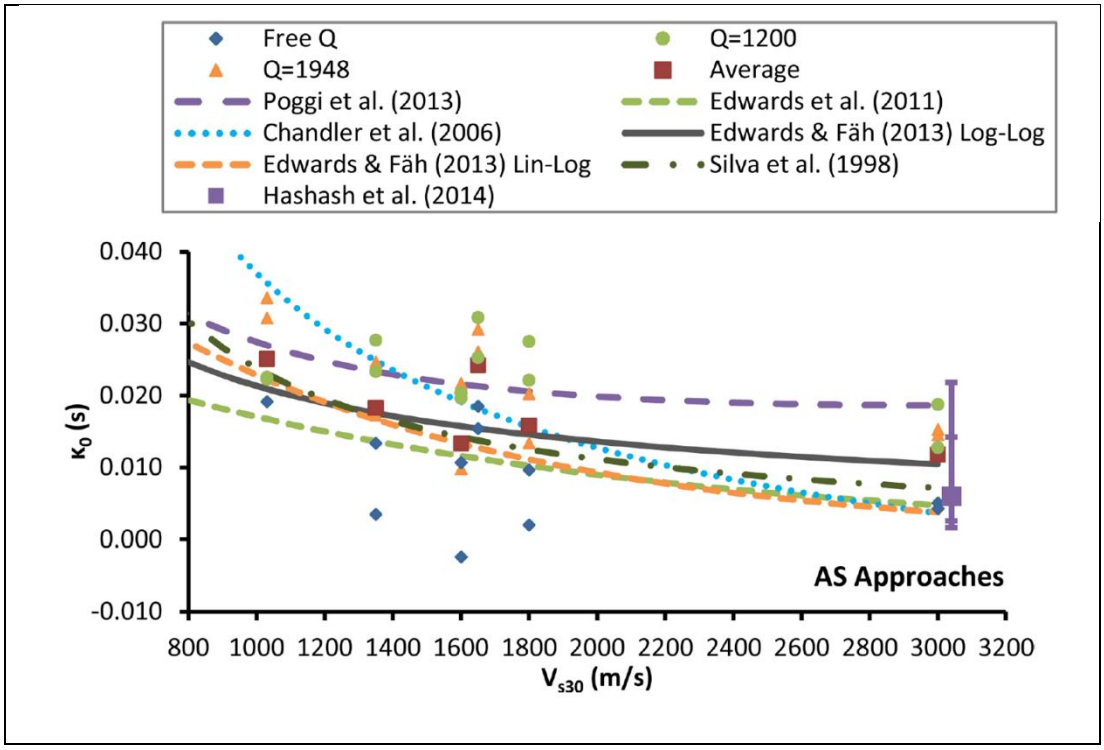


Figure 3.3: Comparison of existing Vs_{30}-κ_0 relations.

Also, κ should be evaluated more carefully, *as a site amplification component cannot be excluded even for rock sites, especially for low-seismicity context when* κ *are estimated from limited spectral windows* [Perron et. al., 2017]. For this reason, while evaluating κ, it is also important to check if the frequency band ($f_E - f_x$) chosen have any significant site amplification at a frequency in this selected frequency band. Horizontal-to-Vertical Spectral Ratio (HVSR) or standard spectral ratio (SSR) analyses are performed for this matter and are listed here while they are related to κ evaluations performed:

Horizontal-to-vertical spectral ratio, HVSR approach was first introduced by Nakamura [1989], who very recently shared his opinion and clarified a few misunderstandings about his method [Nakamura, 2019]. Later, Lermo et. al. [1993] generalized Nakamura method for S-wave amplifications. Since then, the method is vastly used in the scientific community to identify the peak frequencies and the site amplification at those frequencies. In the SESAME Project (Site EffectS assessment using AMbient Excitations, [2004]), some recommendations for implementation of HVSR technique on ambient vibrations were given.

Though exceptions can be found in the literature, there is a general consensus that HVSR approach can reveal the fundamental resonant frequency of most sites but tends to underestimate the level of ground motion amplification compared with the classic standard spectral ratio (SSR), [Zhu et. al., 2020]. Nakamura [2019] have clarified the underestimation problem by proposing a technique to correct measured HVSR as modified Quasi Transfer Spectrum (QTS). For this to be applicable, a reference rock site is needed and such reference is often difficult to find in practice; thus, the single-station HVSR technique is at least good to detect the site resonant frequency.

To evaluate the resonant frequency of a given site using spectral ratio methods, the common applications are either utilizing the complete wave form (from P arrival to the end of S coda) or partial (typically S-wave window) waveform. Then the spectral ratios are computed on either pseudospectral acceleration, PSA or Fourier amplitude spectrum, FAS of each recording, and finally the average of overall spectral ratios are defined as average spectral ratio curves. From these average spectral ratio curves, all significant peak frequencies (f_s) can be found. In SESAME guidelines [2004] the selection of f_s values was set to have certain criteria, (e.g., HVSR larger than 2.00). From all f_s, if multiple, either the first peak frequency (f_0) or the highest peak frequency (f_p) can be picked as site resonant frequency. Bora et. al. [2016] pointed out that the PSA at high frequencies is not controlled by the Fourier spectrum of ground motion at the corresponding frequencies, but rather by the entire FAS. Stafford et.al. [2017] mentioned that response spectral ratios are scenario dependent, and this dependency is strong at high frequencies. However, many researchers used PSA and FAS interchangeably, which may be one source of discrepancy in resonant frequencies. In addition to that, choice of smoothing techniques will affect the value of spectral ratio and subsequently the qualification of significant peaks [Zhu et.al., 2020].

In their recent study in examining site resonant frequency using HVSR at 207 KiK-net sites in Japan, Zhu et. al. [2020] investigated how different factors in the process affected the determination of resonant frequency, including using Fourier amplitude spectral, FAS ratio or (5% damped) pseudospectral acceleration (PSA) ratio, the degree of smoothing to spectrum, the definition of significant peaks, and the choice of the first or the highest peak frequency when there are multiple peaks. They concluded that for sites with multiple comparable peaks, the FAS ratios should be preferred over PSA ratios, indicating that for a single clear peak utilizing both PSA

and FAS made little difference. They also suggested to take the highest peak frequency, f_p, rather than the first peak frequency, f_0 for site resonant frequency for corresponding site.

Palmer et. al. [2020] studied $M_w \geq 3.5$ earthquakes in terms of κ and Q factor for Eastern and Western Canada. They applied two methods to evaluate κ, a modified version of classical S-wave acceleration method and a new stacking method and compared their results. They initially considered events up to 150 km epicentral distance for Eastern Canada, and 100 km for Western Canada. The S-wave portion of the signal was defined for a window of 15 s and the horizontal component record was defined as the geometric mean of the two component Fourier Amplitude Spectra, FAS. For the HVSR computations, they used Konno-Ohmachi [1998] smoothing method with a "*b"* value of 20 and also used the S-wave portion of the records. The f_E values were chosen as 1.5 times the corner frequency, f_c. They neglected any frequency dependence in Q over the limited frequency range considered to evaluate κ. For each station they searched for a Q value trying out from 1000 to 6000 in increments of 100. For each trial Q value, they applied the corresponding attenuation correction to the spectra before computing κ. The value of the κ_0 at each station was defined as the weighted mean of the attenuation corrected κ values. They denoted stations that could be impacted by site amplification, based on visual inspection of HVSR. They noted that κ measurements are quite sensitive to details of data selection criteria and methodology, and may be significantly influenced by site effects, resulting in large site-to-site variability.

Site classification methodologies for free-field strong motion stations, where no site information is available, and these were reviewed and validated with Wenchuan aftershock recordings while the limitations and uncertainties of the HVSR results were discussed by Wen et. al. [2011]. Forty-four sets of strong motion recordings were selected from the Wenchuan aftershocks with surface wave magnitudes of M_s 3.8 – 6.5, and with up to 268.8 km epicentral distance, R_{epi}. Assignments of weights established from HVSR values at each pseudospectral period in terms of four methods are given for one station to evaluate the differences among these methods chosen in their study. They could check their results with the known soil properties on the stations that were utilized. Later Ren et. al. [2013] evaluated site effects in the same region from 96 aftershocks of 12th May, 2008 Wenchuan earthquake (M_w = 7.9) at 28 stations using generalized inversion technique (GIT) and standard spectral ratios, SSR.

The selected dataset is with M3.7 – M6.5 and the hypocentral distance, R_{hyp}, range are between 30 km – 150 km for their dataset.

Li et al. [2020] analyzed the source, path and site effects of the 2019 M_s 6.0 Changning earthquake (17th June 2019) and eight aftershocks with surface wave magnitudes, M_s of 4.1 – 6.0 and hypocentral distances, R_{hyp} 9 km – 300 km by applying both GIT and HVSR. The quadratic mean of the two horizontal components were assigned as average horizontal FAS for HVSR calculations. The data were divided into a mountain group and a basin group, based on the travel path and station location, and the κ_0 values are evaluated for these two main groups as well as station based κ_0 values.

As we see in κ evaluations, a uniform procedure is not applied for measuring the resonant frequency in HVSR calculations as well, and are not without uncertainties. Zhu et.al. [2020] have summarized the definitions of the significant peaks from different authors for data compiled from KiK-net (Japanese Seismic-motion Seismograph Networks) sites and illustrated the differentiated results showing these uncertainties.

The nonlinear site effects are investigated for soft soil properties in terms of κ for Japanese KiK-Net database by Cabas and Ji [2020] and Ji et. al. [2021]. Their findings show that κ and κ_0 estimates are affected by soil nonlinearity, and that this influence is station dependent. When soil nonlinearity is introduced, they found out that κ and κ_0 estimates higher than that of the linear-elastic regime especially for sites with V_{s30} less than 300 m/s with up to 20% increase. It should be kept in mind that they also examined the effects of the frequency band selection on κ estimates by comparing a predetermined fixed-frequency window with an automated procedure.

These latest significant peak frequency checks are utilized therefore in this PhD thesis, where there was relevance need and are presented under section “7. Numerical Results”.

3.3. Interoperator Variability

Douglas et. al. [2010] have mentioned about large variations in κ between analysts and tied it to the selection of f_E and f_x and to the procedure followed being non-automatic and quite time-consuming and also subjective because analysts can have different views on the selection of the pre-event, P-wave and S-wave portions of

the record. This non-automatic procedure of choosing the appropriate f_x is resolved in the new method of f_x selection in this PhD thesis, which is explained under section "4. New Automatic selection procedure for spectral flattening frequency (f_x)".

A robust fit is applied lately in κ evaluation practices due to differences between resulting κ values for the same individual record from different researchers (interoperator variability) to show the possible variability. Usually, this variability is illustrated as error bars on the individual kappa values at the κ versus R_{epi} plots. One example can be seen in Perron et. al. [2017] as illustrated in Figure 3.4.

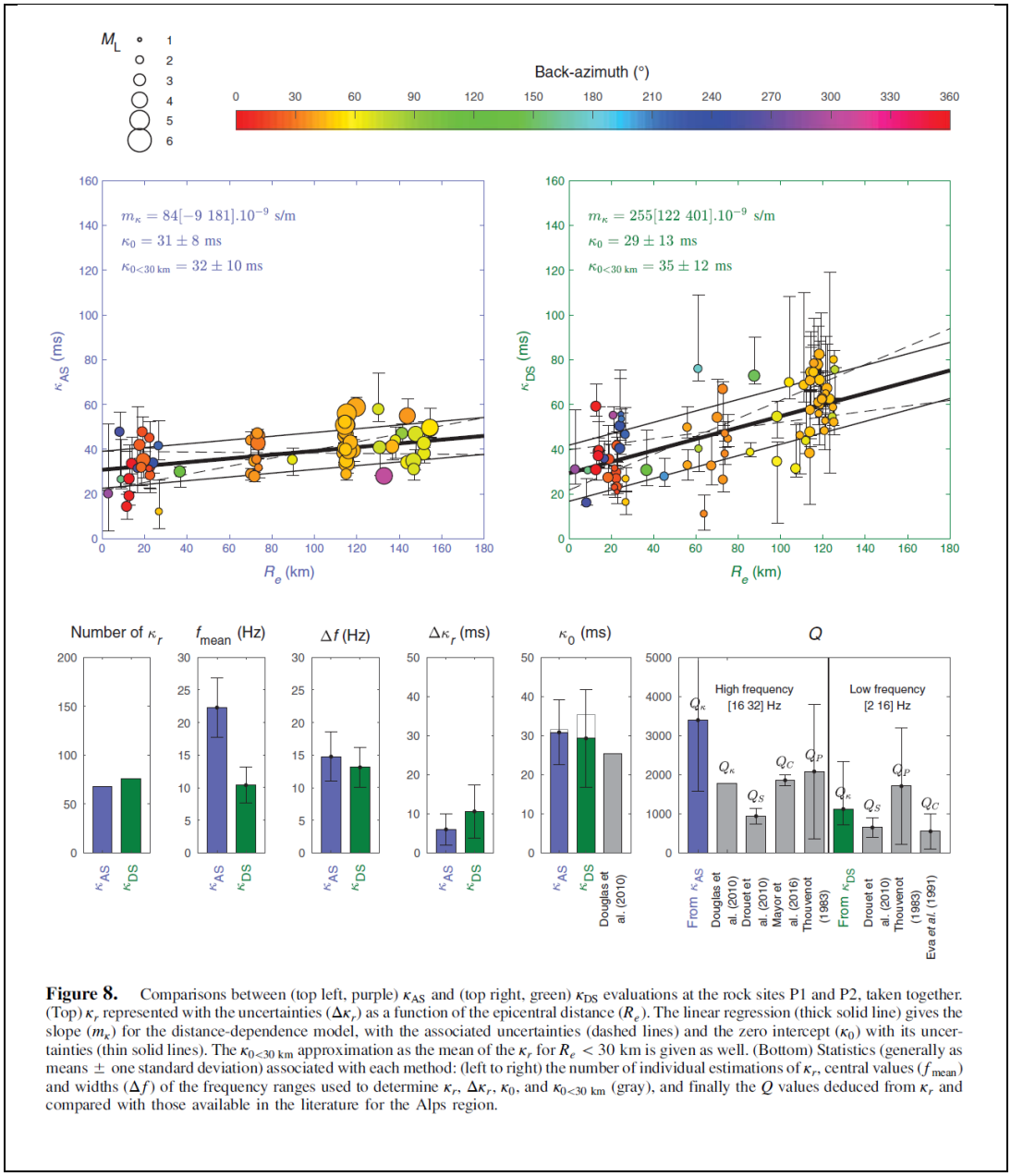


Figure 8. Comparisons between (top left, purple) κ_{AS} and (top right, green) κ_{DS} evaluations at the rock sites P1 and P2, taken together. (Top) κ_r represented with the uncertainties ($\Delta\kappa_r$) as a function of the epicentral distance (R_e). The linear regression (thick solid line) gives the slope (m_κ) for the distance-dependence model, with the associated uncertainties (dashed lines) and the zero intercept (κ_0) with its uncertainties (thin solid lines). The $\kappa_{0<30\ km}$ approximation as the mean of the κ_r for $R_e < 30$ km is given as well. (Bottom) Statistics (generally as means $\pm$ one standard deviation) associated with each method: (left to right) the number of individual estimations of κ_r, central values (f_{mean}) and widths (Δf) of the frequency ranges used to determine κ_r, $\Delta\kappa_r$, κ_0, and $\kappa_{0<30\ km}$ (gray), and finally the Q values deduced from κ_r and compared with those available in the literature for the Alps region.

Figure 3.4: Variance of kappa illustrated via error bars.

The error bars for κ_{AS} (equivalent for our κ for each record-event) can be up to 45 ms for the near site events as seen in Figure 3.4. The authors actually have tried out a new procedure to overcome the interoperator variability, but still had such great uncertainty levels for some records in hand (especially the near site recordings). Figure 3.5 is showing this new procedure [Perron et. al., [2017]:

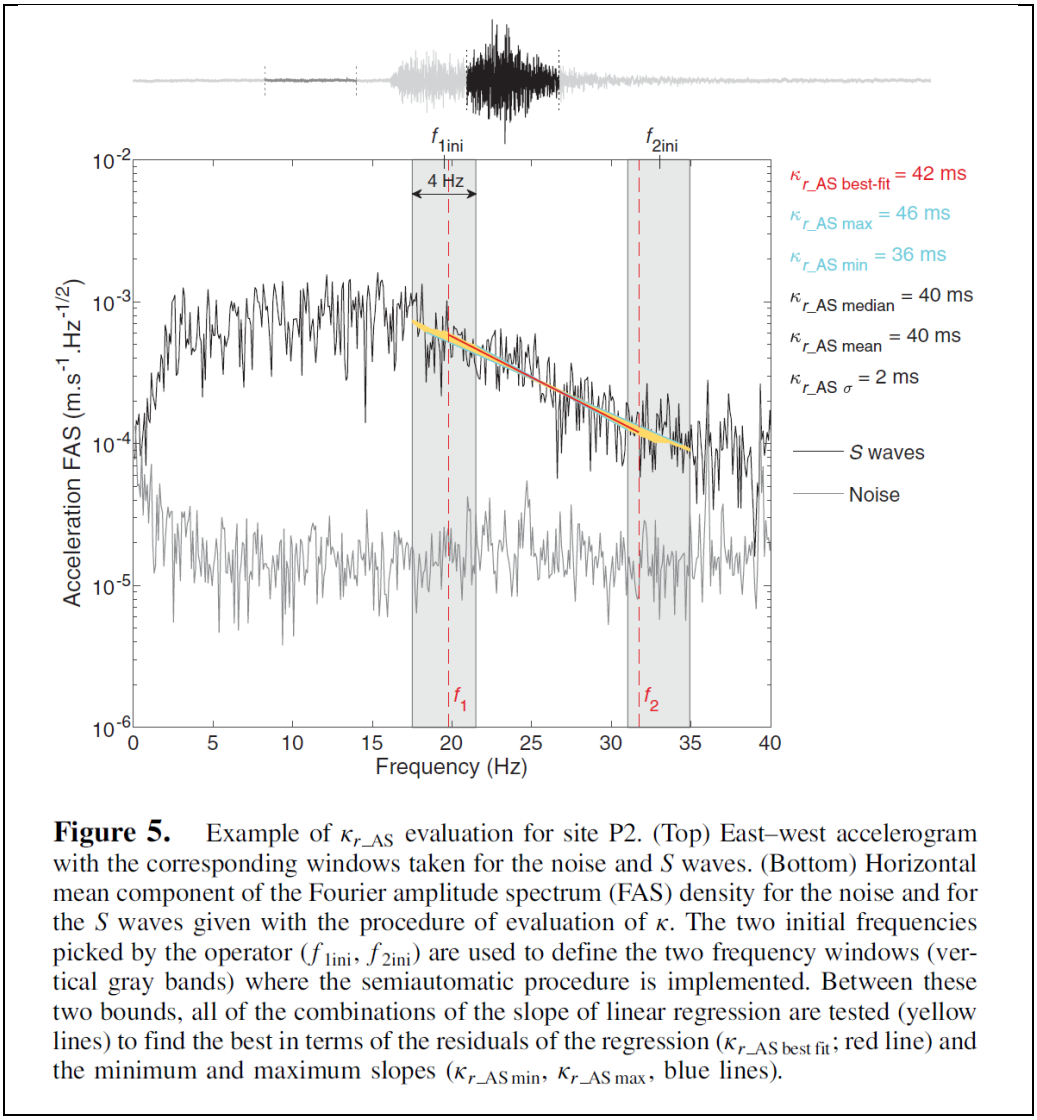


Figure 5. Example of κ_{r_AS} evaluation for site P2. (Top) East–west accelerogram with the corresponding windows taken for the noise and *S* waves. (Bottom) Horizontal mean component of the Fourier amplitude spectrum (FAS) density for the noise and for the *S* waves given with the procedure of evaluation of κ. The two initial frequencies picked by the operator (f_{1ini}, f_{2ini}) are used to define the two frequency windows (vertical gray bands) where the semiautomatic procedure is implemented. Between these two bounds, all of the combinations of the slope of linear regression are tested (yellow lines) to find the best in terms of the residuals of the regression ($\kappa_{r\_AS\ best\ fit}$; red line) and the minimum and maximum slopes ($\kappa_{r\_AS\ min}$, $\kappa_{r\_AS\ max}$, blue lines).

Figure 3.5. New procedure to reduce the interoperator variability.

The selected 4 Hz frequency band iterated between frequencies as f_E and f_x could work only if the initial f_E and f_x are selected reasonably. In this paper Perron et. al [2017] have applied a 5% cosine taper on the signal which could be the reason why a distinctive flattened portion of FAS is no longer perceived. For this purpose, the

maximum 35 Hz of evaluation of f_x could be misleading, but yet the procedure of applying Δf (herein 4 Hz), is a very valuable tool that would reduce the interoperator variability, especially if the maximum f_x selection could be set before the flattening portion of FAS begins. The high uncertainty reflected in error bars in Figure 3.4, therefore could come from the initially selected f_E and f_x values in this study. Selecting initially f_E = 10 Hz and f_x = 35 Hz and still applying 4 Hz frequency band to iterate will no longer reflect the right tendency of FAS for kappa, and will result with high error bars. In fact, the nature of the error bars reflects that the f_x selection is highly sensitive than the f_E selection (Figure 3.4), higher error for the higher decay.

While working on this PhD thesis study the new procedure of f_x selection is proposed that does not allow such tendency (Figure 3.6). It is clearly seen that the error is less than the values seen worldwide, as well as the median kappa values are almost at the mean location of the robust regression (not so much outliners).

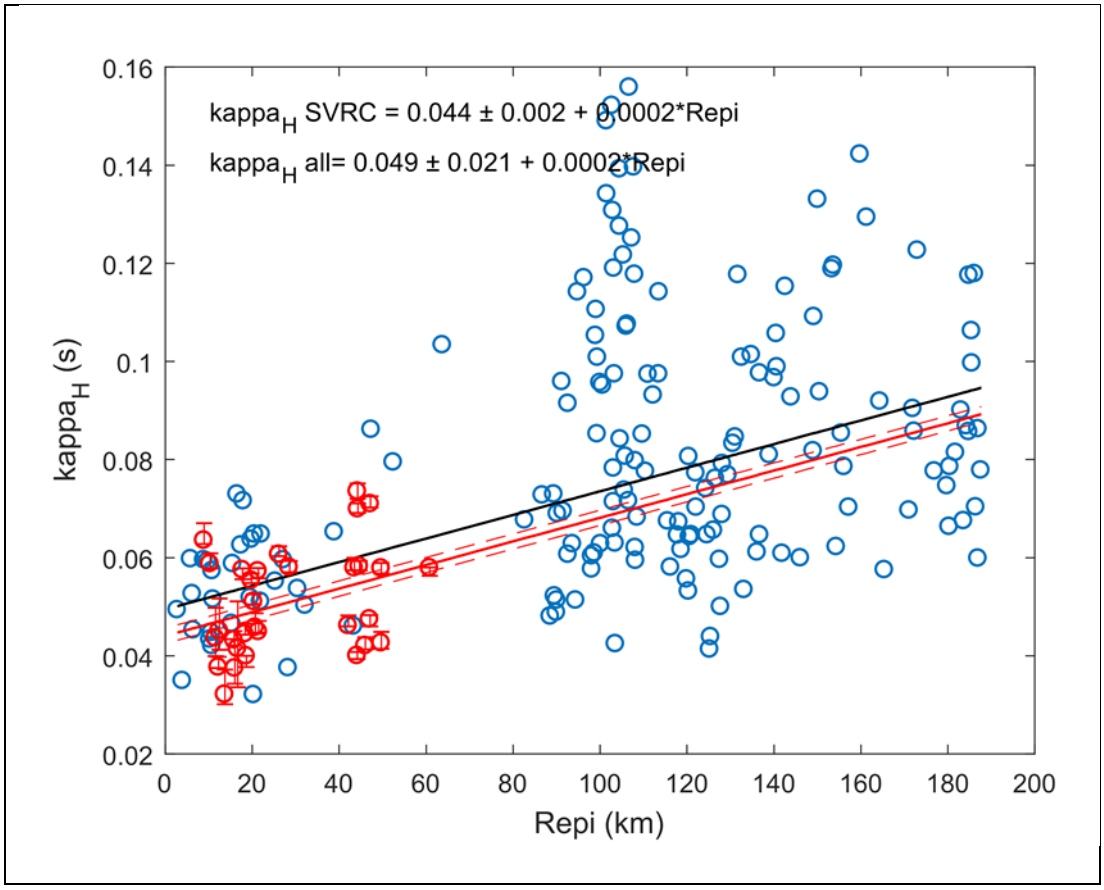


Figure 3.6: SVRC (KOERI) station kappa error bars indicated in red.

3.4. Additional Uncertainties

That is also important to point out a few more uncertainties mentioned in literature. These are related to directivity and depth of the earthquake or to instrument housing and location, meaning if the instrument is in a borehole or in a cave, etc. Some studies about these issues are cited here:

To understand the sources of the variability observed in κ and κ_0 at a single site, 10 Japanese Kiban–Kyoshin Seismic-motion Seismograph Network (KiK-net) downhole arrays were selected in Ji et. al [2020] and the systematic contributions from ground-motion directionality was investigated. It was observed that κ estimated from a single horizontal component was orientation dependent. In addition, the influence of ground-motion directionality was a function of local site conditions that they classified according to National Earthquake Hazard Reduction Program (NEHRP) site classes. They proposed an orientation-independent κ value, which is not affected either by ground-motion directionality or by the events' azimuths. In addition, they found that focal depth of events used in κ calculations affected the estimation of the regional attenuation component κ, which, in turn, influenced the within-station variability in the κ_0 model.

This paper is also important as it mentions a polynomial fit to distance dependency in κ evaluations although they did not use it, whereas in this PhD thesis it is taken a further step by analyzing the logarithmic fit to the κ versus distance trend and is given in section "7.3. Sivrice-Pütürge segment of EAF". This is suitable as it is expected that in 200 km distance the soil beneath could show non-linear behavior rather than a linear behavior with no change in the soil medium.

Hollender et. al [2020] use several examples to illustrate how small structures hosting permanent strong-motion stations (often anchored on small concrete slabs) generate soil–structure interaction effects that can amplify the high-frequency part of the earthquake signal (> 10 Hz) by up to a factor of 2–3 for stations on soils. They also show that the installation depth of a station, even if very shallow (i.e., a few meters), can change the recorded response, mainly by de-amplifying the signal in high frequencies (> 10 Hz) by a factor up to 0.3. Such effects imply that there are actual differences between recorded and true free-field signals. Depending on the housing

conditions, these effects can have significant impact on response spectra at high frequencies, and on measurements of the κ parameter.

4. NEW AUTOMATIC SELECTION PROCEDURE FOR SPECTRAL FLATTENING FREQUENCY (f_x)

The selection of the frequency where the exponential decay of the acceleration spectrum becomes flat, f_x, should be performed based on a consistent procedure to minimize the contamination introduced by the noise spectrum.

To express the importance of the f_x selection, the impact of fixed selection as well as the impact of tapering and filtering on κ evaluations are presented here.

In the course of the PhD thesis, a new procedure to select automatically the spectral flattening frequency (f_x) where the exponential decay of the acceleration spectrum becomes flat is developed and presented for the latest κ evaluations. With the proposed selection procedure, the contamination introduced by the noise spectrum could be minimized.

4.1. The Impact of Fixed f_x Selection

In the literature, we can find many fixed $f_E - f_x$ band applications without checking if each and every signal in their database really become flat at the "spectral flattening frequency (f_x)". Again, in literature there are many studies that are checking the spectral decay starting frequency f_E, and with such studies a common application of $f_E > f_c$ is in practice. The "spectral flattening frequency (f_x)" selection is however very important. If one chooses a value at the flattened part of the signal, the decay will be flattened as well and this would cause a much lower value of κ therefore this will result as a higher hazard value which is not reflecting the reality anymore (Figure 4.1). As seen in Figure 4.1, Author2 kappa Fit (orange line) gives a lower value of kappa when compared to Author1 kappa Fit (dark blue line). This figure gives also a good example of interoperator variability mentioned in Section 3.3 of this PhD thesis and will also be used when explaining the low-pass filtering and tapering applications to signal and their effect on the flattened portion of FAS and resulting kappa.

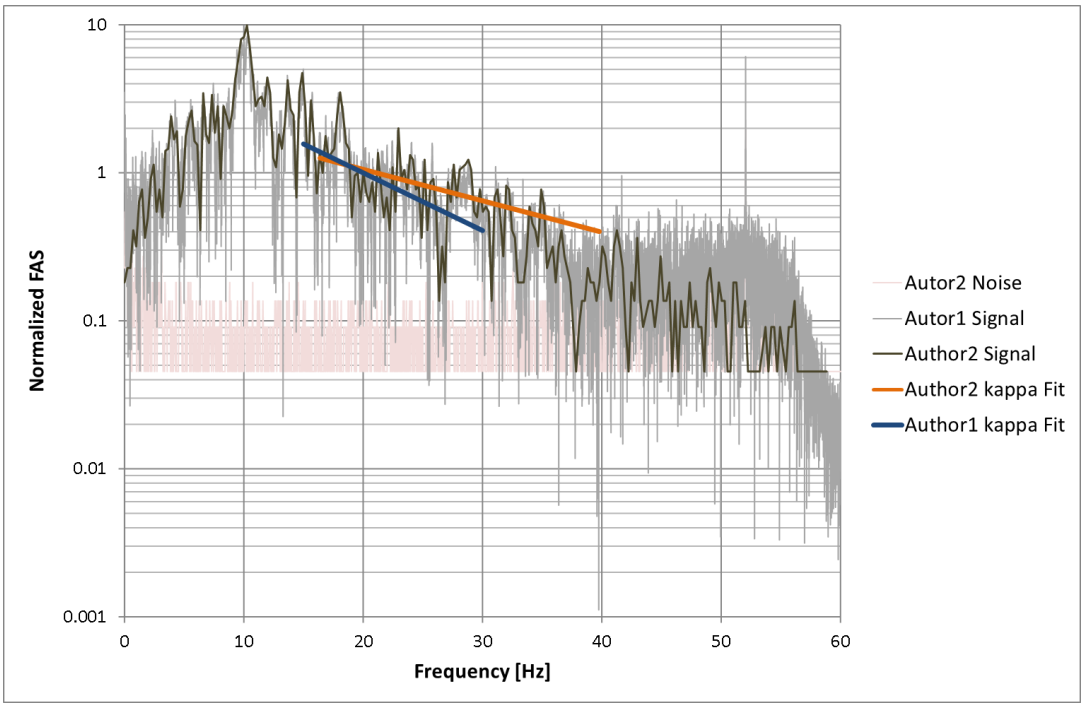


Figure 4.1: An example of kappa estimations with different choice of $f_E - f_x$ bands for the same signal.

Due to heavy load on the number of recordings to be visually checked where this flat area starts in FAS, if an automized system can be applied for selecting spectral flattening frequency (f_x) that does not allow to enter the flat zone of FAS, finally the data analysts can calculate the spectral decay for each and every recording without assuming a "fixed band of $f_E - f_x$" that might result having lower values of κ than expected as illustrated in Figure 4.1.

4.2. The Impact of Tapering and Filtering

As common practice to evaluate the corner frequency, f_c, and other source parameters, where frequency resolution at Fourier amplitude spectrum is important a type of tapering is applied to the signal. Some authors smooth the resulting FAS as well.

Using the tapered signal for FAS during the κ evaluations however could affect the amplitudes of the spectrum where the linear fit is applied. While calculating the frequency content of a signal via Fast Fourier Transform (FFT), the mathematical application has a "spectral frequency leakage" problem, and tapering at the beginning

and the end of the signal is used to overcome this problem with different windows. While trying to fix this problem, the amplitude accuracy could be lost. As during the κ evaluations, the shape of overall FAS and the linear fit to the amplitudes between a selected frequency band on this FAS is dealt, more precaution is needed. For example, it is well known that, if a Tukey window is considered, the frequency resolution is good, but amplitude accuracy is poor. Instead, if a Hanning window is considered, the frequency resolution is also good and the amplitude accuracy is fair, slightly better than Tukey windowing.

While Hanning window does a good job of forcing the ends to zero, it also adds distortion to the wave from being analyzed in the form of amplitude modulation; i.e., the variation in amplitude of the signal over the time record this windowing is applied. Amplitude modulation in a wave form result in sidebands in its spectrum, and in the case of the Hanning window, these sidebands, or side lobes as they are called, effectively reduce the frequency resolution. It is as if the analyzer frequency "lines" are made wider. If a signal component is at the exact frequency of an FFT line, it will be read at its correct amplitude, but if it is at a frequency that is one half of delta *f* (one half the distance between lines), it will be read at an amplitude that is too low. When a linear fit is made for a range of FAS, a different slope for tapered and un-tapered FAS will be achieved. Figure 4.2 shows an example on the effect of such tapering on resulting κ value.

As a summary, in κ evaluations, the concern is the amplitudes, not the single frequency resolution, but a range of frequency band. Losing the true amplitudes could give false κ values as a result.

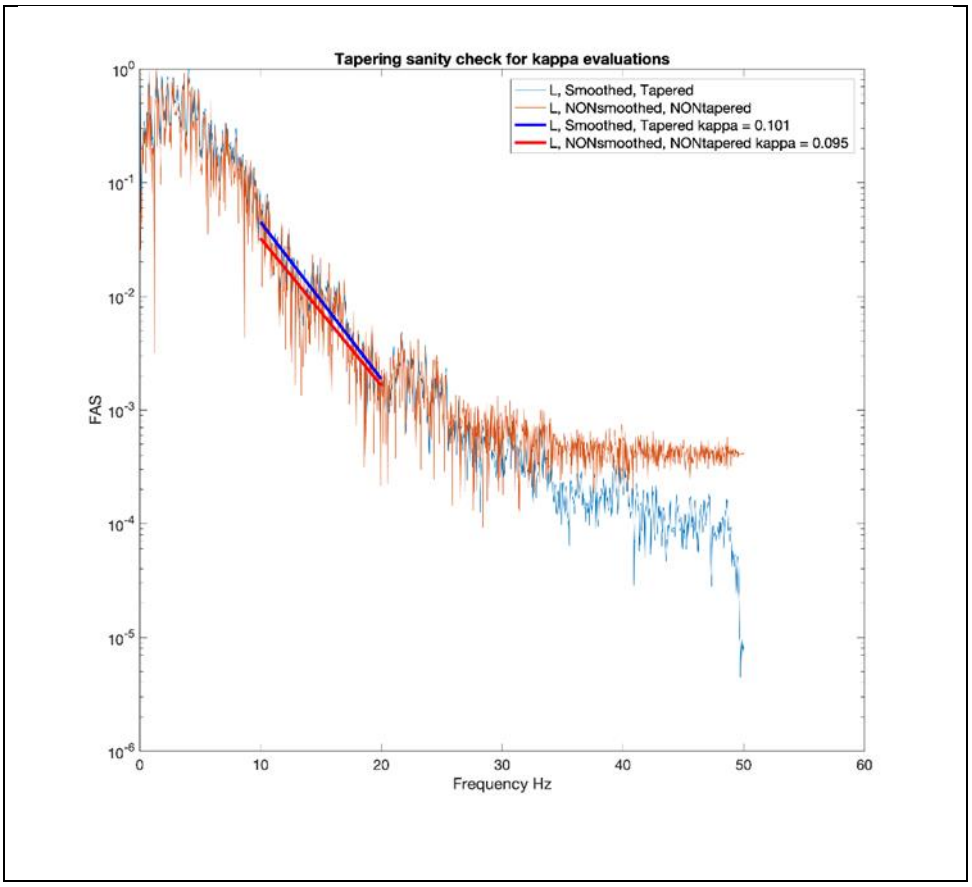


Figure 4.2: Comparison of κ fits for raw and tapered signal. (6% difference in κ values in this example).

Also in Figure 4.1, Author2 signal is tapered and then Fourier transformation is made and smoothed as well. Tapering results with losing the FAS flattening shape that can be visually still seen in Author1 FAS signal in grey. This gives a false indication to the scientist as if the linear fit could be applied at higher frequencies although the flattened FAS is reached but no longer can be visually seen. Assigning the correct FAS flattening frequency, f_x therefore, has significant importance.

Smoothing could also be dangerous as the amplitudes that a line fit is made could be lost. It is also seen in Figure 4.1 that the resulting κ value for Author2 does no longer represents the linear fit of the signal in investigation, thus results in a lower κ value that would affect the hazard calculations as mentioned in Biro and Renault [2012].

Another good example about the possible effects of tapering and smoothing can be given from Edwards et. al. [2015]. The $M_L > 2$ for all Swiss stations at the rock sites of the Alps are in review in this referenced article. In their study, the signals were first tapered for the whole record using a Hanning window of 5% width, then the noise and

S-wave windows were manually selected. These selected windows then were re-tapered with Hanning window of 2.5% width and then the FFT was applied.

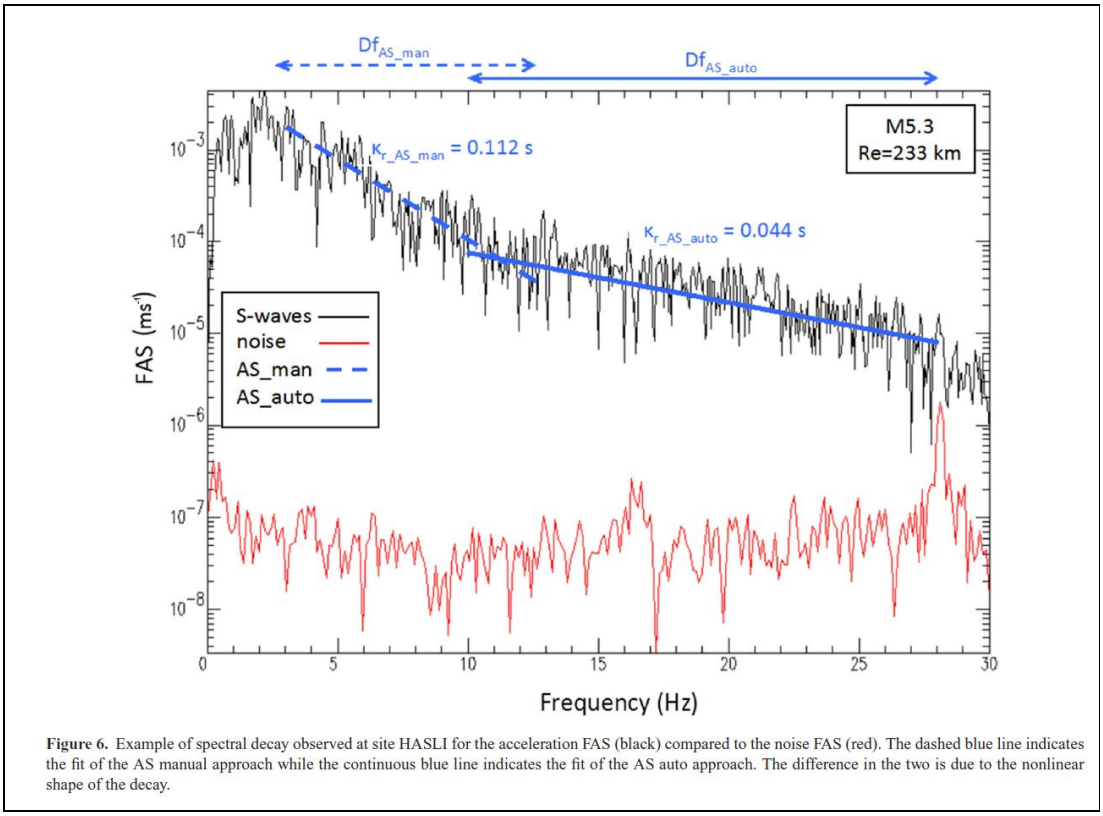


Figure 6. Example of spectral decay observed at site HASLI for the acceleration FAS (black) compared to the noise FAS (red). The dashed blue line indicates the fit of the AS manual approach while the continuous blue line indicates the fit of the AS auto approach. The difference in the two is due to the nonlinear shape of the decay.

Figure 4.3: An example of spectral decay of FAS.

It can no longer be identified if the bilinear form in Figure 4.3 from in Edwards et. al. [2015] is actually a result of double tapering and smoothing and/or really the signal gives such FAS form due to microseismic events in their dataset. An automation is made in this study for κ evaluations which identifies the later decay, thus a very low κ value (2.5 factor difference in between two κ values evaluated here). The cost of such results is enormous as discussed in Biro and Renault [2012].

A methodological mistake of computing κ above the usable frequency of the record (low-pass corner) could also be encountered. For example, if a filtering of low-pass at 20 Hz is applied to the signal, the amplitudes of FAS above 20 Hz is filtered out. A linear fit to FAS at any frequency greater than 20 Hz for κ evaluation cannot be applied anymore. The signal itself is no longer representing the correct amplitudes at $f \geq 20$ Hz (Figure 4.4).

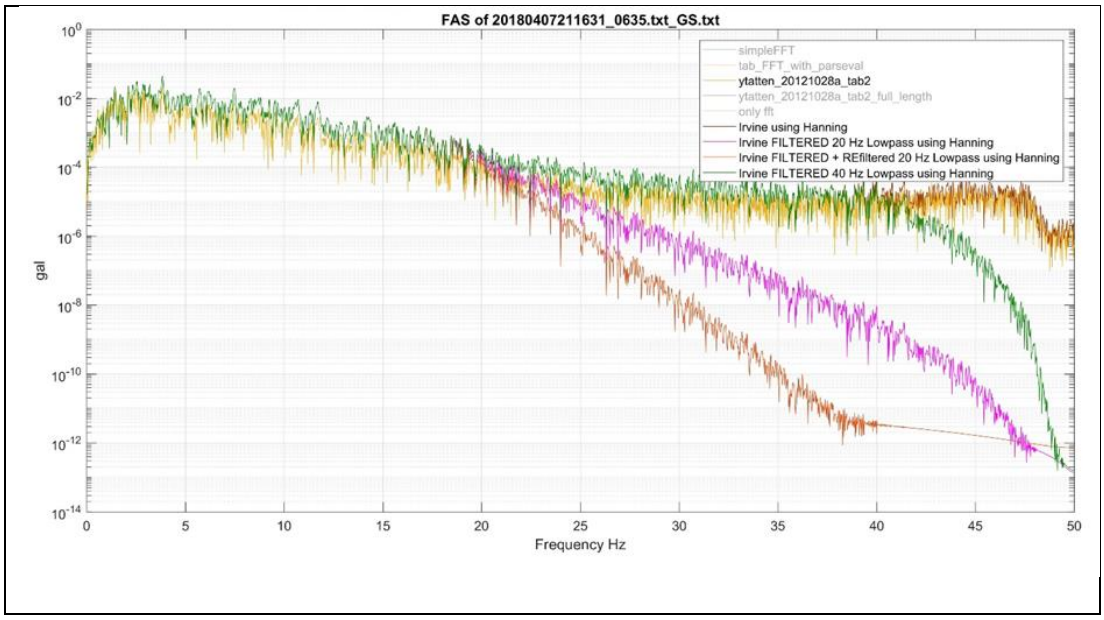


Figure 4.4: The effect of low pass filtering to a signal on FAS.

It should be noted that for this PhD thesis no filtering or tapering is applied to the dataset for κ evaluations as the impact of applying tapering to the lengthened S-wave portion was high and mathematically could not anymore justify that we have chosen an S-wave portion of the signal with actual amplitudes observed. A bandpass filter did not influence the κ estimation at high frequency region of the spectrum as the f_x was picked simply by checking the noise signal with the new procedure developed for this PhD thesis.

4.3. The New Procedure for f_x Selection

A new approach to automize the pick of f_x is developed in the course of the PhD thesis. In this new approach, the whole data recording is taken into account before picking the S-wave portion and is Tukey windowed and smoothed. The Fourier Amplitude of both noise and signal are plotted together in semi-logarithmic base with FAS in logarithmic values, and polynomial fits are applied to both as shown in Figure 4.5.

If the fitted polynoms are intersected after f_E, then the intersection frequency is set as f_x. When there is no intersection, the minimum difference occurring frequency to a previously set initial f_x (f_{xi}) is picked. Depending on the soil properties of the

stations, different f_{xi}'s were observed to be applicable. By this way a possible fit to higher frequencies are made possible up to the limitations of the station.

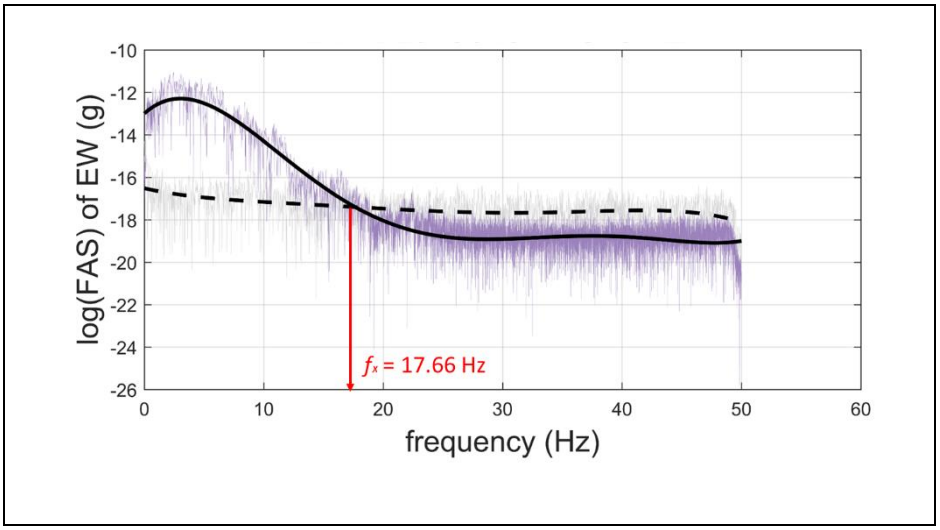


Figure 4.5: Example of the newly developed automized f_x pick.

Then the evaluation phase of κ can be achieved by picking an S-wave portion of the signal, no tapering and filtering applied with the pre-set f_E according to corner frequency, f_c and the automatically selected f_x. An example of κ estimation for the signal in Figure 4.5 is illustrated in Figure 4.6.

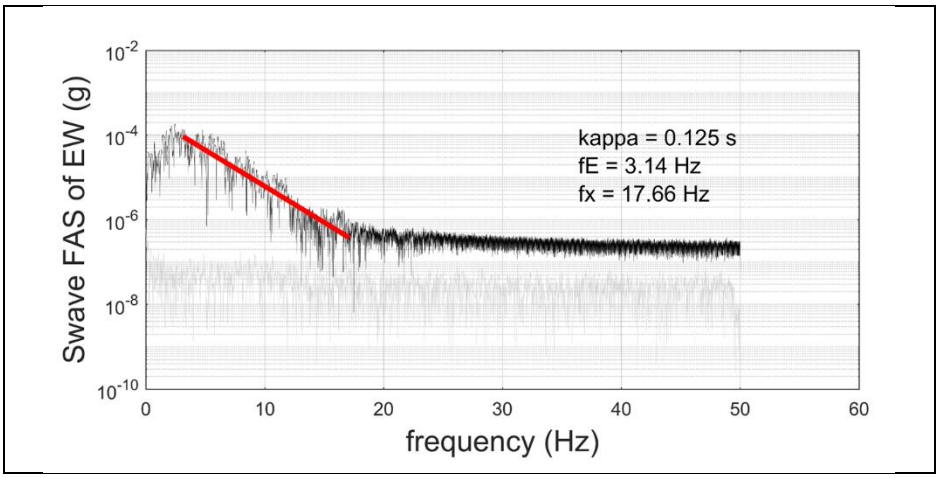


Figure 4.6: Example of κ estimation after the newly developed automized f_x pick from Figure 4.5.

5. LINEAR FIT versus ROBUST FIT

In the course of the evaluation practices for both individual event κ and κ_0 evaluations, least squares linear fit is applied regardless of the dataset if it is allowable or not. This approach also did not give the error indication of such approach. Nevertheless, the traditional ordinary least squares estimate for regression models are highly sensitive to outliers. To overcome this limitation, robust regression analysis is performed lately for both individual event κ and κ_0 evaluations.

In Turkey only ordinary least squares estimate for regression models were used since the first application of Anderson and Hough [1984] Method. In this PhD thesis, for κ evaluations of Sivrice-Pütürge Segment of EAF, the robust regression fit is applied for the first time for a dataset in Turkey. This procedure is first selected due to the recognizable outlier effect of ARPR station of KOERI. Also, the same fitting procedure is followed for AFAD stations in the region and the results are given under section “7.3. Sivrice-Pütürge Segment of EAF”.

It is suggested to use robust regression rather than linear regression fit for all datasets in the future, as the outlier effect might not be recognizable by visual observation for κ_0 and especially event based individual κ evaluations.

5.1. Linear Regression Fit

If the data shows a leaner relationship between two variables, the line that best fits this linear relationship is known as a least squares linear regression line. The term “least squares” is used because it is the smallest sum of squares of errors, which is also called the "variance."

As mentioned before the least squares linear regression fit was applied in the original Anderson and Hough [1984] Method, and since then is applied to databases for κ estimations.

The main disadvantages of linear least squares are limitations in the shapes that linear models can assume over long ranges, possibly poor extrapolation properties, and sensitivity to outliers. For this reason, lately the robust regression fit is applied in the field of κ evaluations.

5.2. Robust Regression Fit

Robust regression uses a method called “iteratively reweighted least squares” to assign a weight to each data point. This method is less sensitive to large changes in small parts of the data. As a result, robust linear regression is less sensitive to outliers than standard linear regression.

In weighted least squares, the fitting process includes the weight as an additional scale factor, which improves the fit. The weights determine how much each response value influences the final parameter estimates. A low-quality data point (for example, an outlier) should have less influence on the fit. To compute the weights w_i, one can use predefined weight functions.

The iteratively reweighted least squares algorithm automatically and iteratively calculates the weights. At initialization, the algorithm assigns equal weight to each data point, and estimates the model coefficients using ordinary least squares. At each iteration, the algorithm computes the weights w_i, giving lower weight to points farther from model predictions in the previous iteration. The algorithm then computes model coefficients using weighted least squares. Iteration stops when the values of the coefficient estimates converge within a specified tolerance. This algorithm simultaneously seeks to find the curve that fits the bulk of the data using the least-squares approach, and to minimize the effects of outliers.

The iteratively reweighted least-squares algorithm follows this procedure:

- Start with an initial estimate of the weights and fit the model by weighted least squares.
- Compute the adjusted residuals. The adjusted residuals are given by

$$r_{adj} = \frac{r_i}{\sqrt{1 - h_i}} \tag{5.1}$$

where r_i are the ordinary least-squares residuals, and h_i are the least-squares fit leverage values. Leverages adjust the residuals by reducing the weight of high-leverage data points, which have a large effect on the least-squares fit.

- Standardize the residuals. The standardized adjusted residuals are given by

$$u = \frac{r_{adj}}{Ks} = \frac{r_i}{Ks\sqrt{1-h_i}} \tag{5.2}$$

where *K* is a tuning constant, and s is an estimate of the standard deviation of the error term given by *s* = MAD/0.6745.

MAD is the median absolute deviation of the residuals from their median. The constant 0.6745 makes the estimate unbiased for the normal distribution. If the predictor data matrix *X* has *p* columns, the software excludes the smallest *p* absolute deviations when computing the median.

- Standardize the residuals. The standardized adjusted residuals are given by

$$w_i = \begin{cases} (1-u_i^2)^2 & ,|u_i| < 1 \\ 0 & ,|u_i| \geq 1 \end{cases} \tag{5.3}$$

- Estimate the robust regression coefficients *b*. The weights modify the expression for the parameter estimates *b* as follows

$$b = \hat{\beta} = (X^T WT)^{-1} X^T W y \tag{5.4}$$

where *W* is the diagonal weight matrix, *X* is the predictor data matrix, and *y* is the response vector.

- Estimate the weighted least-squares error

$$e = \sum_{1}^{n} w_i (y_i - \hat{y_i})^2 = \sum_{1}^{n} w_i r_i^2 \tag{5.5}$$

where w_i are the weights, y_i are the observed responses, $\hat{y_i}$ are the fitted responses, and r_i are the residuals.

- Iteration stops if the fit converges or the maximum number of iterations is reached. Otherwise, perform the next iteration of the least-squares fitting by returning to the second step.

6. κ ESTIMATIONS in TURKEY

In terms of κ evaluations for Turkey, the main focus was mainly in Western Turkey region, whereas the HVSR evaluations have more coverage in terms of location in Turkey. Main studies of HSVR in Turkey are calculated from microtremor measurements. For this PhD thesis the HVSR are evaluated from real events and is used as visual inspection for site amplification at the peak frequencies whether these interfere with the κ evaluation frequency ranges similar to Palmer et. al. [2020] which is mentioned above.

For northwestern Turkey, Askan et. al. [2014] have developed regional κ_0 estimates for two NEHRP site classes, Site C and Site D. This was performed by combining all κ value estimations from all stations at the same type of NEHRP site class. In this paper a multivariable linear regression involving different site classes with respect to distance was provided for regional kappa evaluation in Turkey. Simulations of two big earthquakes, 1999 Gölkaya (M_w=5.2) and 1999 Düzce (M_w=7.1), that struck the region were used to validate their proposed κ model. The dataset used in their study was collected from events with magnitudes between $3.0 < M_w < 6.0$, where 60 out of 142 events are between the magnitude bin of $3.0 < M_w < 4.0$. For κ estimations, events within 200 km epicentral distance, R_{epi} and a fixed value of 5 s S-wave window of the records were selected. Although they found no indication of magnitude dependency in their study, they suggested further evaluation with more complete datasets that might yield different results for magnitude dependency of the κ parameter.

Kurtulmus and Akyol [2015] have analyzed local earthquakes in the central west Turkey, with magnitude range of $2.0 < M_L < 5.6$ and hypocentral distance, R_{hyp} ranging from 3.5 km to 205 km. They compared vertical motion generalized inversion technique (GIT) site transfer functions with HVSR estimates and as a result they concluded that HVSR might underestimate the site response. The authors did not include the regional Q attenuation effect for the κ_0 estimations and represented the resulting κ-distance relations of 27 stations in their study without the Q correction which yielded at some stations a negative trend of κ-distance relationship.

Tanircan and Dikmen [2018] used a magnitude range of $3.0 \leq M_L \leq 4.8$, with up to 200 km epicentral distance, R_{epi} to estimate horizontal average κ values for three downhole arrays and two engineering bedrock situated instrument recordings at the western side of the Bosporus, Istanbul. A 5-15 s portion of the S and noise window was selected for spectral analysis depending on the magnitude and distance of the earthquakes. They used constant Q by pointing out that in large distances Q dominates the κ value estimate, therefore uncertainty in κ increases with increasing distance. The resulting κ_0 values for each station were also checked whether they correspond to the V_{s30} - κ_0 relations with hard rock conditions studied in the literature. They noted that the recordings of downhole arrays might be affected by reflections from different velocity interfaces depending on the depth they are overlain resulting that the κ values might be overestimated.

In terms of spectral analysis of earthquake sequences after a main earthquake event, many studies have been published in literature among which Durukal et. al. [1998], Durukal and Catalyurekli [2004] can be listed related to this PhD thesis.

Durukal et. al. [1998] have evaluated seismic parameters, including κ, of 1st October, 1995 Dinar earthquake (M_w = 6.0) and its aftershocks. A parametric analysis was attempted to understand the correlation of damage distribution with the fault parameters. In terms of κ evaluations, the mainshock at four stations ranging with epicentral distances, R_{epi} from 25 km – 110 km, the aftershock of 11th October, 1995 (M_s = 4.1) at five mobile stations established after the mainshock ranging epicentral distances, R_{epi} from 12.80 km – 14.25 km, and for the events recorded at Dinar station were evaluated separately.

While determining the seismic moments, M_o corner frequency, f_c and other spectral parameters, Durukal and Catalyurekli [2004] have also evaluated the κ values and HVSR for the 84 events with magnitudes changing between M_L 1.93 and 6.04 and within 40 km of hypocentral distance, R_{hyp} during 21st August 1999 and 29th December 1999 period in Kocaeli and Düzce regions. They found average κ values of 0.056 s for NEHRP D Site Class and 0.041 s for NEHRP C Site Class. They also pointed out that κ tended to increase with earthquake magnitude. For their HVSR results, in terms of amplification for both NEHRP C and D Site Classes the levels of amplifications were similar, and in terms of frequency behavior, the C-type soil had larger high frequency content than D-type soil.

If the datasets utilized in Turkey region are introducing more site, source, path and interoperator variability due to selection of methods, those studies are not cited here in this PhD thesis.

7. NUMERICAL RESULTS

Before presenting the numerical results of this PhD thesis, it is vital to mention about the available datasets for κ evaluations, since this identifies if the results are representative of the region, or location under investigation. Many of the literature related to κ evaluations are not listed or mentioned in this PhD thesis due to the incomparable nature of incomplete datasets which result inconsistencies mentioned under section "2.3. Inconsistency between Application Phases".

As indicated in section "3.1. Stress Drop and Magnitude Dependency / Independency" without having a complete database with good spread of magnitude variety from both near and far field events, the source and path behavior of the region under investigation cannot be identified with a good correlation. Due to lack of data, the application so far is to take a limited magnitude range and/or wide range of distance including path uncertainties to overcome the problem of having not enough near field recorded events. As mentioned before even stacking all records together from different stations are sometimes applied due to paucity of the data. It should be kept in mind that the correlation in such cases presented are not representative anymore.

The majority of the κ related literature of especially last decade is utilizing low seismic databases with hard rock conditions due to the target selection of the hazard and risk studies at low seismic regions, like PRP Project of Switzerland. In the course of this project also small magnitude adjustments to present at time GMPEs (NGA) were made.

Former NGA model GMPEs depend on datasets of events $M \geq 4.0$ and reported by many authors that they overpredicted the peak ground acceleration (PGA) for $M \leq 4.0$ earthquakes, and slightly over predicted PGA from the $4.2 \leq M \leq 4.8$ earthquakes (Ancheta et. al. [2013]). While realizing the V_s– κ correction functions to these former NGA GMPEs in the course of PRP Project however, the effect of such corrections at high frequencies, also including PGA for hard rock target sites were significantly high. One example of a site under investigation for Abrahamson and Silva [2008] GMPE correction to a target site is given in Figure 7.1 [Biro and Renault, 2012]. The need to update these GMPEs with a better spread of database rose after such findings.

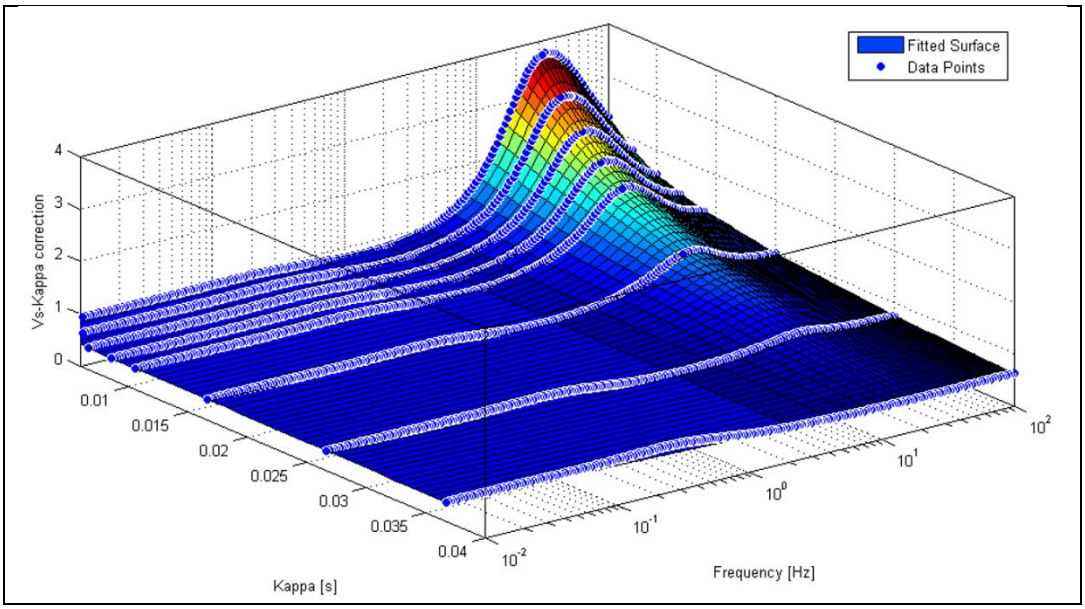


Figure 7.1: Example parameterization of $V_S - \kappa$ correction functions by fitting a surface to the evaluated correction functions.

To build up a better fit of GMPEs for also low seismic events, new generation GMPEs, now called "Ground Motion Models (GMMs)", are generated under NGA-2 Project. Worldwide dataset of events recorded from shallow crustal earthquakes in active tectonic regimes with $M \geq 4.0$ and events from California with $3.0 < M < 5.45$ recorded between 1998 – 2011 were collected and for the NGA-West2 ground motion database [Ancheta et. al., 2014].

The dataset event distribution of former and new NGA databases for shallow crustal earthquakes in active tectonic regimes can be seen in Figure 7.2 [Ancheta et. al., 2013]. Open blue squares are stations included in the NGA-West1, solid red squares are stations added from worldwide events and orange triangles are stations added from California only from small-to-moderate magnitude events (magnitudes 3 to 5.5). As an outcome new GMPEs (GMMs) were derived by Abrahamson et. al. [2013, 2014], Boore et. al. [2013, 2014], Campbell and Bozorgnia [2013, 2014], Chiou and Youngs [2013, 2014], Idriss [2013, 2014]. A comparison of these GMMs for their application limits is made by Gregor et. al. [2014] and these should be kept in mind while practicing earthquake hazard calculations.

For stable continental regions, the new NGA-East ground motion database includes selected events with $M > 2.5$, distances up to 3500 km recorded in the Central and Eastern North America (CENA) region since 1976 [Goulet et. al., 2021]. The event distribution for this database is given in Figure 7.3.

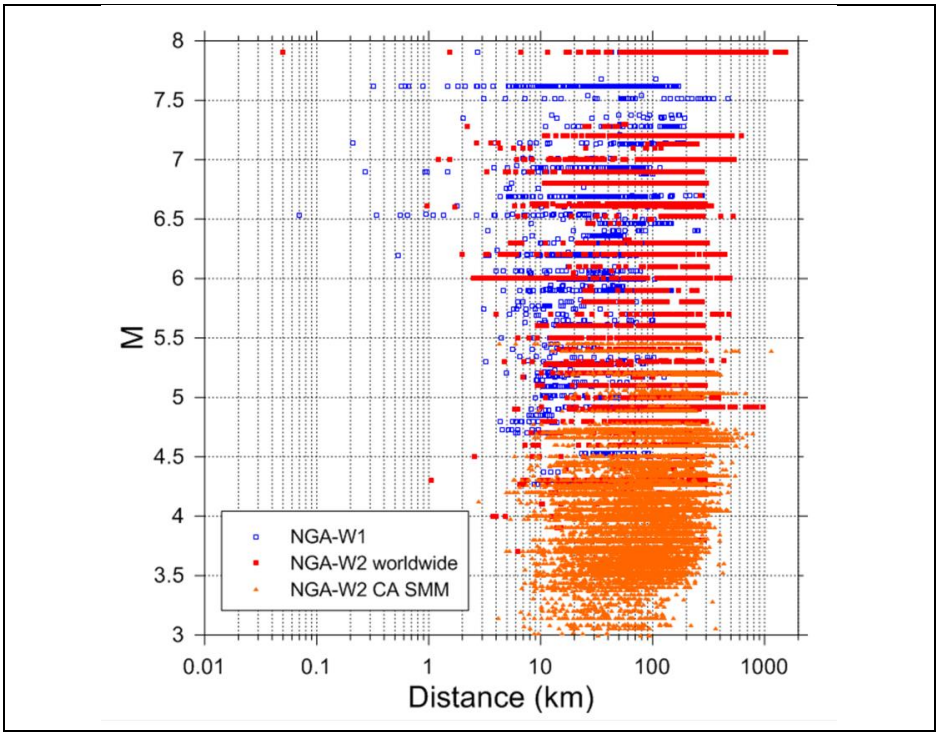


Figure 7.2: Magnitude-distance distribution of strong-motion records in the NGA-West2 database (magnitudes 3 to 7.9).

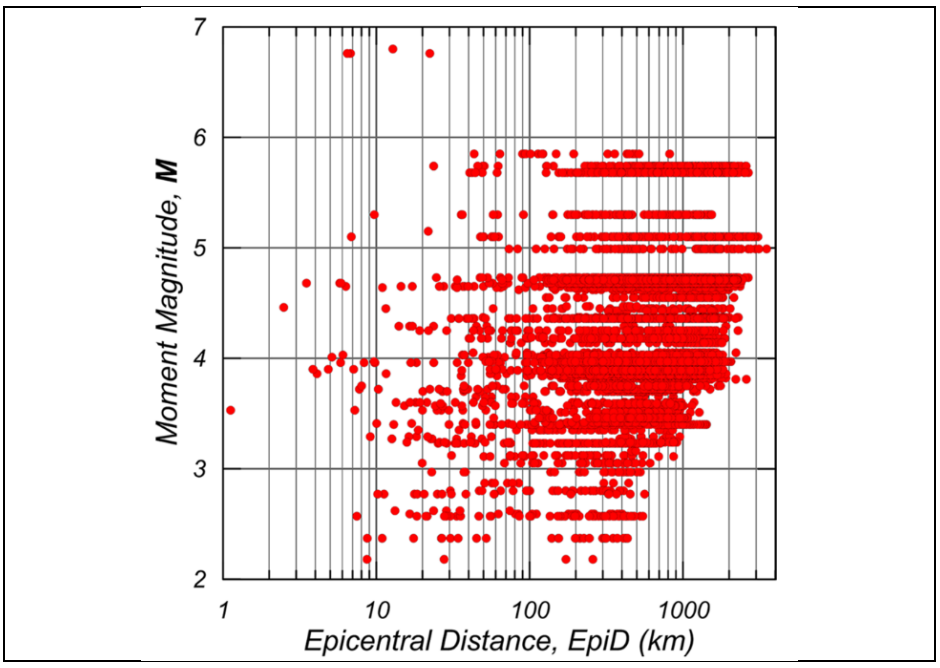


Figure 7.3: Magnitude versus distance coverage of recordings in the NGA-East ground-motion database.

It is clearly seen in Figure 7.3 that even with the latest gathered datasets for low seismic regions, the overall recorded $R_{epi} \leq 200$ km events from all stations are rare

and a station based κ_0 cannot be derived. In fact, the trial of a regional κ_0 evaluation process in Ktenidou et. al. [2021] is given in detail under section "2.3.2. Inconsistency in κ_0 Evaluations" of this PhD thesis.

Also, to address specifically subduction zones, NGA-Sub database is gathered for the first time [Bozorgnia and Stewart, 2020] and a regionalized GMM is modeled by Abrahamson and Gülerce [2020] with this database.

These new GMMs, as mentioned above, consist of selected regional $M \geq 2.5$ or $M \geq 3.0$ events and many not listed κ related literature still utilizes events with $M < 3.0$ with a pre-assumption of magnitude independency in such evaluations. As the amplitude of such low magnitude events does not reach high spectral values to visually detect the spectral decay in FAS, and with the help of tapering, filtering and smoothing to such records the noise floor information of the record is lost, and a false indication is given as if the spectral decay can be further even up to 80 Hz of the spectrum.

Turkey however is a highly seismic active region and lately has the advantage of strong ground motion networks (KOERI and AFAD) that many events are recorded. KOERI network has both weak and strong ground motion devices overall Turkey, and has more dense networks in some regions, mainly in Marmara or western Turkey region. AFAD strong motion network has grown larger since its first deployment but the databases released by this Agency have differences prior to 2020 and after June 2020. The former AFAD earthquake database website was closed to public reach from 25th January until 16th June, 2020. A new database is released and the access of a full dataset of events is now only possible if a non-robotic selection by hand is made for maximum 10 data at each time. As of 9th December 2020, starting from 19th August 1976, the total number of recordings with $M \geq 3.5$ within $R_{epi} \leq 200$ km of each AFAD station that recorded the relevant events is 44'224. To make a comparison from the previous database with the same criteria for magnitude and epicentral distance from 19th August 1976 until 2nd October 2018 recorded events count to 8'187 whereas this amount is now 28'363 with the new AFAD database for the same time period. This amount is almost 3.5 times higher than the previous database. These recordings now are no longer consistent of three dimension (East-West, North-South and Vertical (Up-Down) in one ascii file, but are separately available.

Another important issue is that now some of the events with the same name and location from the same station, have different magnitudes assigned. One example is with event ID: 250300, that occurred on 28th February, 2000. The former database lists

this event as M_d = 3.9 whereas the new database lists this event with M_w = 4.4. If the old database is considered to be utilized, there is a need to check the M_w values assigned to these events individually visiting the new AFAD database. This cannot be automated as no event ID set the same between former and new AFAD datasets.

Some of the results presented here in this PhD thesis utilizes the former AFAD database while they were evaluated before June 2020 and the time-consuming gathering of the data from the new AFAD database is not essential due to the progress achieved during these evaluations as explained below. When a more detailed evaluation is going to be made in these cases in the future, it is suggested to use the new AFAD database, if AFAD allows to distribute the necessary data needed directly to these future studies. It is apparent that downloading 10 events by hand selecting each of the 44'224 events even for $M \geq 3.5$ within $R_{epi} \leq 200$ km case up to 2020 is not possible and still does not reflect what is needed for a full scale of magnitude and distance to achieve the best fit of κ and κ_0 evaluations.

In the progress of the PhD study, first a location with seismic activity recorded up to 50 km range was selected and investigated. Van region had such case especially for one station, Station 6501 from AFAD strong ground motion network. The results showed that Q interference existed even at near ranges and could not be disregarded. Another important find is that the dataset showed vast variance especially for the events that are $M_L < 4.0$.

As the focus of κ_0 evaluations were mainly on stiff - hard rock site conditions after realization of its effect on hazard and risk calculations [Biro and Renault, 2012], the focus is given to stiff - hard rock AFAD stations with $V_{s30} \geq 720$ m/s within Turkey region and an end product is published and presented in 17th World Conference on Earthquake Engineering 27 September-2 October, 2021. The full paper was accepted for the original date of conference (October 2020), but due to the worldwide pandemic situation, the conference was postponed to 2021 and presented online. The dataset utilized for the evaluations for this reason is from the formal AFAD database.

During the course of the PhD thesis two significant earthquakes namely, Sivrice-Elazığ and Samos (Izmir-Seferihisar offshore) earthquakes, occurred in Turkey region. On 24th January, 2020, Sivrice-Elazığ earthquake with M_w = 6.8 (AFAD) hit the region causing damage and loss of life. Many recordings were available before and after the Sivrice-Elazığ incident that are originated from Sivrice-Pütürge segment of EAF and gave an opportunity for abundant amount of ground motion data originated only from

this fault segment source. This gave the possibility for the first time in literature and κ evaluation history to have a significant database of events originating from the same source, which may reduce significantly the source uncertainties for κ evaluations. This segment originated events were evaluated for both KEORI and new AFAD databases. The KOERI evaluation results were published in Soil Dynamic and Earthquake Engineering (SDEE) journal.

Samos earthquake (30th October 2020) with M_w = 6.9 (reported by KOERI whereas M_w = 6.6 reported by AFAD) was also damaging, especially the Izmir region, and was evaluated in terms of κ with new AFAD data and the results are presented in the following relevant subchapter of this PhD thesis in section "7.4. Izmir Region".

It is also worth to mention OECD Nuclear Energy Agency (NEA) "Kappa Workshop: Earthquake Ground Motions on Rock Sites" that was held on 25th - 28th May 2021. The workshop brought together the most important experts in this area from academia, regulatory bodies, international organizations and industry representatives involved is the seismic hazard analysis and seismic design and assessment of nuclear facilities. During the four-day workshop, participants exchanged the most recent research results on κ evaluations. The opening presentation by Norm A. Abrahamson have mentioned that available ground motion data on hard rock sites does not show the strong increase in high frequency ground motions predicted by current kappa scaling models. During the presentations of four days, Biro and Renault [2012] was cited by all presenters except one case study presentation and was observed that the same issues mentioned at this reference are still applicable for many regions. The discussions have proven that the results presented in this PhD thesis can provide good input to worldwide applications due to the good amount of especially near site event records as well as different AFAD station soil properties including very hard rock conditions.

7.1. Van Region

The main goal of this section of the PhD thesis is to estimate κ_0 at some of the Disaster and Emergency Management Agency (AFAD) strong motion stations in Van region which has significant number of records from $M_L \geq 3.5$ events within 50 km

range. The data used in this study is collected from the former strong ground motion recording database of AFAD, which includes the events from 1984 until April 2018.

At the first step, the hypocentral distances, R_{hyp}, are evaluated for each recording with $M_L \geq 3.5$. Epicentral distances, R_{epi} are used where there was no depth information. κ evaluations are carried out for the events that were located in the near site with $R_{hyp} \leq 50$ km to see the effect of the path attenuation $Q(f)$ in 50 km range.

The signal-to-noise ratio, SNR are checked and only the records with SNR ≥ 3.0 were taken into consideration. After the selection of the usable records, the strong ground motion data are baseline corrected and the S-wave portion of the records are chosen to proceed for the κ calculations.

Estimation of κ is done by the original method of Anderson and Hough [1984] for each selected strong ground recording the components of NS, EW, and UD separately. For the horizontal recordings the mean value of the two estimated horizontal κ values is calculated as a resulting κ value for that event. First the spectral decay parameter κ is estimated by obtaining a linear least square fit to the logarithm of spectrum of acceleration versus frequency of each recording between f_E, the frequency where the spectral amplitude acquires a maximum, and f_x, the frequency where the exponential decay of the acceleration spectrum becomes flat. While processing the data, the selection of f_E and f_x are made both as automated fixed values, and by visual examination and interactive manual selection to see the difference in the effect of the selection. For the final outcome of the estimated κ values, the manually selected f_E and f_x are favored (Figure 7.4).

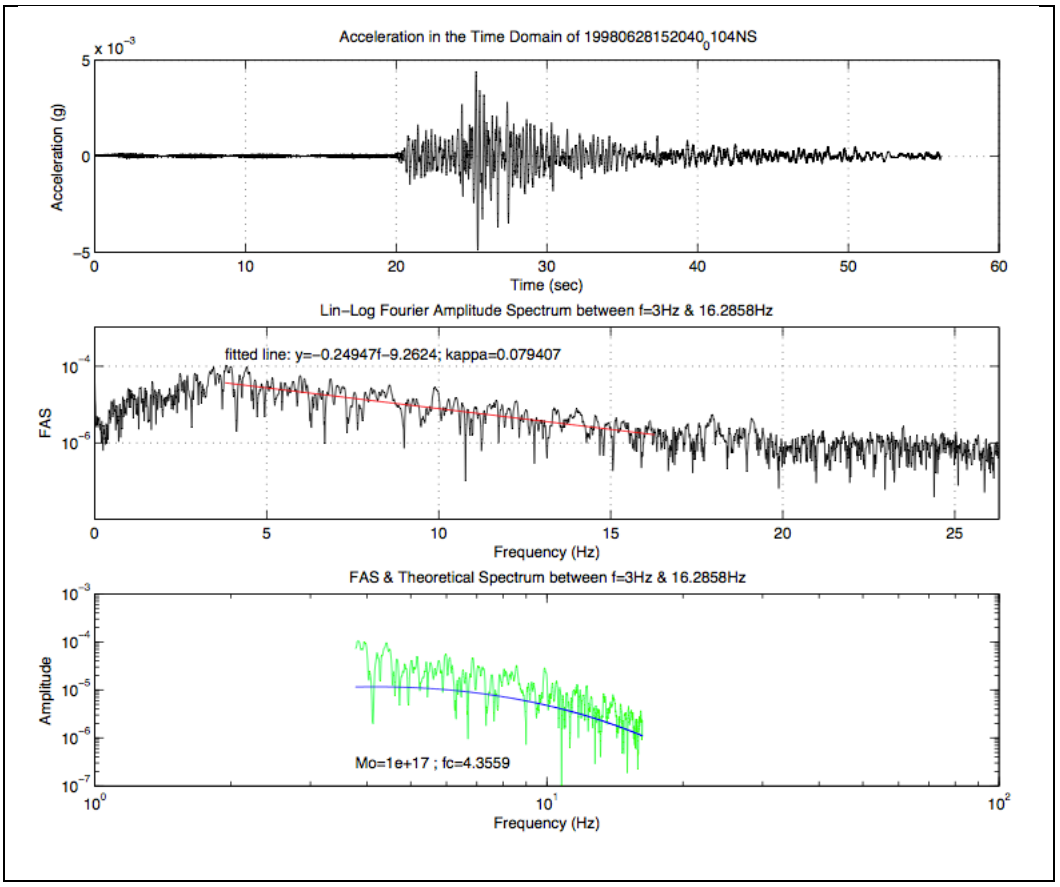


Figure 7.4: Example of manually selected f_E and f_x. Here the decay starts at f_E =3 Hz and ends around manually selected f_x =16.29 Hz instead of fixed f_E =2 Hz and f_x =20 Hz.

Using an ω^2 source spectrum, the theoretical S-wave acceleration spectrum may also be expressed as [Anderson and Hough, 1984]:

$$A(f) = S(f)\frac{e^{-\pi\kappa f}}{R} \tag{7.1}$$

Thus, κ were estimated using both Equation 2.1 and Equation 7.1 separately; where,

$$S(f) = C.M_o\frac{(2\pi f)^2}{1+\left({}^{f}/_{f_c}\right)} \tag{7.2}$$

and,

$$C = \frac{F_s R_{\theta,\varphi}}{4\pi\rho\beta^3} \tag{7.3}$$

where, the free surface factor F_s = 2, the horizontal rms radiation pattern factor $R_{\theta,\varphi} = 0.63/\sqrt{2}$, the density ρ = 2.7 g/cm^3, and S-wave velocity β = 3.3 km/s.

Furthermore, to check if the f_E value is greater than the corner frequency, f_c of the event, Andrews [1986] procedure is applied that is explained under the section "2.3.1. Inconsistency in κ Evaluations".

Finally, after calculating the κ value for each component of the event at a distance to the recording AFAD stations, the value of the spectral decay parameter at zero epicentral distance, κ_0 as an approximation, is evaluated where dataset allowed near site events, considering with linear distance dependency.

The AFAD station 6501 at Van province has given reasonable κ values and only this station is represented here. V_{s30} value for this station is 363 m/s. The spectral decay parameter κ is estimated for each recording between the range of values of f_E = 2 Hz and f_x = 20 Hz for this station according to the methodology above. For horizontal κ values, the mean value of NS and EW component κ values are calculated if the difference between these two components is lower than 20%.

The κ_0 of each recording only for mean horizontal direction is estimated for S-wave velocity β = 3.3 km/s and the fixed value of stochastic model path attenuation Q = 400 and Q = 1200. The resulting κ_0 values using the Equations 7.4 and 7.5 are listed in Table 7.1 and Table 7.2 respectively.

$$\kappa = \kappa_0 + \kappa_R R_{hyp} \tag{7.4}$$

where,

$$\kappa_R = {}^{1}/_{\beta Q} \tag{7.5}$$

Table 7.1: Estimated values of κ_0 for Station 6501 with pre-set Q = 400.

eventID	M_L	R_{hyp} **(km)**	κ **NS (s)**	κ **EW (s)**	κ **UD (s)**	**mean** κ **(horizontal) (s)**	**estimated** κ_0 **(s)**
20111025145506	5.5	43.9	0.0698	0.0733	0.0565	0.0716	0.0383
20111024152806	4.8	35.8	0.0594	0.0686	0.0523	0.0640	0.0238
20111026031626	4.8	29.4	0.0404	0.0506	0.0352	0.0455	0.0369
20111024082826	4.7	30.0	0.0463	0.0503	0.0333	0.0483	0.0232
20111028094755	4.5	35.1	0.0529	0.0582	0.0418	0.0556	0.0256
20111026151447	4.4	28.9	0.0630	0.0703	0.0502	0.0667	0.0290
20111024124924	4.3	22.5	0.0460	0.0584	0.0377	0.0522	0.0448
20111025165616	4.3	33.4	0.0531	0.0631	0.0436	0.0581	0.0352
20111026120525	4.3	27.9	0.0480	0.0476	0.0312	0.0478	0.0328
20111026032713	4.2	29.7	0.0435	0.0600	0.0401	0.0518	0.0267
20111028084808	4.2	30.6	0.0547	0.0677	0.0535	0.0612	0.0293
20111028195949	4.2	24.9	0.0465	0.0584	0.0368	0.0525	0.0380
20111024103024	4.1	22.0	0.0506	0.0645	0.0432	0.0576	0.0336
20111027052918	4.1	31.7	0.0293	0.0446	0.0241	0.0370	0.0409
20111028002532	4.1	24.0	0.0488	0.0608	0.0387	0.0548	0.0129
20111025232527	4.0	29.3	0.0501	0.0577	0.0403	0.0539	0.0366
20111026084927	4.0	19.2	0.0496	0.0555	0.0340	0.0526	0.0317
20111026041458	3.9	23.8	0.0249	0.0318	0.0206	0.0284	0.0380
20111027212039	3.9	11.4	0.0465	0.0607	0.0564	0.0536	0.0103
20111026053429	3.6	22.8	0.0163	0.0233	0.0098	0.0198	0.0450
20111024091757	3.5	25.1	0.0310	0.0442	0.0230	0.0376	0.0025

Table 7.2: Estimated values of κ_0 for Station 6501 with pre-set Q = 1200.

eventID	M_L	R_{hyp} (km)	κ NS (s)	κ EW (s)	κ UD (s)	mean κ (horizontal) (s)	estimated κ_0 (s)
20111025145506	5.5	43.9	0.0698	0.0733	0.0565	0.0716	0.0605
20111024152806	4.8	35.8	0.0594	0.0686	0.0523	0.0640	0.0398
20111026031626	4.8	29.4	0.0404	0.0506	0.0352	0.0455	0.0550
20111024082826	4.7	30.0	0.0463	0.0503	0.0333	0.0483	0.0381
20111028094755	4.5	35.1	0.0529	0.0582	0.0418	0.0556	0.0407
20111026151447	4.4	28.9	0.0630	0.0703	0.0502	0.0667	0.0467
20111024124924	4.3	22.5	0.0460	0.0584	0.0377	0.0522	0.0594
20111025165616	4.3	33.4	0.0531	0.0631	0.0436	0.0581	0.0465
20111026120525	4.3	27.9	0.0480	0.0476	0.0312	0.0478	0.0497
20111026032713	4.2	29.7	0.0435	0.0600	0.0401	0.0518	0.0408
20111028084808	4.2	30.6	0.0547	0.0677	0.0535	0.0612	0.0443
20111028195949	4.2	24.9	0.0465	0.0584	0.0368	0.0525	0.0535
20111024103024	4.1	22.0	0.0506	0.0645	0.0432	0.0576	0.0462
20111027052918	4.1	31.7	0.0293	0.0446	0.0241	0.0370	0.0520
20111028002532	4.1	24.0	0.0488	0.0608	0.0387	0.0548	0.0289
20111025232527	4.0	29.3	0.0501	0.0577	0.0403	0.0539	0.0487
20111026084927	4.0	19.2	0.0496	0.0555	0.0340	0.0526	0.0465
20111026041458	3.9	23.8	0.0249	0.0318	0.0206	0.0284	0.0477
20111027212039	3.9	11.4	0.0465	0.0607	0.0564	0.0536	0.0223
20111026053429	3.6	22.8	0.0163	0.0233	0.0098	0.0198	0.0507
20111024091757	3.5	25.1	0.0310	0.0442	0.0230	0.0376	0.0140

κ values for Station 6501 according to the trend with distance are illustrated in Figure 7.5 and Figure 7.6. κ_0 values estimated for $M_L \geq 4.0$ in $R_{hyp} \leq 50$ km due to this trend are 0.0389 s for mean horizontal and 0.0203 s for vertical recordings. The red marker events are $M_L < 4.0$ events and are excluded for κ_0 estimations due to the visible discrepancy at $3.5 \leq M_L < 4.0$ range, which suggests there could be magnitude dependency.

It is clearly seen that an estimation of κ_0 for each recording cannot be taken into account as a resulting value, as the values for Q = 400 differ from 0.0025 s (0.0129 s for $M_L \geq 4.0$) to 0.0450 s (Table 7.1) and the values for Q = 1200 differ from 0.0140 s (0.0289 s for $M_L \geq 4.0$) to 0.0605 s (Table 7.2). This is due to the path attenuation effect related to the event distance to station even when the qualified strong ground motion records are mainly within $R_{hyp} \leq 50$ km.

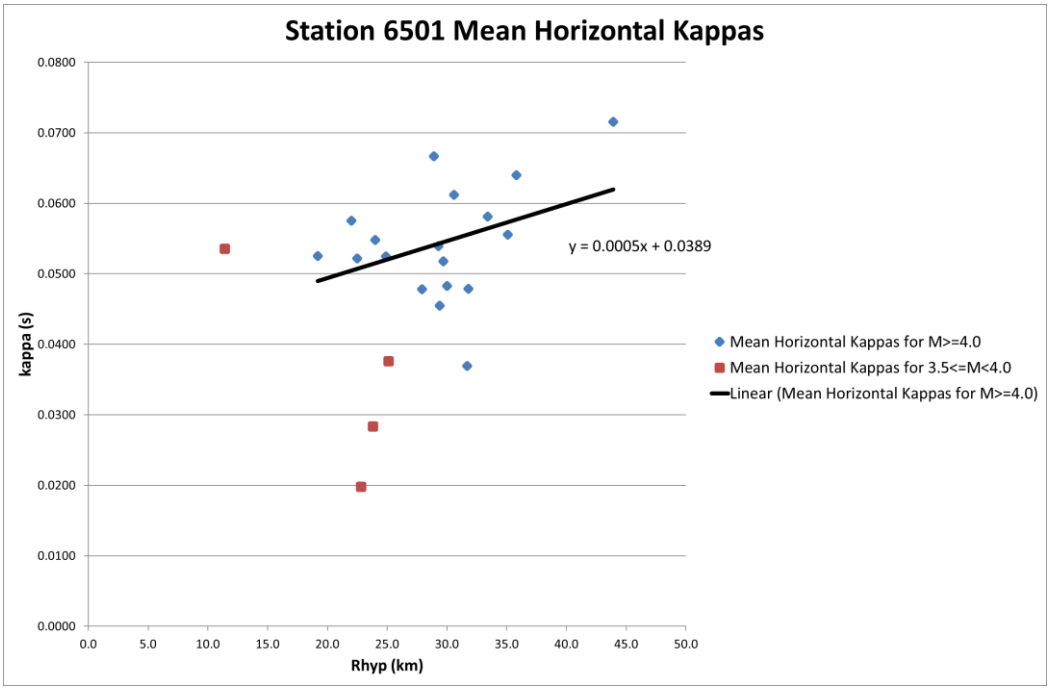


Figure 7.5: Mean horizontal κ trend at Station 6501. Resulting κ_0 is 0.0389 s.

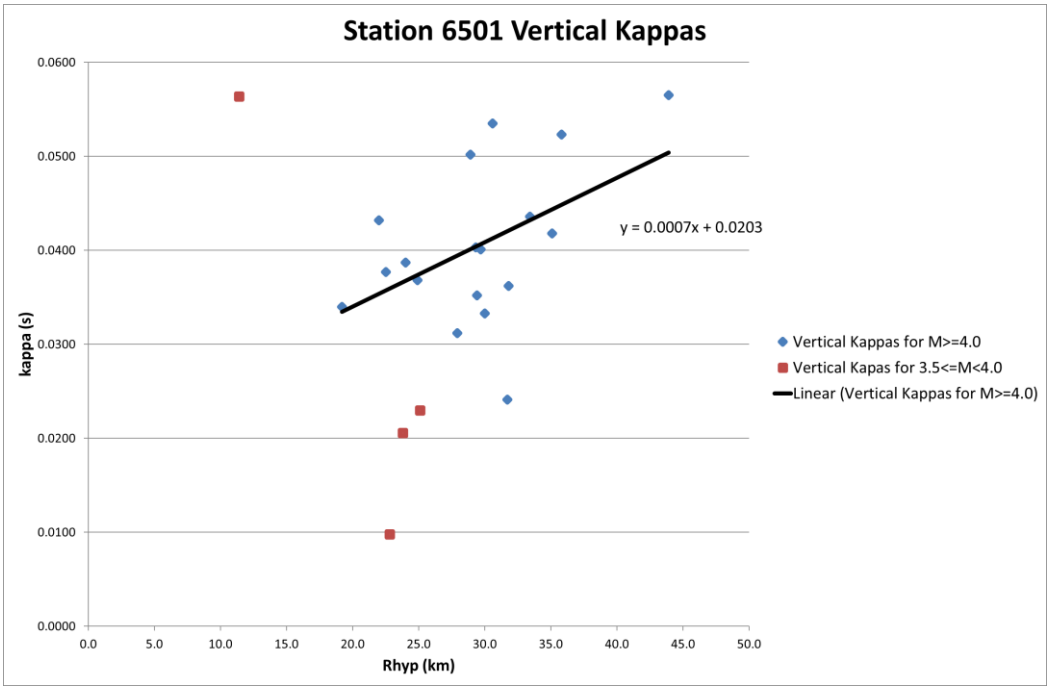


Figure 7.6: Vertical κ trend at Station 6501. Resulting κ_0 is 0. 0203 s.

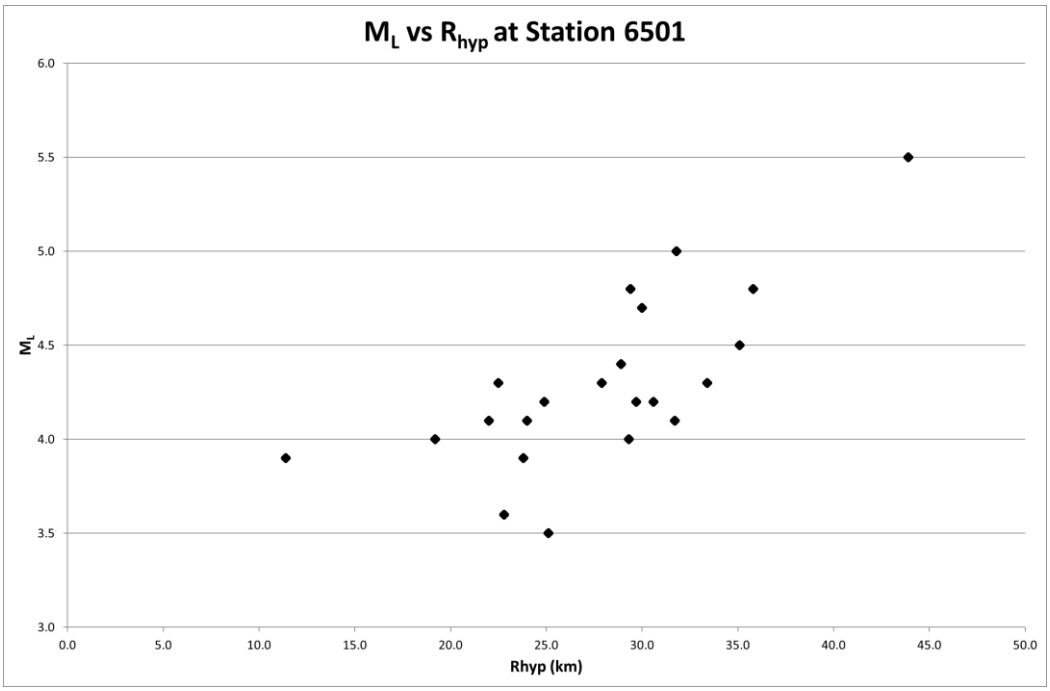


Figure 7.7: M_L vs R_{hyp} distribution of selected events at Station 6501.

For this station, there is only one strong ground motion record where $R_{hyp} \leq 20$ km and have magnitude $M_L < 4.0$ (Figure 7.7). If lower magnitude events are added, the stress drop issue mentioned before as in Ktenidou et. al. [2017] could occur. Actually, for this station records it is clearly seen that $M_L < 4.0$ already has such an issue, or indicates a magnitude dependency.

A part of this study is published [Biro et. al., 2019] and presented in 5th International Conference on Earthquake Engineering and Seismology (5ICEES), on 8-11 October, 2019, METU, Ankara. Later the Turkish version of the conference paper with some additions to the original conference paper is published in Turkish Journal of Earthquake Research [Biro et. al., 2020].

7.2. Hard Rock AFAD Stations in Turkey

Due to the effect of κ on seismic hazard calculations, especially in host-to-target adjustment of GMPEs, where the host represents soft rock and the target represents hard rock sites, the scientific community has focused first on gathering hard rock-based station seismic data to evaluate the spectral decay parameter to be able to assign reliable target κ values for hard rock sites. For this reason, in this section of the PhD thesis, the focus is on the estimation of κ at zero epicentral distance, κ_0 at the Disaster

and Emergency Management Agency, AFAD strong ground motion stations with V_{s30} ≥ 720 m/s within Turkey region.

The dataset used for analyses are from 1984 until November 2019 from AFAD formal database. The events with hypocentral distance, $R_{hyp} \leq 50$ km and $R_{hyp} \leq 100$ km with local magnitude, $M_L \geq 3.5$ are compared for the resulting κ_0. The V_{s30} values as well as different κ_0 results from different setups mentioned in "Remarks" column of the table at these stations are given in Table 7.3. Some hard rock-based AFAD stations were excluded due to insufficient records or the selection criteria such as signal to noise ratio, SNR and are not listed here. Also, only the free field stations are taken into consideration.

Table 7.3: AFAD hard rock stations and κ_0 evaluations.

Stn #	**LAT**	**LON**	**City**	**Province**	V_{s30} **(m/s)**	κ_0 **(s)**	$M_{L,\min}$	$M_{L,\max}$	**Remarks**
118	37.0362	35.3184	Adana	Çukurova	946	0.019	3.5	4.5	$50<R_{hyp}\leq 84$km
701	36.8944	30.6667	Antalya	Muratpaşa	920	0.010	4.2	5.2	
705	36.1951	29.6474	Antalya	Kaş	1113	0.029	3.5	6.0	$R_{hyp}>40$km
1101	40.14106	29.9774	Bilecik	Merkez	901	0.039	3.6	5.2	
2016	37.80441	29.24003	Denizli	Honaz	805	0.041	3.5	6.0	
2302	38.39231	39.67541	Elazığ	Maden	907	0.028	3.5	5.2	
3506	38.39443	27.08211	Izmir	Konak	771	0.012	3.5	5.3	$R_{hyp}\leq 100$km
3506	38.39443	27.08211	Izmir	Konak	771	0.022	3.5	5.3	$R_{hyp}\leq 50$km
3511	38.4213	27.2563	Izmir	Pınarbaşı	827	0.009	3.5	6.2	
3514	38.4762	27.1581	Izmir	Bayraklı	836	0.005	3.5	6.2	
3520	38.478	27.2111	Izmir	Bornova	875	0.027	3.5	6.2	
3525	38.3723	27.1084	Izmir	Yeşilyurt	745	0.011	3.5	6.2	$M_L\geq 3.5$
3525	38.3723	27.1084	Izmir	Yeşilyurt	745	0.019	4.0	6.2	$M_L\geq 4.0$
4404	38.19588	38.87385	Malatya	Pütürge	1380	0.049	3.5	5.5	$R_{hyp}\leq 100$km
4404	38.19588	38.87385	Malatya	Pütürge	1380	0.024	3.6	4.2	$R_{hyp}\leq 30$km
4802	37.03304	27.43997	Muğla	Bodrum	747	0.021	3.5	5.3	$R_{hyp}\leq 100$km
4802	37.03304	27.43997	Muğla	Bodrum	747	0.014	3.5	5.3	$R_{hyp}\leq 30$km
8105	40.90278	31.15198	Düzce	Merkez	914	0.023	3.6	4.7	

The hypocentral distances, R_{hyp} are calculated for each recording and where there is no depth information, the epicentral distances, R_{epi} are used. In Figure 7.8, only the

selected events, at total 711 events (1422 horizontal components), are represented to illustrate the distribution of R_{hyp} vs V_{s30}. In further analysis some eliminated stations could as well be included if enough event is recorded and the uncertainties and errors could be resolved.

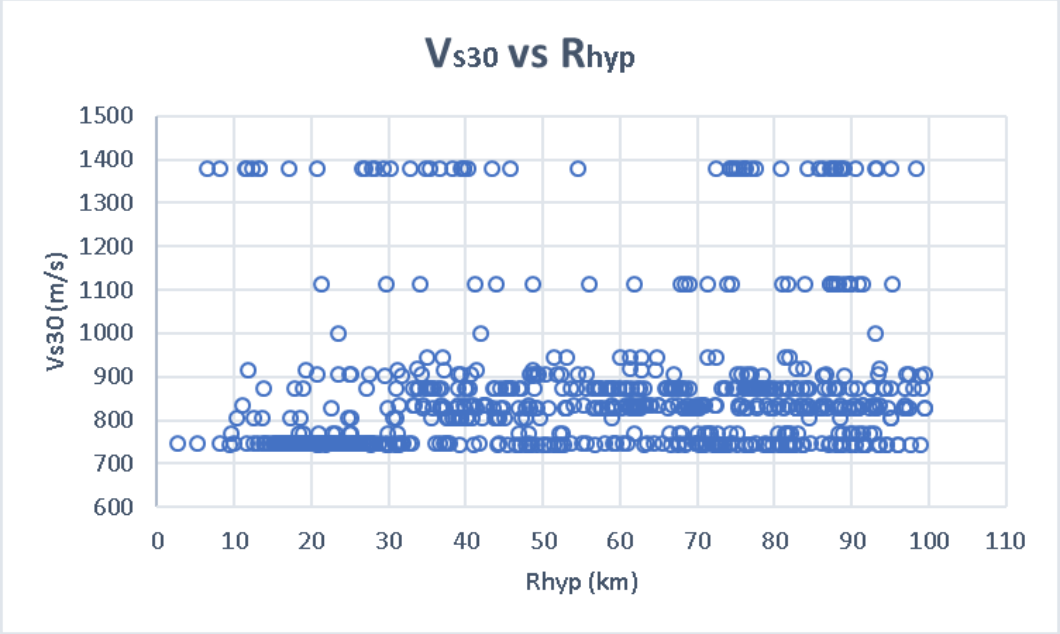


Figure 7.8: Distribution of selected events in terms of R_{hyp} and V_{s30} for AFAD hard rock stations.

This distribution gives a fair number of events to evaluate κ with only $R_{hyp} \leq 50$ km for hard rock case. At some stations even $R_{hyp} \leq 30$ km can be evaluated with significant amount of events as input data.

Estimation of κ is done by the original method of Anderson and Hough [1984] for each selected strong ground recording the components of NS, and EW separately.

First the spectral decay parameter κ is estimated by obtaining a linear least square fit to the logarithm of S wave spectrum of acceleration versus frequency of each recording between f_E, the frequency where the spectral amplitude acquires a maximum, and f_x, the frequency where the exponential decay of the acceleration spectrum becomes flat. While processing the data, the selection of f_E and f_x are made both as automated fixed values, and by visual examination and interactive manual selection to see the difference in the effect of the selection. Different windows for $f_E - f_x$ band are selected for some stations after the visual inspection to evaluate κ where a fixed

frequency band could not capture the decay of the event. For the final outcome of the estimated κ values, the manually selected f_E and f_x are favored.

For the horizontal recordings the mean value of the two estimated horizontal κ is calculated as a resulting κ value for that event. If the two horizontal estimated κ values differ from each other more than 25%, these are excluded.

Finally, after calculating the κ value for each horizontal component of the event at a distance to the recording hard rock-based AFAD stations, the value of the spectral decay parameter at zero epicentral distance, κ_0 as an approximation, is evaluated considering with linear distance dependency (Equation 7.4).

As mentioned above, at some stations $R_{hyp} \leq 30$ or $R_{hyp} \leq 50$ km could be evaluated with many event input data. At station 3506, where V_{s30} = 771 m/s, $R_{hyp} \leq$ 50 km events resulted κ_0 = 0.022 s, whereas if all the events up to R_{hyp} = 100 km are taken into account the resulting κ_0 value is estimated as 0.012 s. This may be due to two 1977 event recordings giving high kappa values around 0.050 s with M_L = 4.8 and M_L = 5.3 in $R_{hyp} \leq 30$ km distance. In another station, 4404 with V_{s30}.= 1380 m/s, R_{hyp} $\leq$ 30 km selection criteria gives κ_0 = 0.024 s, whereas if all events are included up to R_{hyp} =100 km, κ_0 is estimated 0.049 s. Same trend as in station 4404 is seen at station 4802 (V_{s30} = 747 m/s), where κ_0 = 0.014 s when the maximum R_{hyp} is 30 km, and κ_0 = 0.021 s if $R_{hyp} \leq$ 100km. In Figure 7.6 the $R_{hyp} \leq 100$ km cases of stations 4404 and 4802 are illustrated in red, when $R_{hyp} \leq 30$ or 50 km is applicable. For the case of station 3506 it is favored the $R_{hyp} \leq 100$ km κ_0 estimation at this moment.

The κ estimations are also checked if $M_L \geq 3.5$ and $M_L \geq 4.0$ selection criteria defers in the resulting κ_0 values. Only in Station 3525 there is significant difference at the results as seen in Table 7.3. $M_L \geq 4.0$ case is favored at Figure 7.9. Station 701 has only $M_L \geq 4.2$ events recorded and could be compared with $M_L \geq 4.0$ selection criteria.

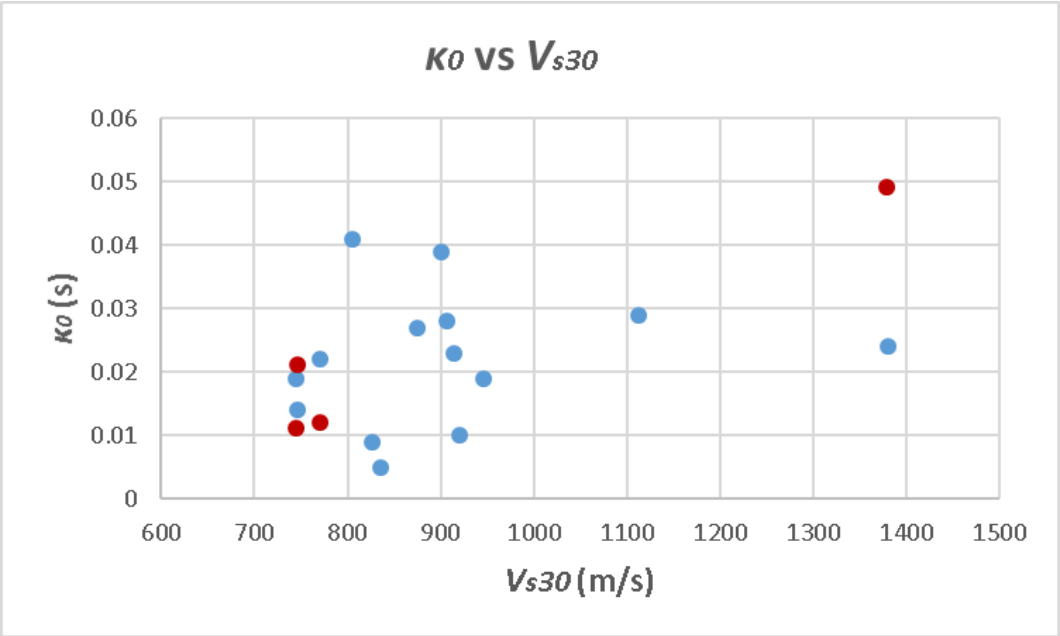


Figure 7.9: Distribution of evaluated κ_0 values with V_{s30} for AFAD hard rock stations.

During the course of this phase of the PhD thesis, κ_0 evaluations were realized according what is applied in the common literature. It is observed that the pre-assumption of no Q interference up to 100 km distance by Ktenidou et. al. [2016a] does not apply for the hard rock stations in Turkey. While trying to achieve no need for Q correction $R_{hyp} \leq 100$, ≤ 50 and ≤ 30 km are tried out and all presented significantly different resulting κ_0 values. As mentioned above, at some stations $R_{hyp} \leq 30$ or $R_{hyp} \leq 50$ km could be evaluated and a comparison with $R_{hyp} \leq 100$ km resulting κ_0 values could be made. These results suggests that a Q correction is needed to be applied during the κ_0 evaluations for the datasets in hand.

Station 3514 at Bayraklı, Izmir location resulted with κ_0 value of 0.005 s. In section 7.4, this station is evaluated in terms of Sesame earthquake of 30th October, 2020 and will be compared. Station 4404 Pütürge, Malatya is further discussed in section "7.3. Sivrice-Pütürge Segment of EAF" under section "7.3.2. AFAD Results".

It is therefore not reasonable at this point to set a correlation between κ_0 versus V_{s30} before resolving the discrepancy of such results, even though the scientific community has tried out such relationships with these two parameters with smaller databases involving fewer data before.

7.3. Sivrice-Pütürge Segment of EAF

For Sivrice-Pütürge segment of East Anatolian Fault, the focus is on reducing "different source" effects to be able to establish a better path attenuation definition between a selected specific source and the corresponding station under investigation to estimate κ_0. A first attempt in literature to introduce a constraint on selecting the events only originating from a single fault source is achieved in this section of PhD thesis. To be able to achieve this, a sufficient dataset representing a good range of different magnitude events recorded at numerous stations for the region is necessary. Traditionally, while performing regional or station-based kappa evaluations, events that are recorded at a station from all different seismic sources are included in the database and this creates a presumption as if the database is sufficient for a good fit and regression for evaluation. In fact, the path related to these events differs and an uncertainty according to this effect is introduced and cannot be differentiated.

In this part of the PhD thesis, the seismic sources in this region could be distinctly identified as two main fault sources which are North Anatolian Fault (NAF) and East Anatolian Fault (EAF). There are also some minor seismic sources that produce earthquakes in the region, but those can be separated from NAF and EAF originated events. For example, such an approach cannot be realized where there are basin effects and many events originating from several different seismic sources, such as Izmir region (mid-western Turkey).

To reduce the mentioned "different source" effect on κ evaluations, only the events generated from Sivrice-Pütürge segment of East Anatolian Fault are considered. This also provided a regional Q correction that is not influenced by different source generated events during the estimation of the zero epicentral spectral decay parameter, κ_0 for stations under consideration.

The NAF is studied in depth in literature, whereas studies related to EAF are rare. For this reason, this section of the PhD thesis is also valuable for EAF related sources, mainly for Sivrice-Pütürge segment of EAF.

Restricting the dataset with events generated only from one segment source gave also the opportunity to check the reliability of a direct linear fit between κ and epicentral distance, R_{epi} to estimate κ_0 values for far stations when compared with a fit that is constrained with a regional path correction which can now be evaluated from

source-based event κ values estimated in the region. This attempt to estimate κ_0 values is also the first for Turkey related κ evaluations in literature.

The automated selection procedure developed in the course of this PhD thesis for f_x yielded a good fit to the dataset. The stations are also examined for the peak frequencies (f_p) of HVSR whether these peak frequencies intercepted with the frequency band considered in the κ evaluations when needed. The HVSR calculations additionally provided information on the soil properties at the station locations. The findings are considered to be useful for understanding the effect of κ versus R_{epi} fit on the estimation of station-based κ_0 values and also could give good insight of what could be expected for similar site characteristics at this region. Furthermore, the proposed procedure for obtaining spectral flattening frequency, f_x may improve compatibility among κ evaluations, and reduce selected frequency band related uncertainties.

7.3.1. KOERI Results

Kandilli Observatory and Earthquake Research Institute (KOERI) stations located around the Sivrice-Pütürge segment of EAF have recorded many events that matched the sought criteria for a dataset that represents a good range of different magnitude events recorded at numerous KOERI stations for the region.

This section is also important as it will be the first to evaluate kappa and HVSR at those KOERI stations under investigation for this region.

7.3.1.1. Dataset

The dataset used for Sivrice-Pütürge segment related events are the recordings gathered from weak motion and strong motion stations of KOERI during October 2017 until June 2020 [Web 2]. The events with $M_L \geq 3.5$ and with epicentral distance, $R_{epi} \leq$ 200 km were considered so that the path attenuation *Q(f)* from far field recordings will less interfere. If the selected events are less than four events, the station with these events were excluded from the database.

The weak motion station with the station code SVRC had recorded events between 8.9 km and 60 km along the Sivrice-Pütürge segment of EAF. Unfortunately, the M_L6.5 January 2020 event is clipped out in this station. KHMN station had only

five events before the selection criteria was applied and was excluded from both the κ_0 and HVSR evaluations. The station ERZN which had recorded only high noise was also excluded. The station YEDI had a defective vertical sensor and was used for the κ overall evaluations but was excluded from HSVR evaluations. Strong motion stations ESGZ, ESIJ and MDYO were installed during the aftershock sequence of January 2020 earthquake and the first event recorded by these stations is dated on 16th February, 2020. The magnitude range is between M_L3.5 and M_L 5.1 at these three newly installed stations. The selected event magnitude and the epicentral distance ranges for each station are listed in Table 7.4. The stations KMRS and YEDI each had five events after filtering the events with high noise with signal-to-noise ratio (SNR) less than 3 and were included for the overall κ evaluations while defining the seismic quality factor (Q) effect, but excluded in the site-specific evaluations.

Table 7.4: The selected event magnitude and the epicentral distance ranges for each KOERI station.

Station Code	**Magnitude Range (M_L)**	**Epicentral Distance Range (R_{epi})**
ARPR	$3.5 \leq M_L \leq 6.6$	95-115 km
BNGB	$3.5 \leq M_L \leq 5.1$	120-200 km
DARE	$3.5 \leq M_L \leq 5.1$	120-160 km
DYBB	$3.5 \leq M_L \leq 5.1$	90-130 km
ESGZ	$3.5 \leq M_L \leq 5.1$	2-45 km
ESIJ	$3.5 \leq M_L \leq 5.1$	3-65 km
GAZ	$3.5 \leq M_L \leq 5.1$	170-190 km
ILIC	$3.5 \leq M_L \leq 4.7$	120-145 km
KHMN	$3.9 \leq M_L \leq 5.1$	150-195 km
(KMRS)	$3.5 \leq M_L \leq 5.1$	170-190 km
MDYO	$3.6 \leq M_L \leq 5.1$	10-26 km
SVAN	$3.5 \leq M_L \leq 5.1$	150-200 km
SVRC	$3.5 \leq M_L \leq 4.7$	8-60 km
URFA	$3.5 \leq M_L \leq 5.1$	80-135 km
(YEDI)	$3.5 \leq M_L \leq 6.6$	135-175 km

The events were evaluated by their signal-to-noise ratios (SNR) and if the SNR < 3 then those events were filtered out from the database. While calculating the SNR, Tukey window was applied with a smoothing degree of 3 to the whole recording of the event. The weak motion recordings had clipping or discontinuity problems even though they passed the SNR ≥ 3 criteria, so all events were examined visually and filtered out if the data was clipped or had discontinuity. The remaining events are illustrated in Figure 7.10 and Figure 7.11 together with the KOERI station locations.

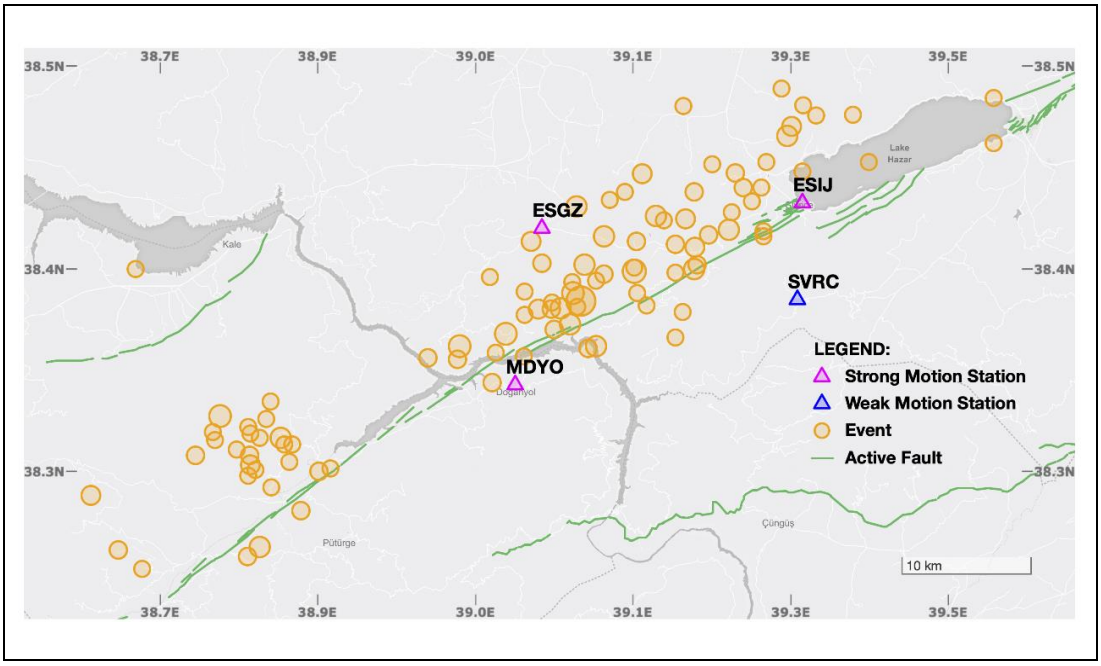


Figure 7.10: The distribution of selected events with near stations.

SVRC is a weak motion station (blue), whereas ESGZ, ESIJ and MDYO are strong motion stations (pink) in Figure 7.10.

ERZN and KHMN were eliminated at the beginning of compiling database. KMRS and YEDI were included for overall κ evaluations but excluded for station-based κ_0 evaluations for having only five events listed after passing the selection criteria. Weak motion stations are represented with blue, whereas strong motion stations with pink triangles in Figure 7.11.

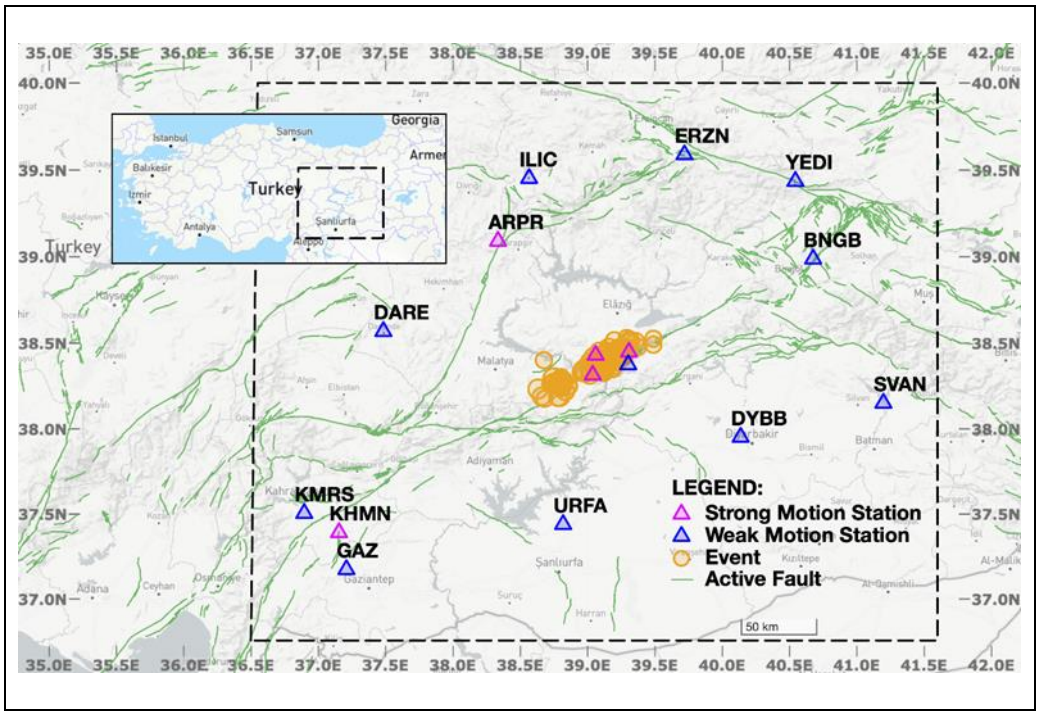


Figure 7.11: The distribution of selected events with far stations.

7.3.1.2. Methodology Used

To evaluate the spectral decay parameter, κ, with the selected events, as a first step, the S-wave arrival and the end instant of the S-wave were determined utilizing the Arias intensity and Cumulative Root Mean Square (CRMS) respectively. The arrival of S-wave was set to the 5% of the Husid plots of the Arias Intensity, whereas the end instant of the S-wave was detected from where the CRMS curve started to decay.

While evaluating the Fourier amplitude spectrum of the selected S-wave window, no tapering has been applied and if applied then the impact of tapering on the resulting κ values was as high as 30%.

The selection of the beginning of the fit mentioned in Equation (2.1) has a condition of $f_E > f_c$ for each recording. For the current evaluation phase, f_E was set to minimum 2 Hz, and f_x selection was automated through checking the noise spectrum and the acceleration spectrum by fitting a polynomial at the linear-logarithmic scale. If the polynomial curves intersect each other this was set as f_x, if not an initial f_{xi} was set to check the smallest difference in the polynomials (Figure 7.12). In the upper part of this figure, purple line trace is the FAS of the whole record and grey line trace is the

FAS of the noise segment of the record. In the lower part, black line trace is the FAS of S-wave window and red line is linear least squares fit between f_E and f_x to estimate κ.

The initially set f_{xi} values were corrected by checking the other event f_x values estimated at the same station. For the dataset of stations with codes ESGZ, ESIJ, and MDYO, the f_{xi} was finally set to 30 Hz, for ILIC, SVRC and URFA stations to 25 Hz and for the remaining stations to 20 Hz. By this way a fit to higher frequencies were made possible up to the limitations of the station. This procedure yielded a very good fit for the decay portion of the spectrum of horizontal components in 200 events out of 203 that were in the database. Three events were modified after checking visually and it was observed that these necessary modifications were due to noise levels being at the limit state of SNR >= 3, but the resulting κ values differed only maximum 1%. An example of the f_E and f_x values identified for this dataset are illustrated in Figure 7.13.

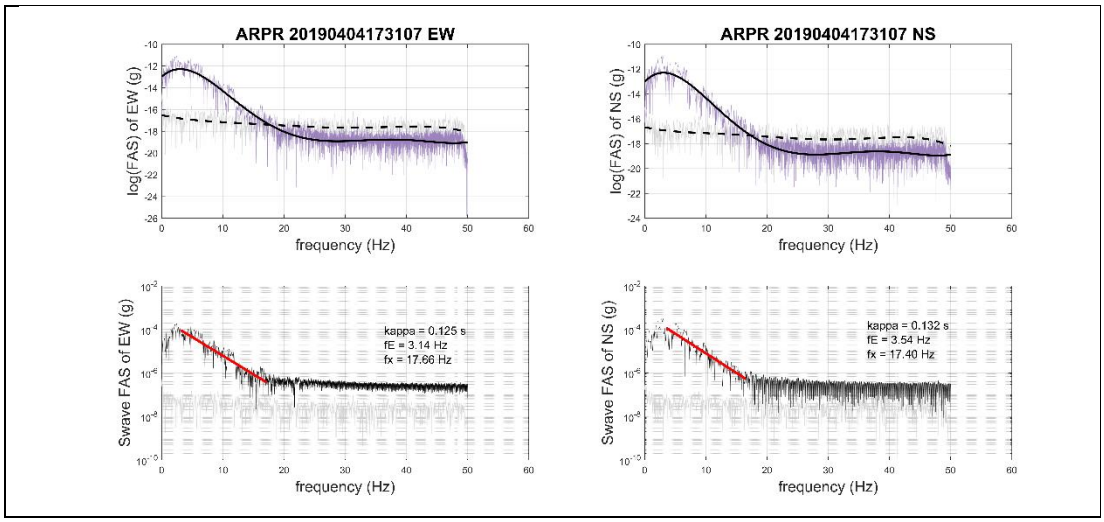


Figure 7.12: κ evaluation for two components of an event recorded at station ARPR.

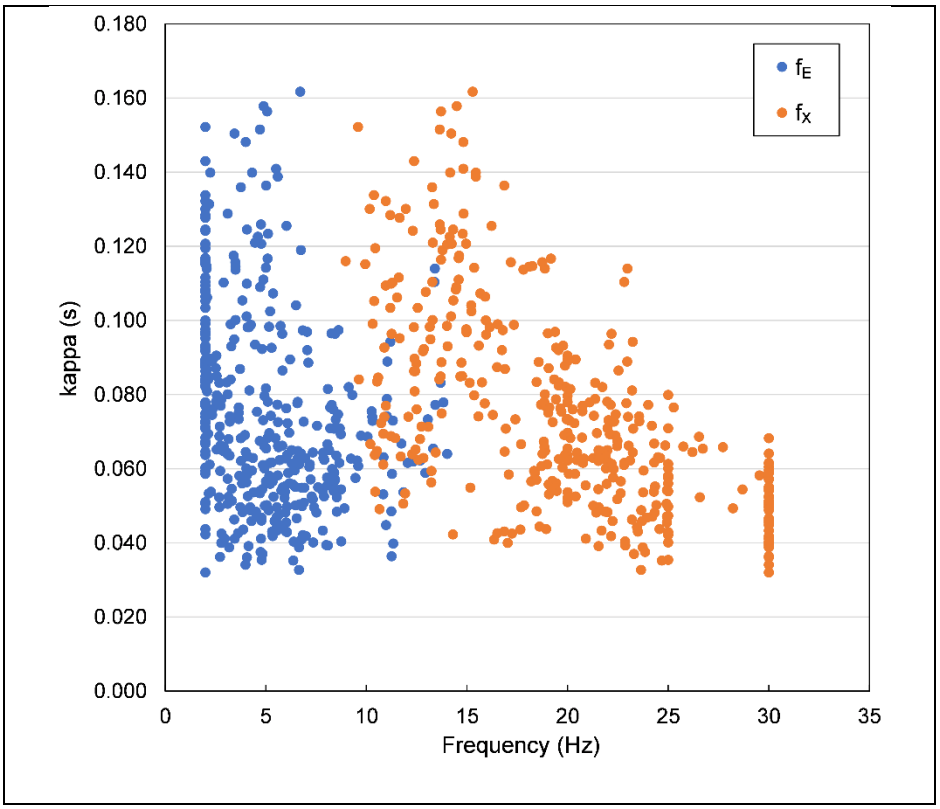


Figure 7.13: f_E (in blue) and f_x (in orange) distribution with respect to horizontal components' κ's from all events at all stations.

The geometrical mean horizontal κ values (κ_H) were calculated if the two directional κ estimations (κ_{EW} and κ_{NS}) did not differ more than 25% between each other. Also, the difference between f_E and f_x, Δf, was set to be minimum 8 Hz. If one directional component had passed this evaluation, but the other did not, it was still considered (thus used) after checking visually and if the estimated κ values of each component were almost the same.

Finally, after calculating the κ_H value for each event at a distance to the recording KOERI stations, the value of the spectral decay parameter at zero epicentral distance, κ_0, as an approximation, was evaluated considering with a linear distance dependency and can be formulated as following:

$$\kappa = \kappa_0 + \kappa_H R_{epi} \tag{7.6}$$

A semi logarithmic distance dependency model was also considered while checking the correlation between the κ_H value and R_{epi} for the database and can be represented as the following equation:

$$\kappa = \kappa_0 e^{\kappa_H R_{epi}} \quad (7.7)$$

It should be noted that no filtering or tapering is applied to the dataset for κ evaluations as the impact of applying tapering to the lengthened S-wave portion was high and mathematically could not anymore justify that we have chosen an S-wave portion of the signal, which still has P-wave and noise effects inside. And a bandpass filter does not influence the κ estimation high frequency region of the spectrum, as we pick the f_x simply by checking the noise signal as mentioned before.

7.3.1.3. κ Results

There are 12 out of 15 stations as listed in Table 7.4 that passed all the boundary conditions of the selection criteria mentioned above. When plotted for different magnitude bins, the horizontal mean event κ, κ_H and R_{epi} distribution had different linear trends (Figure 7.14). Correlation between κ_H and R_{epi} were established via robust multiple linear regression to reduce outlier effects as it is encountered for ARPR station in the database. By doing so, the correlation coefficient, R^2 from an ordinary linear least squares fit was improved from 0.28 (low) to 0.52 (moderate) for overall kappa estimations in the region. Also, instead of a linear distance dependency a semi logarithmic distance dependency model was carried out. When compared with ordinary linear model, the semi logarithmic model improved the correlation coefficient R^2 = 28 up to R^2 = 0.50 (Figure 7.15). A slightly better correlation between κ_H and R_{epi} for the database was achieved via robust multiple linear regression model compared to the semi logarithmic model, so the resulting κ_0 values from the robust multiple linear regression model are represented here.

Even restricting the dataset with events only generated by a single fault source rather than evaluating all events recorded at KOERI stations, there seems to be a magnitude dependency as seen in Figure 7.14 and Figure 7.15. In these figures, orange trend represents $4.0 > M \geq 3.5$, green trend represents $4.5 > M \geq 4.0$, red trend represents $5.0 > M \geq 4.5$, blue trend represents $M \geq 5.0$, and black dashed line represents the overall fits.

The magnitude dependency has been an issue discussed among many scientists dealing with uncertainties of GMPEs and is sometimes observed and mentioned for station-based kappa (κ_0) values as observations as pointed out before in the section "3.1. Stress Drop and Magnitude Dependency/Independency" of this PhD thesis.

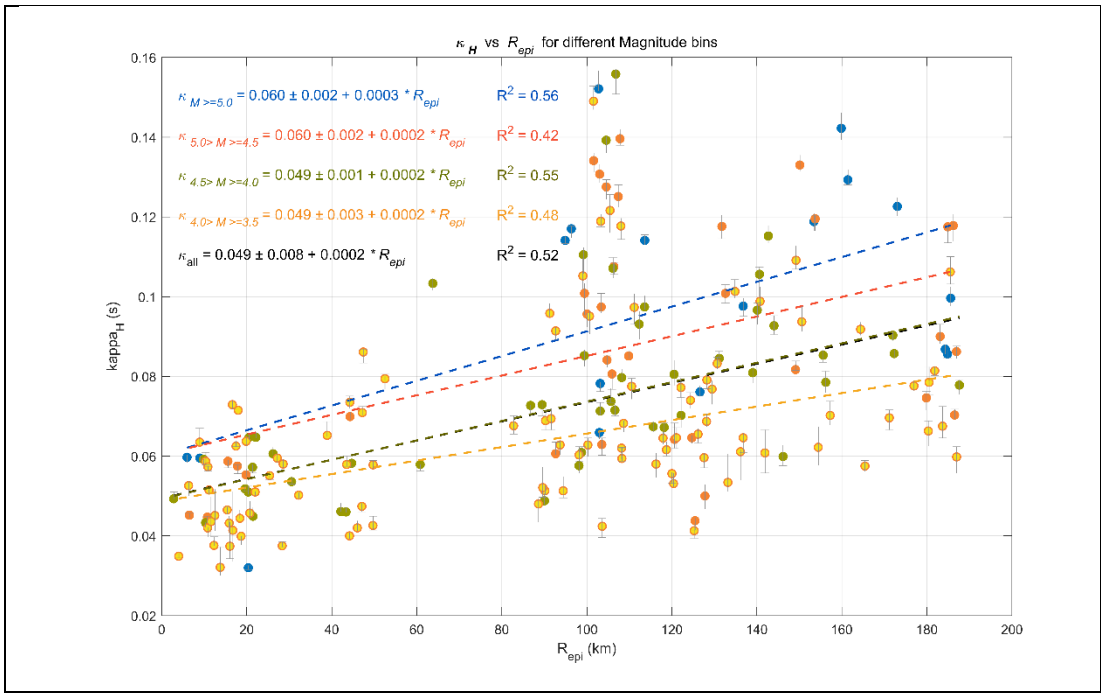


Figure 7.14: The horizontal event kappa, κ_H vs R_{epi} at different magnitude bins via robust multiple linear regression model.

Since the stations KMRS and YEDI had only five events selected, κ_0 values for those two stations were not calculated, but the κ_H values were included for overall tendency of κ_H vs R_{epi} for the region.

While investigating the correlation between κ_H and R_{epi}, a semi logarithmic distance dependency model was carried out (Figure 7.15). The same magnitude dependency that was encountered with preferred robust multiple linear regression model is also seen in logarithmic space. For each magnitude bin, the correlation coefficient for robust multiple linear regression model was higher than the robust logarithmic regression model and therefore was chosen for this study. Even though the correlation coefficient for the robust linear regression model is slightly better (R^2 = 0.52) (Figure 7.14) than the robust logarithmic regression model (R^2 = 0.50) (Figure 7.15), the variance for robust logarithmic model resulted with a lower value of ± 0.003 s when compared with the robust linear with ± 0.008 s variance for κ_0 from all event

median κ_H values. This tendency changes when considered for each magnitude bin though. Better variance values are achieved for all bins with $M_L \geq 4.0$ with robust multiple linear regression model.

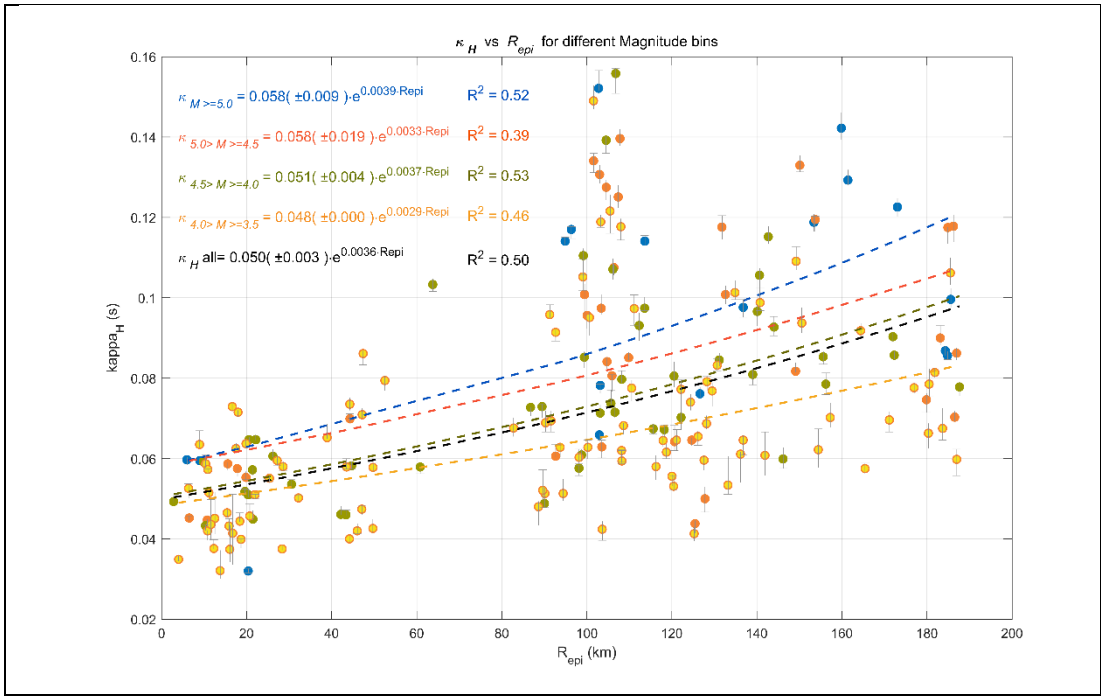


Figure 7.15: The horizontal event kappa, κ_H vs R_{epi} at different magnitude bins via robust logarithmic fit model.

Also, a sensitivity study was done to see the effect of station ARPR resulting median κ_H values to the overall κ_H and R_{epi} fit. When excluded, the correlation coefficient of both multiple linear and logarithmic regression models yielded to 0.63 and κ_0 for both resulted 0.048 with different variance values of ± ~0.00 s for robust linear and ± 0.005 s for robust logarithmic model. It is preferred to keep ARPR results in the database for the evaluations as it might give insight for possible other network, like AFAD stations, investigations around this station location.

Finally, the station-based results of κ_0 are given in Figures 7.16 –7.39. In these figures, blue circles indicate median κ_H values evaluated from all stations, whereas red circles indicate station based median κ_H values. The slope of the κ_H vs R_{epi} fit were then favored constrained as suggested by Douglas [2010].

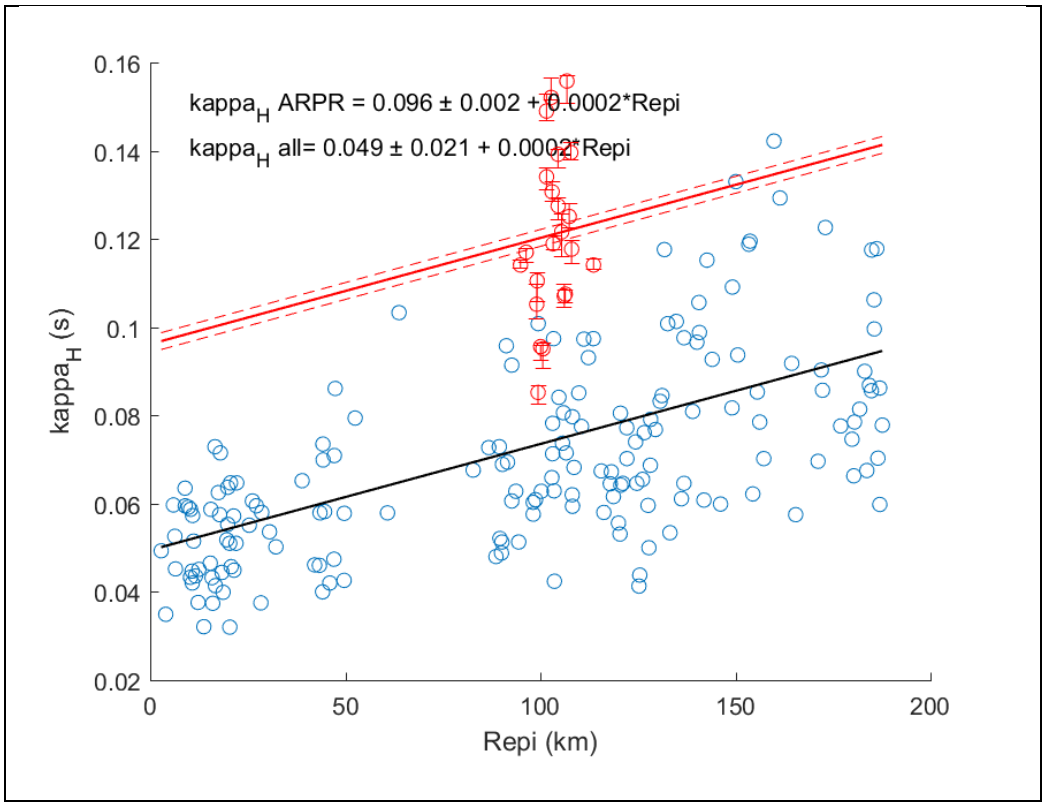


Figure 7.16: The constrained to overall κ_H vs R_{epi} fit for ARPR station.

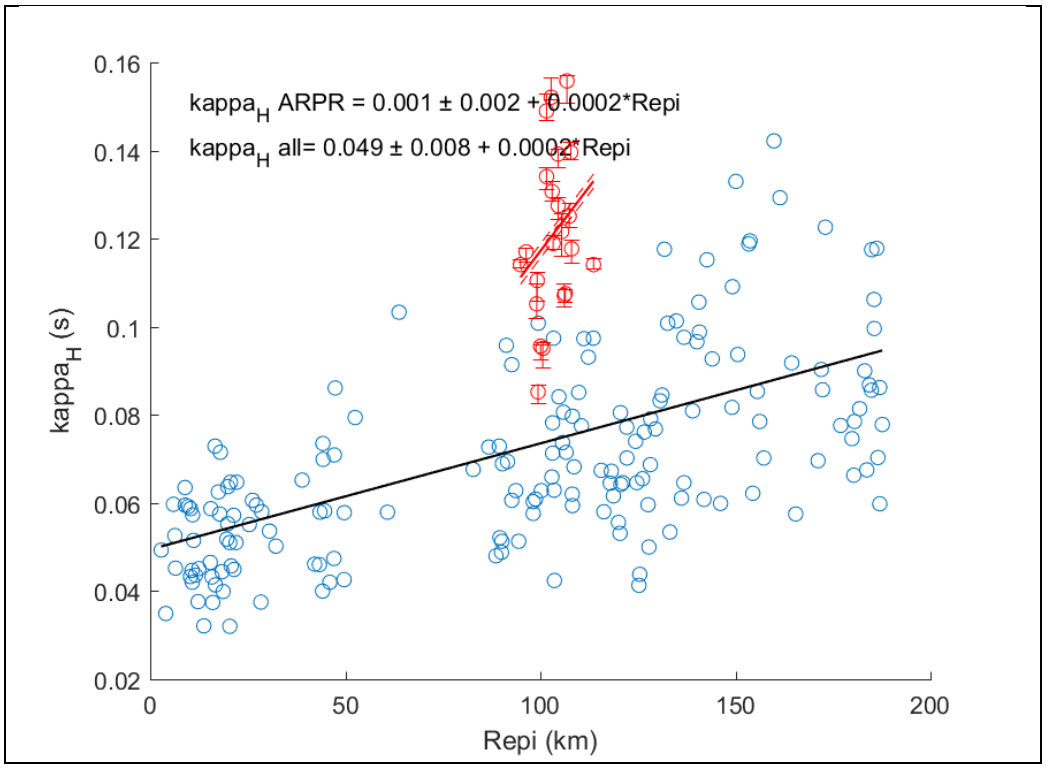


Figure 7.17: The unconstrained to overall κ_H vs R_{epi} fit for ARPR station.

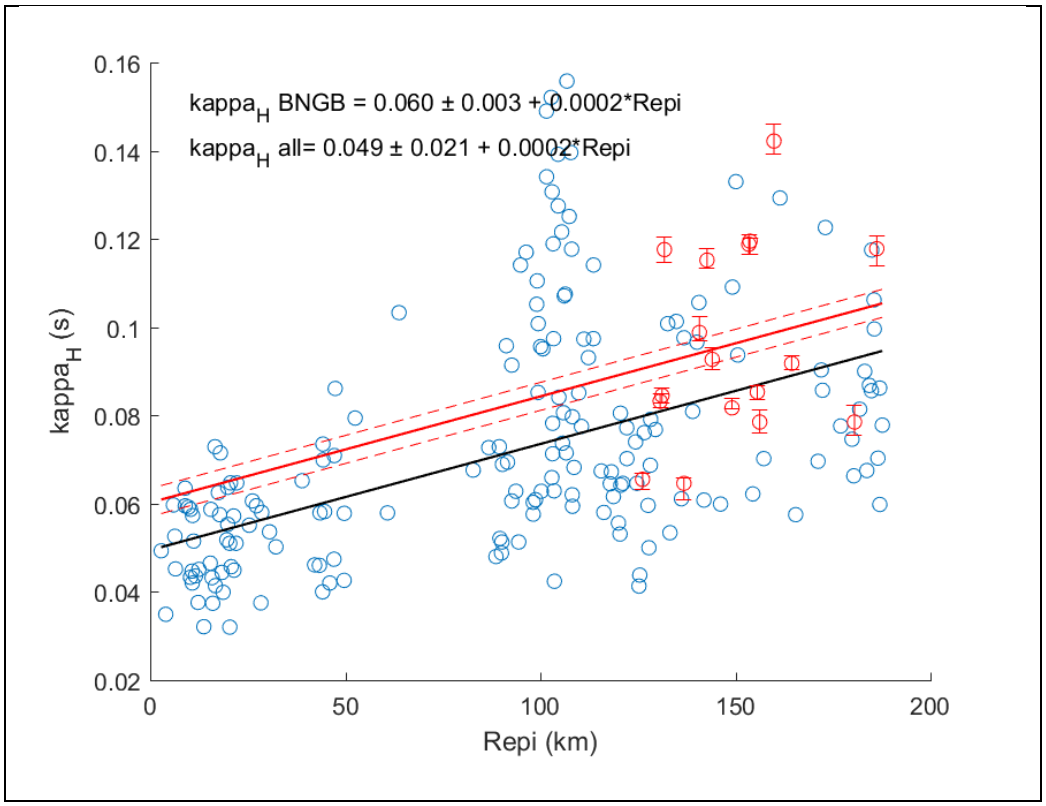


Figure 7.18: The constrained to overall κ_H vs R_{epi} fit for BNGB station.

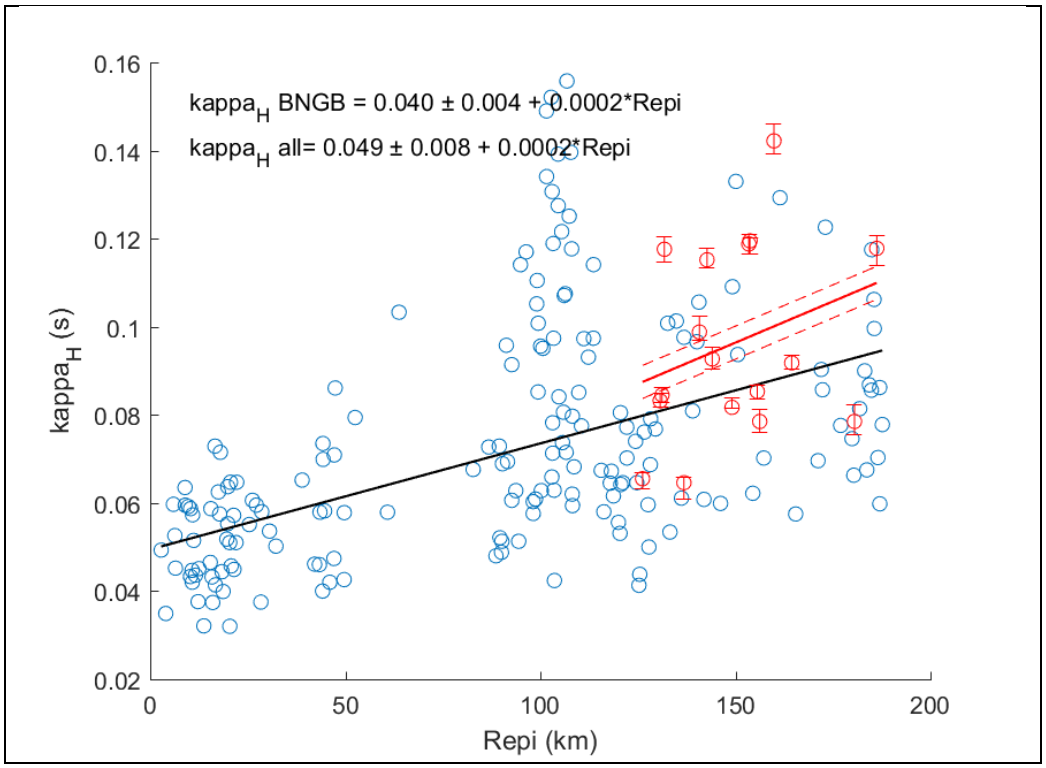


Figure 7.19: The unconstrained to overall κ_H vs R_{epi} fit for BNGB station.

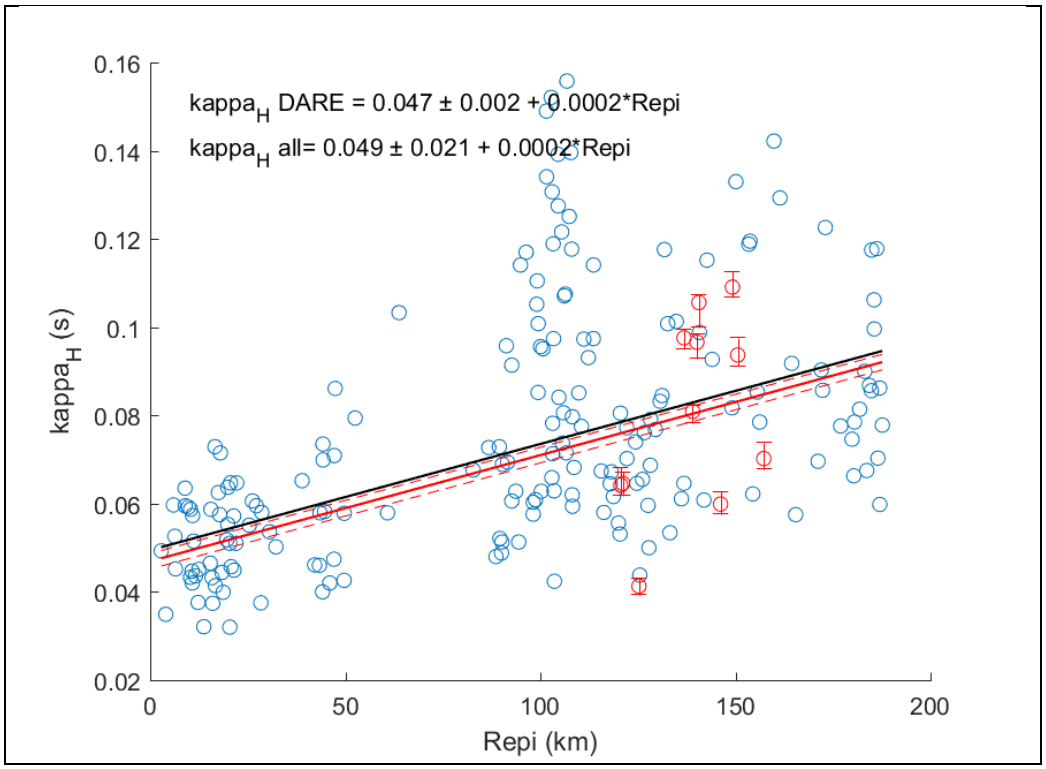


Figure 7.20: The constrained to overall κ_H vs R_{epi} fit for DARE station.

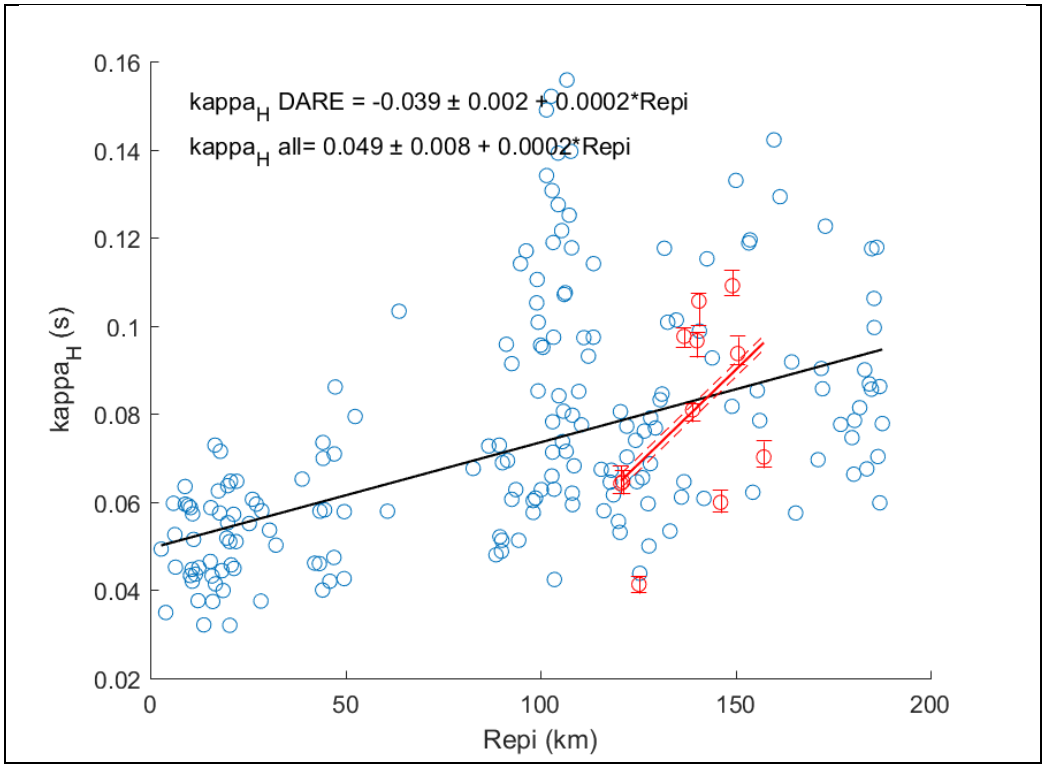


Figure 7.21: The unconstrained to overall κ_H vs R_{epi} fit for DARE station.

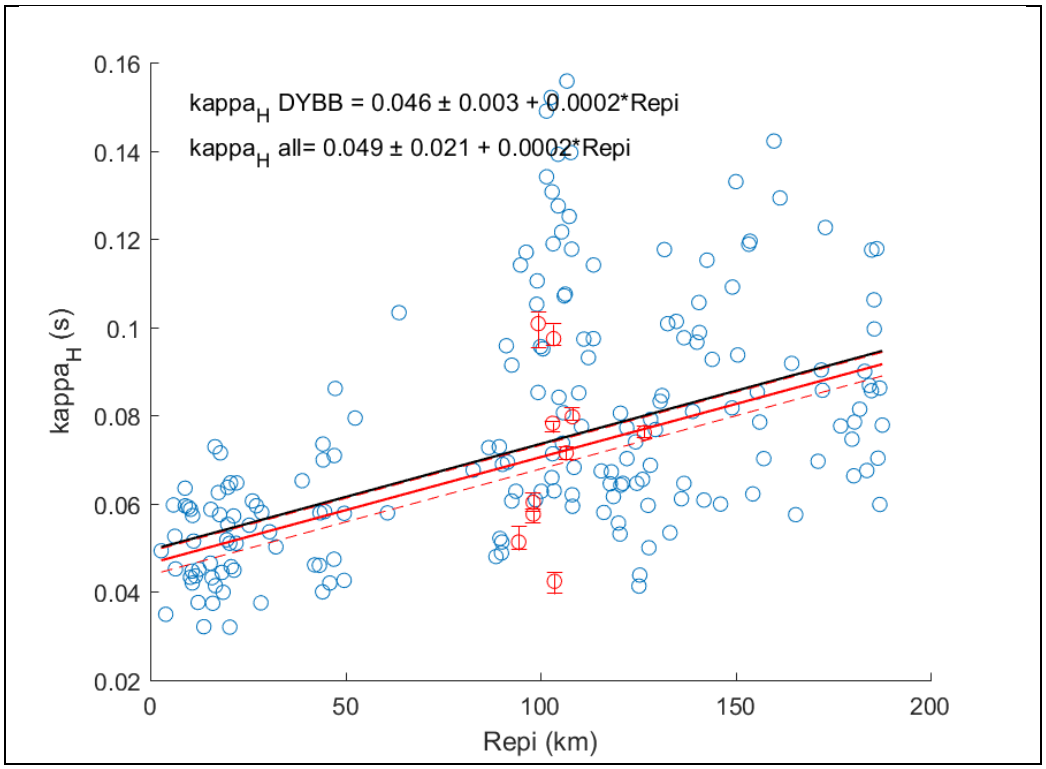


Figure 7.22: The constrained to overall κ_H vs R_{epi} fit for DYBB station.

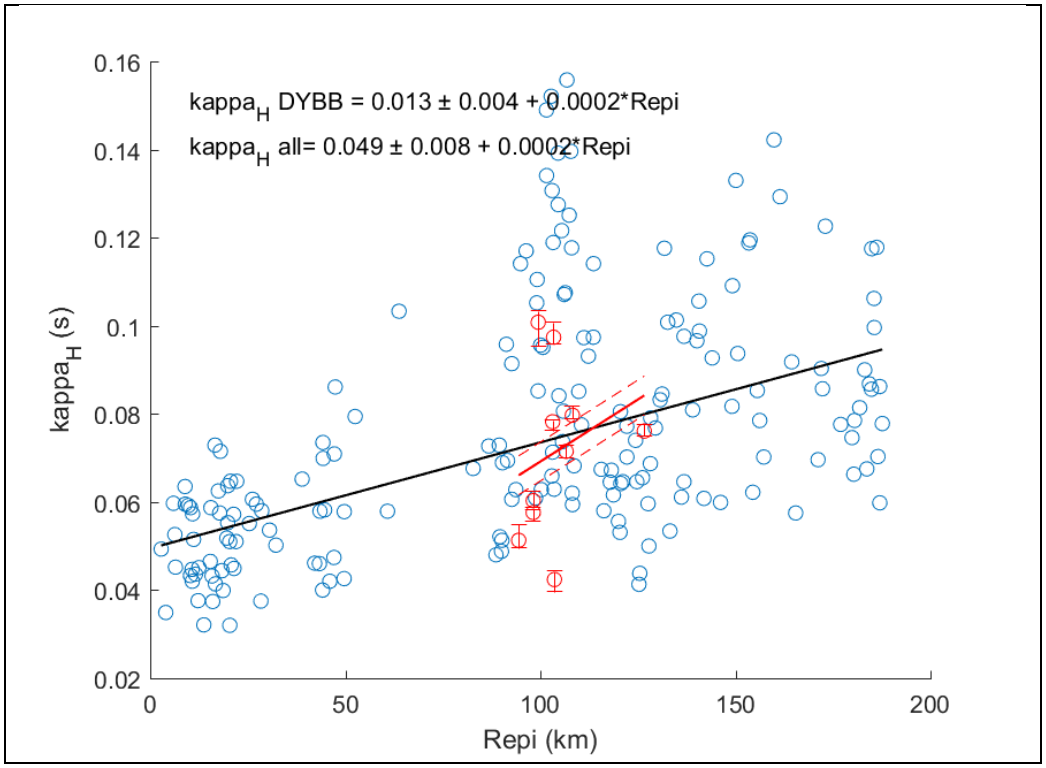


Figure 7.23: The unconstrained to overall κ_H vs R_{epi} fit for DYBB station.

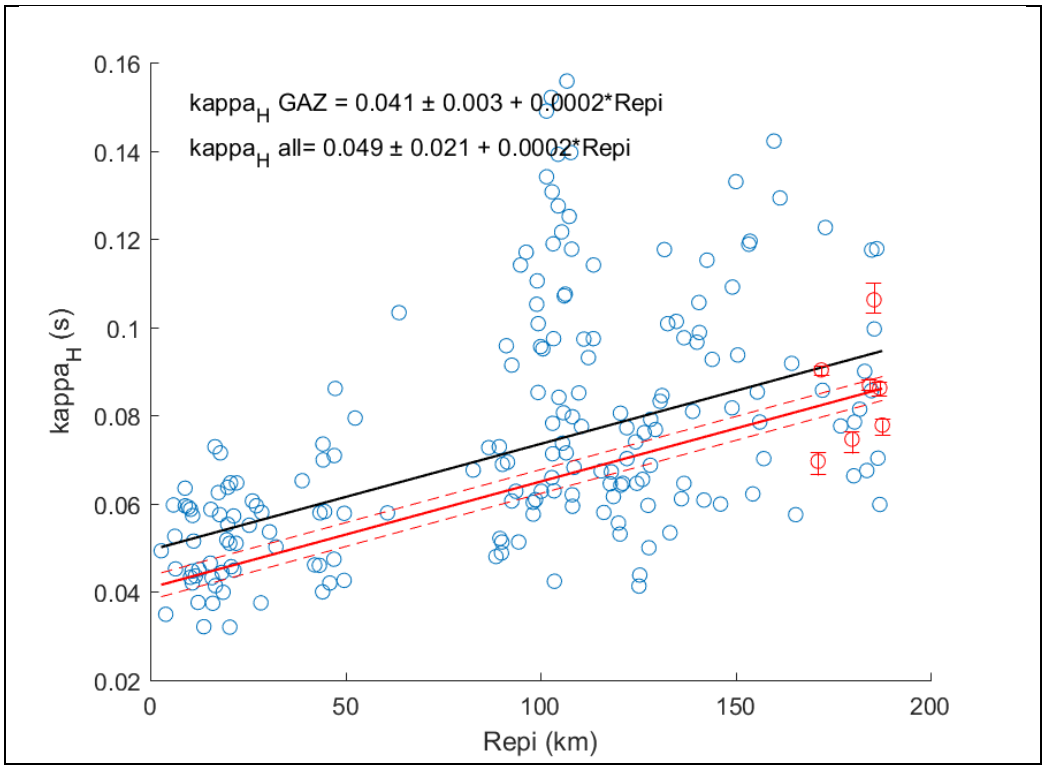


Figure 7.24: The constrained to overall κ_H vs R_{epi} fit for GAZ station.

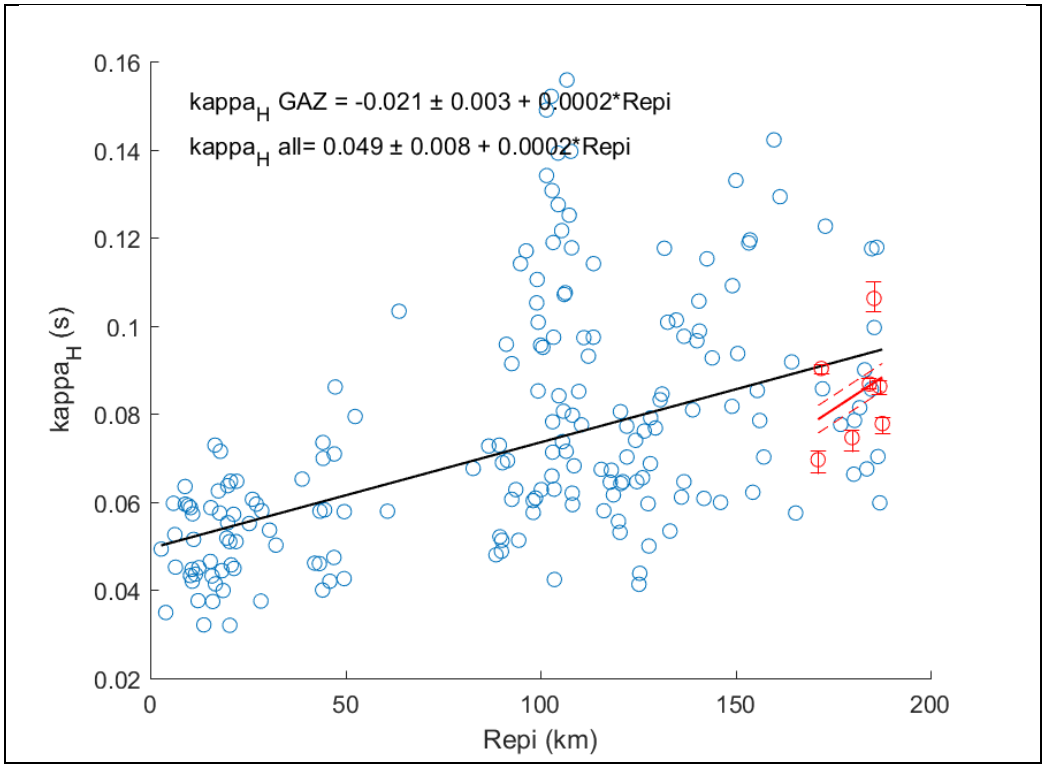


Figure 7.25: The unconstrained to overall κ_H vs R_{epi} fit for GAZ station.

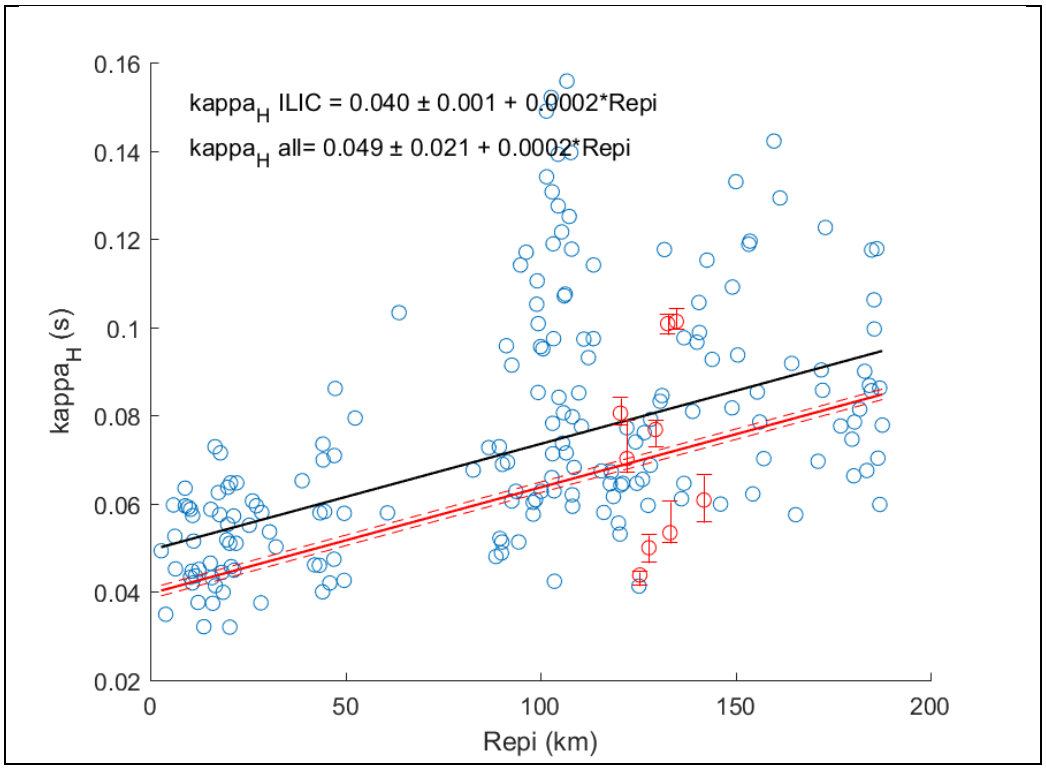


Figure 7.26: The constrained to overall κ_H vs R_{epi} fit for ILIC station.

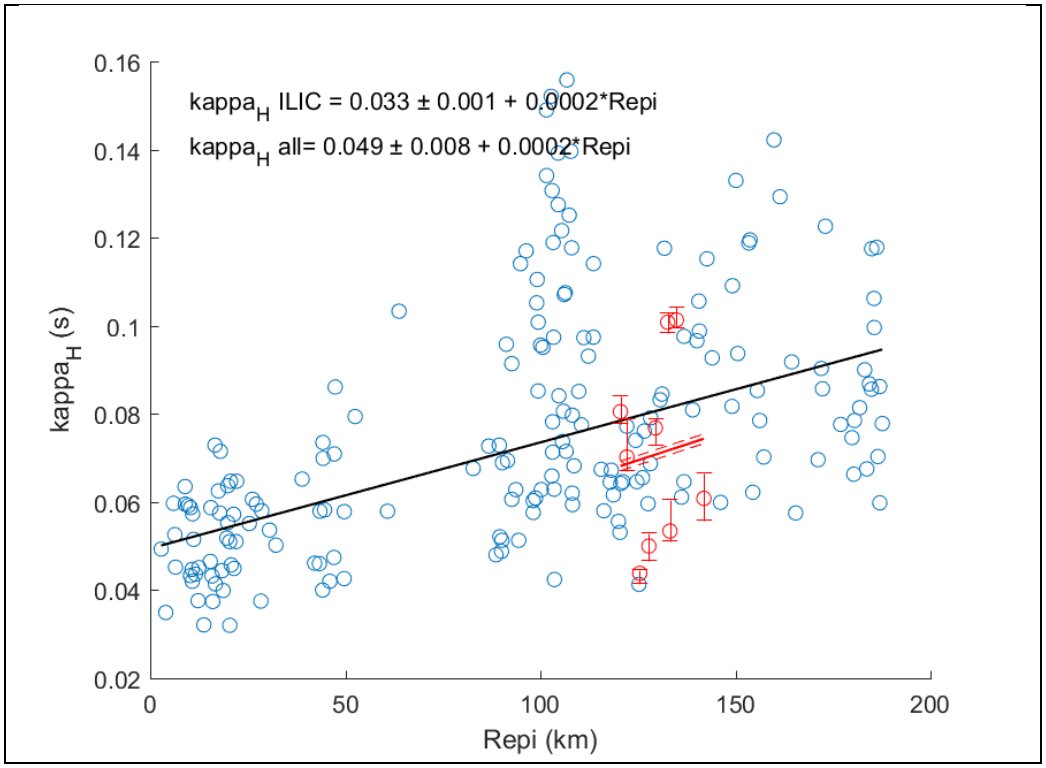


Figure 7.27: The unconstrained to overall κ_H vs R_{epi} fit for ILIC station.

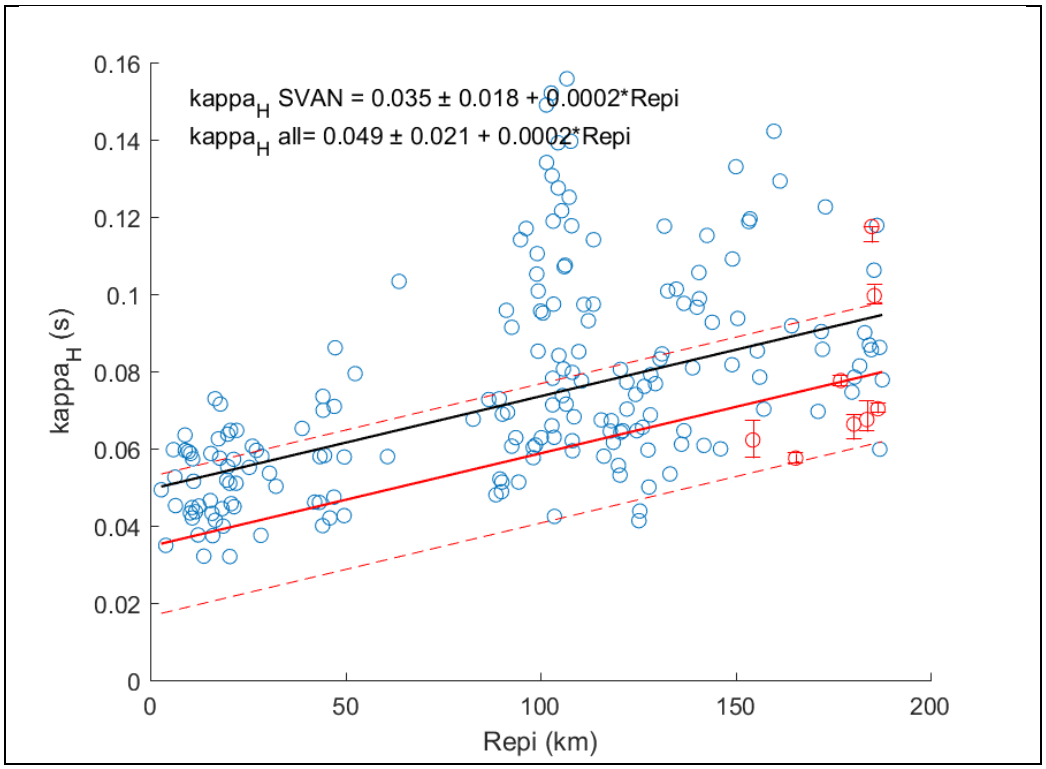


Figure 7.28: The constrained to overall κ_H vs R_{epi} fit for SVAN station.

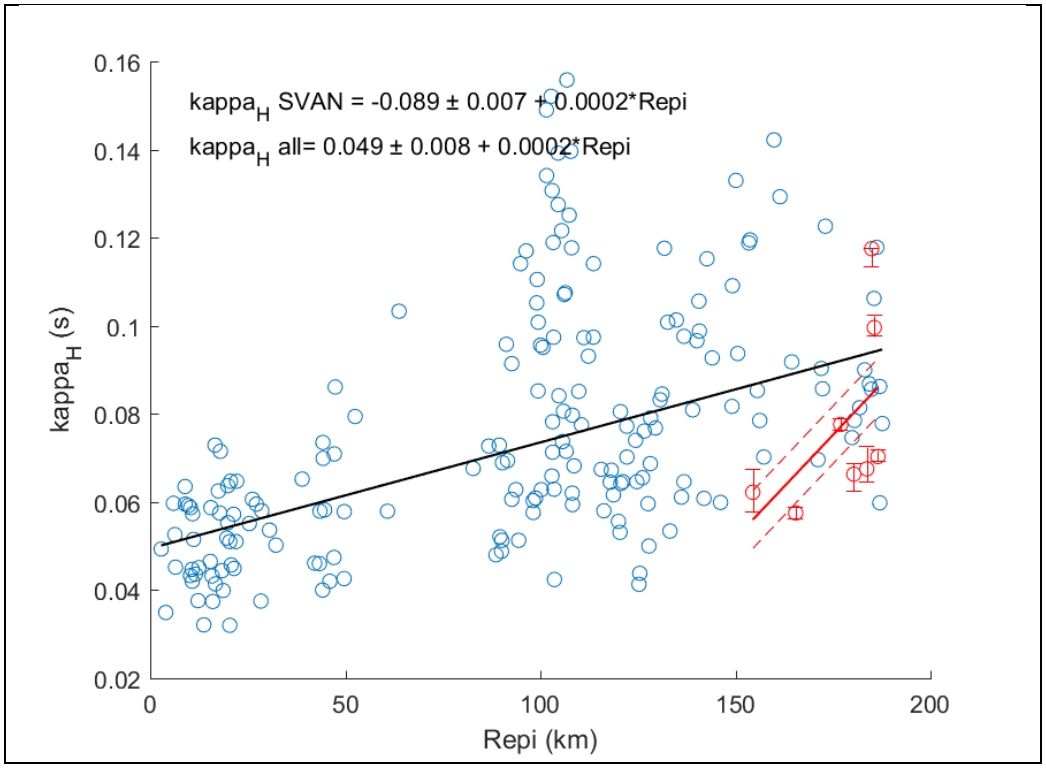


Figure 7.29: The unconstrained to overall κ_H vs R_{epi} fit for SVAN station.

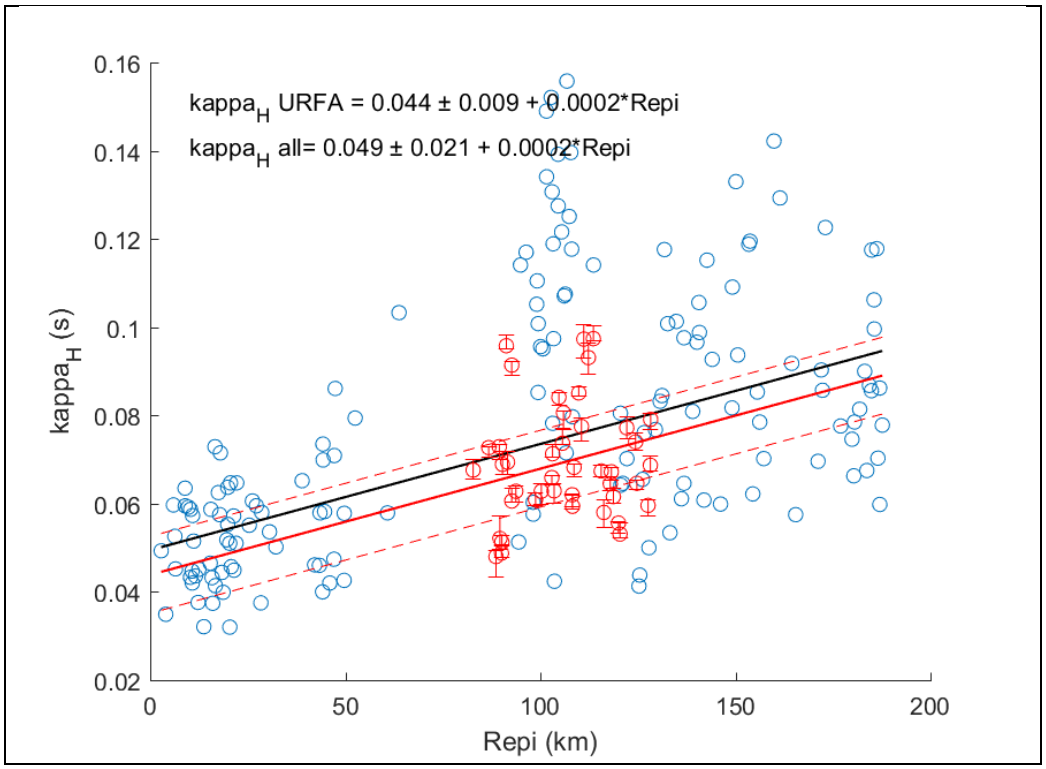


Figure 7.30: The constrained to overall κ_H vs R_{epi} fit for URFA station.

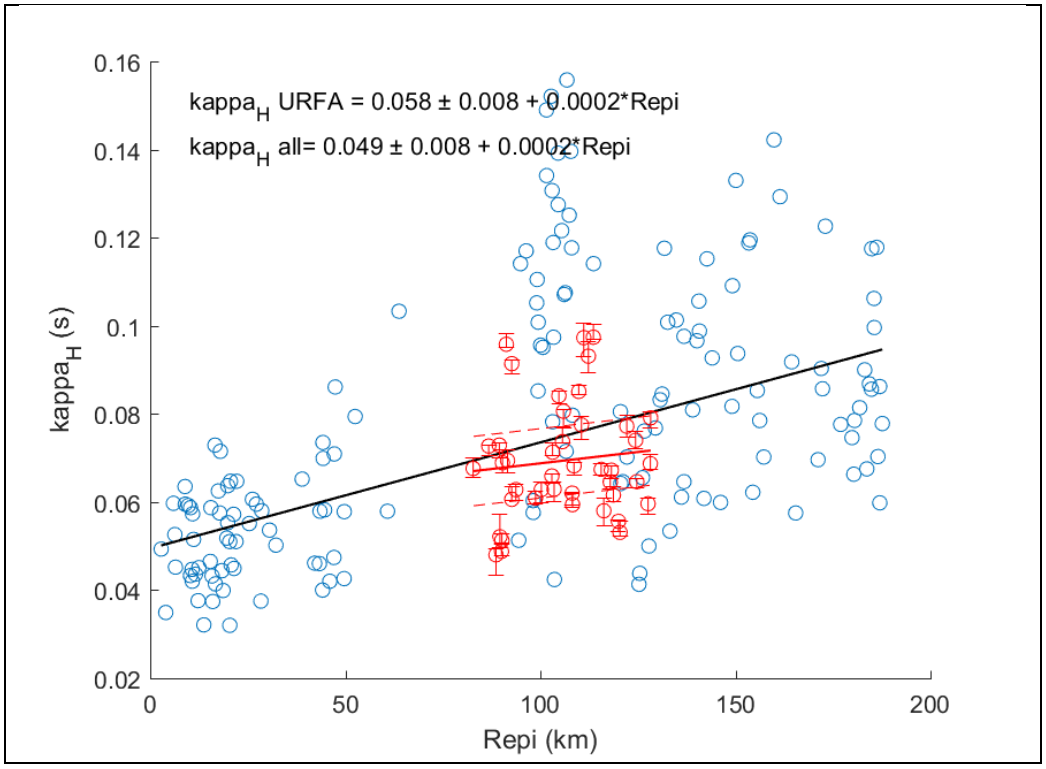


Figure 7.31: The unconstrained to overall κ_H vs R_{epi} fit for URFA station.

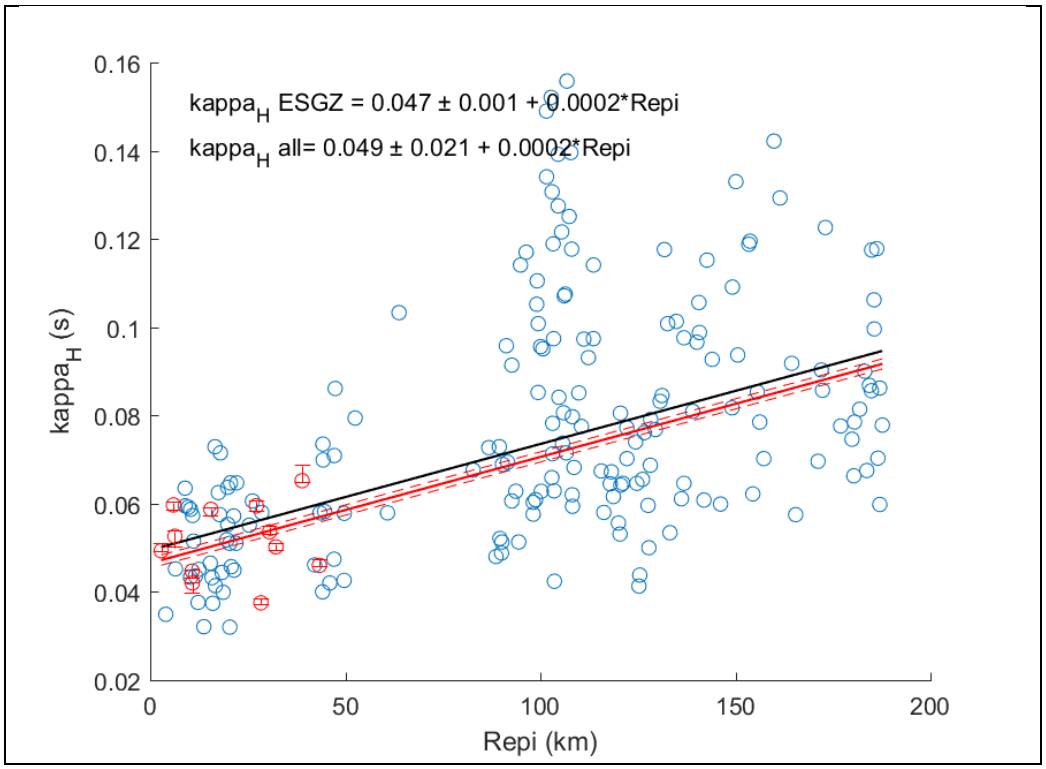


Figure 7.32: The constrained to overall κ_H vs R_{epi} fit for ESGZ station.

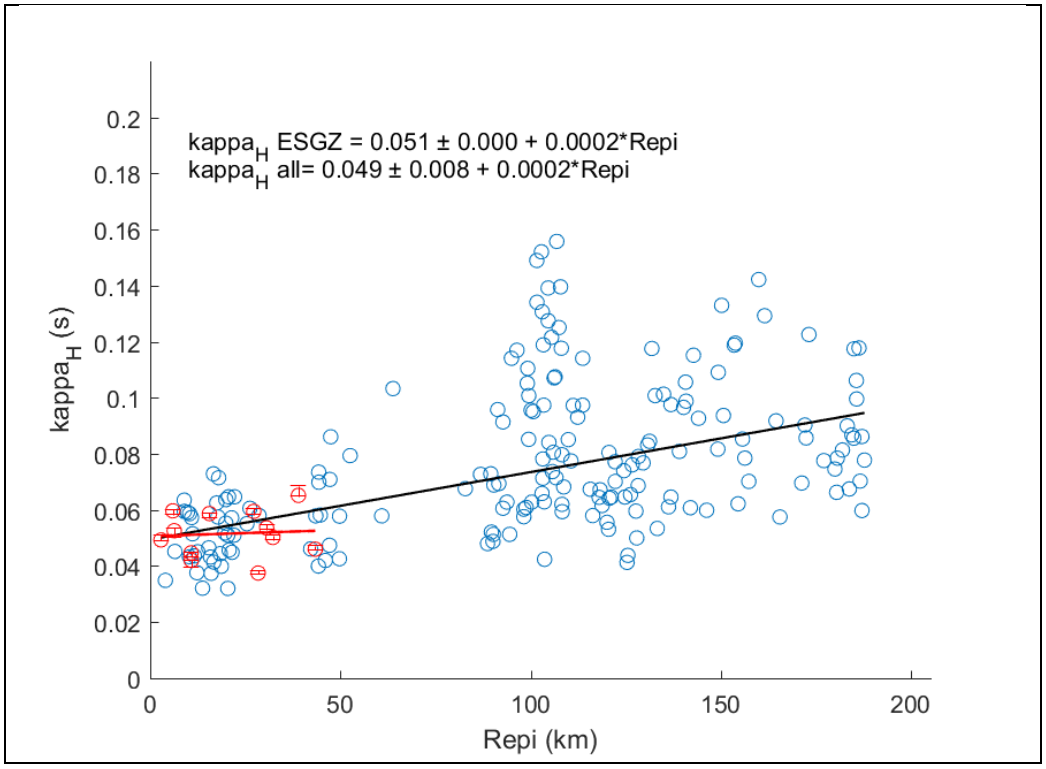


Figure 7.33: The unconstrained to overall κ_H vs R_{epi} fit for ESGZ station.

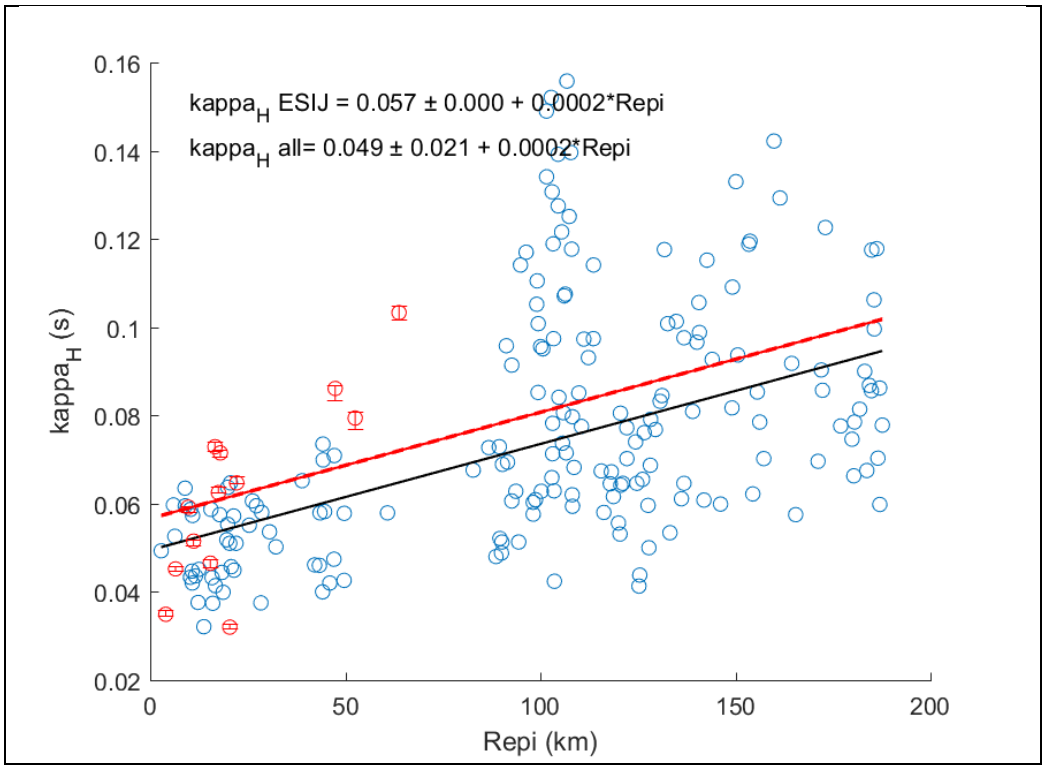


Figure 7.34: The constrained to overall κ_H vs R_{epi} fit for ESIJ station.

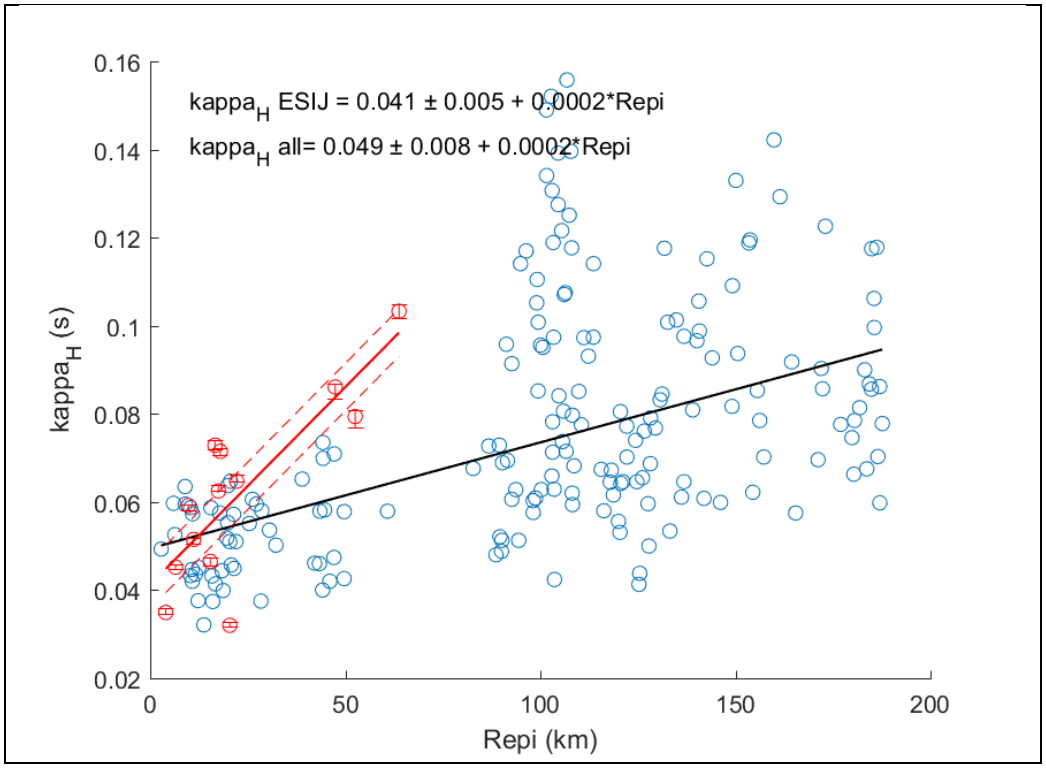


Figure 7.35: The unconstrained to overall κ_H vs R_{epi} fit for ESIJ station.

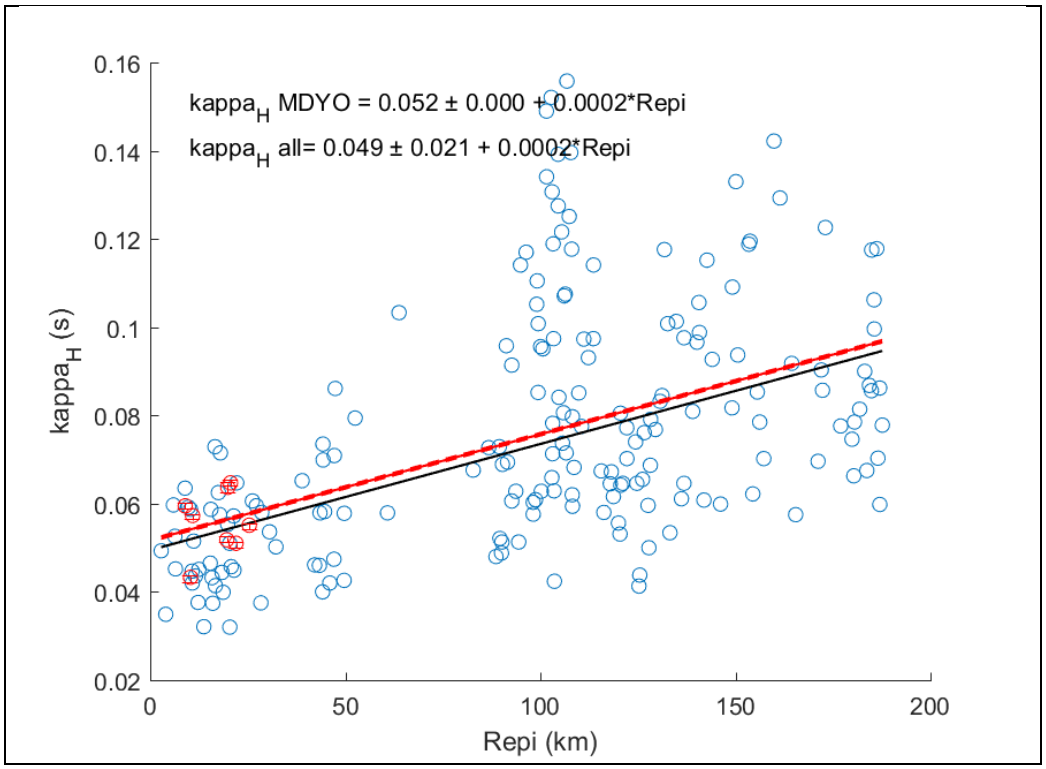


Figure 7.36: The constrained to overall κ_H vs R_{epi} fit for MDYO station.

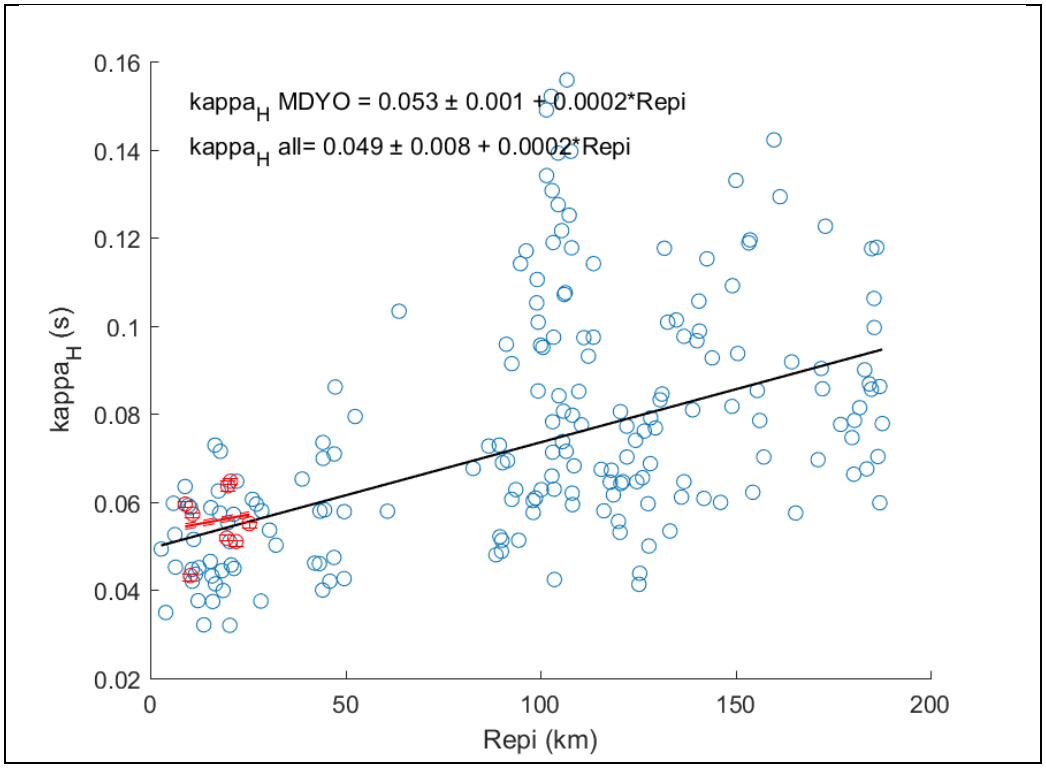


Figure 7.37: The unconstrained to overall κ_H vs R_{epi} fit for MDYO station.

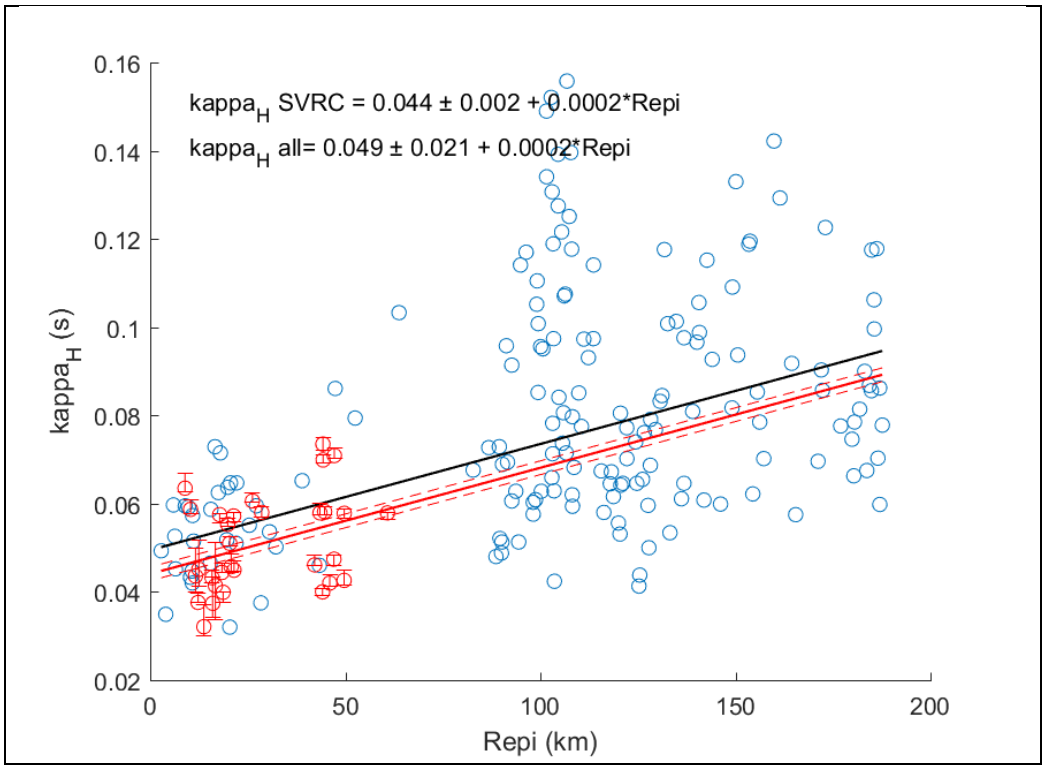


Figure 7.38: The constrained to overall κ_H vs R_{epi} fit for SVRC station.

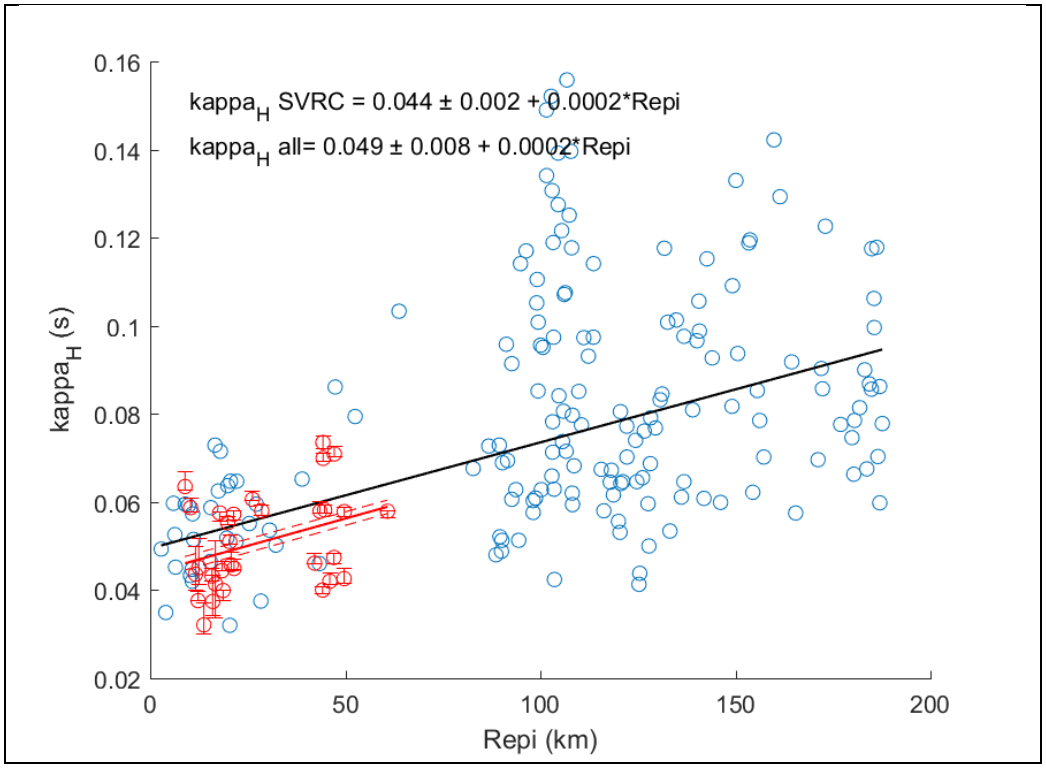


Figure 7.39: The unconstrained to overall κ_H vs R_{epi} fit for SVRC station.

It is clearly seen in Figure 7.16 and Figure 7.17 that station ARPR κ_H results are significantly higher than all of the other stations. This station recorded events that are

95-115 km in range of epicentral distance away from the Sivrice-Pütürge segment and M_L differs from 3.5 to 6.6. During κ_0 evaluations, if the κ_H vs R_{epi} fit is constrained, the result is 0.096 (± 0.002) s, whereas if the fit is unconstrained, it is ~0.00 (± 0.002) s as listed in Table 7.5. The constrained fit κ_0 value indicates ARPR is on soft soil or the Q effect there is different than the rest of the area, whereas the unconstrained fit κ_0 value indicates that this station should be located on stiff-hard rock. The need to check for the site amplifications as well as the peak frequencies at those amplification peaks could give more information of the station site which will be discussed below under relative topics.

Table 7.5: Station based κ_0 estimations with constrained and unconstrained fit. Constrained fit is favored in the current study.

Station Code	**κ_0 (s) constrained κ_H vs R_{epi} robust fit**	**κ_0 (s) unconstrained κ_H vs R_{epi} robust fit**
ARPR	0.096 ± 0.002	~0.00 ± 0.002
BNGB	0.060 ± 0.003	0.040 ± 0.004
DARE	0.047 ± 0.002	-0.038 ± 0.002
DYBB	0.046 ± 0.003	0.011 ± 0.004
ESGZ	0.047 ± 0.001	0.051 ± ~0.00
ESIJ	0.057 ± ~0.00	0.042 ± 0.005
GAZ	0.041 ± 0.003	-0.021 ± 0.003
ILIC	0.040 ± 0.001	0.033 ± 0.001
MDYO	0.052 ± ~0.00	0.053 ± 0.001
SVAN	0.035 ± 0.018	-0.089 ± 0.007
SVRC	0.044 ± 0.002	0.044 ± 0.002
URFA	0.044 ± 0.009	0.057 ± 0.008

When the events recorded were near field events, the constrained versus unconstrained fits resulted with very close κ_0 values with very low variance, as seen in Figures 7.16 –7.39.

It is also observed significantly low variance of event based median κ_H from the robust linear fits to the acceleration Fourier spectrum between automatically selected

$f_E - f_x$ band. These variations are illustrated in Figures 7.16 –7.39 with error bars on each median κ_H value.

As mentioned before, at the time of the evaluation period the AFAD data were closed to access, and only the data available from KOERI were evaluated. As seen in Figure 7.11, except four near site stations, all stations of KOERI are installed in far field between 80 to 200 km away from the single fault source in consideration (Table 7.4). Out of four near site stations, SVRC is a weak motion station and suffers from saturation at large magnitudes for near site large events. The remaining three strong motion stations ESGZ, ESIJ and MDYO were installed during the aftershock sequence of M_L6.5 January 2020 earthquake and includes events from mid of February 2020 until June 2020 for our dataset.

There is also constraint on the event magnitude and distance selection in this study. The events with $M_L \geq 3.5$ and with epicentral distance, $R_{epi} \leq 200$ km were considered and if the selected events are less than four events for the station at evaluation process, the station with these events were excluded from the database. It should be kept in mind that, as also indicated in Palmer et. al. [2020], if the database consists $M \geq 3.5$ events, the linear trend obtained is statistically not significant even when choosing all events recorded from all seismic sources, instead of a single fault source, in the maximum epicentral distance set for evaluations, instead of a single fault source as chosen in this section of the PhD thesis. As this study is a first attempt to introduce a constraint on selecting the events only originating from a single fault source, it should be kept in mind that the correlation cannot yet be compared with the previous related studies on kappa evaluation.

Among the scientists evaluating κ for Turkey region, this study is the first to apply a robust fit and show the constrained versus unconstrained. Until now unconstrained least squares linear fits are realized and the correlation was not under investigation. Our new discussion on the comparison of such fits now could be a value for Turkey related studies.

7.3.1.4. HVSR Evaluations and Results

HVSR evaluations were utilized to check if the frequency bands chosen to evaluate κ values for each station were applicable and were not coupled with site

amplification. Also, these evaluations could give us the site class differentiation between our sites, e.g., if one was a harder soil site than another, as there are no V_{s30} information for these sites.

The complete waveform of the recordings was selected if SNR was equal or greater than 3. PSA and Konno-Ohmachi [1998] windowed FAS were computed. The smoothing coefficient b = 20 and b = 40 were applied and b = 20 is favored for the results as in Zhu et.al. [2020] and Palmer et.al. [2020]. While obtaining the HVSR for both PSA and FAS, the geometrical mean of north-south (NS) and east-west (EW) components were divided to the vertical component of the record as suggested in SESAME [2004]. The overall average HVSR of the recordings per site, for both PSA and FAS, were determined and the significant peak frequencies were selected if mean $HVSR_{FAS}$ or mean $HVSR_{PSA}$ amplitudes reached a peak more than 2.00. The results for $HVSR_{FAS}$ are given in Table 7.6 and are favored for HVSR results. The amplitudes more than 2.00 and assigned to significant peak frequencies, *fs* are shown in boldface characters, indicating softer layers are present at those stations when compared with stations that had lower amplitude values. If multiple peaks were observed, all were listed under *fs* and the highest amplitude responding values, if in excess of the value 2.00, are shown in boldface characters in Table 7.6.

The results can also be visualized in Figure 7.40 as a summary, where $HVSR_{FAS}$ for each selected event is shown with grey-colored lines, the mean $HVSR_{FAS}$ curve with its variation (mean ± one standard deviation) are shown with solid black line traces, and the mean $HVSR_{PSA}$ is shown with dashed red line are illustrated. These findings also are in agreement with the findings and suggestions in Bora et. al. [2016], Stafford et.al. [2017], [Zhu et.al., 2020].

Table 7.6: Station-based $HVSR_{FAS}$ amplitudes and the corresponding peak frequencies.

Station Code	**Mean Amplitude ($HVSR_{FAS}$)**	***fs* (Hz)**
ARPR	**2.46**	**3.1**
ARPR	2.29	5.1
BNGB	1.72	3.2
DARE	1.44	8.9

Table 7.6: Continuation. Station-based $HVSR_{FAS}$ amplitudes and the corresponding peak frequencies.

Station Code	**Mean Amplitude ($HVSR_{FAS}$)**	***fs* (Hz)**
DARE	1.35	0.3
DYBB	**2.46**	**4.4**
DYBB	1.74	0.4
ESGZ	**2.18**	**2.7**
ESGZ	**2.15**	**3.7**
ESIJ	**3.23**	**0.3**
ESIJ	2.92	1.8
GAZ	1.79	0.1
GAZ	1.79	1.3
ILIC	**2.55**	**10.0**
ILIC	2.04	1.2
ILIC	1.74	2.8
MDYO	**2.31**	**4.9**
MDYO	2.09	0.4
MDYO	2.09	1.2
MDYO	2.08	2.3
SVAN	1.66	1.6
SVAN	1.65	0.8
SVRC	**2.13**	**2.5**
SVRC	1.73	1.3
URFA	1.94	0.3
URFA	1.80	6.9
URFA	1.41	1.2

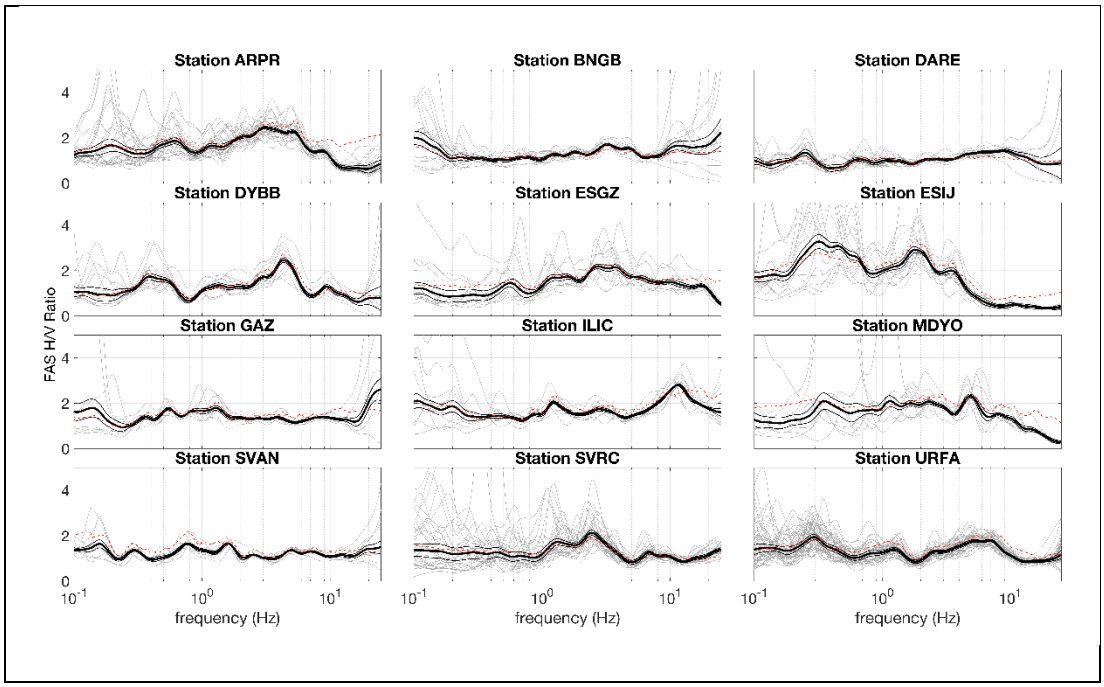


Figure 7.40: HVSR for 12 KOERI stations.

Stations BNGB, DARE, GAZ, SVAN and URFA are characterized by relatively flat $HVSR_{FAS}$ with amplitudes less than 2.00, DARE having the flattest trend than the rest and are assigned to be relatively free of site amplification, namely harder site conditions than the rest of the stations (Figure 7.41). The comparison station DARE is illustrated in solid black in this figure, representing the hardest soil site.

There are no detailed local geological maps available for this region, but from the regional geological information, NEHRP site class A for stations DARE, GAZ, ILIC and SVRC and NEHRP site class B for the remaining eight stations could be vaguely assigned.

Station ILIC has three resonant frequency peaks as listed in Table 7.6, highest occurring around 10 Hz. Station ESIJ has the highest amplitude among other stations with f_p around 0.3 Hz.

It should be noted that the amplitudes are approximate values as they are not corrected with bed-rock amplitudes due to lack of borehole data and soil profiles at these KOERI stations.

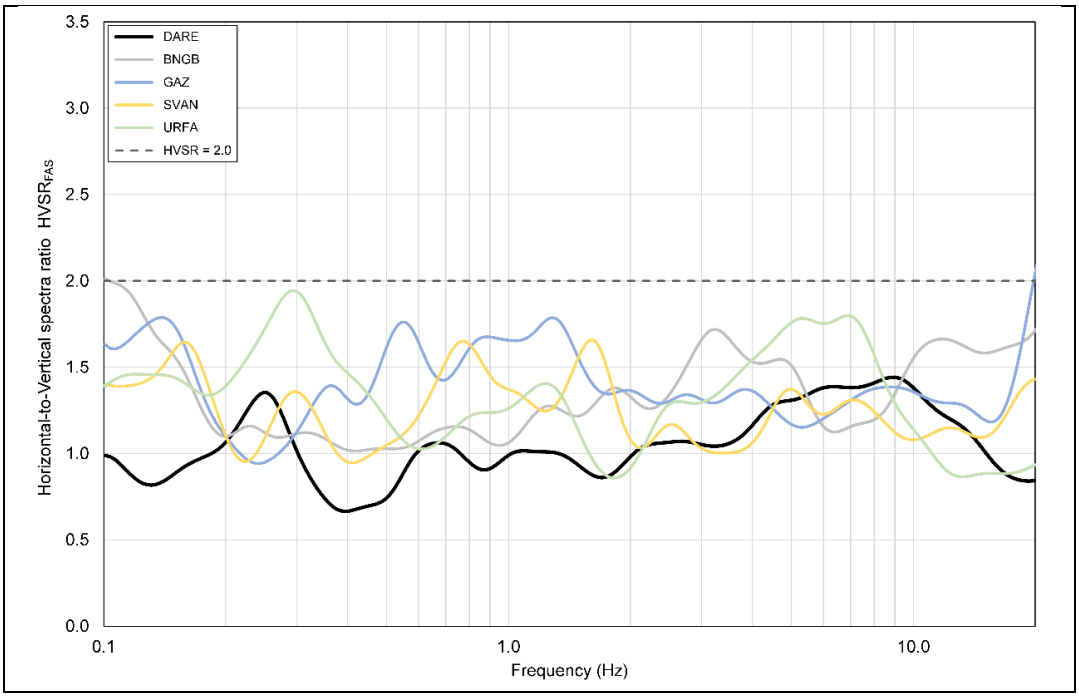


Figure 7.41: $HVSR_{FAS}$ of KOERI stations with amplitudes lower than 2.00.

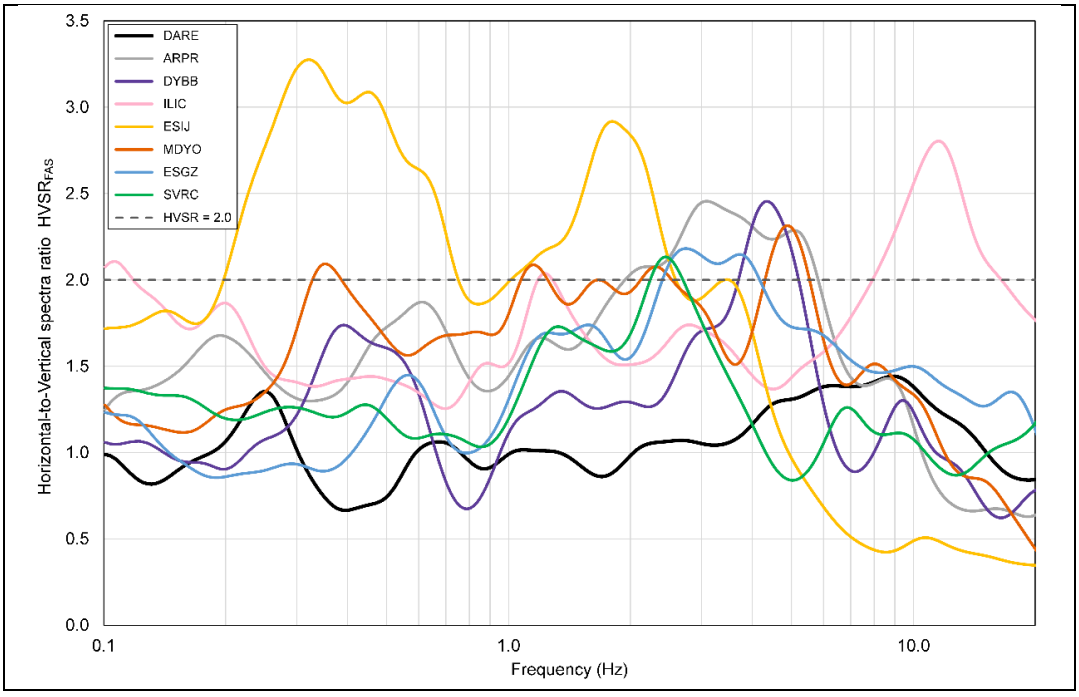


Figure 7.42: $HVSR_{FAS}$ of KOERI stations with amplitudes higher than 2.00.

While Figure 7.41 illustrates the sites with $HVSR_{FAS}$ amplitudes less than 2.00, Figure 7.42 illustrates the sites with $HVSR_{FAS}$ amplitudes higher than 2.00 with comparison station DARE in solid black line.

7.3.1.5. Comparison of κ_0 versus HVSR results and discussion

The assignment of f_E in the current study, indicated that κ_H evaluations are not affected by the site amplification peak frequencies measured from HVSR curves. Even in the case of the station ILIC where the highest amplification is at around 10 Hz, the f_E values were automatically selected higher than 10 Hz due to resulting of corner frequency, f_c for the recordings at this station.

The $HVSR_{FAS}$ maximum amplitudes for the near site stations SVRC, ESGZ, ESIJ and MDYO and the evaluated κ_0 values are in agreement with each other. ESIJ has the highest site amplification among four near site stations with the mean $HVSR_{FAS}$ value of 3.23 also has the highest κ_0 value of 0.057 (± ~0.00) s from constrained κ_H vs R_{epi} fit. The lowest $HVSR_{FAS}$ amplitude at corresponding peak frequency is evaluated for station SVRC as 2.13, a possible NEHRP site class A from regional geological map, and the κ_0 value for this station is the lowest among four stations and is 0.044 (± 0.002) s from constrained κ_H vs R_{epi} fit. ESGZ and MDYO has also the same tendency and the values can be compared from Table 7.5 and Table 7.6. It is clearly seen that the unconstrained fit to κ_H vs R_{epi} does not have such tendency for ESIJ station having the lowest median κ_0 values of 0.042 s with high variation of ± 0.005 among all four near station sites and yet; this station has the highest site amplification among all stations in consideration at around peak frequency 0.3 Hz (Figure 7.43).

Station DARE having the flattest and lowest amplitude trend on $HVSR_{FAS}$ curves has 0.047 ± 0.002 s resulting κ_0 value for constrained, and -0.038 ± 0.002 s for unconstrained κ_H vs R_{epi} fit. ILIC station has a peak around 10 Hz with $HVSR_{FAS}$ amplitude 2.55, and ARPR station has a peak around 3.1 Hz with $HVSR_{FAS}$ amplitude 2.46. Stations DARE, ILIC and ARPR are located at the northeast far end of Sivrice-Pütürge segment as seen in Figure 7.11. In between lies two dam reservoirs, Keban and Karakaya namely. This could be the reason, especially for ARPR, not to fit to the κ_H vs R_{epi} trend in our database (Figure 7.16 and Figure 7.17). Stations DARE and ILIC should also be looked at in precautious manner if they are affected from these two dam reservoirs. Even though DARE seems to have the same κ_H vs R_{epi} tendency of the KOERI database, κ_0 results from constrained κ_H vs R_{epi} fit at this station is higher than expected for a stiff-hard soil as observed in HVSR evaluations.

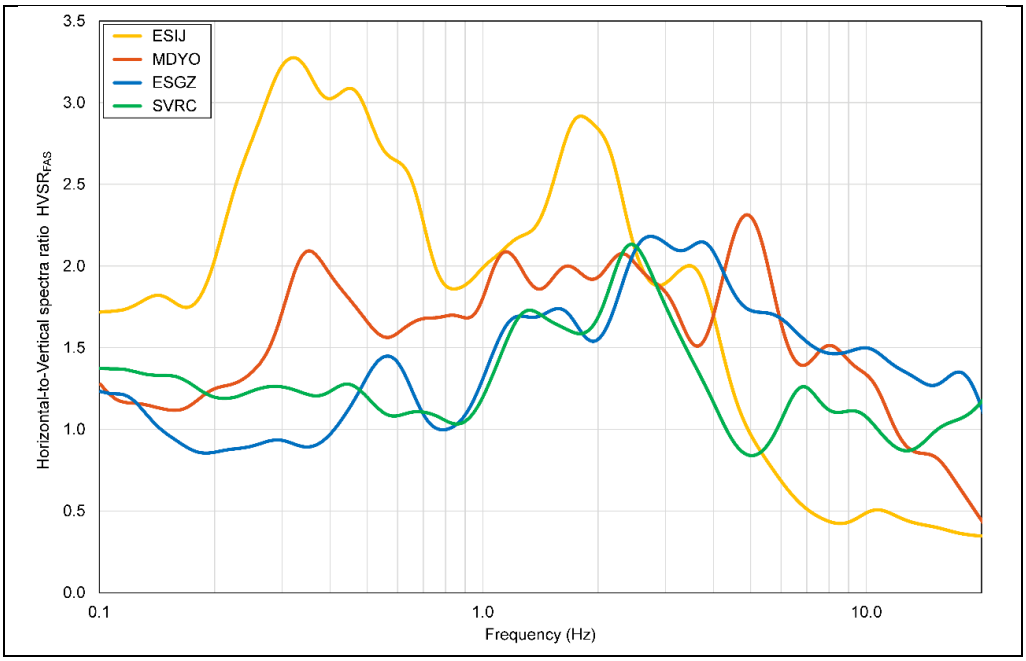


Figure 7.43: $HVSR_{FAS}$ of near site KOERI stations.

The station ARPR which gives very high κ_H results compared to other stations, has actually two $HVSR_{FAS}$ amplitude peaks greater than 2.00 at around 3.1 and 5.1 Hz, and suggest that this station is not on hard rock. However, from Table 7.5, κ_0 result as "~0.00 ± 0.002" from the unconstrained fit would suggest as if this station was on hard rock soil properties.

Station SVAN is listed in the harder site section from our HVSR evaluations as mentioned before and is illustrated in Figure 7.40 and Figure 7.41. The recorded events are in 150-200 km epicentral distance range as mentioned in Table 7.4. For this station the resulting κ_0 value for constrained κ_H vs R_{epi} fit is 0.035 ± 0.018 s, and -0.089 ± 0.007 s for unconstrained. For a softer soil site, at station BNGB, with the highest peak of $HVSR_{FAS}$ 2.46 at around 4.4 Hz, the resulting κ_0 value for constrained κ_H vs R_{epi} fit is 0.060 ± 0.003 s, whereas it is 0.040 ± 0.004 s for unconstrained.

Together with the HVSR findings, it can be visualized as a good indication that unconstrained fits for κ_0 evaluations for far events can give false indications for the station under evaluation. Especially for far stations from the event sequence, the constrained κ_H vs R_{epi} fit is favored over the unconstrained, with keeping in mind that station ARPR has an exceptional case and needs to be studied further with more site classification parameter data when available in the future.

7.3.2. AFAD Results

During the time of the evaluation period for KOERI data, AFAD data were closed to access, so only the data available from KOERI were evaluated as mentioned before. Later, AFAD database was open-source and the data for this region was retrieved and evaluated. These evaluations and the results are presented here.

7.3.2.1. Dataset and Methodology

The dataset used for Sivrice-Pütürge segment related events are the recordings gathered from strong motion stations of AFAD network between July 1994 until February 2021 [Web 3]. The events with $M_L \geq 3.5$ and with epicentral distance, $R_{epi} \leq$ 200 km were considered likewise gathered KOERI database and 106 AFAD stations with such criteria was selected initially. If the selected events are less than eight events, the station with these events were excluded from the AFAD database and therefore 66 AFAD stations were selected for initial phases of the κ evaluations.

The newly developed noise and P- & S-wave selection procedure which was explained under section "2.3.1. Inconsistency in Evaluations", was applied to select the S-wave window of the records. The records were checked for SNR < 3, the Δf between f_E and f_x were set to 8 Hz and the difference between two horizontal κ values (κ_{EW} and κ_{NS}) were allowed to be 25%, the same manner applied for the KOERI database. Instead of setting a minimum value of f_E = 2 Hz, f_E is taken as 1.5 times f_c to follow the trend lately in recent publications. Out of 66 AFAD stations 54 stations have finally passed all these criteria.

The 24th January, 2020, Sivrice-Elazığ earthquake with M_w = 6.8 was recorded by 47 out of 54 stations within the selected range. Most of the 54 stations have V_{s30} information and are listed in Table 7.7 with the magnitude and epicentral distance ranges as well as the number of events that were evaluated. In total, 2049 event records were selected to present. This amount is 204 event records for KOERI database as presented in section "7.3.1. KOERI Results" of this PhD thesis.

Table 7.7: The selected event magnitude and the epicentral distance ranges for each AFAD station.

Station Code	V_{s30}	**Magnitude Range (M_w)**	**Epicentral Distance Range (R_{epi})**	**# of events**
0201	391 km/s	$3.6 \leq M_w \leq 6.8$	47-123 km	29
0204	555 km/s	$3.5 \leq M_w \leq 6.8$	9-83 km	74
0205	660 km/s	$3.5 \leq M_w \leq 6.8$	39-123 km	65
0206	863 km/s	$3.7 \leq M_w \leq 5.2$	73-133 km	8
0207	660 km/s	$3.5 \leq M_w \leq 6.8$	20-107 km	64
0208	-	$3.6 \leq M_w \leq 6.8$	80-166 km	29
0209	-	$3.6 \leq M_w \leq 6.8$	67-163 km	25
0212	-	$3.5 \leq M_w \leq 6.8$	16-91 km	79
0213	-	$3.6 \leq M_w \leq 6.8$	71-145 km	38
1201	529 km/s	$4.2 \leq M_w \leq 6.8$	111-163 km	11
1210	-	$4.0 \leq M_w \leq 6.8$	68-170 km	9
2101	519 km/s	$4.1 \leq M_w \leq 6.8$	99-143 km	24
2102	-	$3.5 \leq M_w \leq 4.2$	33-78 km	8
2104	-	$3.5 \leq M_w \leq 6.8$	39-91 km	23
2105	-	$3.5 \leq M_w \leq 6.8$	38-132 km	51
2106	-	$4.0 \leq M_w \leq 6.8$	76-180 km	25
2107	-	$3.5 \leq M_w \leq 5.3$	35-80 km	78
2301	407 km/s	$3.5 \leq M_w \leq 6.8$	20-66 km	78
2302	907 km/s	$3.5 \leq M_w \leq 6.8$	9-96 km	90
2304	489 km/s	$3.5 \leq M_w \leq 6.8$	12-105 km	26
2305	907 km/s	$3.5 \leq M_w \leq 6.8$	45-149 km	66
2306	663 km/s	$3.5 \leq M_w \leq 6.8$	52-134 km	13
2307	-	$3.5 \leq M_w \leq 6.8$	15-121 km	59
2308	450 km/s	$3.5 \leq M_w \leq 6.8$	2-83 km	127
2309	860 km/s	$3.5 \leq M_w \leq 5.2$	48-83 km	33

Table 7.7: Continuation. The selected event magnitude and the epicentral distance ranges for each AFAD station.

Station Code	V_{s30}	**Magnitude Range (M_w)**	**Epicentral Distance Range (R_{epi})**	**# of events**
2401	314 km/s	$4.3 \leq M_w \leq 6.8$	139-170 km	8
2404	567 km/s	$4.3 \leq M_w \leq 6.8$	158-188 km	10
2408	416 km/s	$4.3 \leq M_w \leq 6.8$	121-152 km	9
2409	875 km/s	$4.0 \leq M_w \leq 6.8$	103-134 km	42
2412	955 km/s	$4.2 \leq M_w \leq 6.8$	126-161 km	9
2414	372 km/s	$4.0 \leq M_w \leq 5.2$	134-185 km	10
2415	444 km/s	$4.0 \leq M_w \leq 6.8$	118-144 km	36
2710	-	$4.0 \leq M_w \leq 6.8$	118-182 km	24
2711	-	$4.0 \leq M_w \leq 6.8$	134-195 km	16
4401	481 km/s	$3.5 \leq M_w \leq 6.8$	27-88 km	105
4404	1380 km/s	$3.5 \leq M_w \leq 6.8$	7-93 km	144
4405	579 km/s	$3.6 \leq M_w \leq 6.8$	88-126 km	41
4407	735 km/s	$3.5 \leq M_w \leq 6.8$	67-98 km	57
4408	-	$3.5 \leq M_w \leq 6.8$	60-133 km	62
4409	-	$4.0 \leq M_w \leq 6.8$	103-147 km	22
4410	-	$4.0 \leq M_w \leq 6.8$	108-146 km	27
4411	-	$3.5 \leq M_w \leq 5.2$	83-100 km	17
4412	-	$3.5 \leq M_w \leq 6.8$	56-94 km	57
4605/4610	315 km/s	$4.1 \leq M_w \leq 6.8$	128-189 km	13
4611	731 km/s	$4.0 \leq M_w \leq 6.8$	132-187 km	13
4614	671 km/s	$4.0 \leq M_w \leq 5.3$	140-201 km	10
4631	543 km/s	$4.0 \leq M_w \leq 6.8$	103-167 km	30
4701	709 km/s	$4.0 \leq M_w \leq 6.8$	166-202 km	24
5809	340 km/s	$4.1 \leq M_w \leq 6.8$	155-187 km	16

Table 7.7: Continuation. The selected event magnitude and the epicentral distance ranges for each AFAD station.

Station Code	V_{s30}	Magnitude Range (M_w)	Epicentral Distance Range (R_{epi})	# of events
5816	-	$4.1 \leq M_w \leq 6.8$	180-188 km	13
6201	-	$3.5 \leq M_w \leq 6.8$	53-126 km	43
6202	-	$4.1 \leq M_w \leq 6.8$	135-181 km	13
6302	936 km/s	$4.1 \leq M_w \leq 6.8$	139-152 km	10
6304	376 km/s	$3.6 \leq M_w \leq 6.8$	82-179 km	36

The 54 AFAD stations and the related events are visualized in Figure 7.44. The distribution of the selected events with near field stations are also illustrated in Figure 7.45.

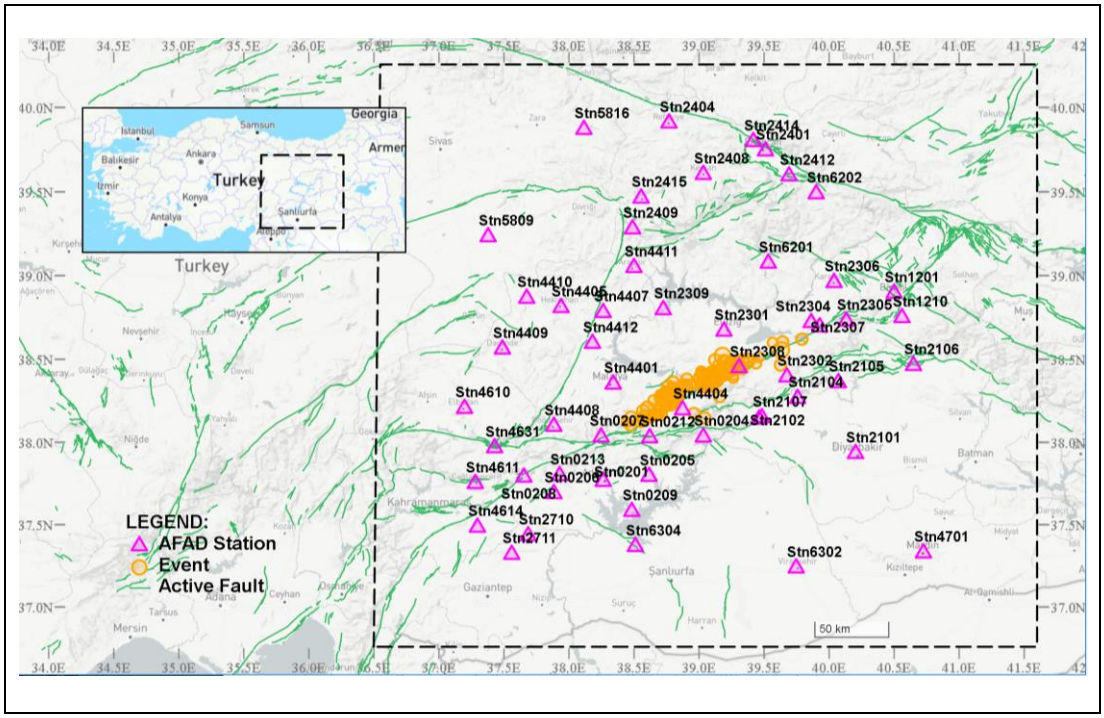


Figure 7.44: The distribution of selected events with selected AFAD stations.

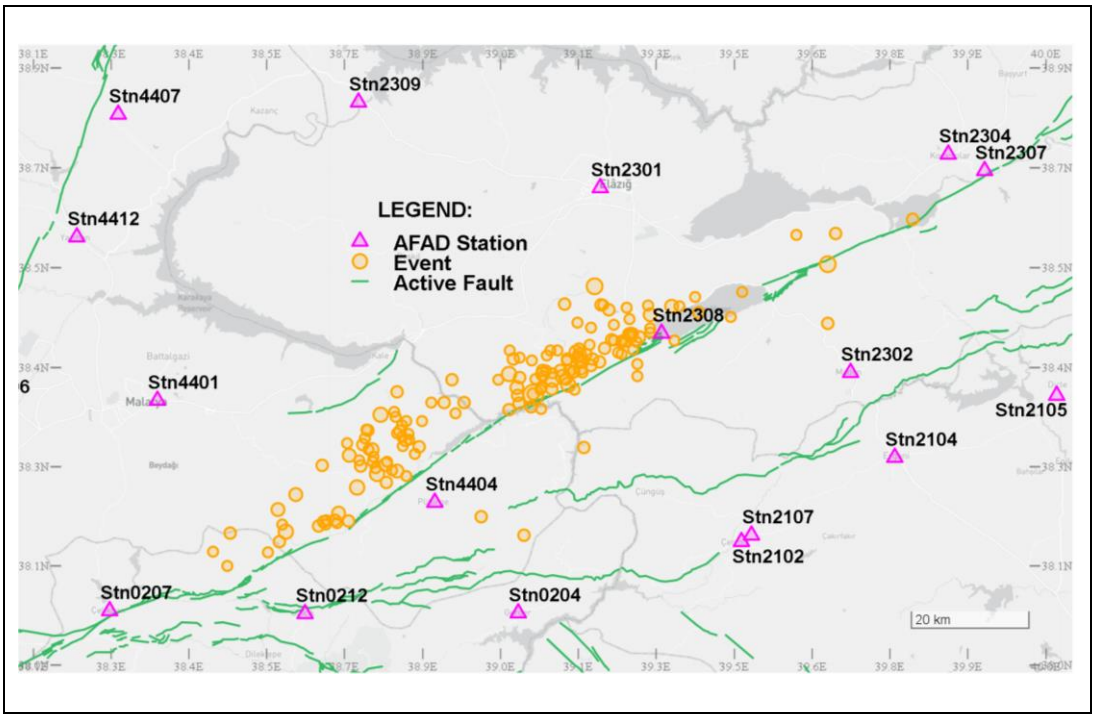


Figure 7.45: The distribution of selected events with near AFAD stations.

7.3.2.2. κ Results

The horizontal mean event κ, κ_H and R_{epi} distribution of 2049 events from 54 AFAD stations are plotted for different magnitude bins such as the KOERI case and the same difference in linear trend is visual as seen in Figure 7.46. As the data allowed to pick even less distance range, maximum R_{epi} = 100 km is also set and the trend of different magnitude bins for κ_H and R_{epi} distribution is given also for this range in Figure 7.47. In these figures, orange trend represents $4.0 > M \geq 3.5$, green trend represents $4.5 > M \geq 4.0$, red trend represents $5.0 > M \geq 4.5$, blue trend represents $M \geq 5.0$, and black dashed line represents the overall fit.

By even restricting the dataset with events only generated by a single fault source rather than evaluating all events recorded at AFAD stations, there seems to be a magnitude dependency as seen in Figure 7.46 and Figure 7.47 as was encountered in KOERI results.

Finally, the station-based results of κ_0 are given in Figures 7.48 –7.155. In these figures, blue circles indicate median κ_H values evaluated from all stations, whereas red circles indicate station based median κ_H values. The slope of the κ_H vs R_{epi} fit were then favored constrained as suggested by Douglas [2010].

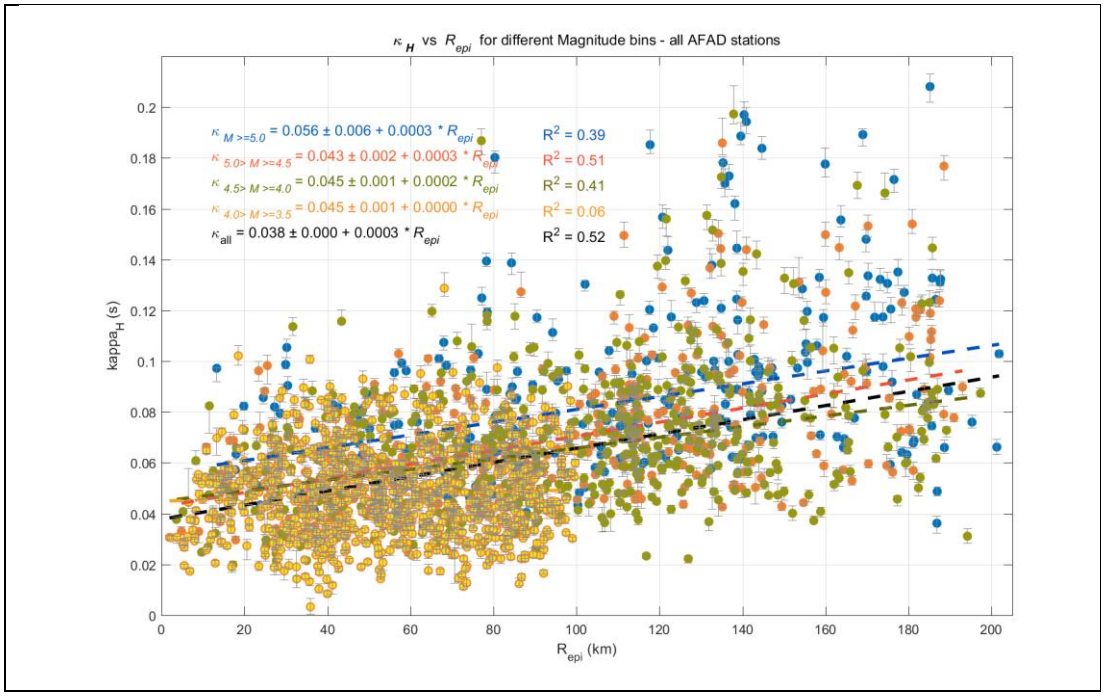


Figure 7.46: The horizontal event kappa, κ_H vs R_{epi} at different magnitude bins via robust multiple linear regression model.

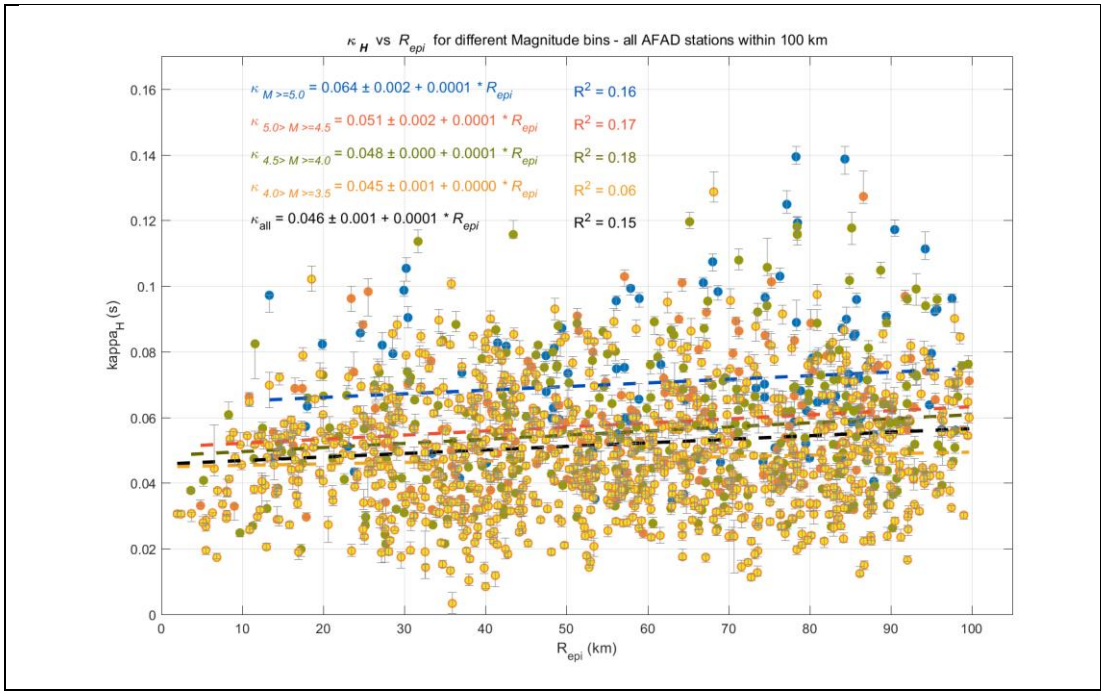


Figure 7.47: The horizontal event kappa, κ_H vs R_{epi} at different magnitude bins via robust multiple linear regression model within 100 km.

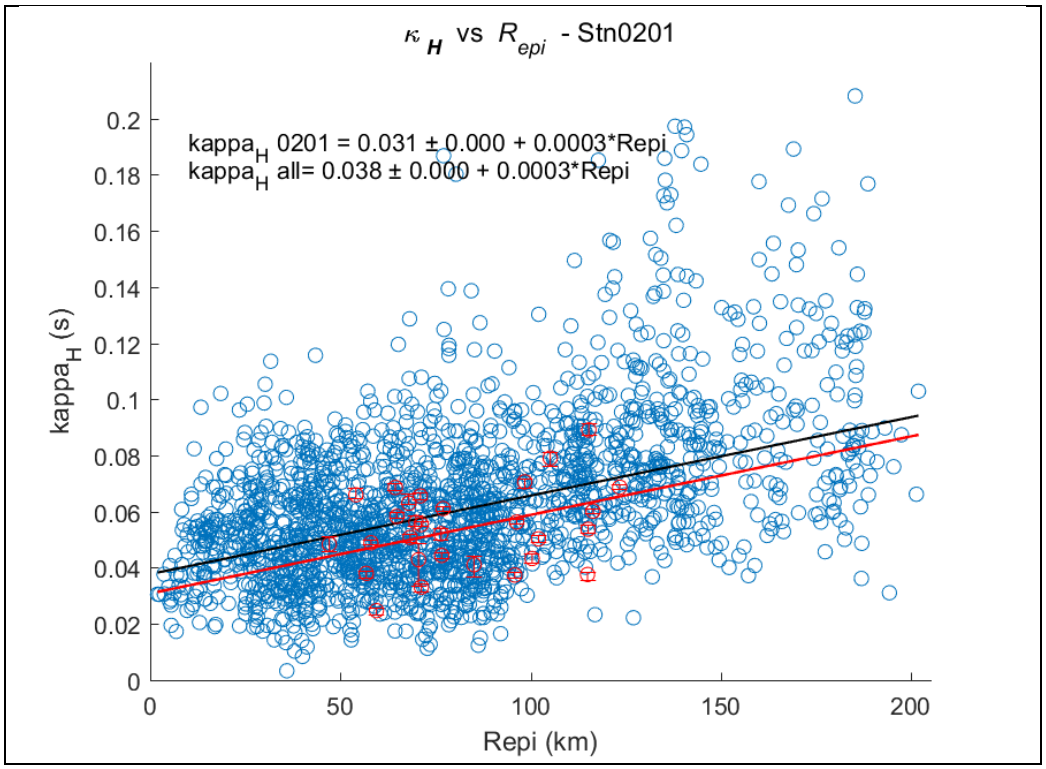


Figure 7.48: The constrained to overall κ_H vs R_{epi} fit for Stn0201.

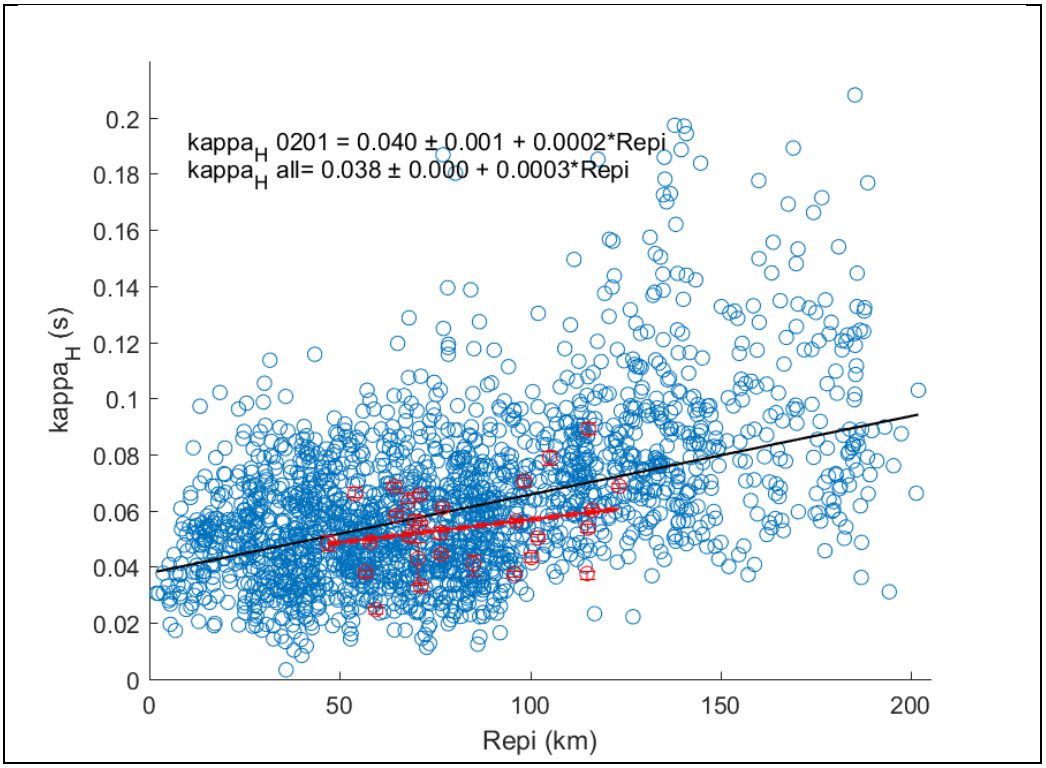


Figure 7.49: The unconstrained to overall κ_H vs R_{epi} fit for Stn0201.

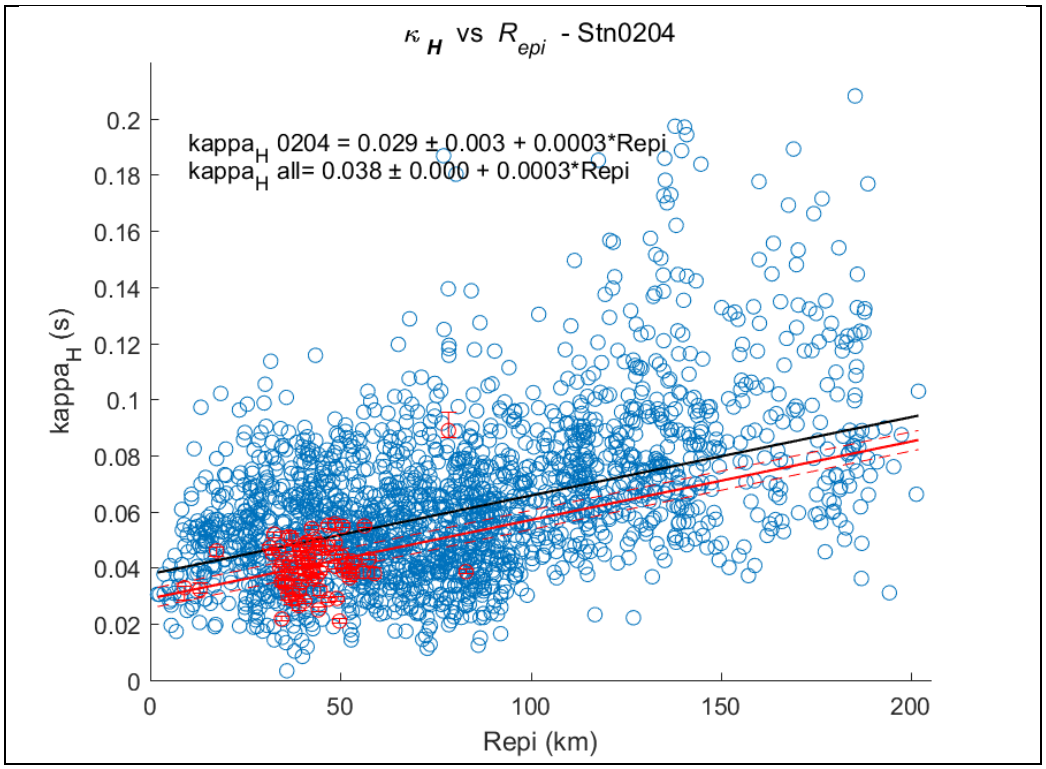


Figure 7.50: The constrained to overall κ_H vs R_{epi} fit for Stn0204.

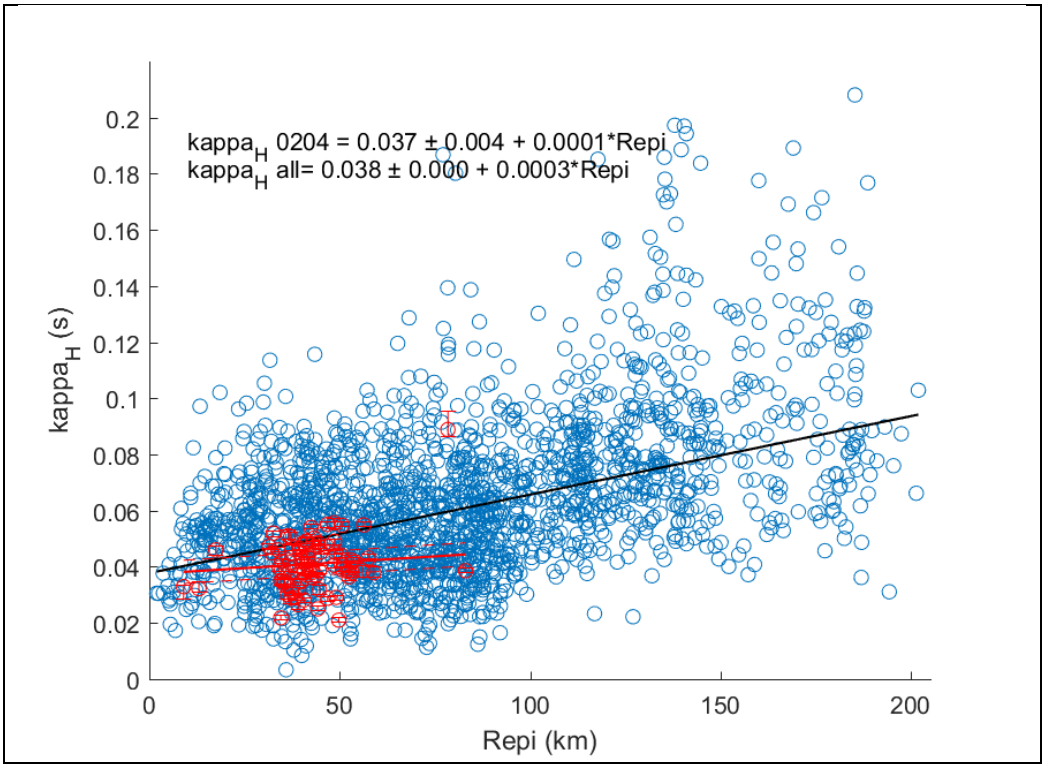


Figure 7.51: The unconstrained to overall κ_H vs R_{epi} fit for Stn0204.

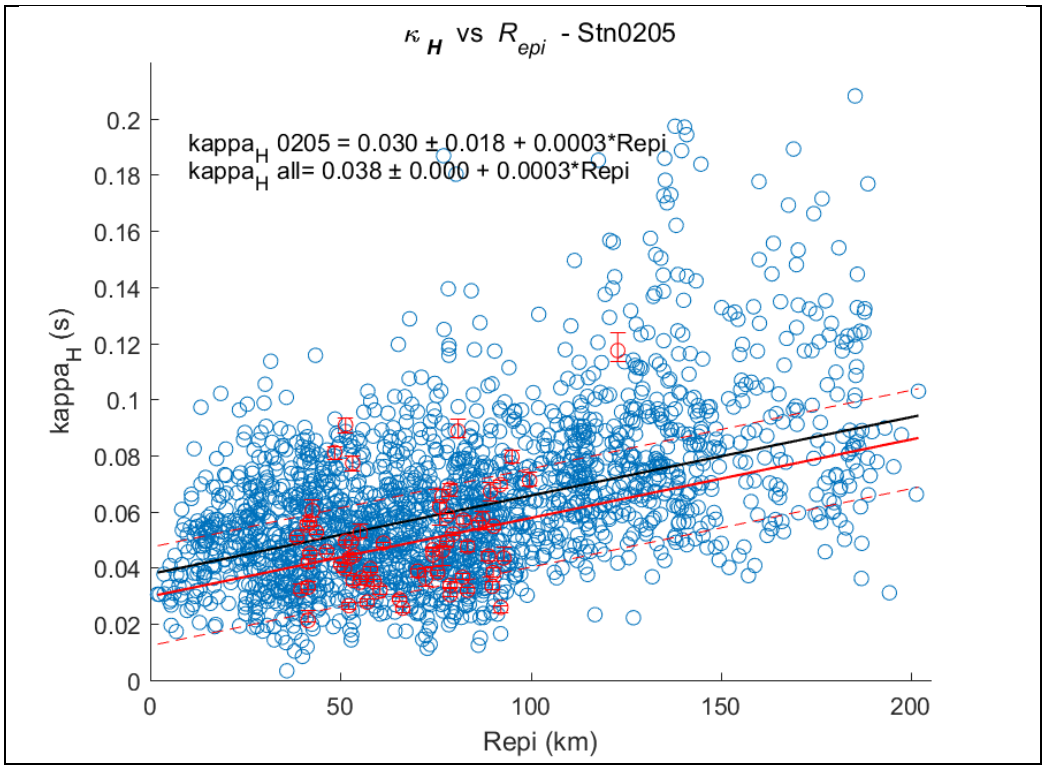


Figure 7.52: The constrained to overall κ_H vs R_{epi} fit for Stn0205.

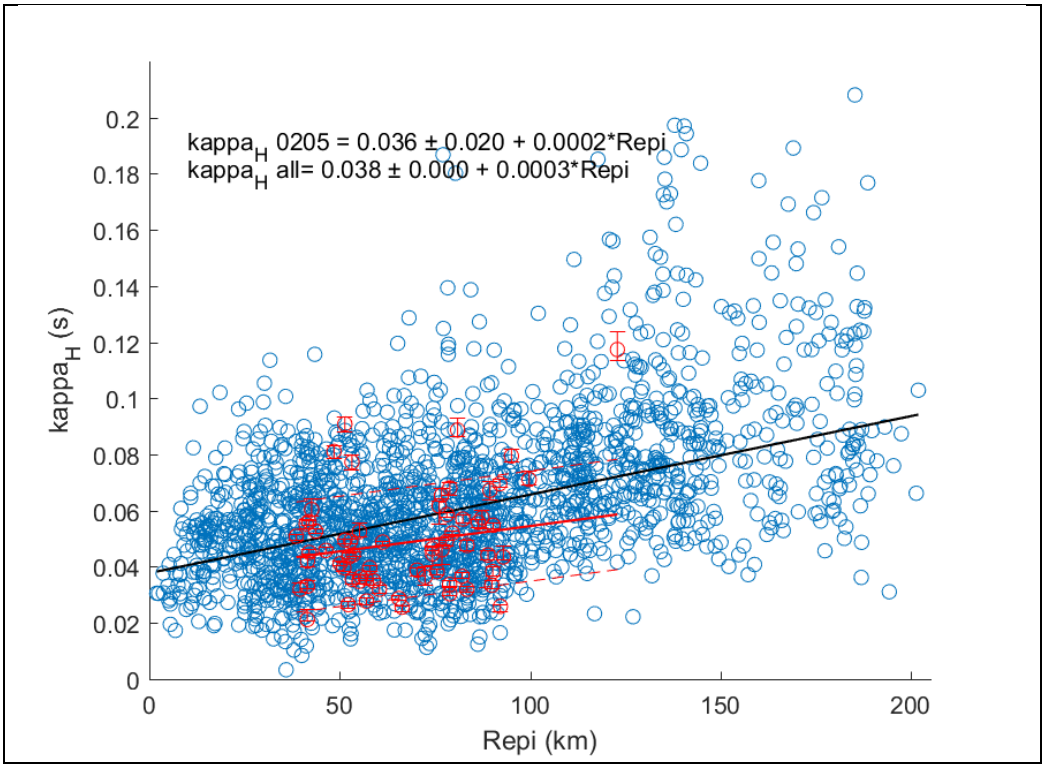


Figure 7.53: The unconstrained to overall κ_H vs R_{epi} fit for Stn0205.

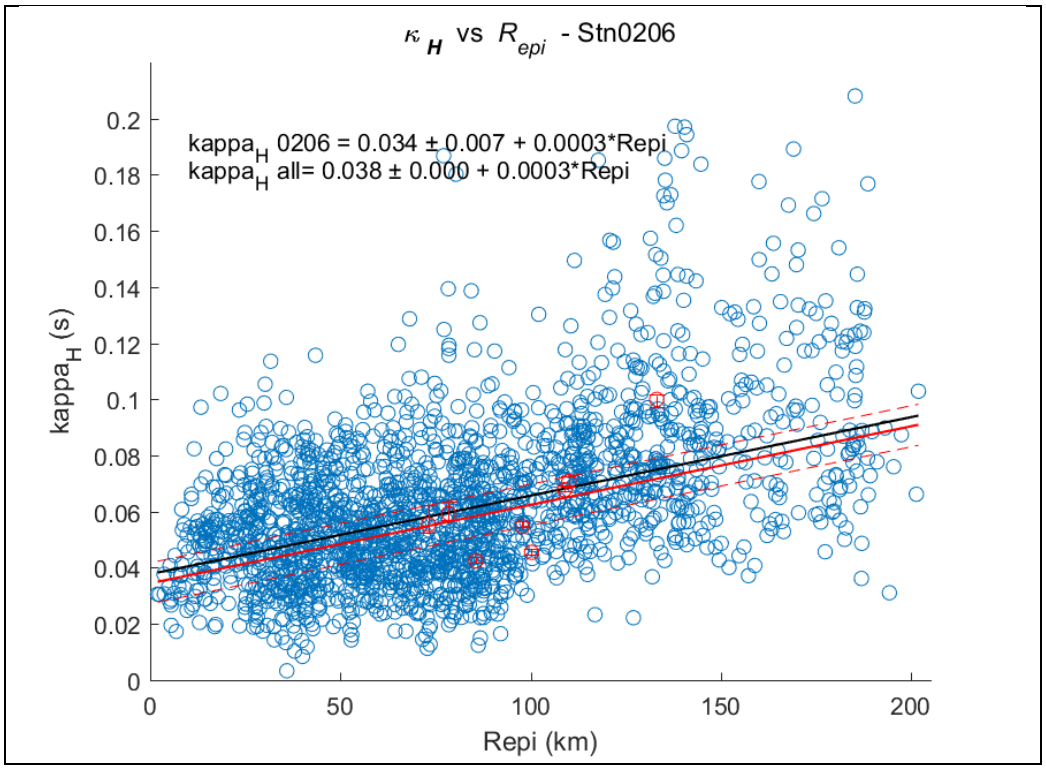


Figure 7.54: The constrained to overall κ_H vs R_{epi} fit for Stn0206.

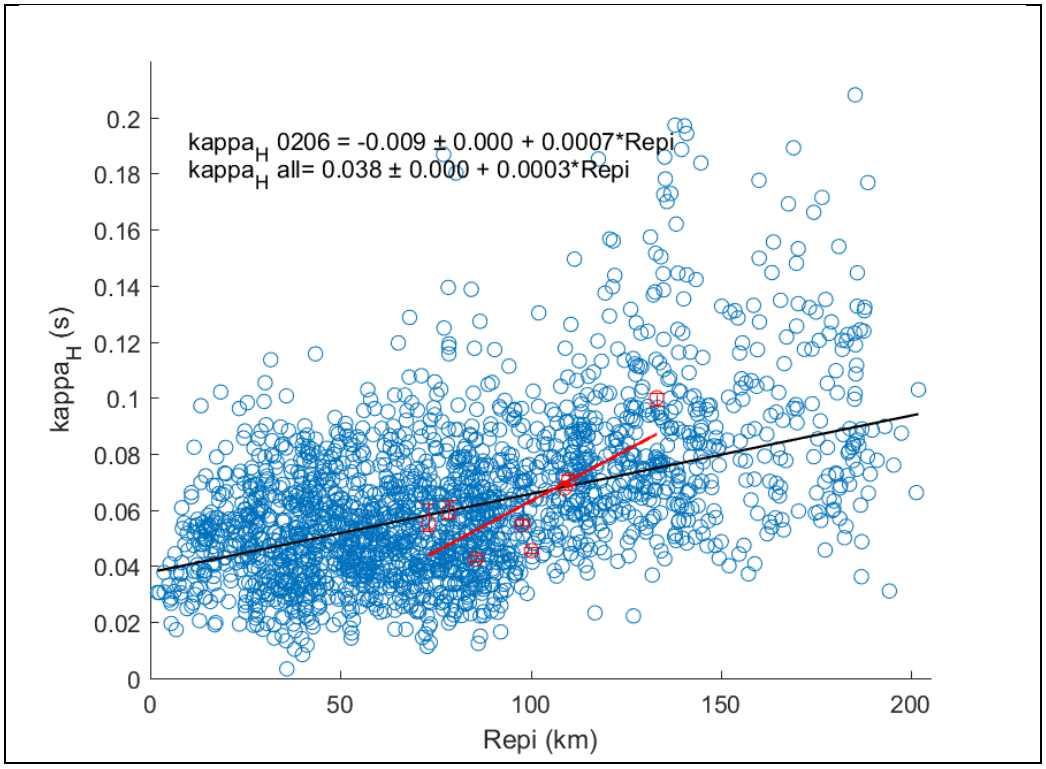


Figure 7.55: The unconstrained to overall κ_H vs R_{epi} fit for Stn0206.

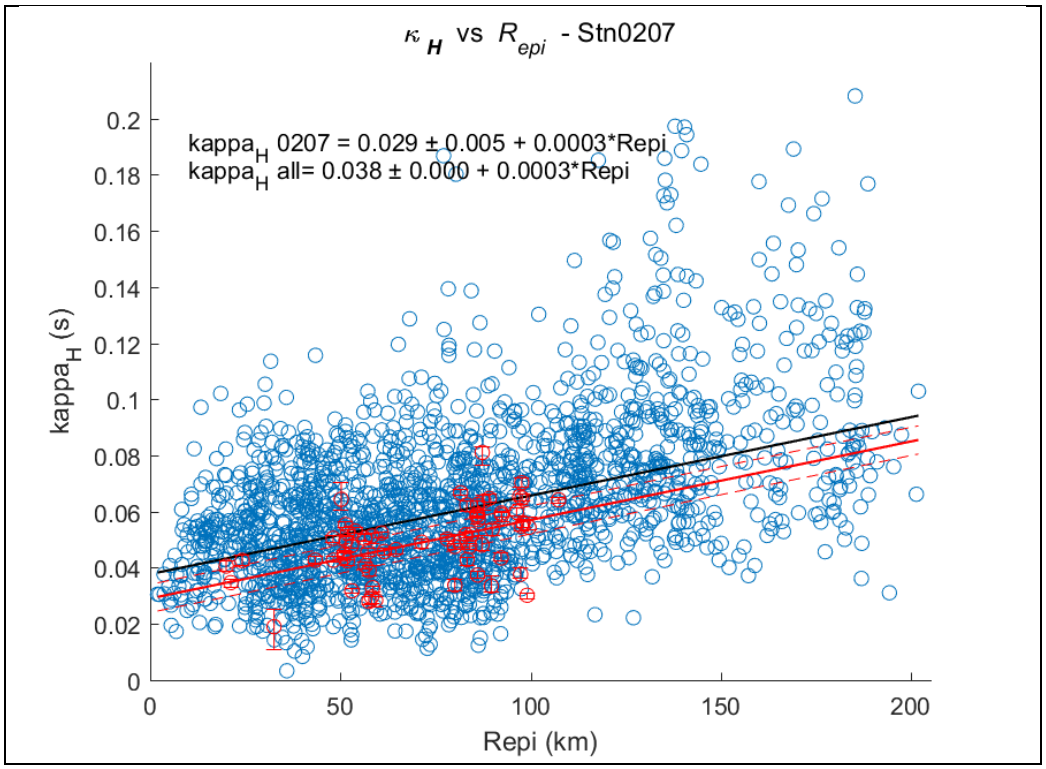


Figure 7.56: The constrained to overall κ_H vs R_{epi} fit for Stn0207.

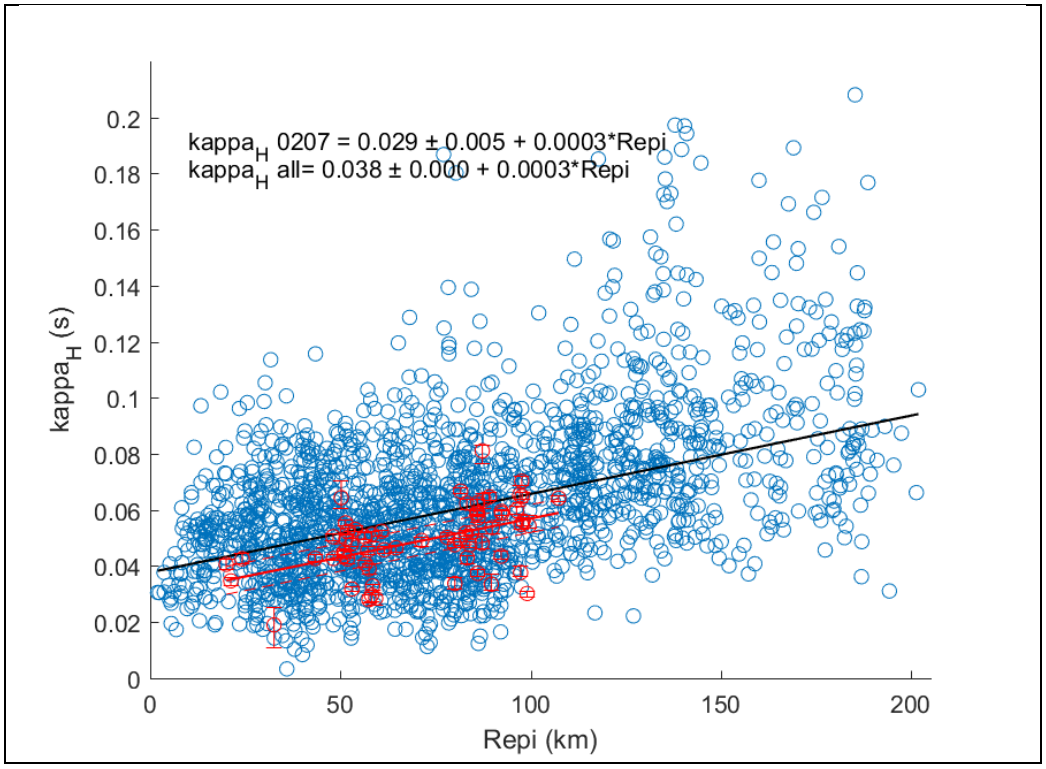


Figure 7.57: The unconstrained to overall κ_H vs R_{epi} fit for Stn0207.

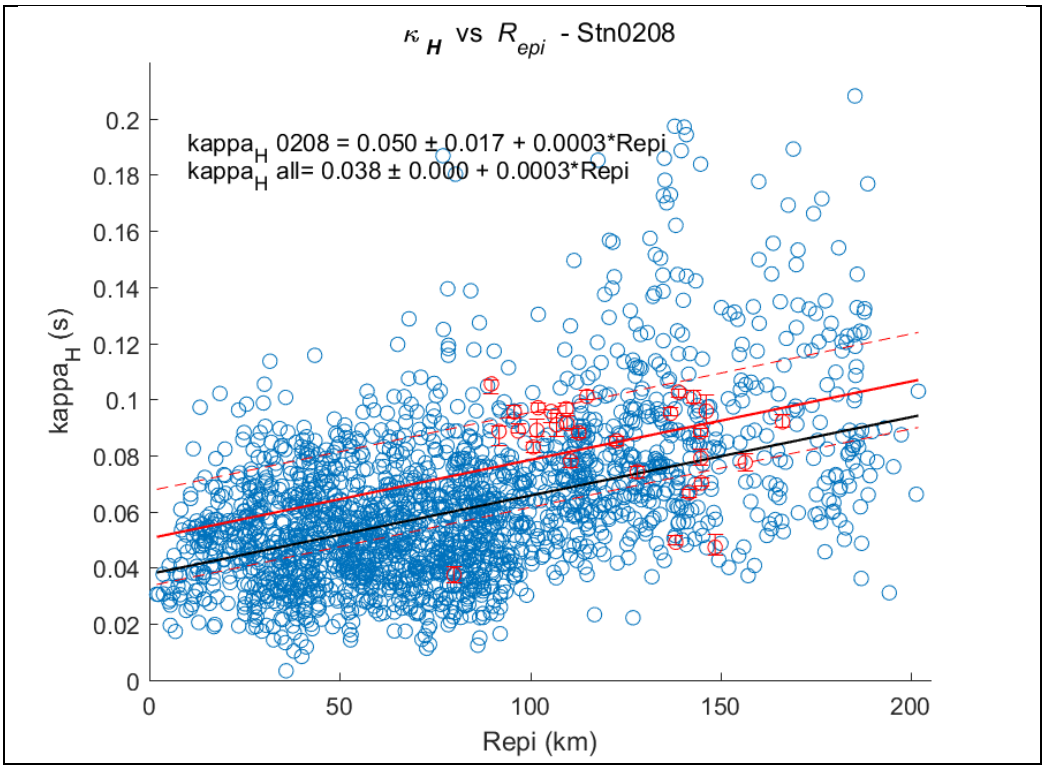


Figure 7.58: The constrained to overall κ_H vs R_{epi} fit for Stn0208.

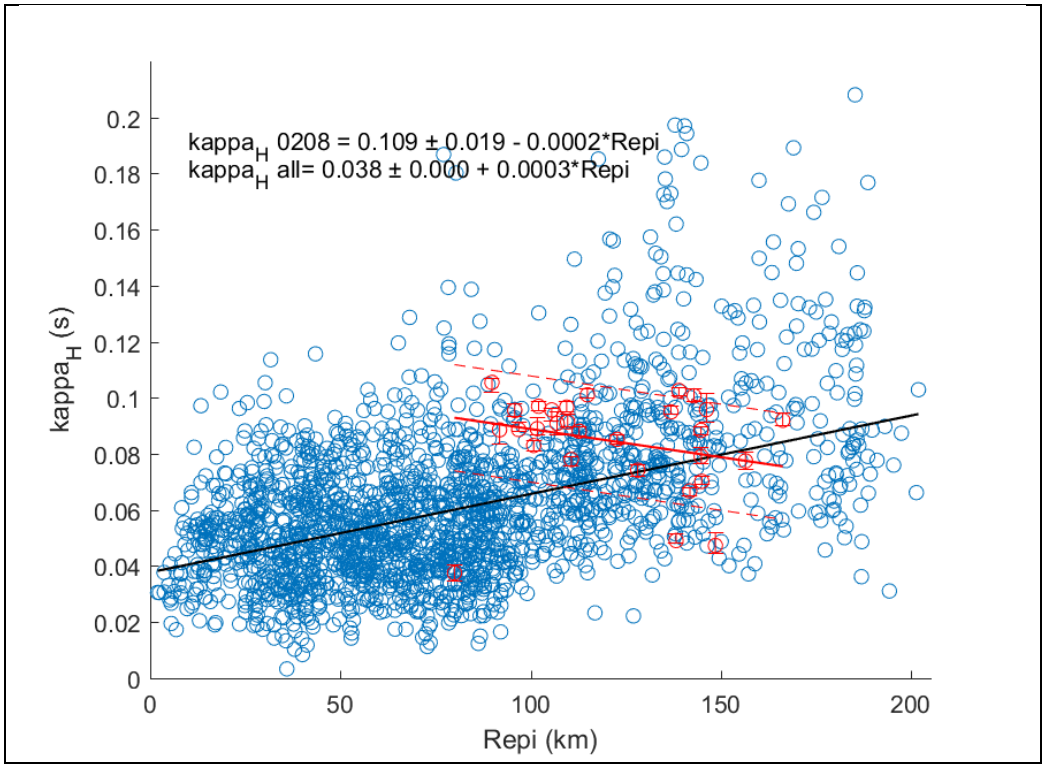


Figure 7.59: The unconstrained to overall κ_H vs R_{epi} fit for Stn0208.

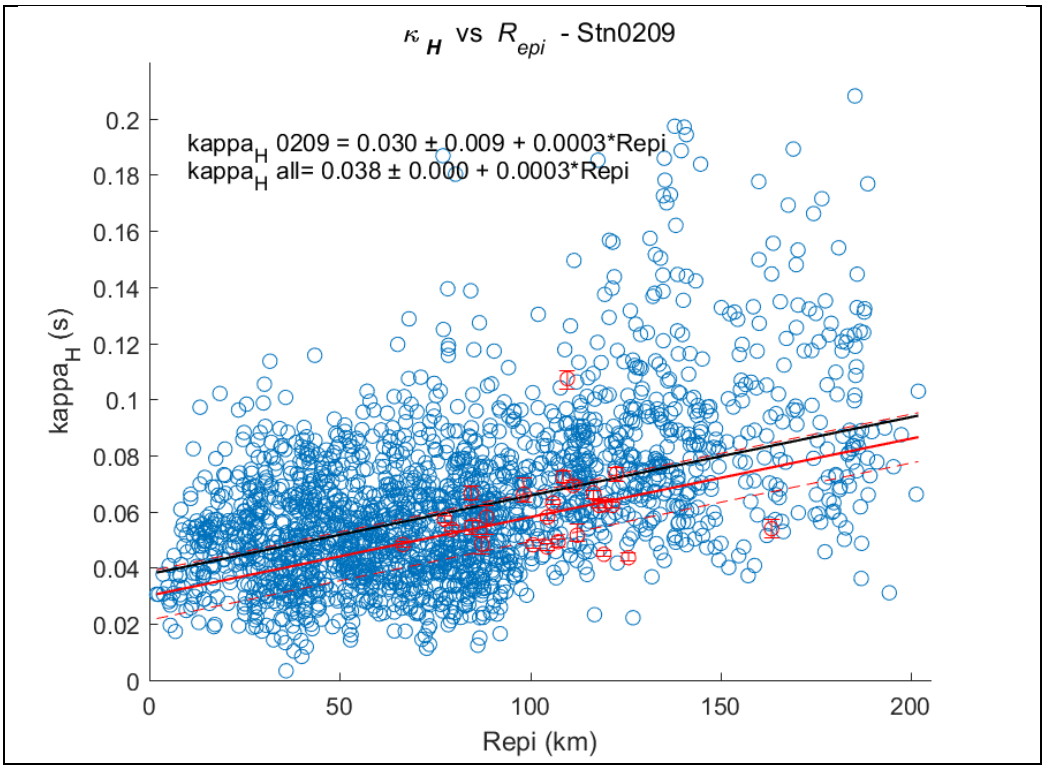


Figure 7.60: The constrained to overall κ_H vs R_{epi} fit for Stn0209.

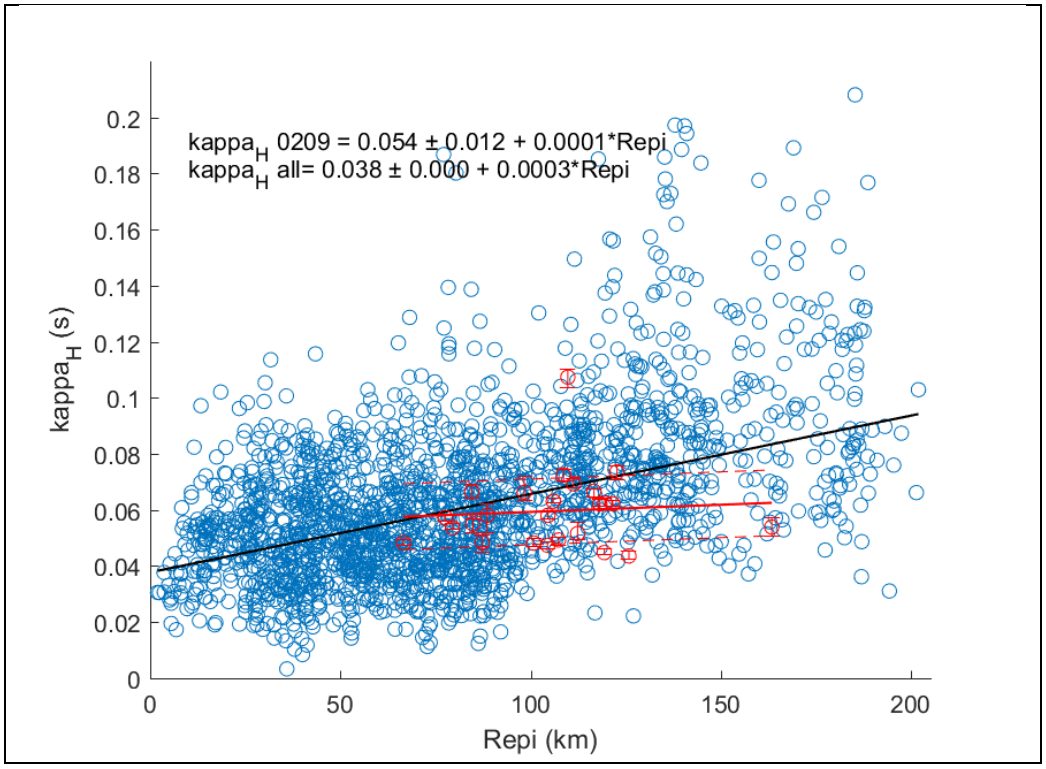


Figure 7.61: The unconstrained to overall κ_H vs R_{epi} fit for Stn0209.

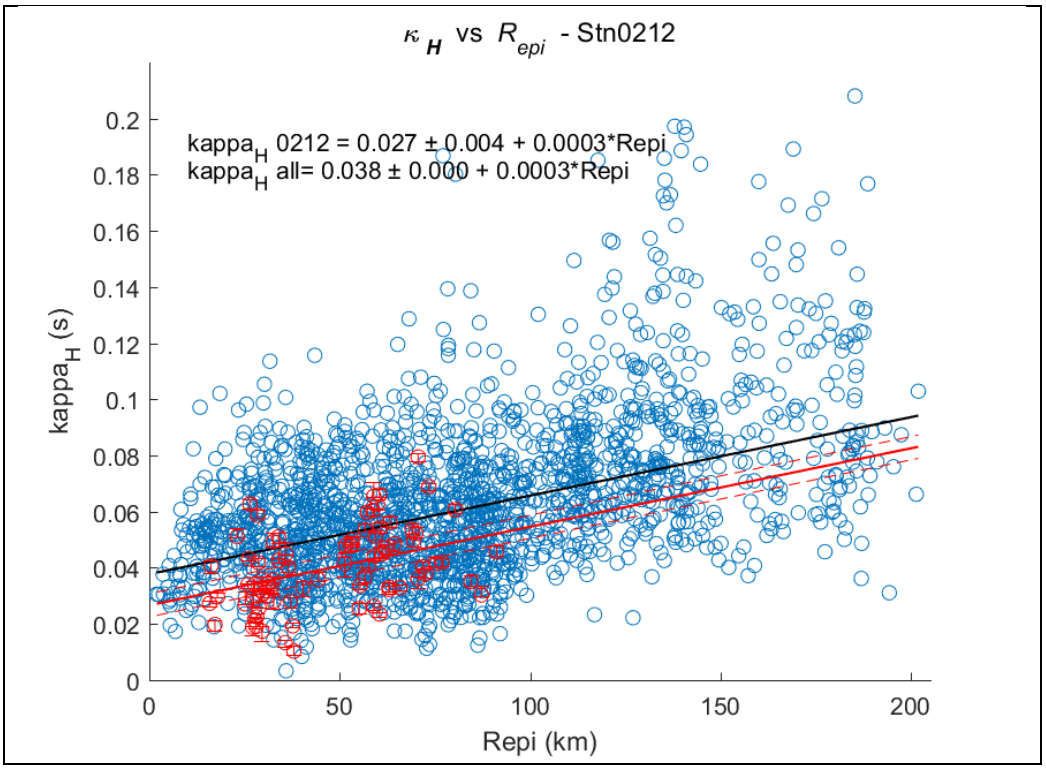


Figure 7.62: The constrained to overall κ_H vs R_{epi} fit for Stn0212.

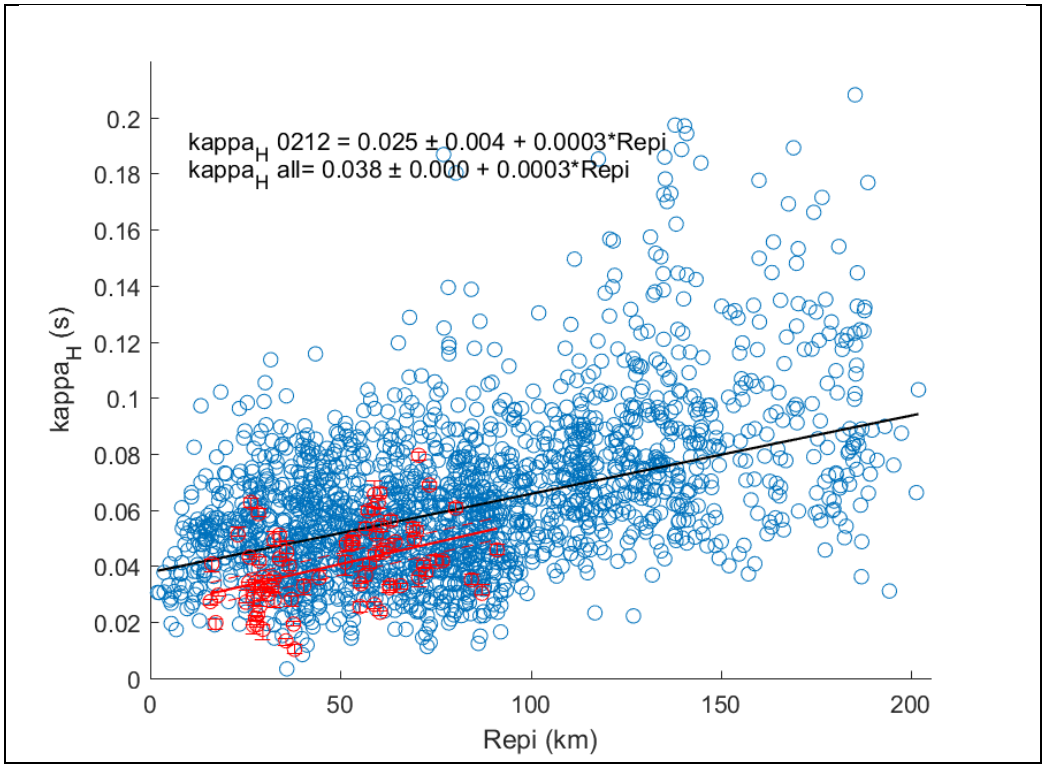


Figure 7.63: The unconstrained to overall κ_H vs R_{epi} fit for Stn0212.

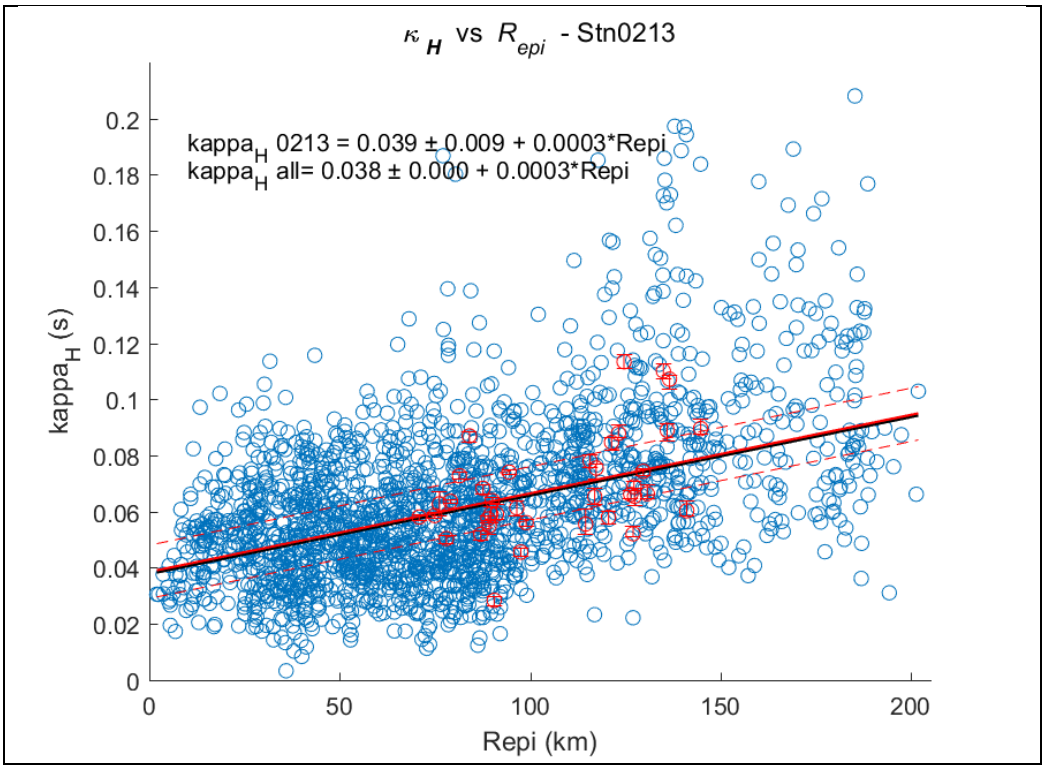


Figure 7.64: The constrained to overall κ_H vs R_{epi} fit for Stn0213.

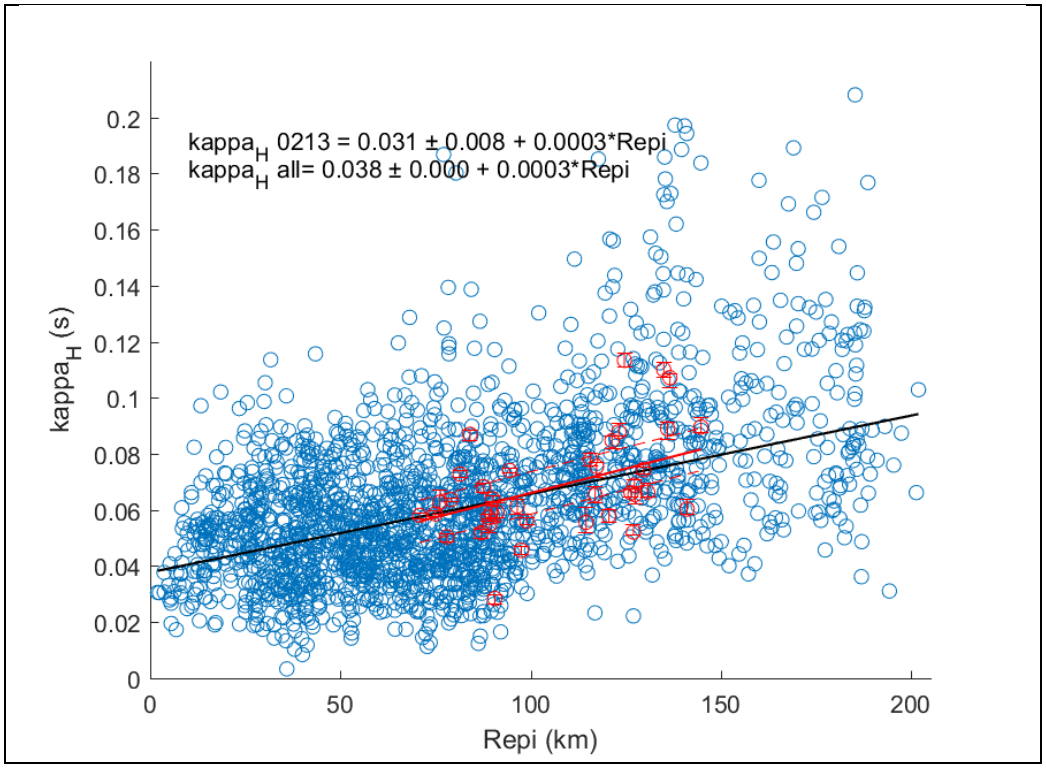


Figure 7.65: The unconstrained to overall κ_H vs R_{epi} fit for Stn0213.

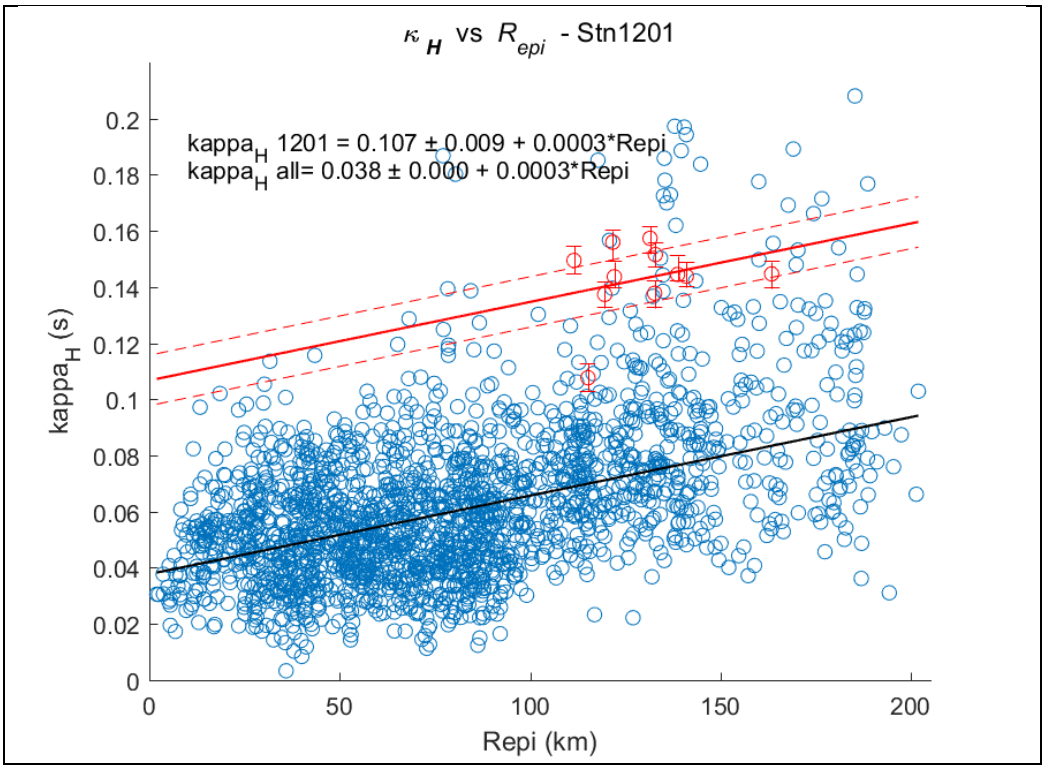


Figure 7.66: The constrained to overall κ_H vs R_{epi} fit for Stn1201.

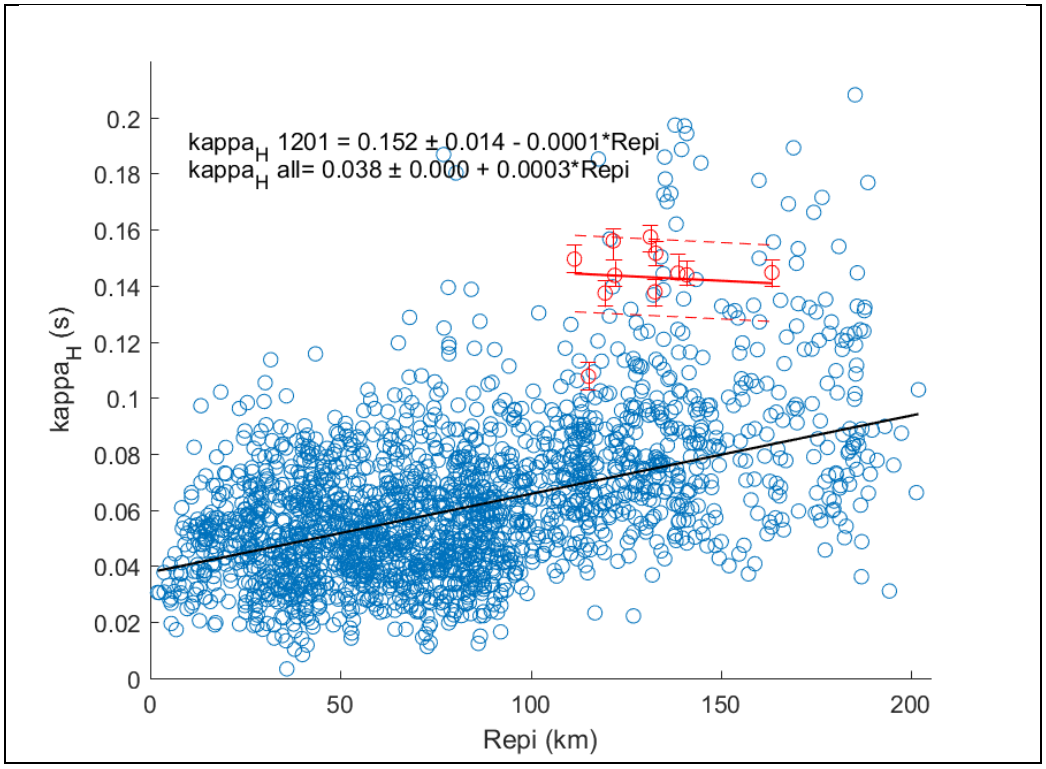


Figure 7.67: The unconstrained to overall κ_H vs R_{epi} fit for Stn1201.

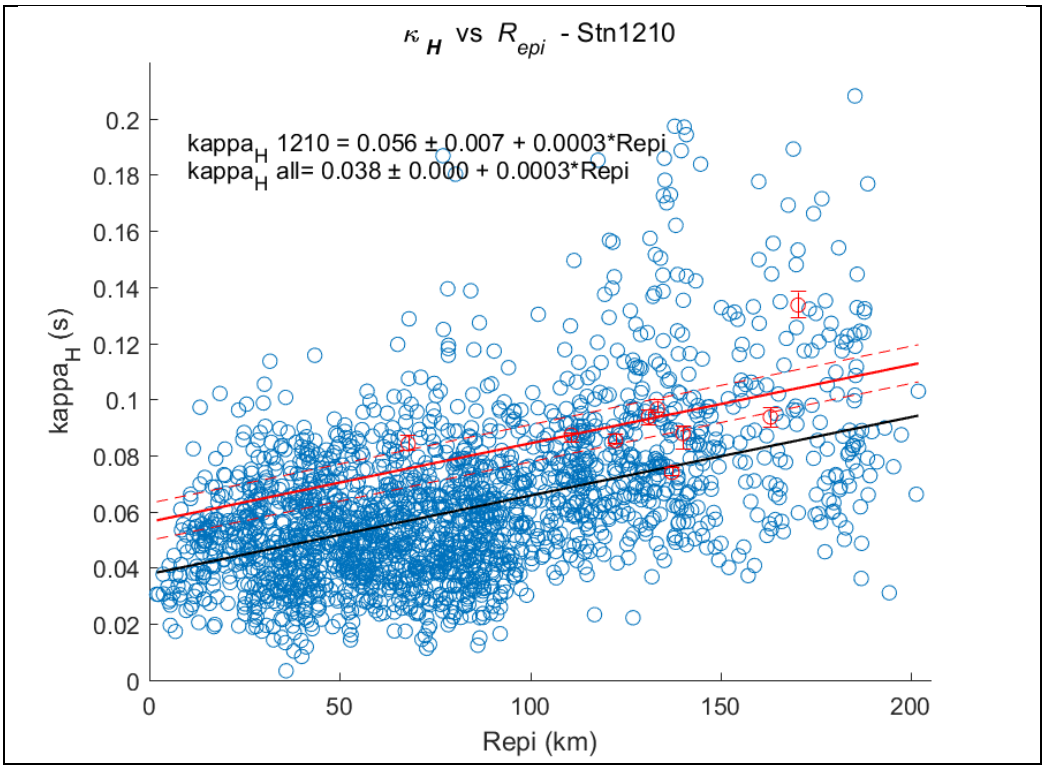


Figure 7.68: The constrained to overall κ_H vs R_{epi} fit for Stn1210.

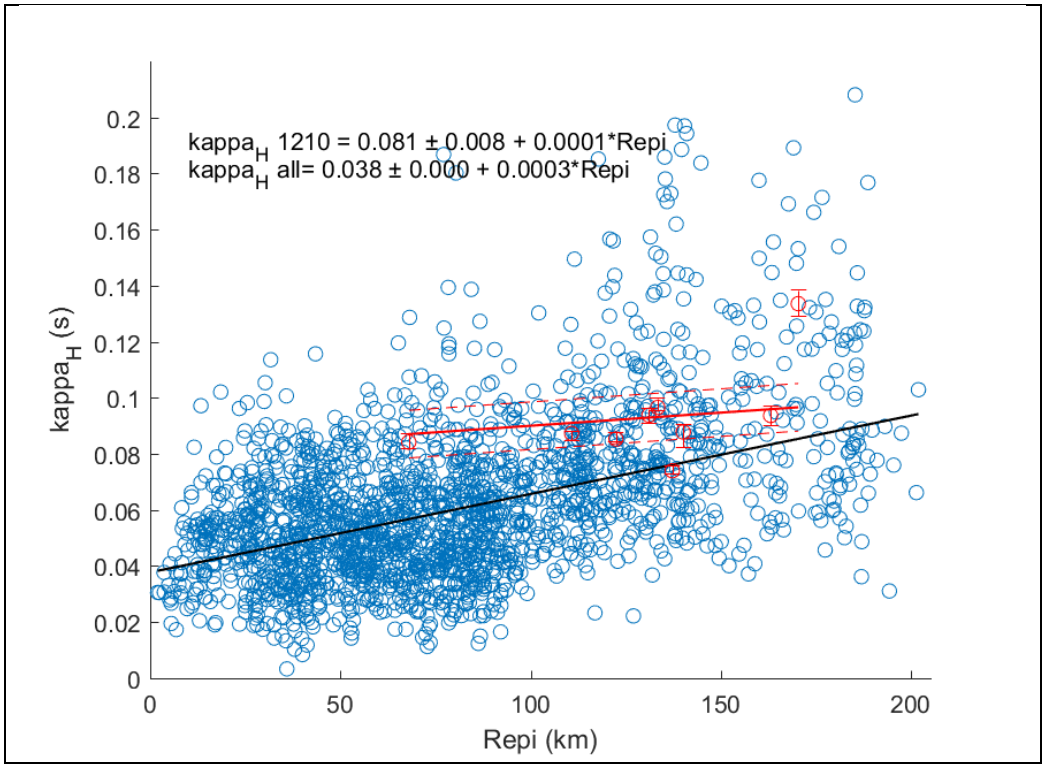


Figure 7.69: The unconstrained to overall κ_H vs R_{epi} fit for Stn1210.

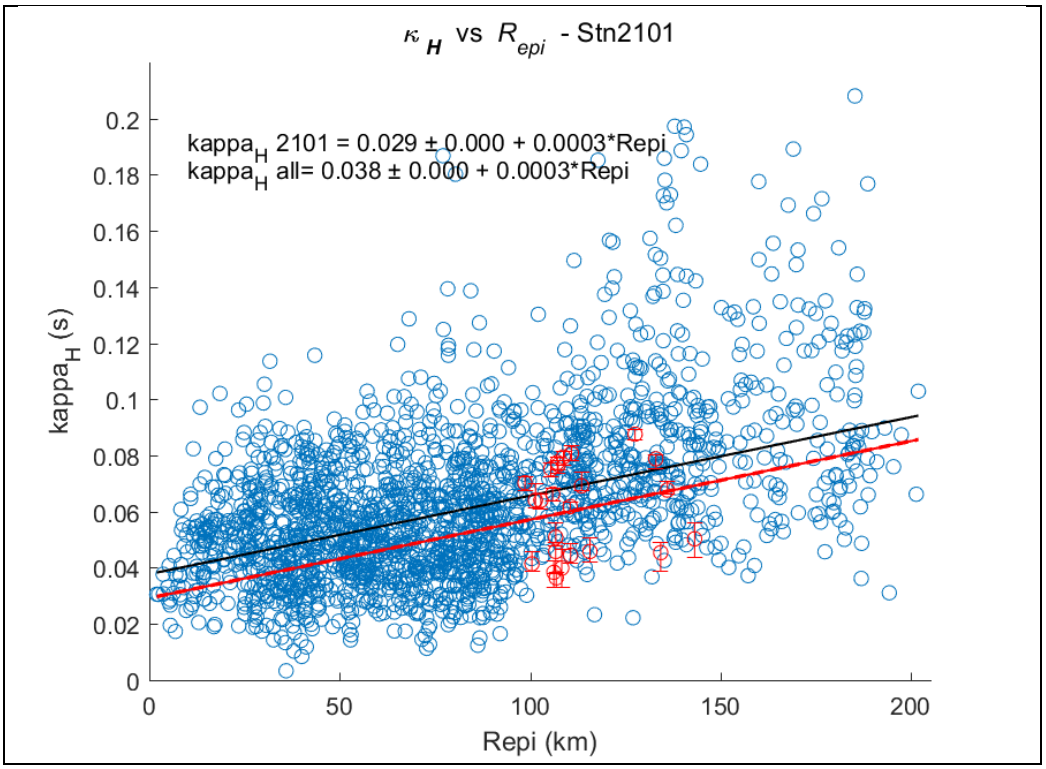


Figure 7.70: The constrained to overall κ_H vs R_{epi} fit for Stn2101.

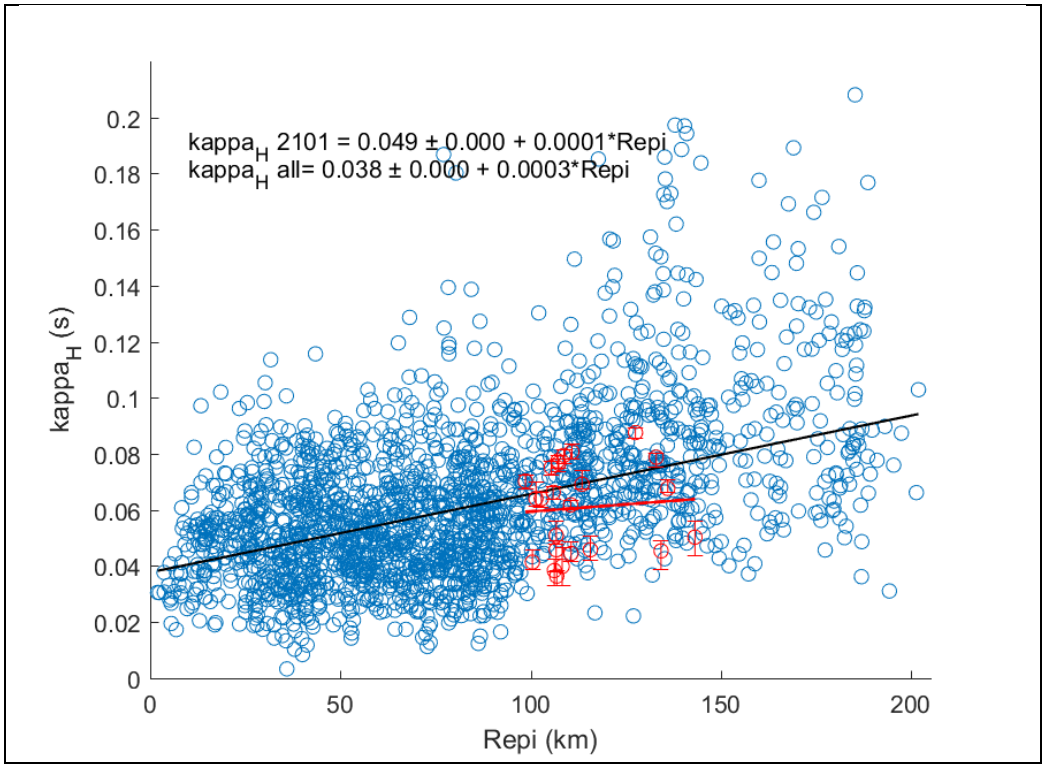


Figure 7.71: The unconstrained to overall κ_H vs R_{epi} fit for Stn2101.

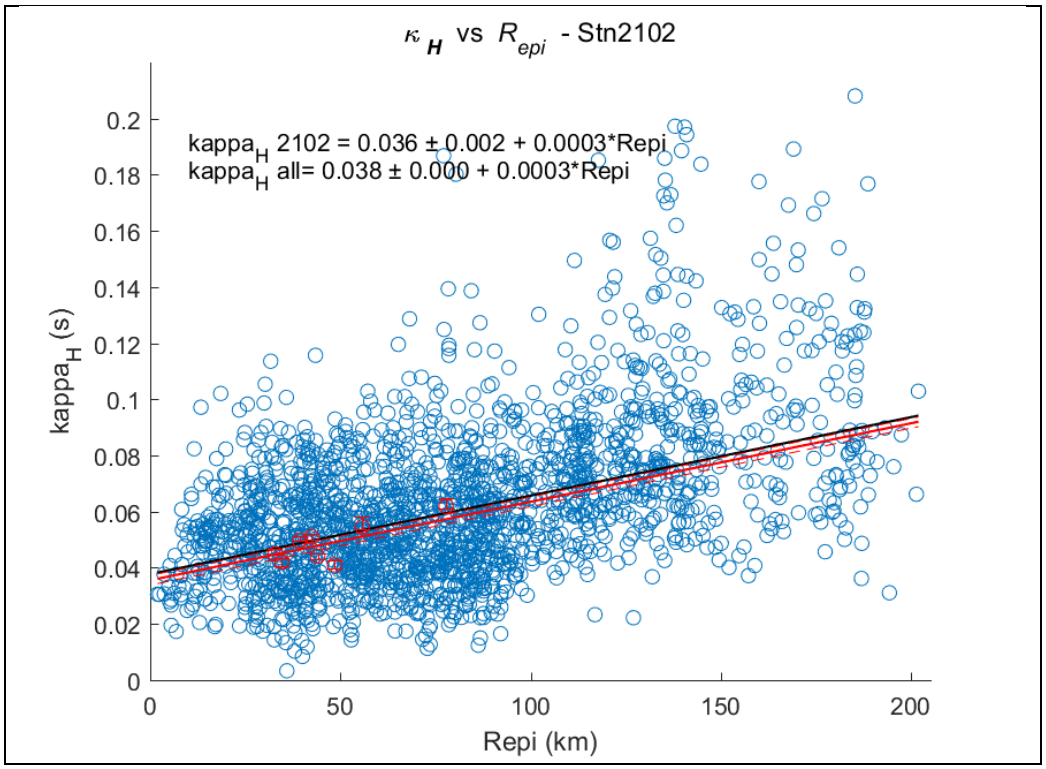


Figure 7.72: The constrained to overall κ_H vs R_{epi} fit for Stn2102.

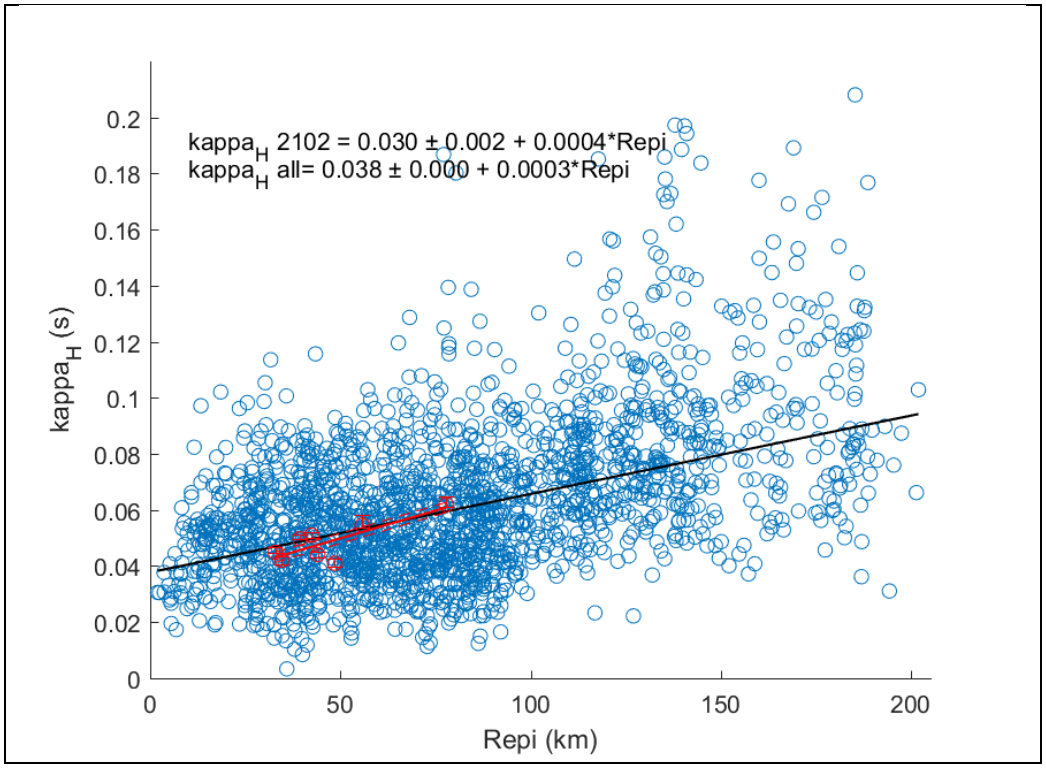


Figure 7.73: The unconstrained to overall κ_H vs R_{epi} fit for Stn2102.

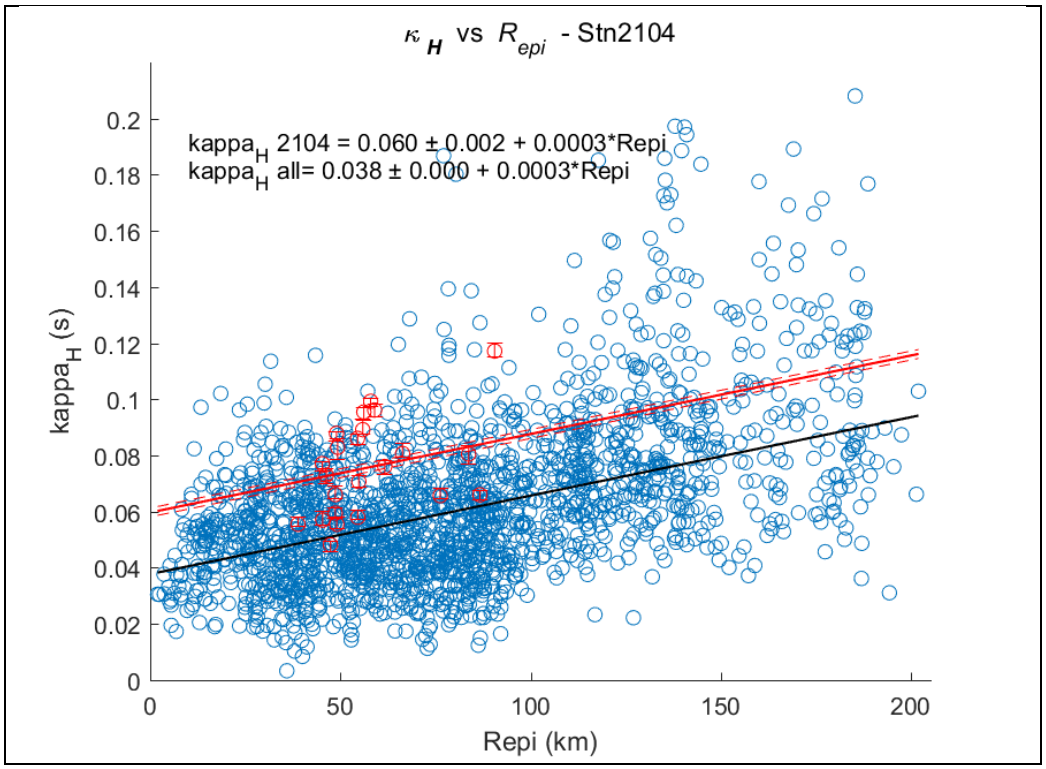


Figure 7.74: The constrained to overall κ_H vs R_{epi} fit for Stn2104.

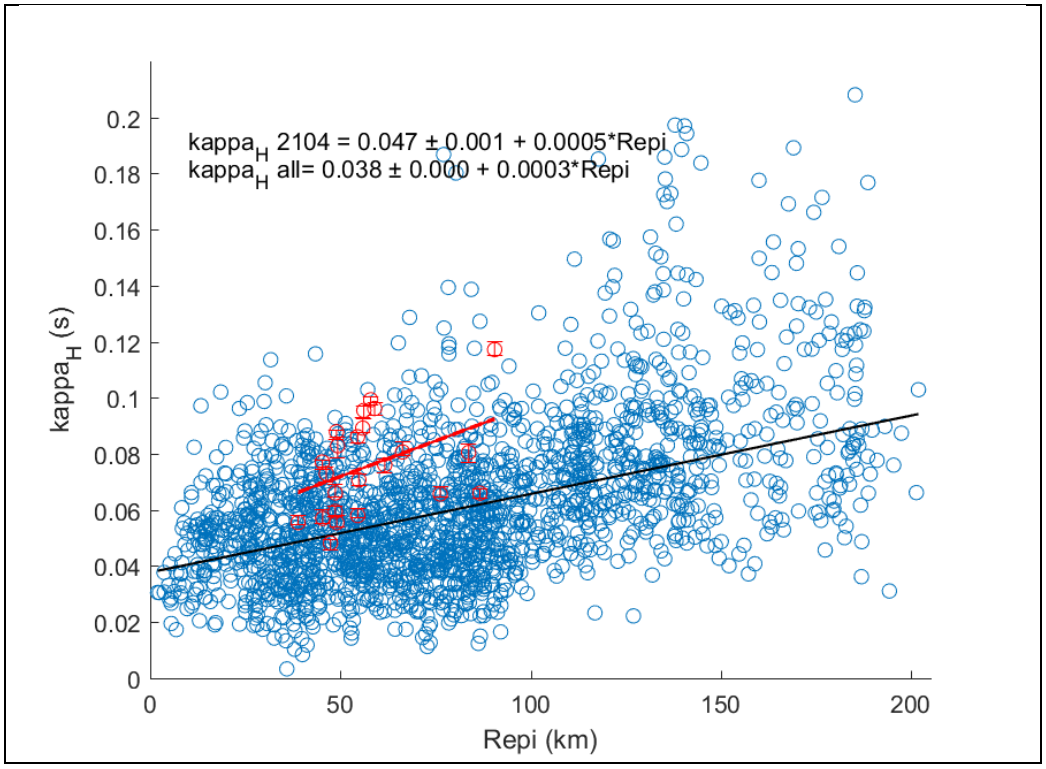


Figure 7.75: The unconstrained to overall κ_H vs R_{epi} fit for Stn2104.

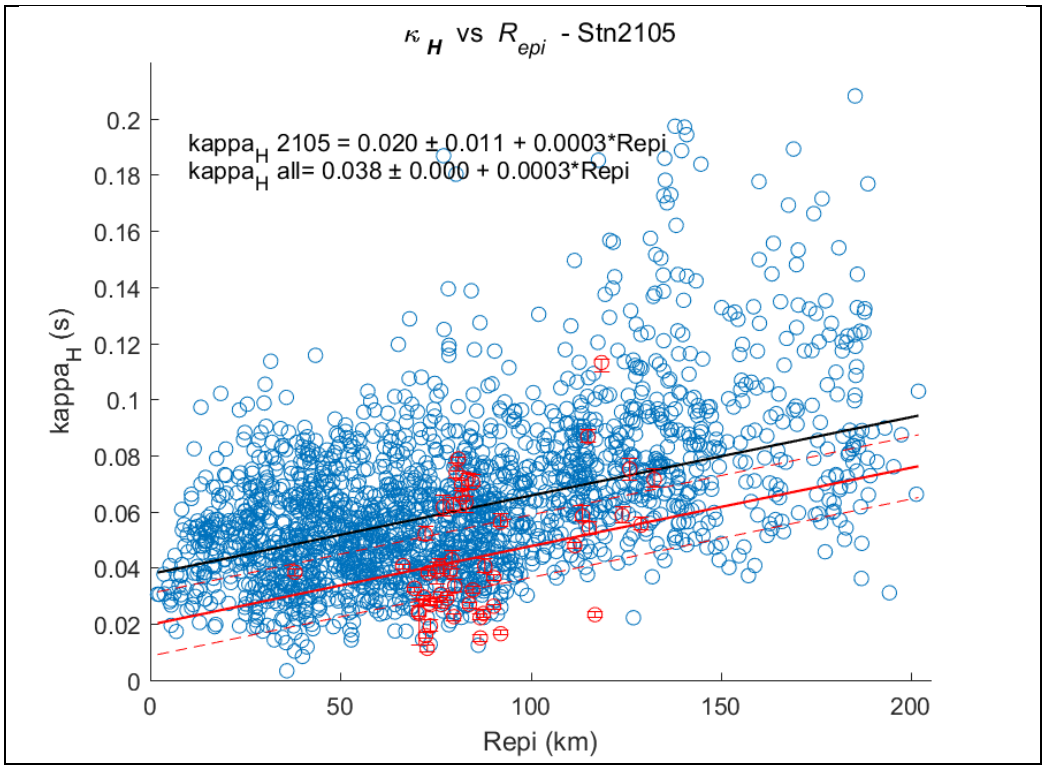


Figure 7.76: The constrained to overall κ_H vs R_{epi} fit for Stn2105.

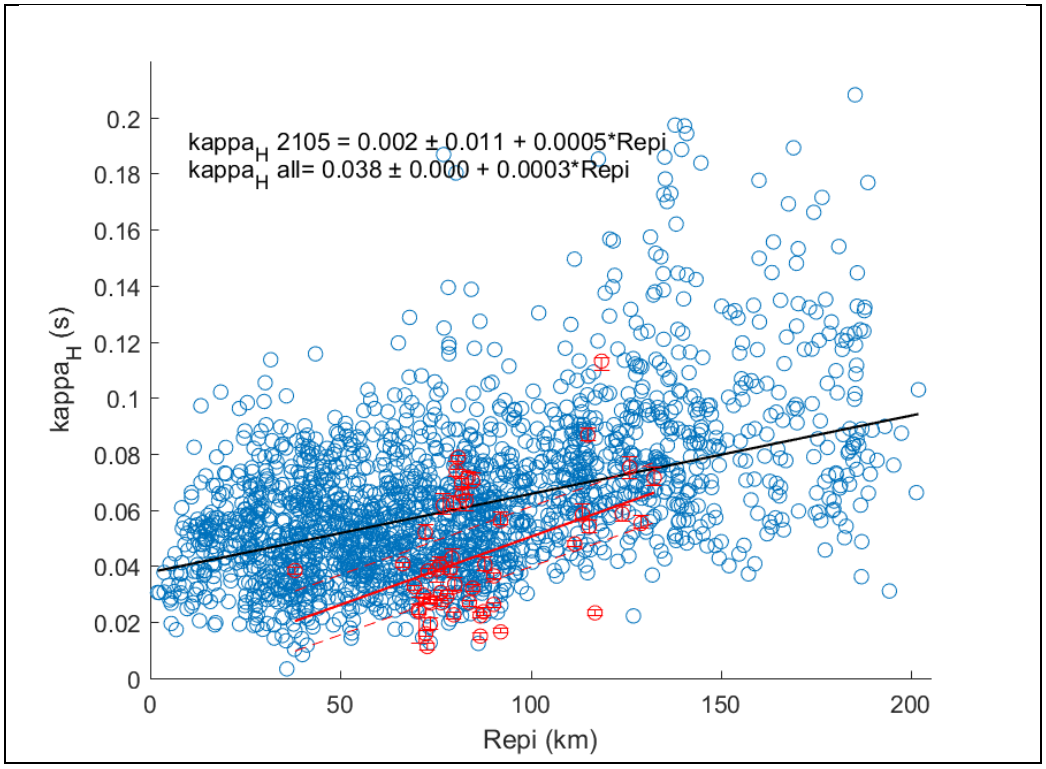


Figure 7.77: The unconstrained to overall κ_H vs R_{epi} fit for Stn2105.

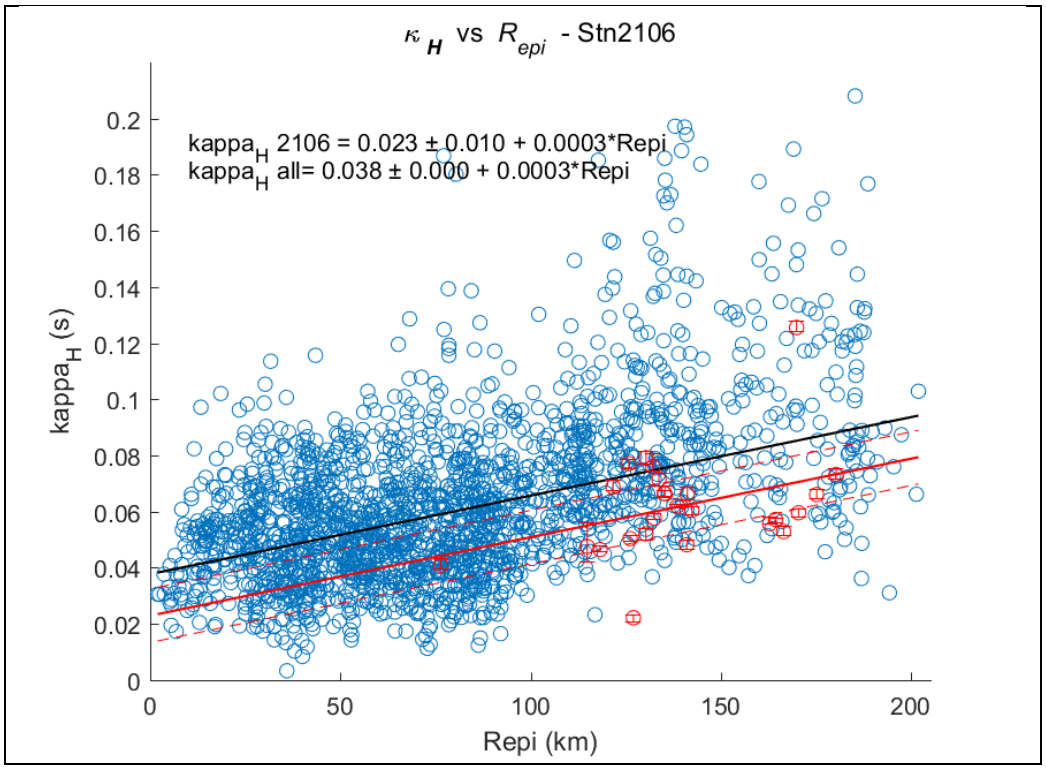


Figure 7.78: The constrained to overall κ_H vs R_{epi} fit for Stn2106.

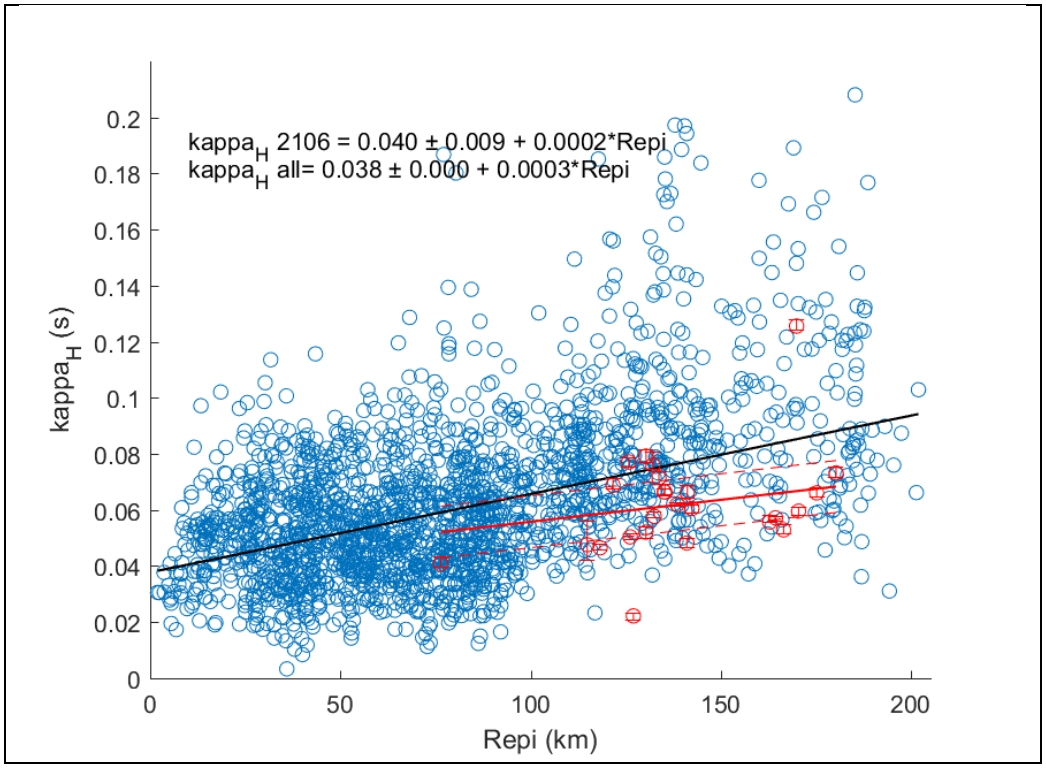


Figure 7.79: The unconstrained to overall κ_H vs R_{epi} fit for Stn2106.

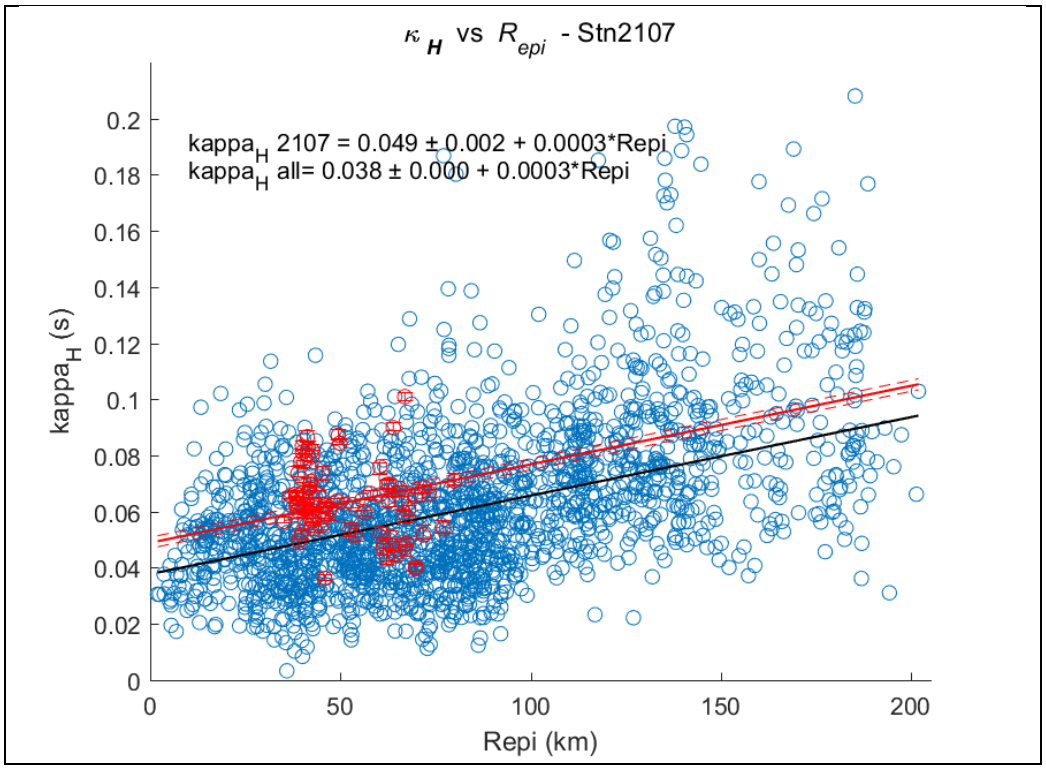


Figure 7.80: The constrained to overall κ_H vs R_{epi} fit for Stn2107.

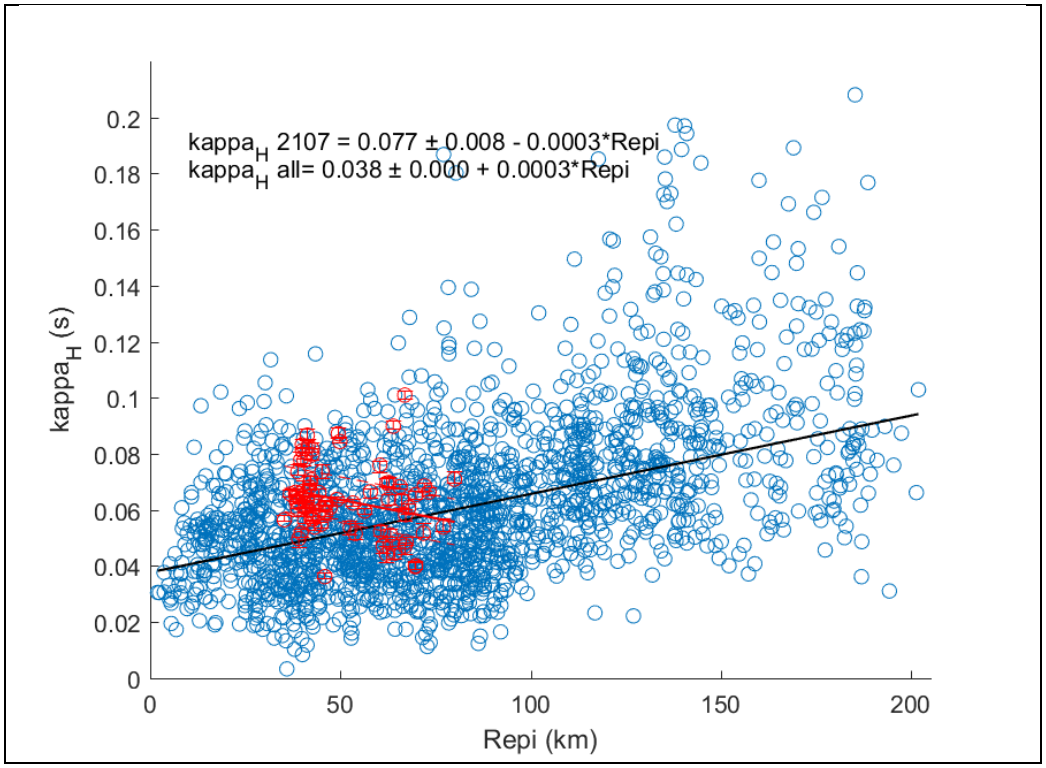


Figure 7.81: The unconstrained to overall κ_H vs R_{epi} fit for Stn2107.

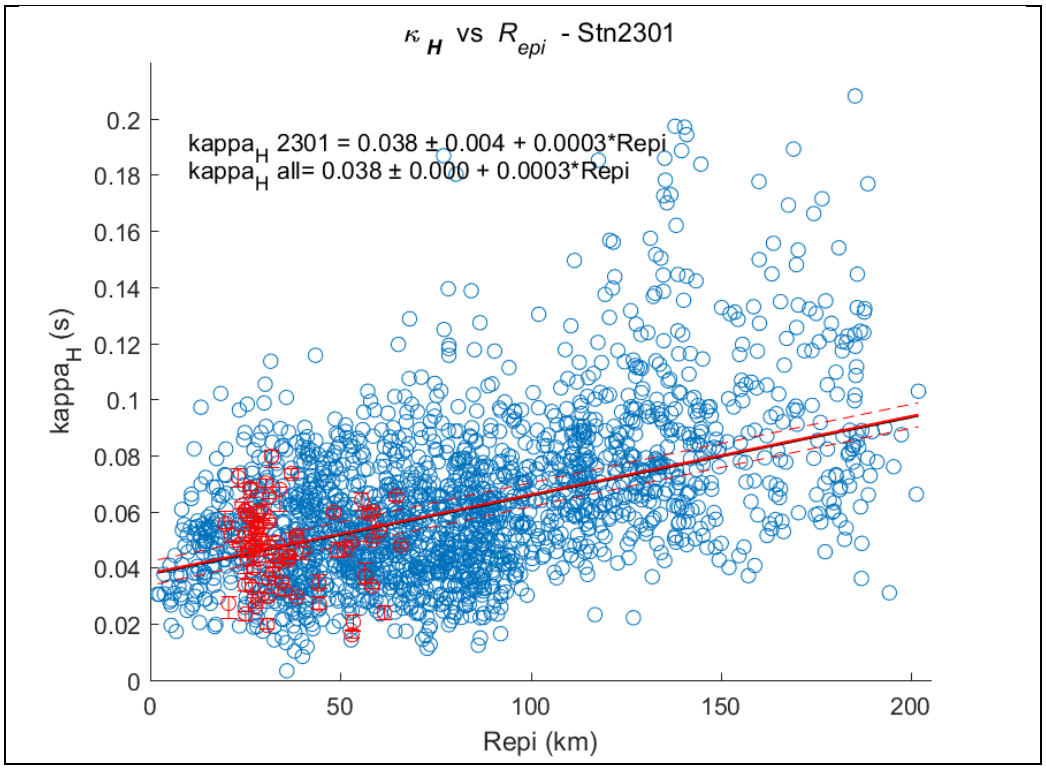


Figure 7.82: The constrained to overall κ_H vs R_{epi} fit for Stn2301.

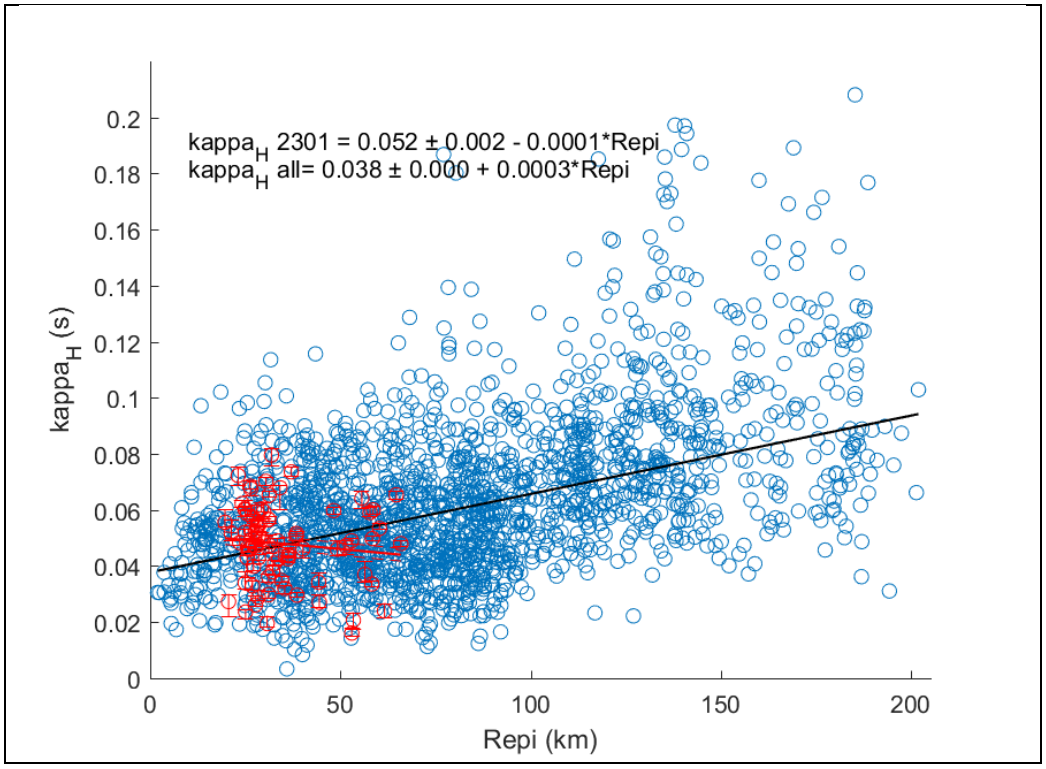


Figure 7.83: The unconstrained to overall κ_H vs R_{epi} fit for Stn2301.

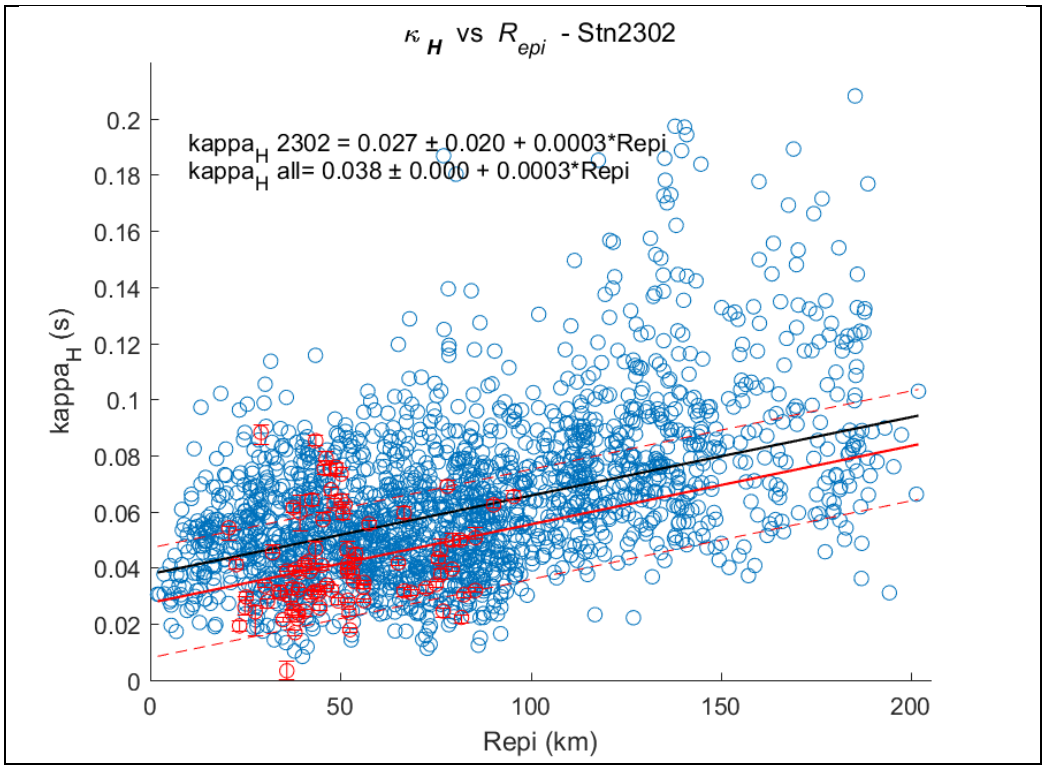


Figure 7.84: The constrained to overall κ_H vs R_{epi} fit for Stn2302.

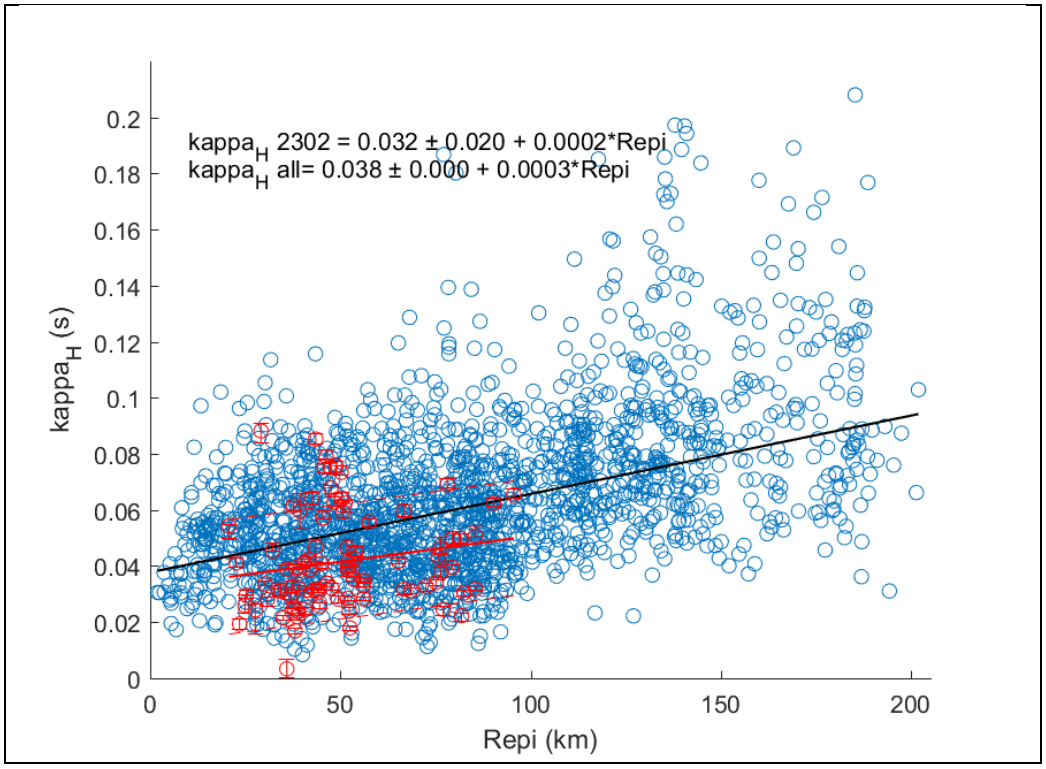


Figure 7.85: The unconstrained to overall κ_H vs R_{epi} fit for Stn2302.

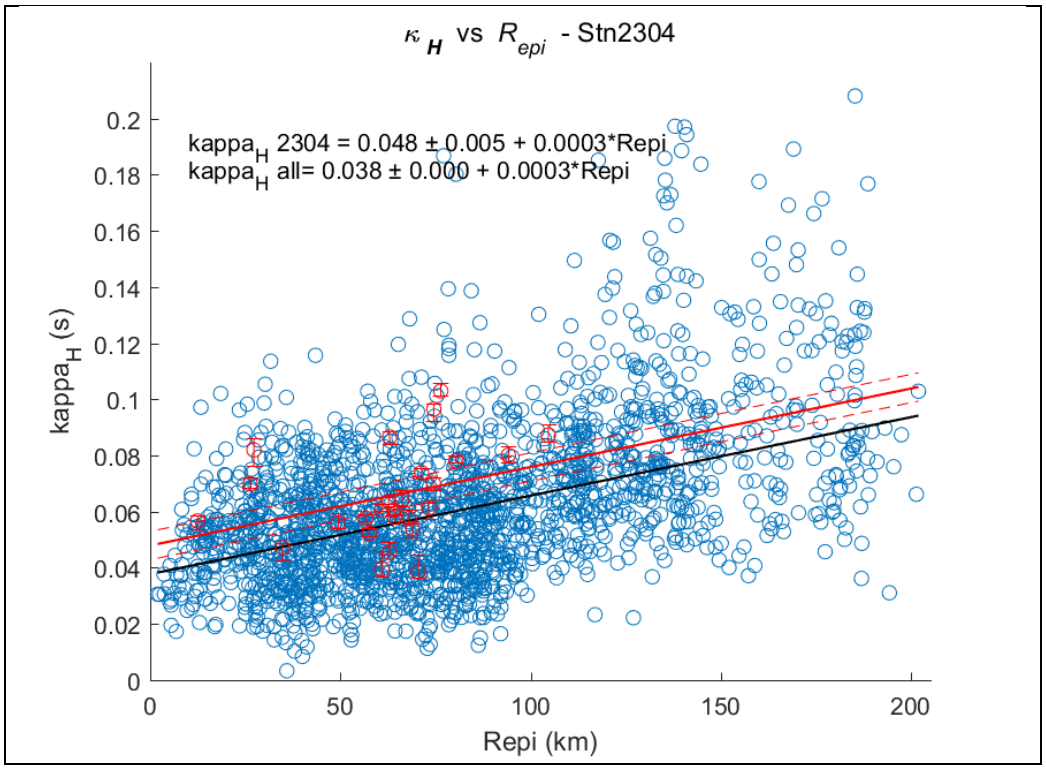


Figure 7.86: The constrained to overall κ_H vs R_{epi} fit for Stn2304.

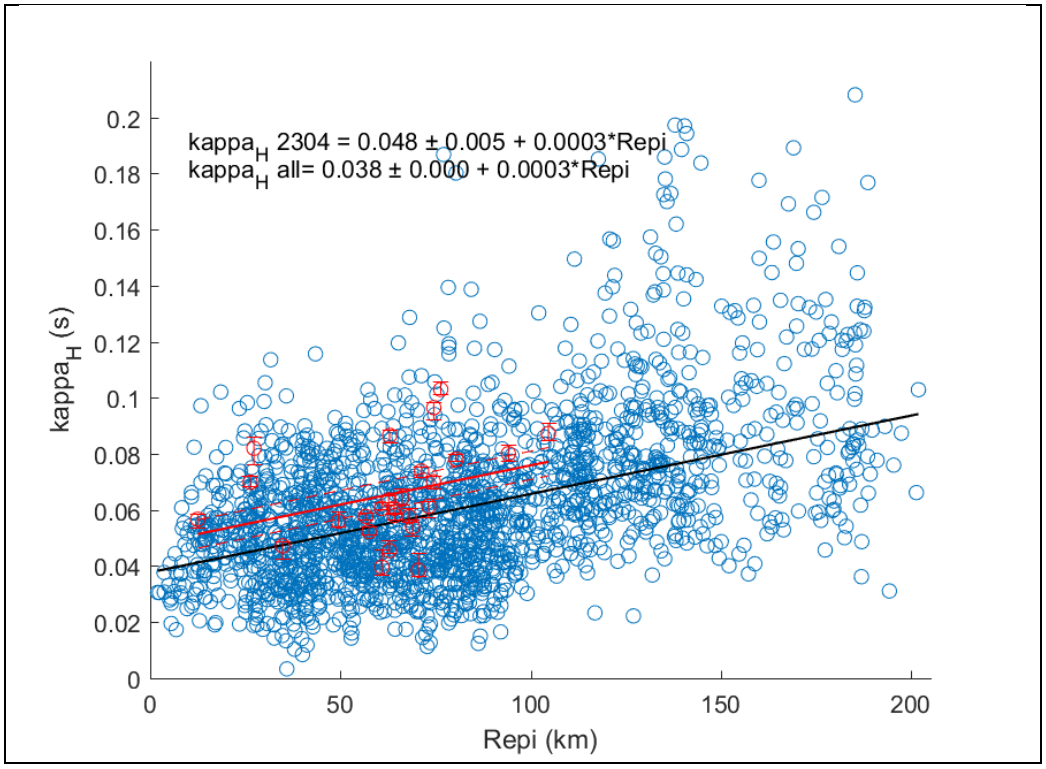


Figure 7.87: The unconstrained to overall κ_H vs R_{epi} fit for Stn2304.

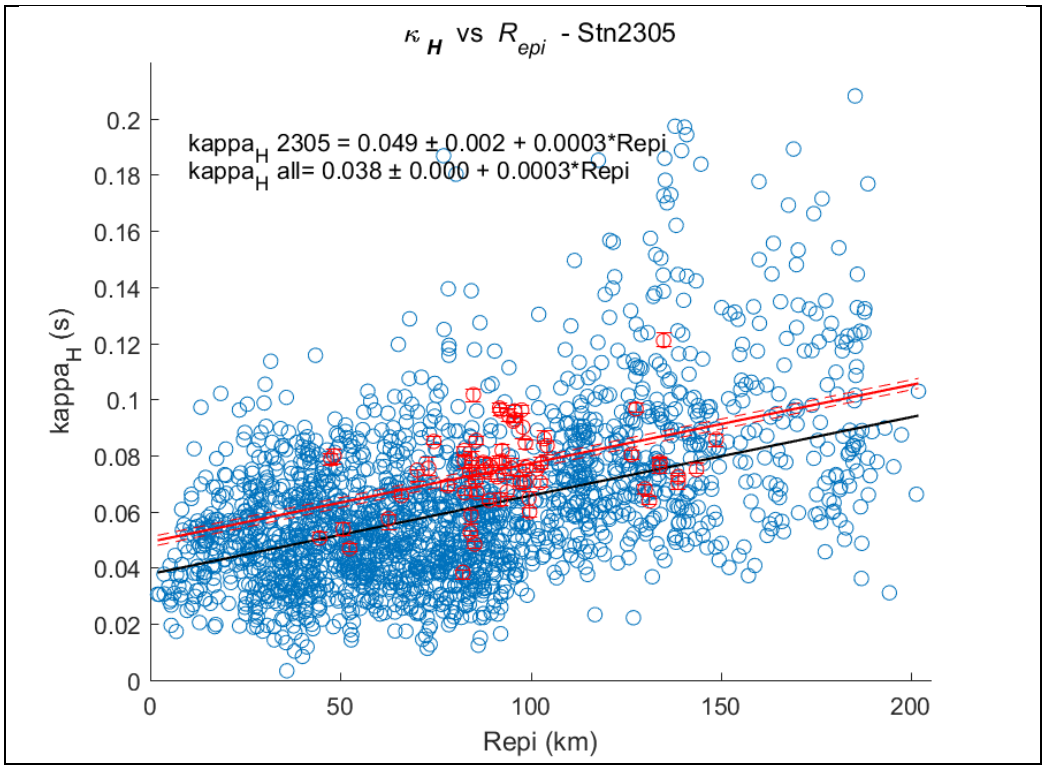


Figure 7.88: The constrained to overall κ_H vs R_{epi} fit for Stn2305.

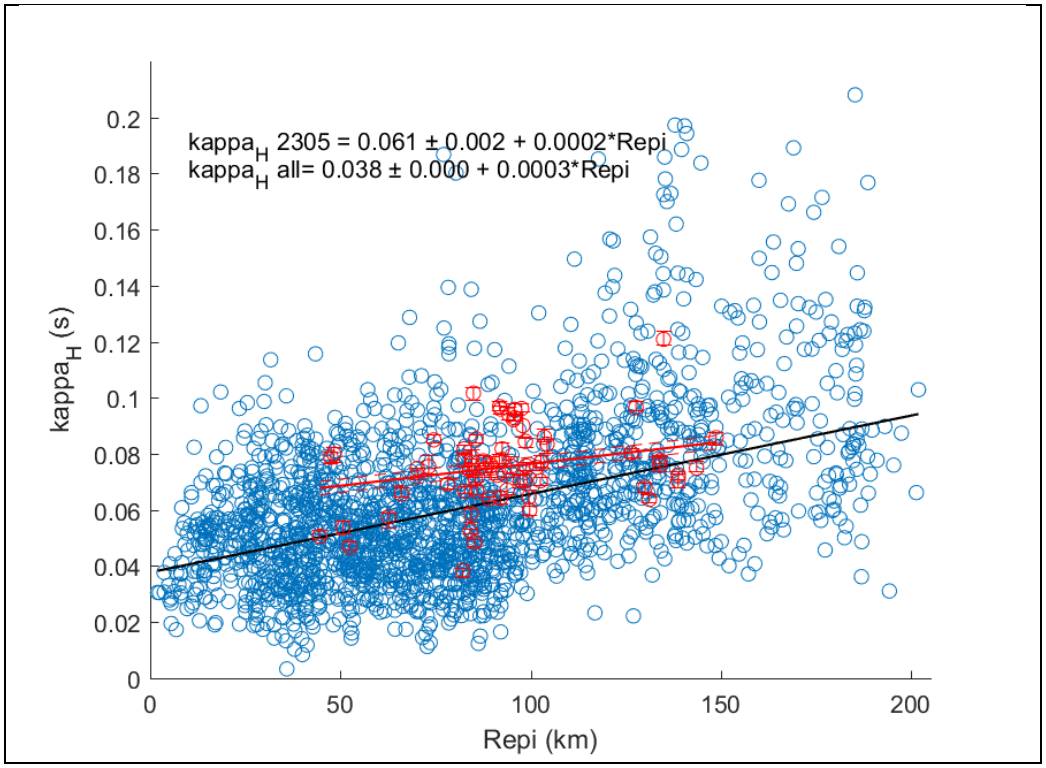


Figure 7.89: The unconstrained to overall κ_H vs R_{epi} fit for Stn2305.

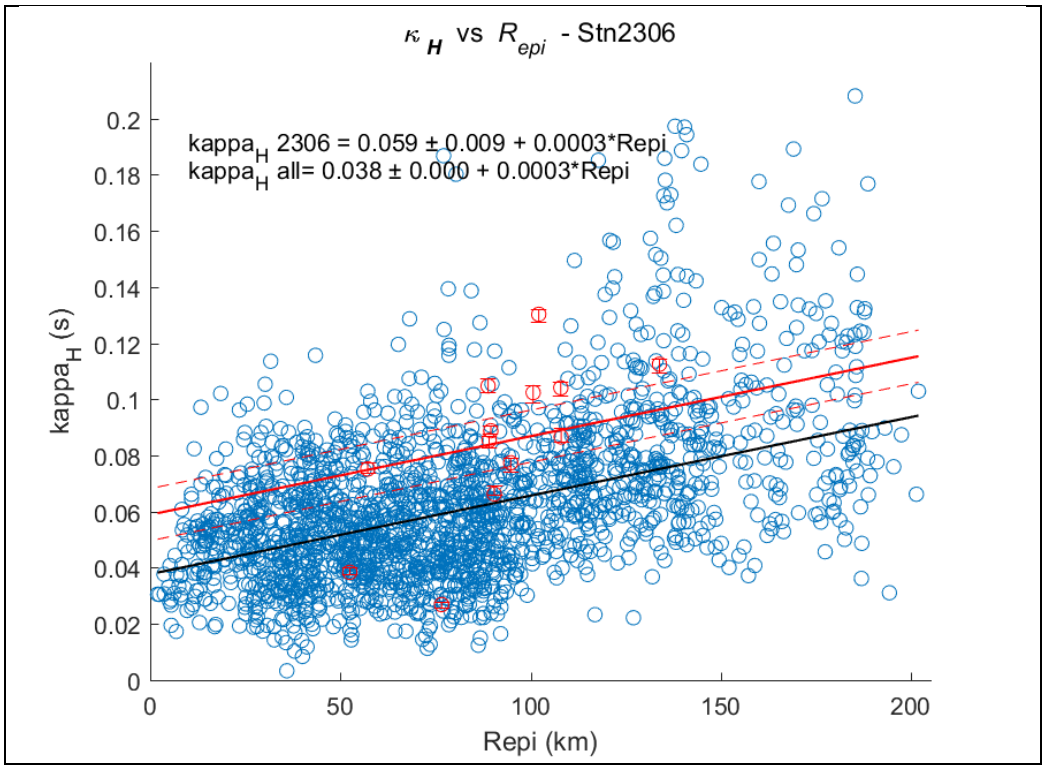


Figure 7.90: The constrained to overall κ_H vs R_{epi} fit for Stn2306.

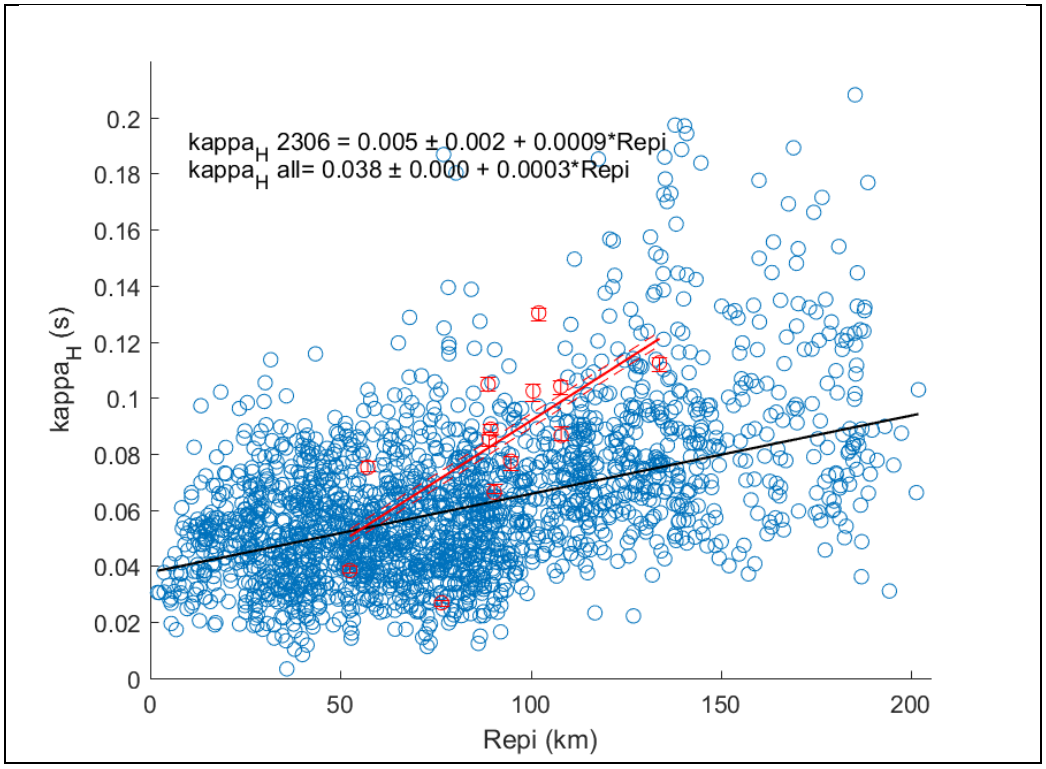


Figure 7.91: The unconstrained to overall κ_H vs R_{epi} fit for Stn2306.

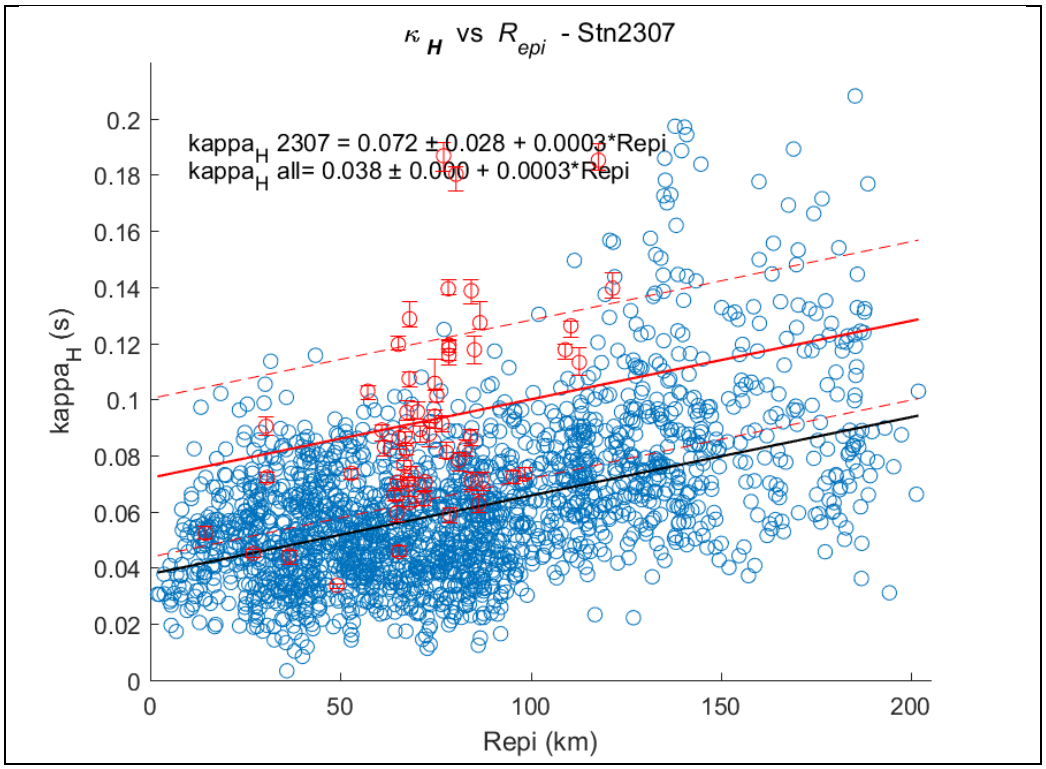


Figure 7.92: The constrained to overall κ_H vs R_{epi} fit for Stn2307.

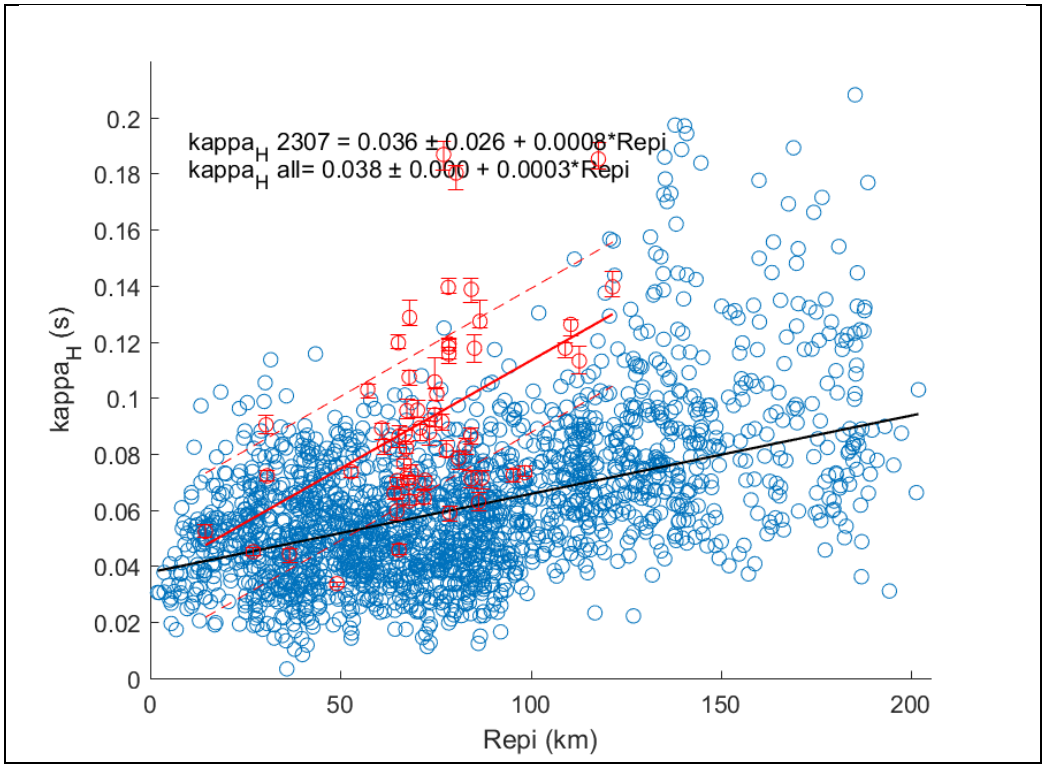


Figure 7.93: The unconstrained to overall κ_H vs R_{epi} fit for Stn2307.

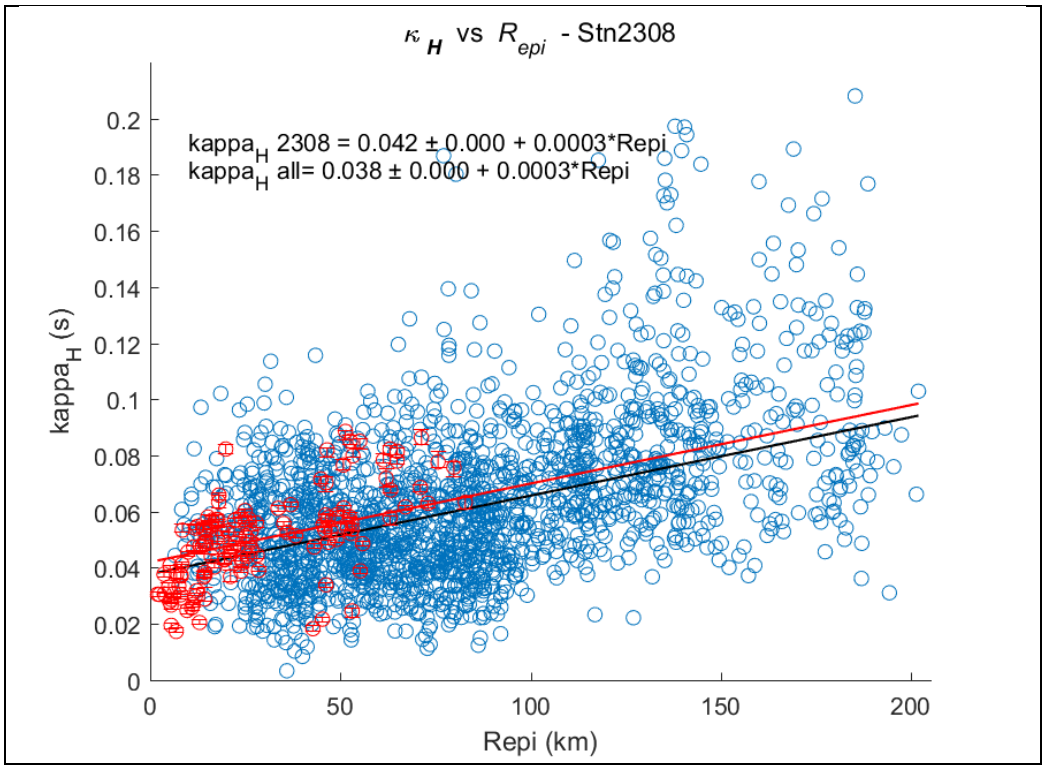


Figure 7.94: The constrained to overall κ_H vs R_{epi} fit for Stn2308.

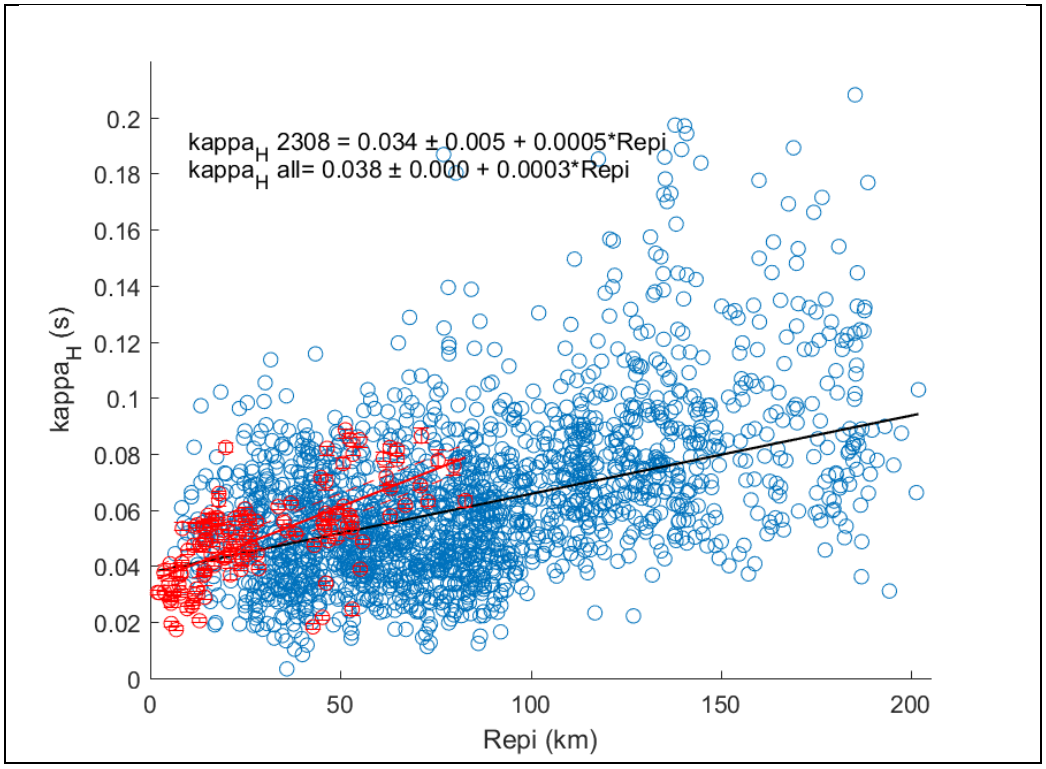


Figure 7.95: The unconstrained to overall κ_H vs R_{epi} fit for Stn2308.

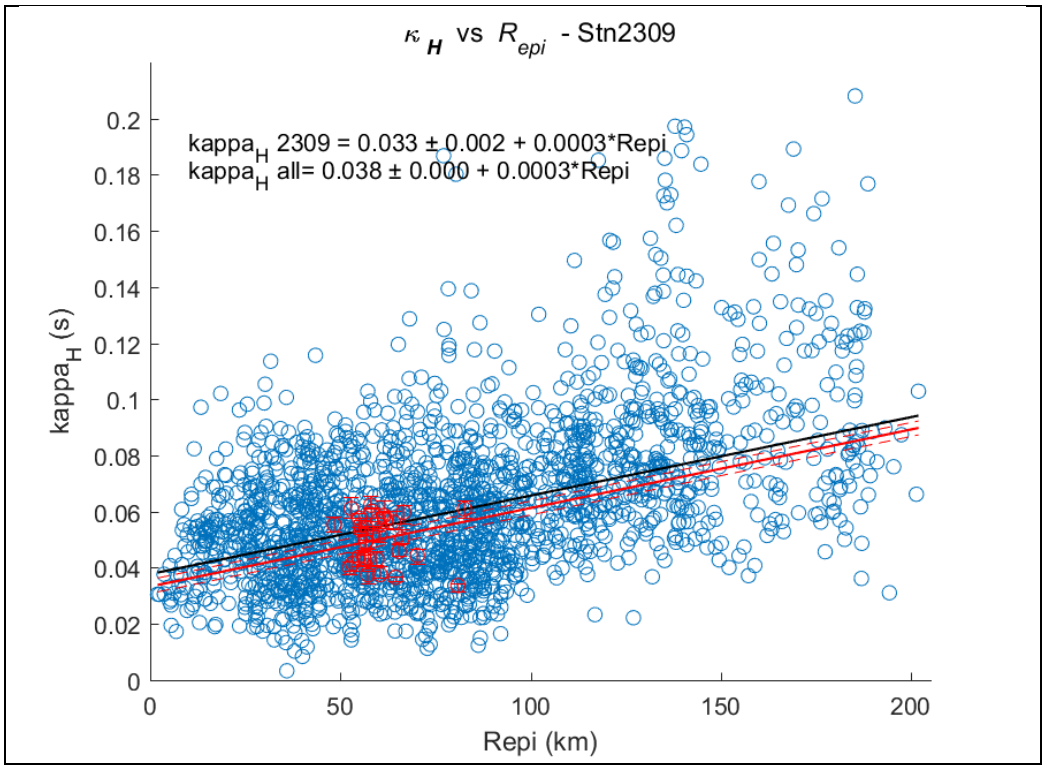


Figure 7.96: The constrained to overall κ_H vs R_{epi} fit for Stn2309.

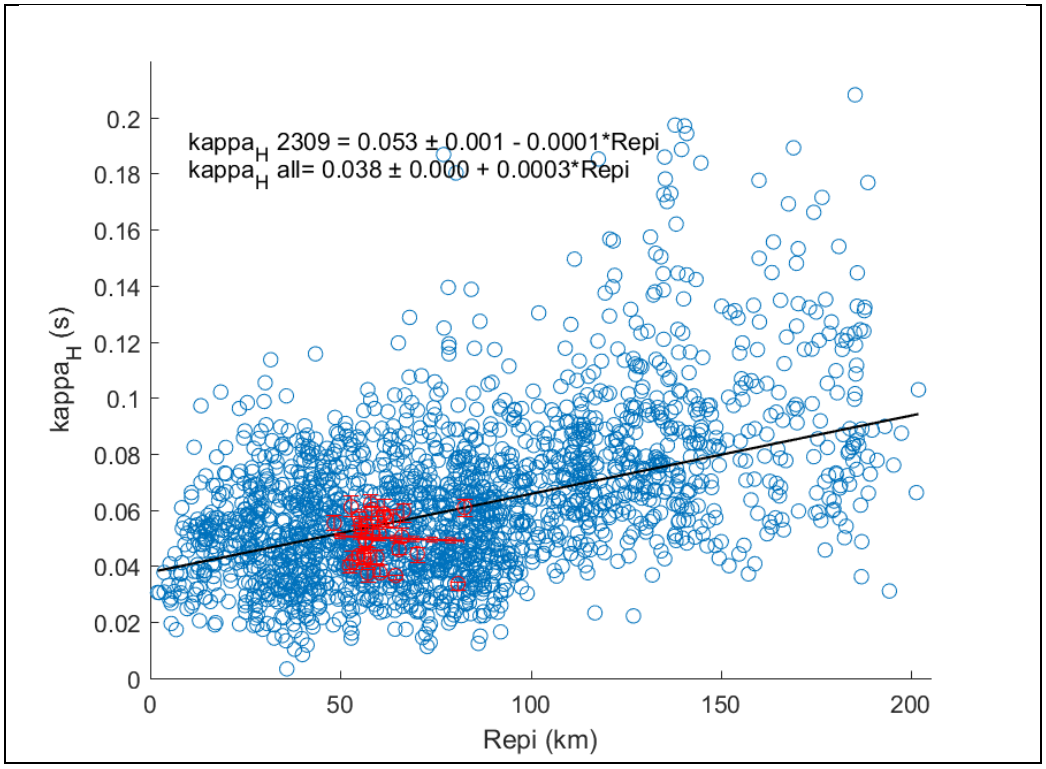


Figure 7.97: The unconstrained to overall κ_H vs R_{epi} fit for Stn2309.

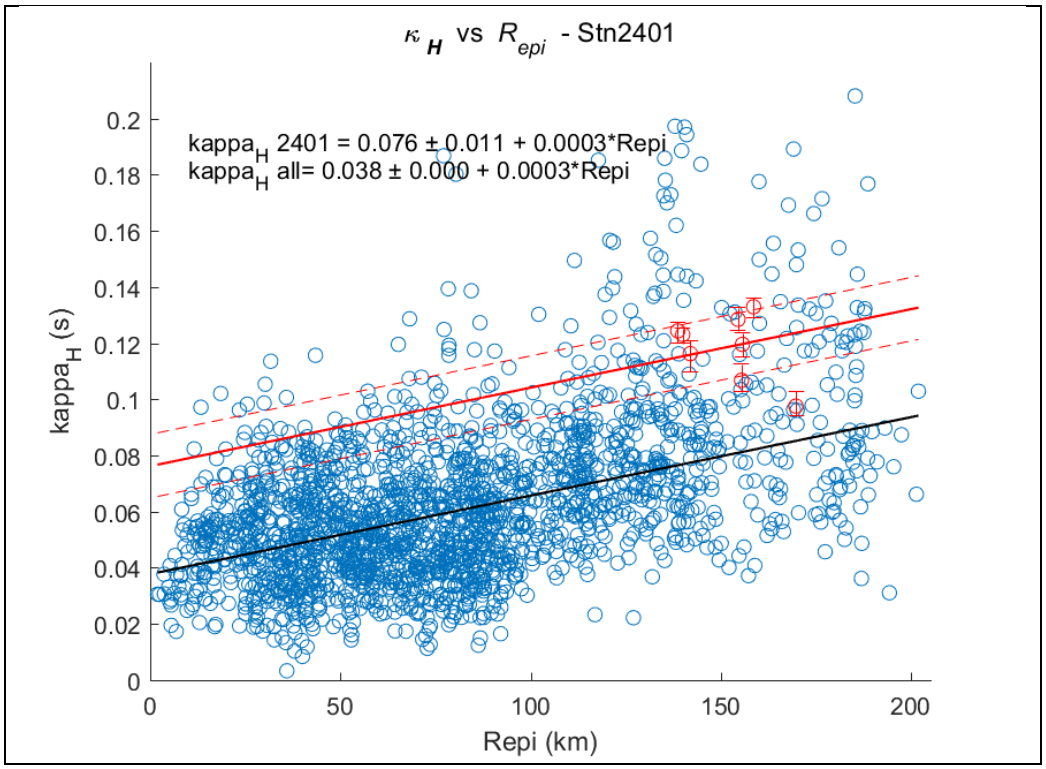


Figure 7.98: The constrained to overall κ_H vs R_{epi} fit for Stn2401.

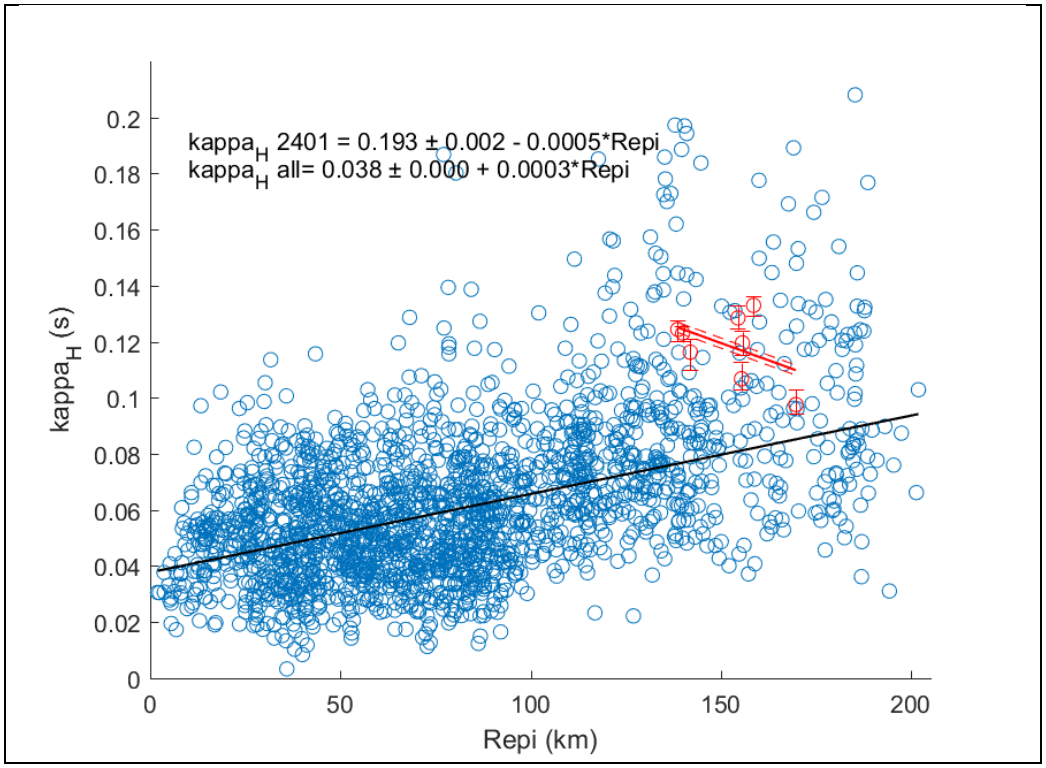


Figure 7.99: The unconstrained to overall κ_H vs R_{epi} fit for Stn2401.

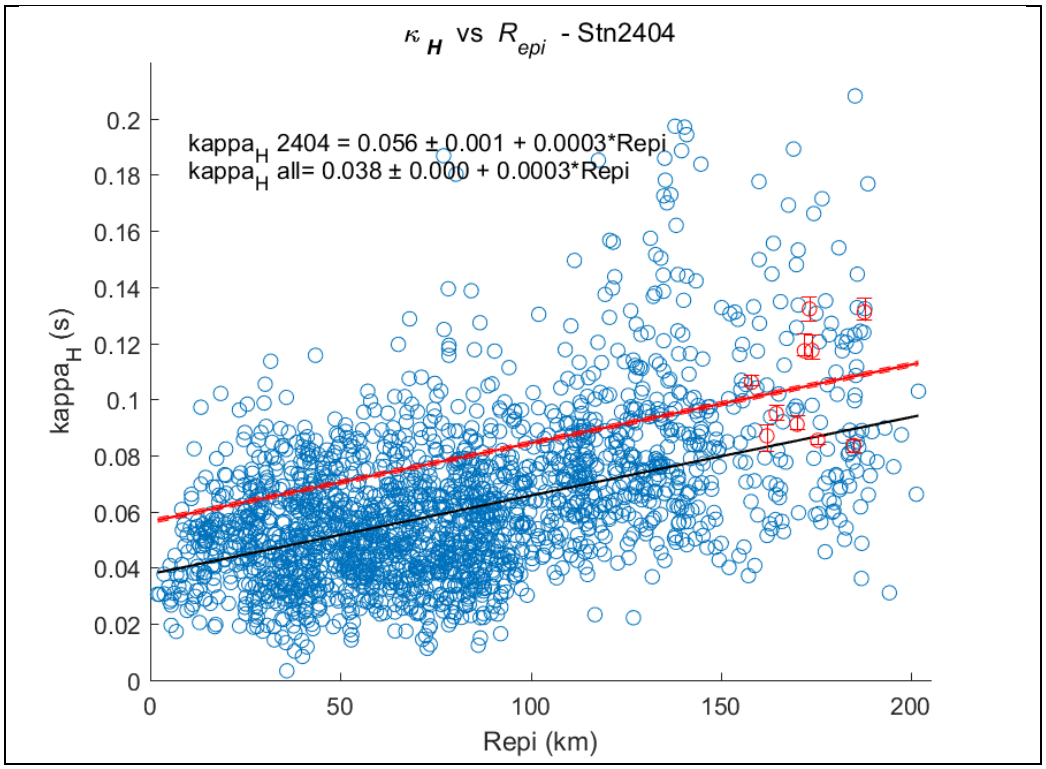


Figure 7.100: The constrained to overall κ_H vs R_{epi} fit for Stn2404.

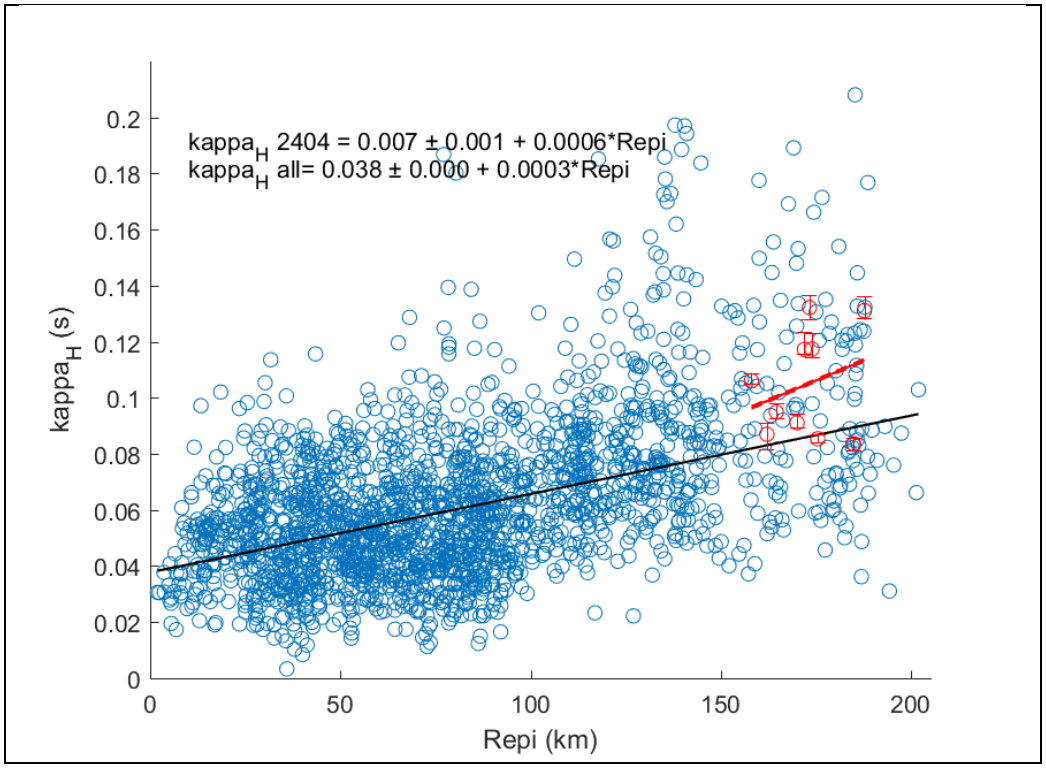


Figure 7.101: The unconstrained to overall κ_H vs R_{epi} fit for Stn2404.

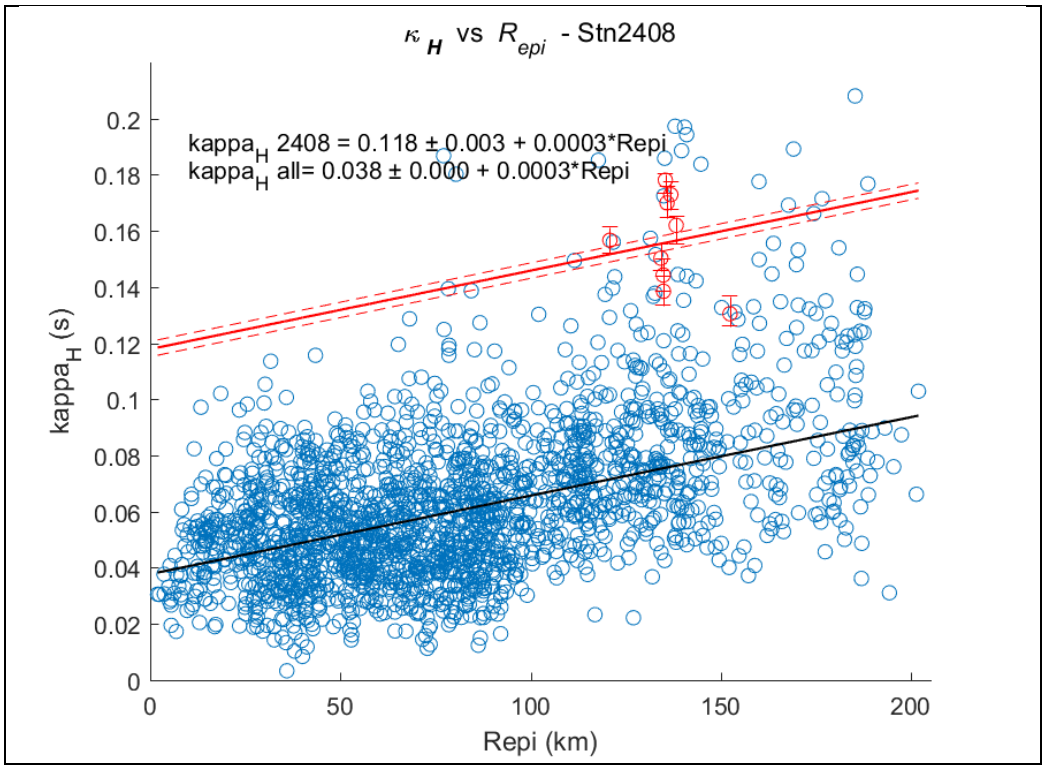


Figure 7.102: The constrained to overall κ_H vs R_{epi} fit for Stn2408.

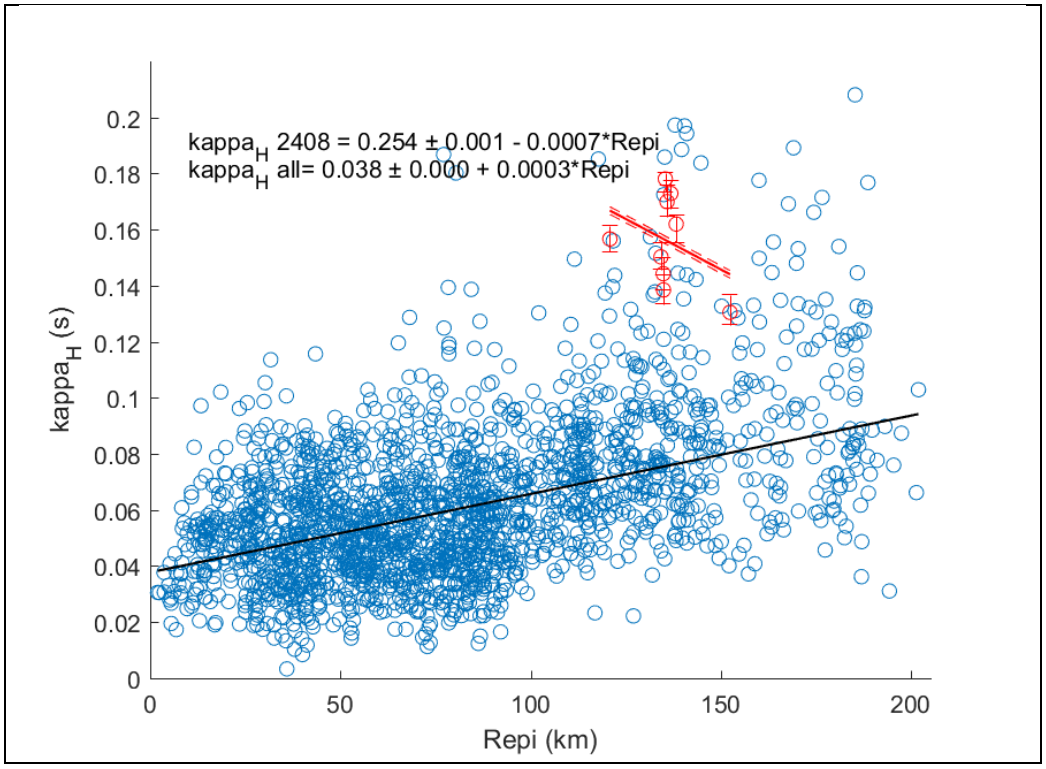


Figure 7.103: The unconstrained to overall κ_H vs R_{epi} fit for Stn2408.

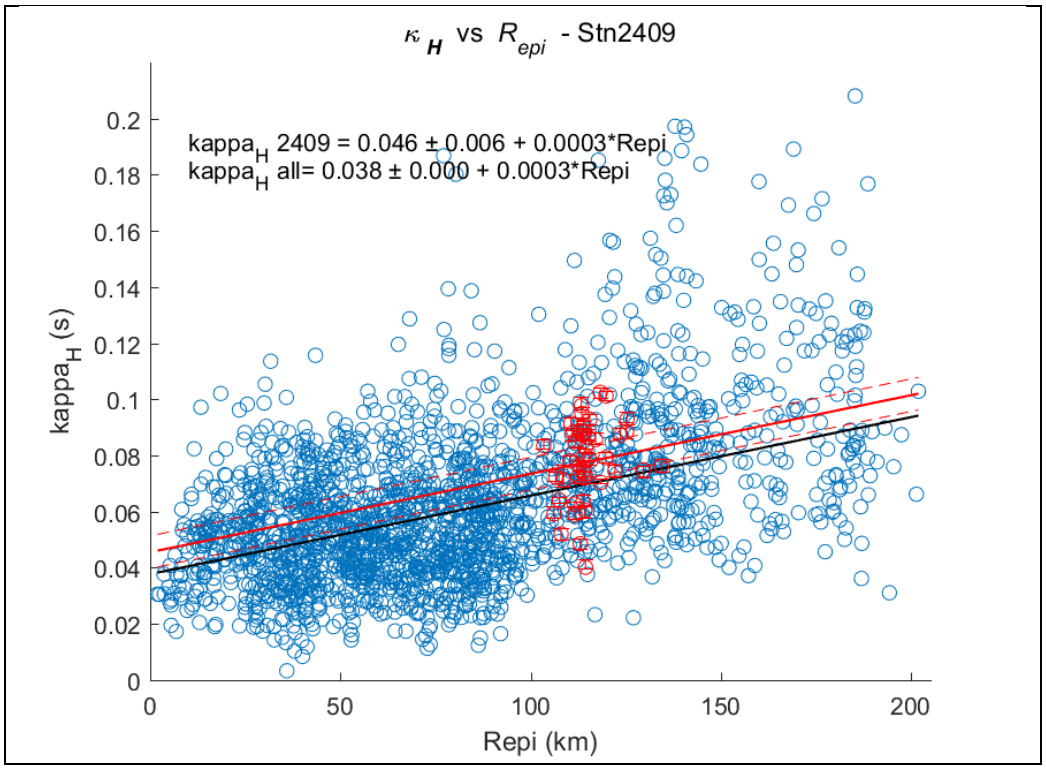


Figure 7.104: The constrained to overall κ_H vs R_{epi} fit for Stn2409.

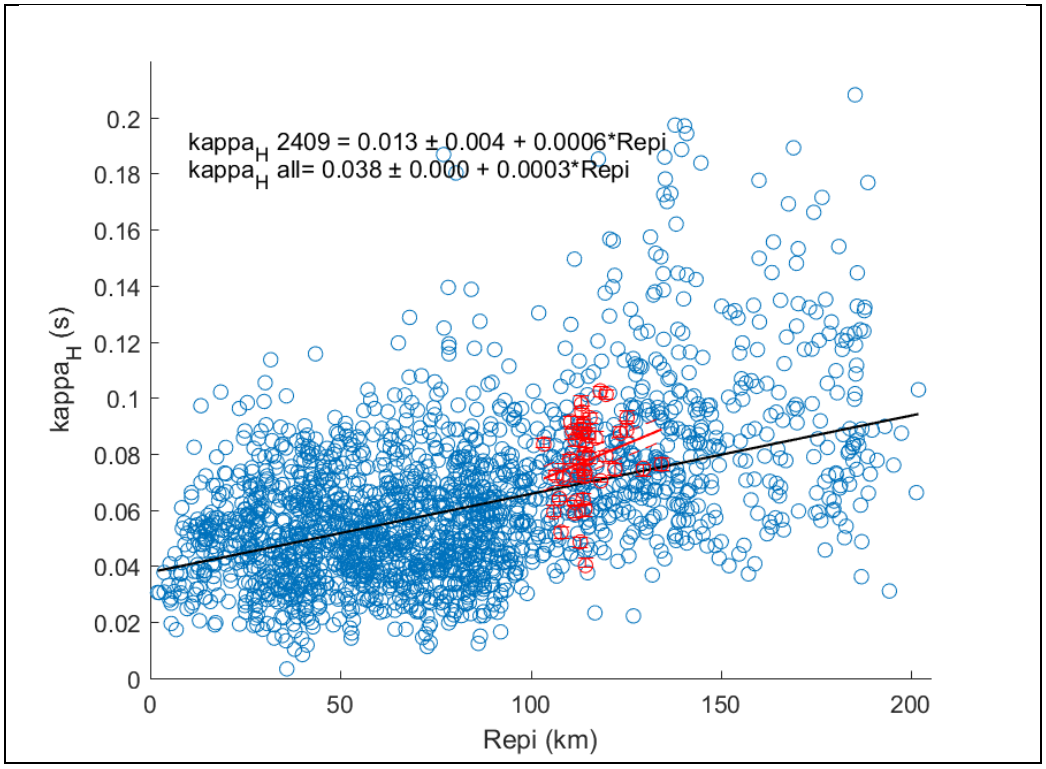


Figure 7.105: The unconstrained to overall κ_H vs R_{epi} fit for Stn2409.

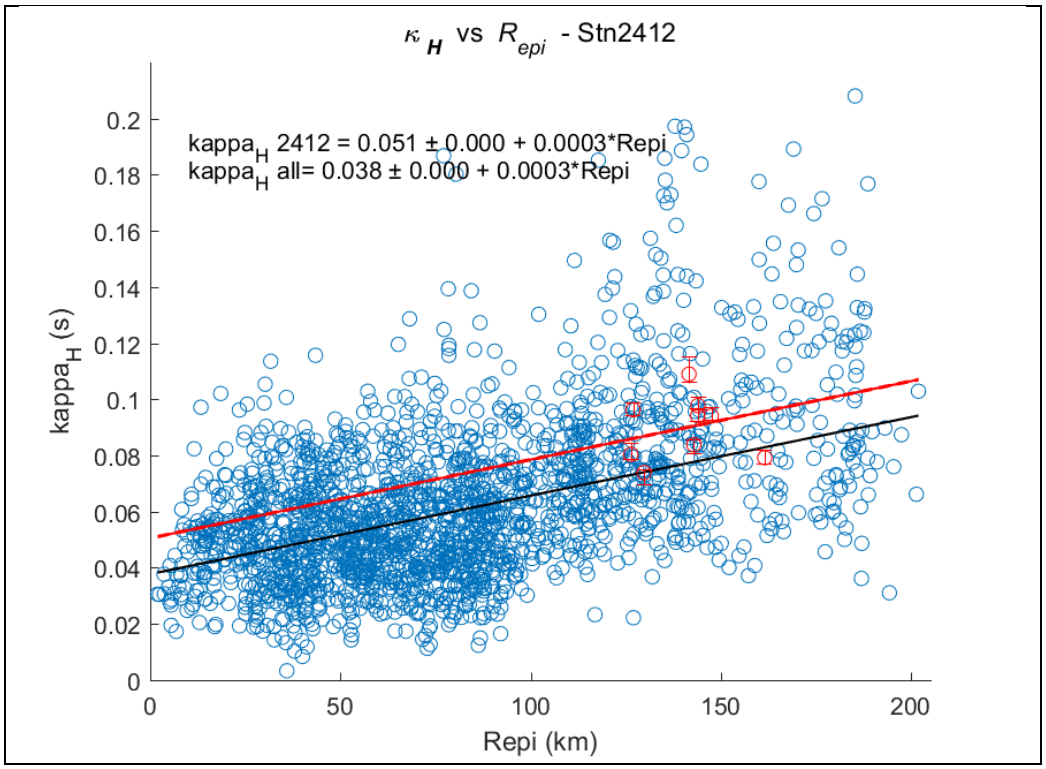


Figure 7.106: The constrained to overall κ_H vs R_{epi} fit for Stn2412.

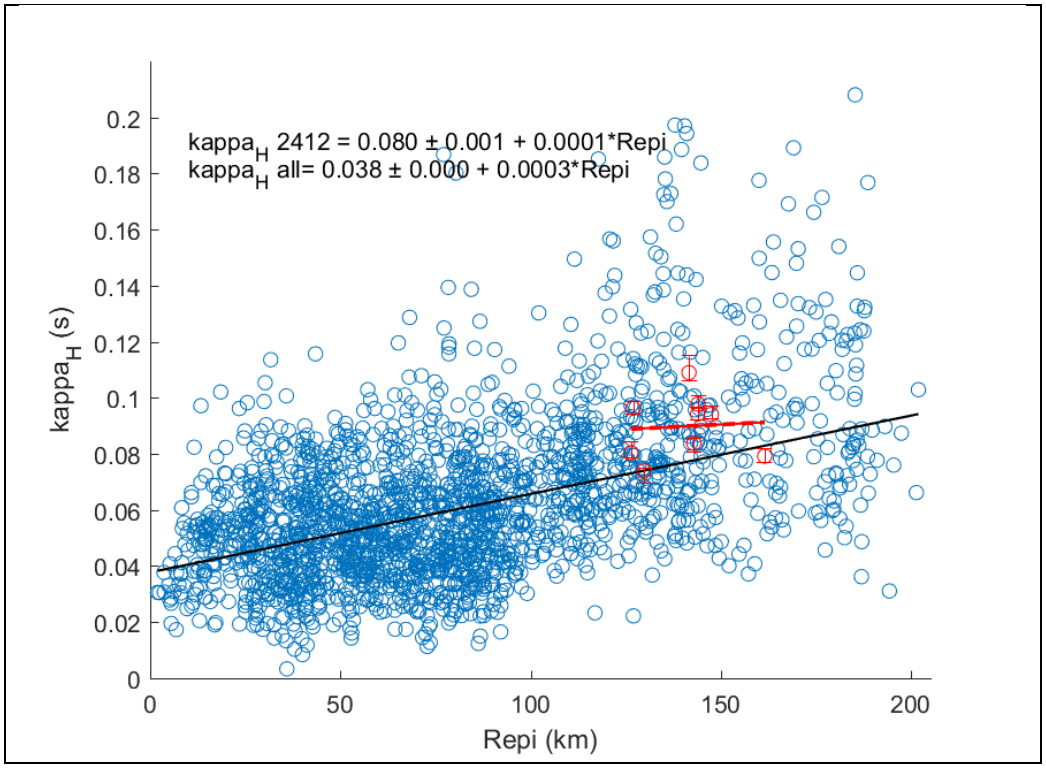


Figure 7.107: The unconstrained to overall κ_H vs R_{epi} fit for Stn2412.

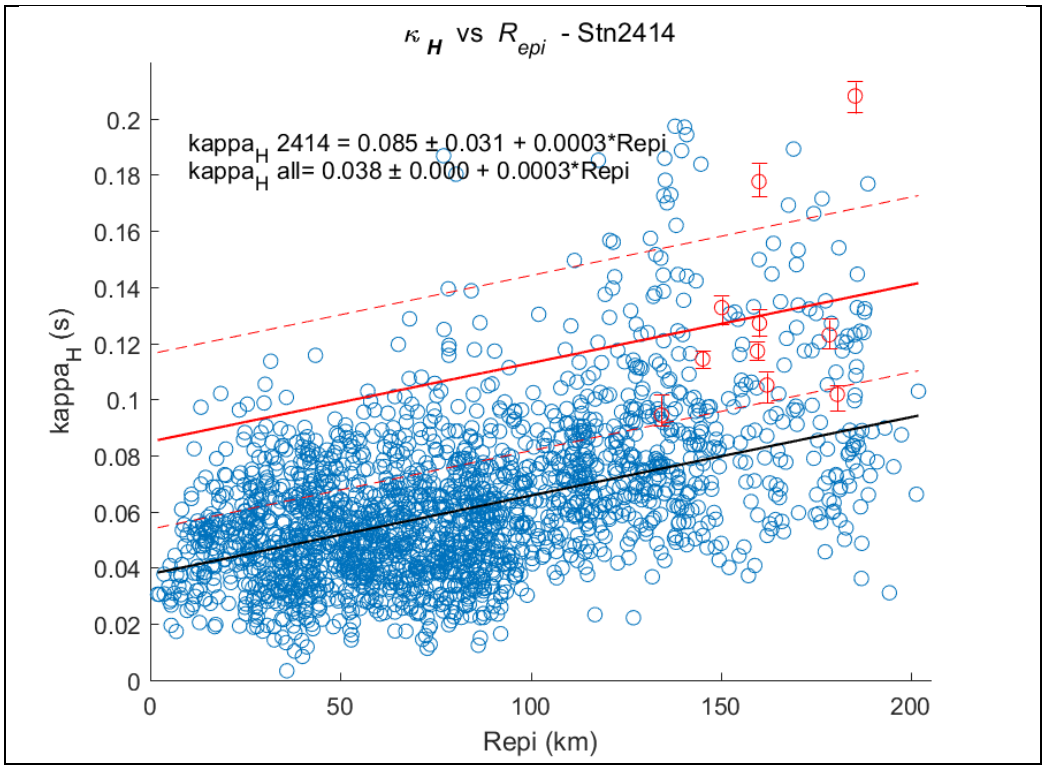


Figure 7.108: The constrained to overall κ_H vs R_{epi} fit for Stn2414.

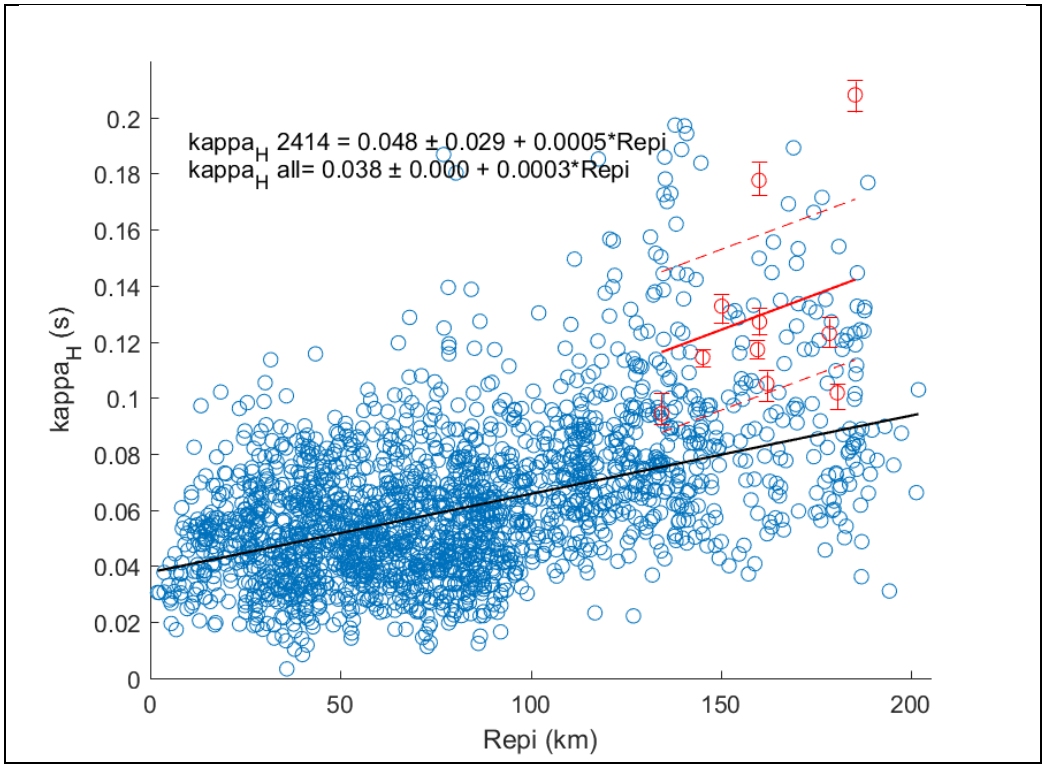


Figure 7.109: The unconstrained to overall κ_H vs R_{epi} fit for Stn2414.

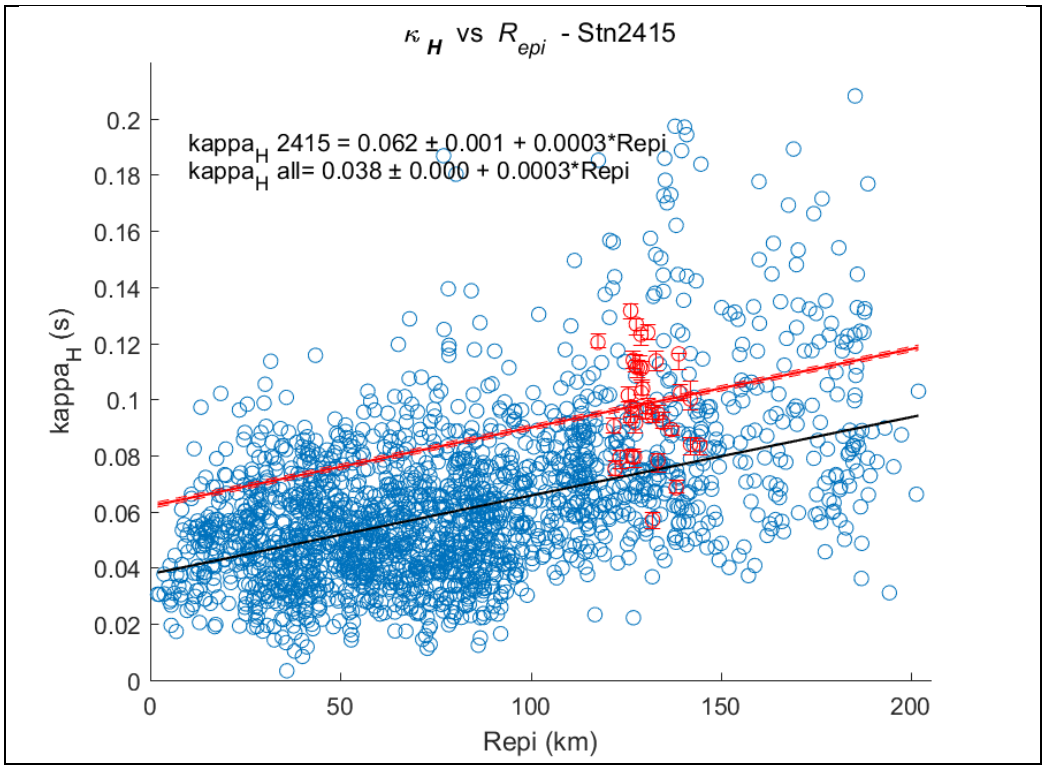


Figure 7.110: The constrained to overall κ_H vs R_{epi} fit for Stn2415.

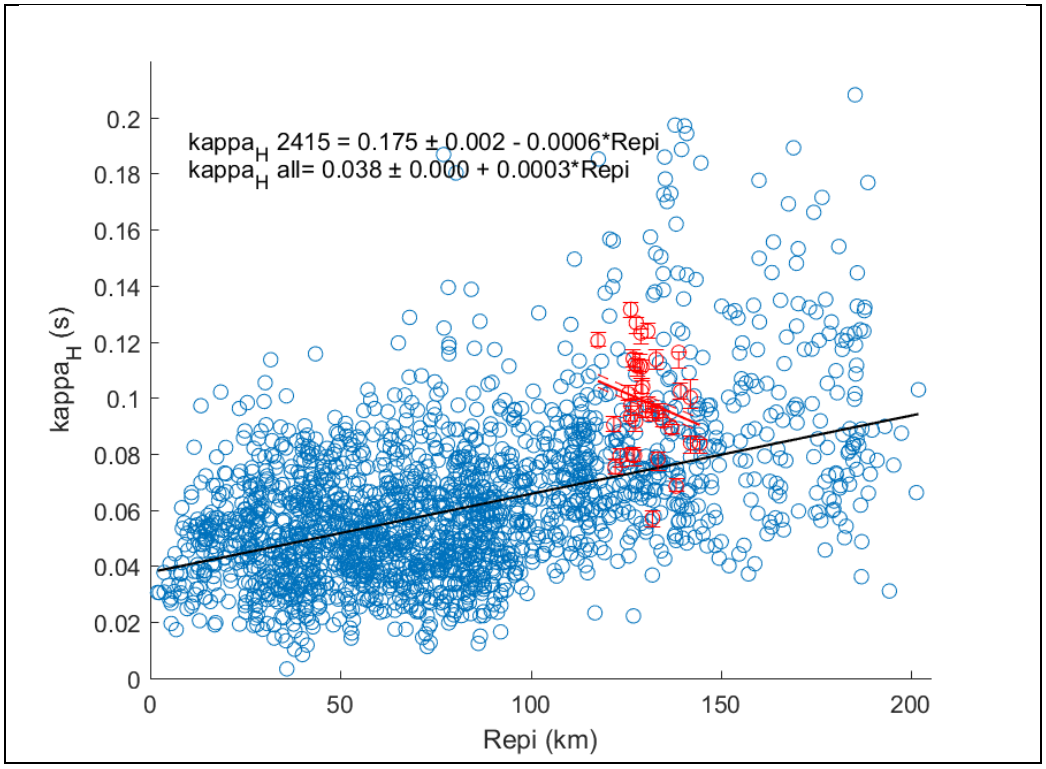


Figure 7.111: The unconstrained to overall κ_H vs R_{epi} fit for Stn2415.

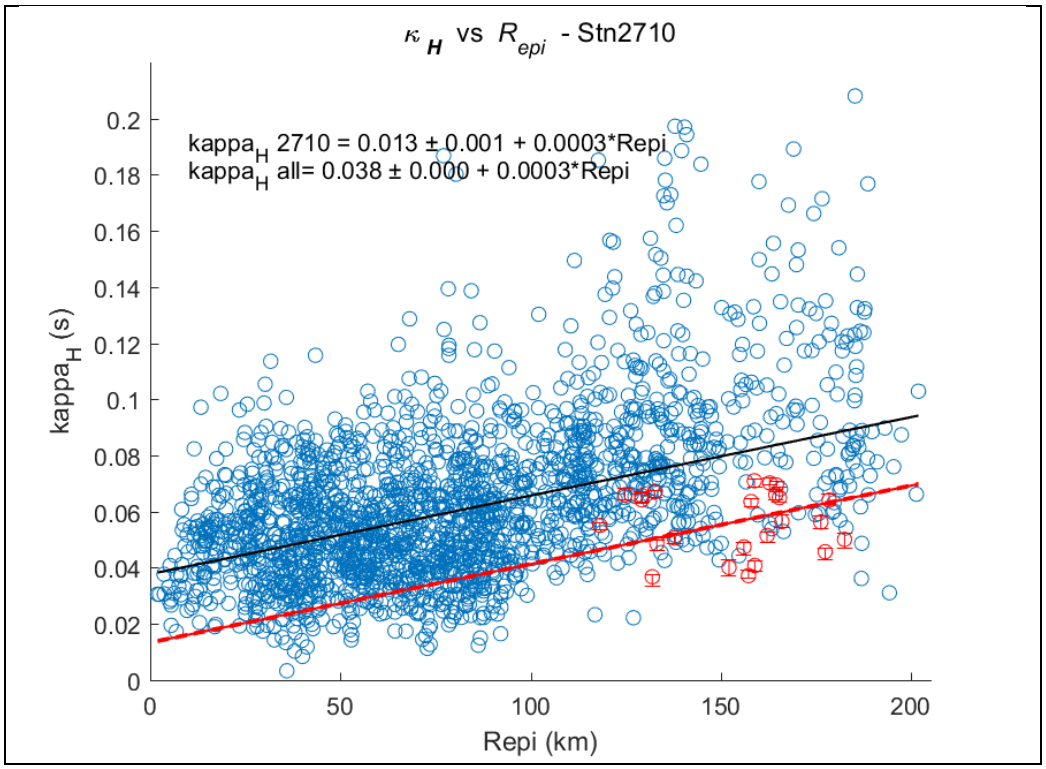


Figure 7.112: The constrained to overall κ_H vs R_{epi} fit for Stn2710.

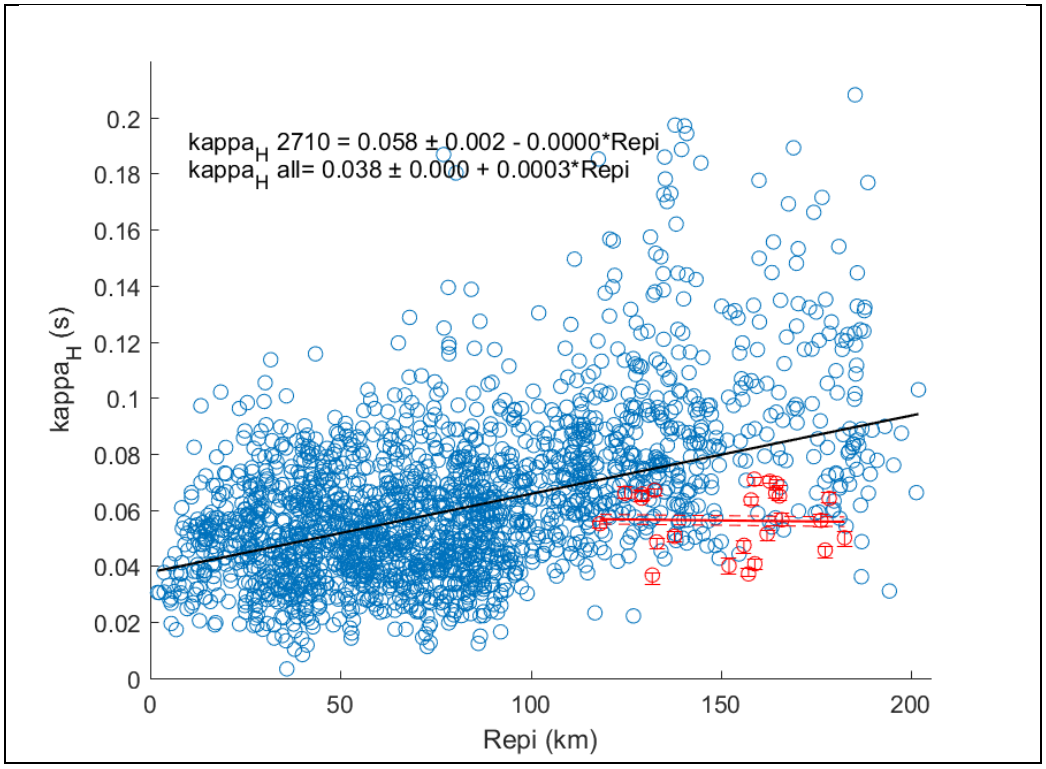


Figure 7.113: The unconstrained to overall κ_H vs R_{epi} fit for Stn2710.

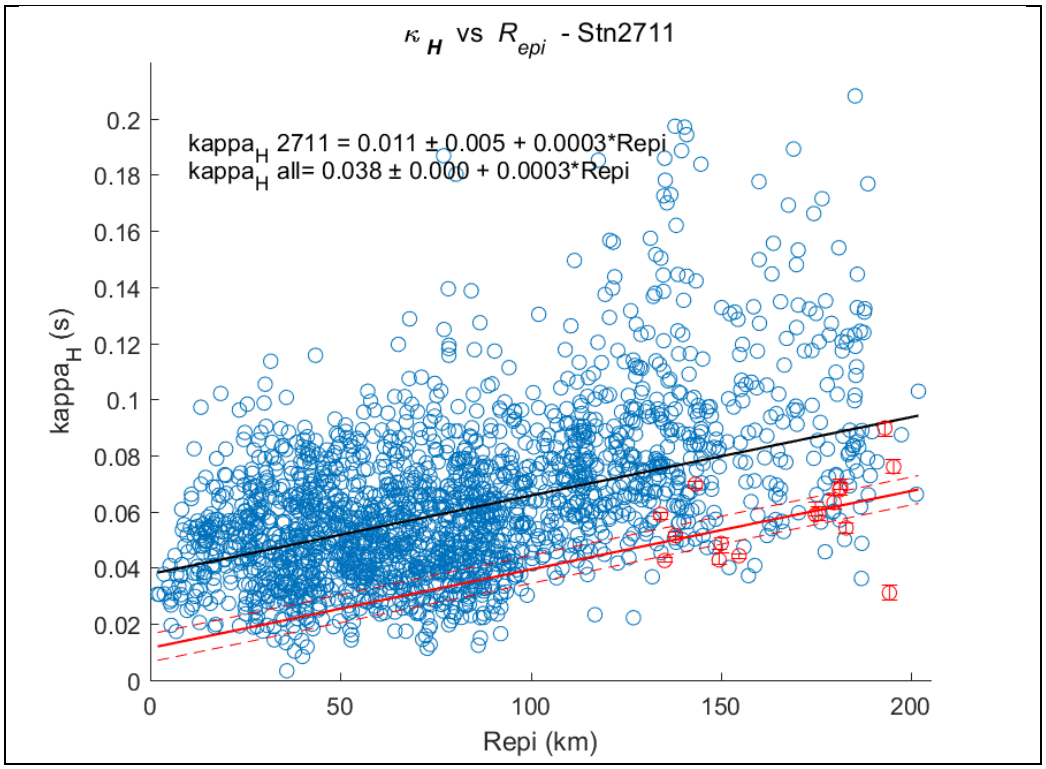


Figure 7.114: The constrained to overall κ_H vs R_{epi} fit for Stn2711.

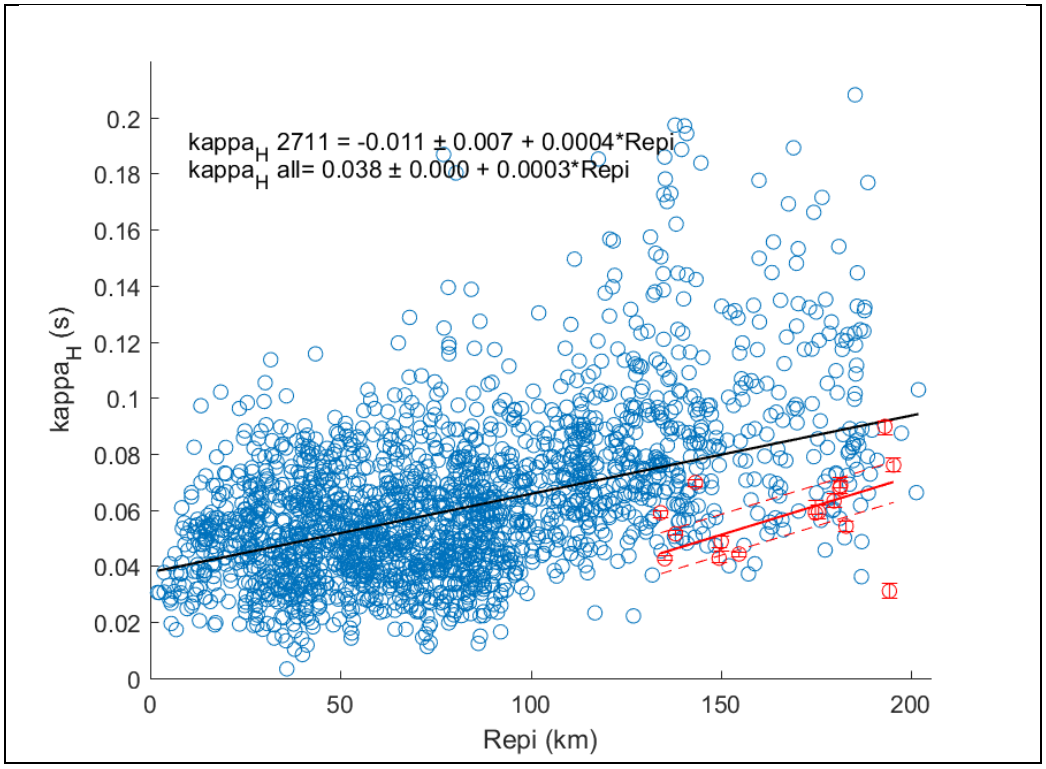


Figure 7.115: The unconstrained to overall κ_H vs R_{epi} fit for Stn2711.

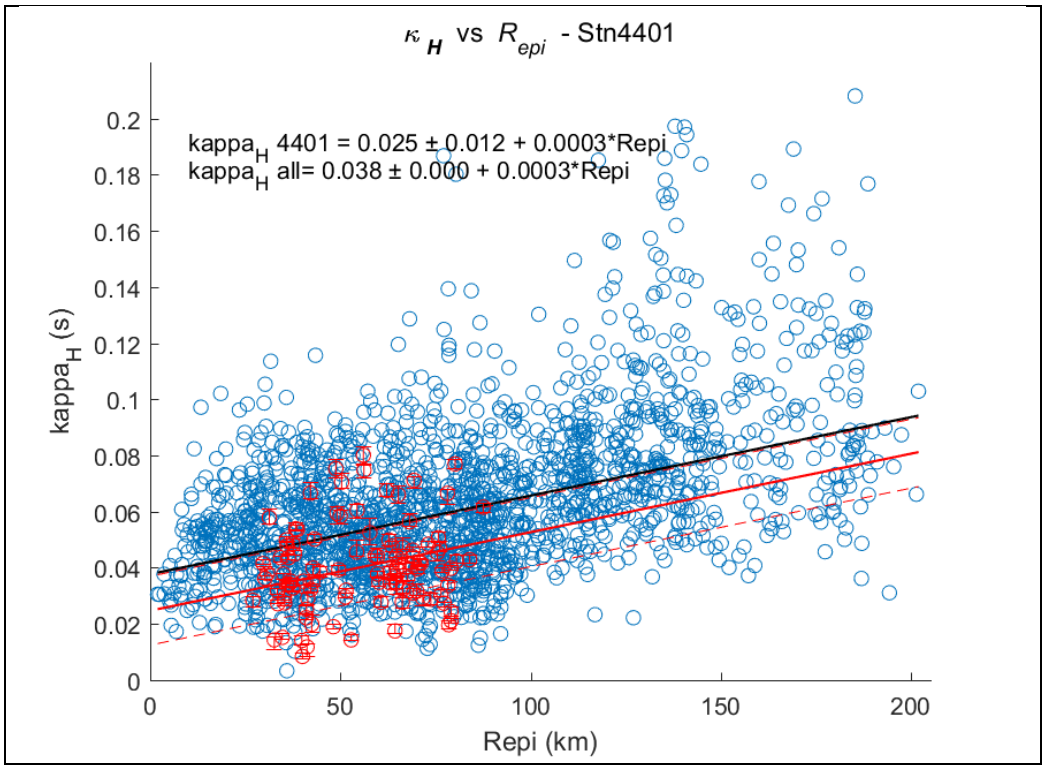


Figure 7.116: The constrained to overall κ_H vs R_{epi} fit for Stn4401.

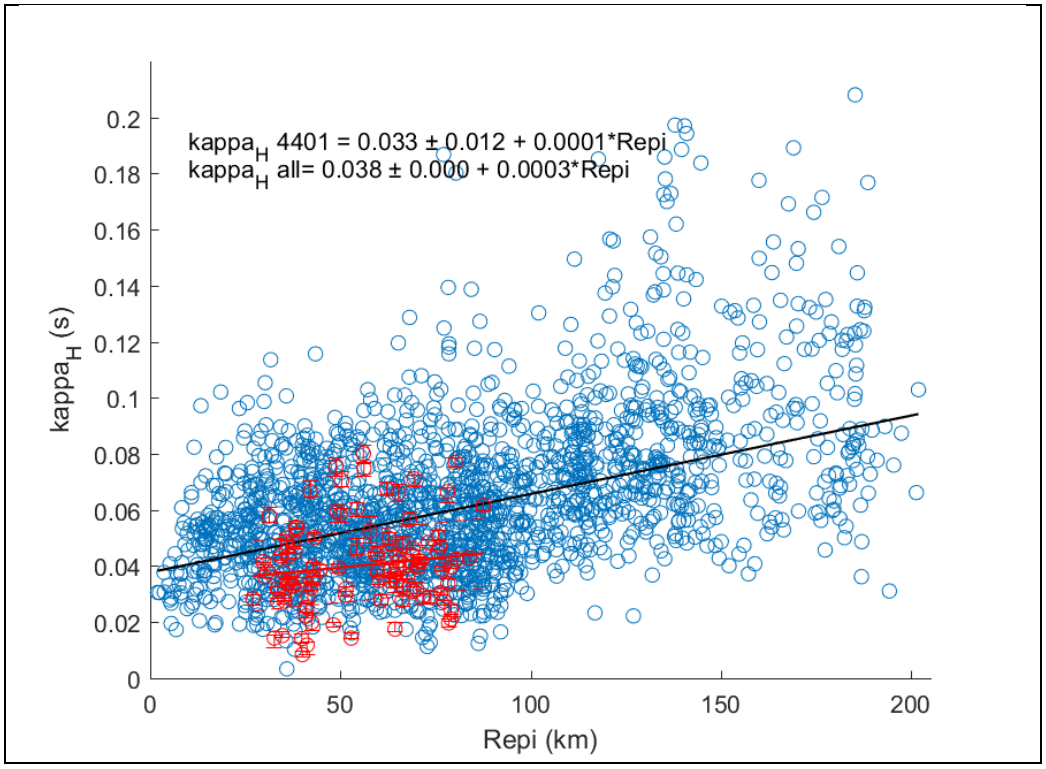


Figure 7.117: The unconstrained to overall κ_H vs R_{epi} fit for Stn4401.

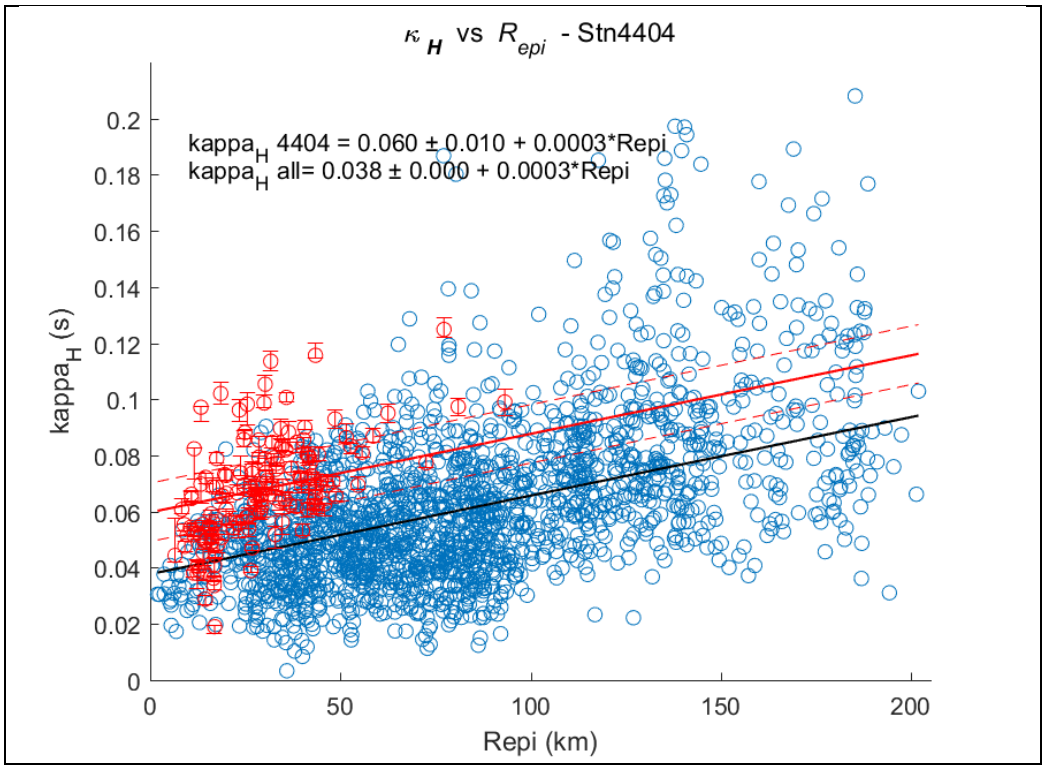


Figure 7.118: The constrained to overall κ_H vs R_{epi} fit for Stn4404.

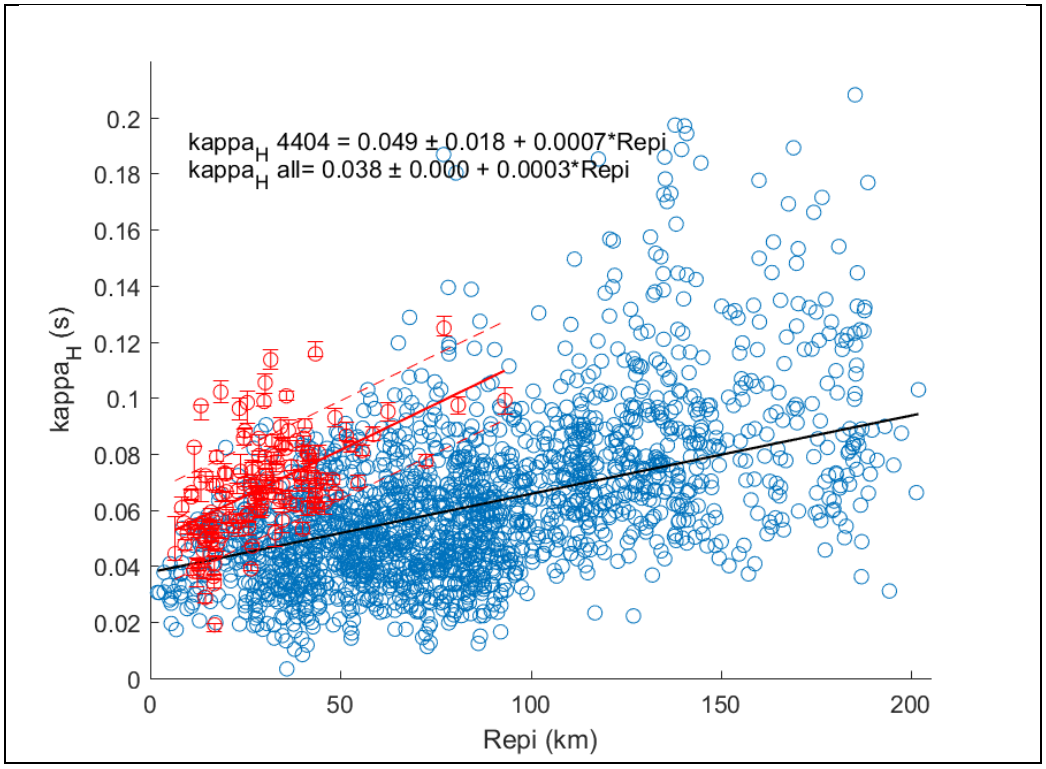


Figure 7.119: The unconstrained to overall κ_H vs R_{epi} fit for Stn4404.

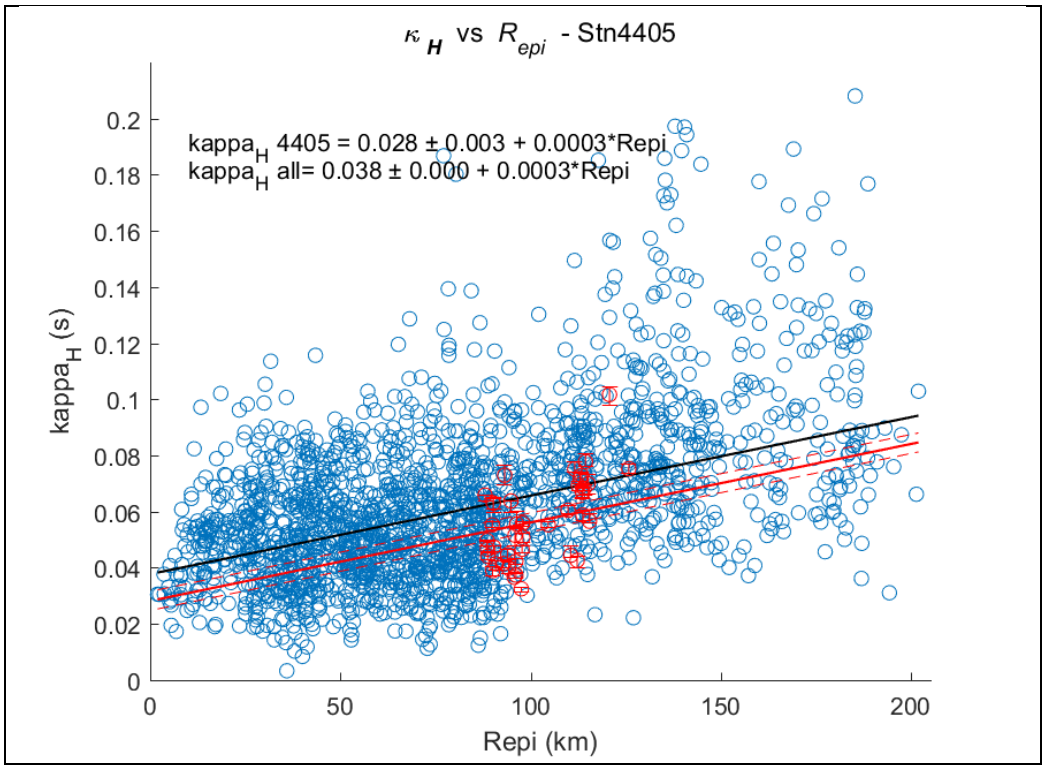


Figure 7.120: The constrained to overall κ_H vs R_{epi} fit for Stn4405.

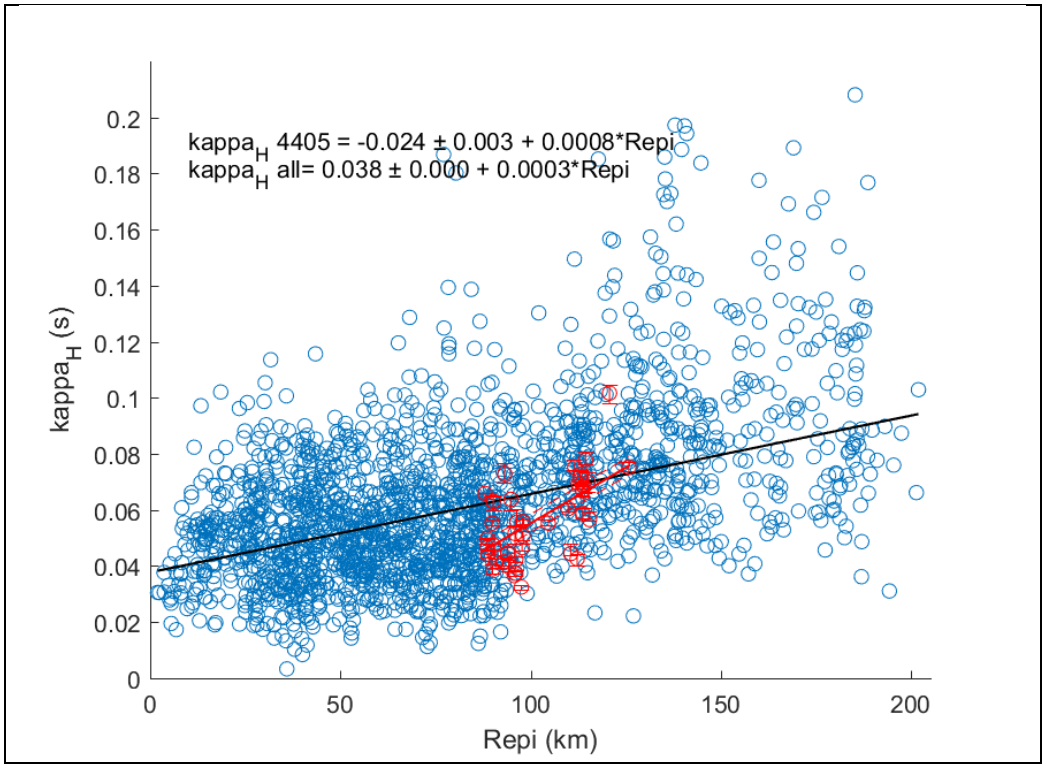


Figure 7.121: The unconstrained to overall κ_H vs R_{epi} fit for Stn4405.

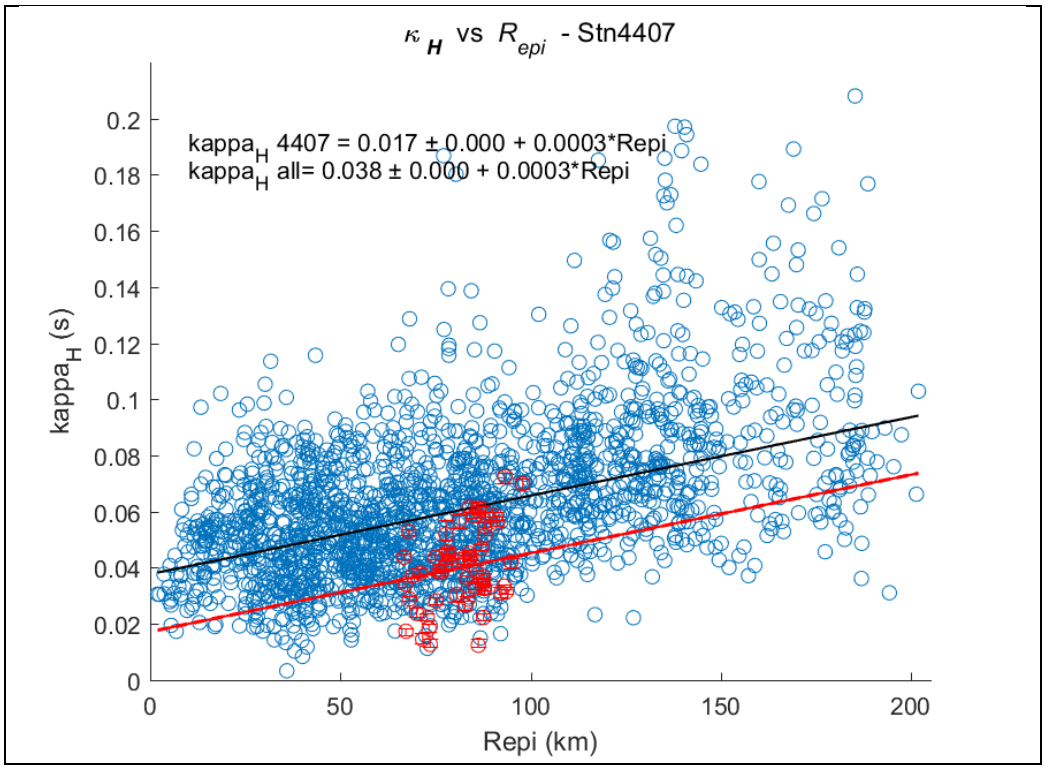


Figure 7.122: The constrained to overall κ_H vs R_{epi} fit for Stn4407.

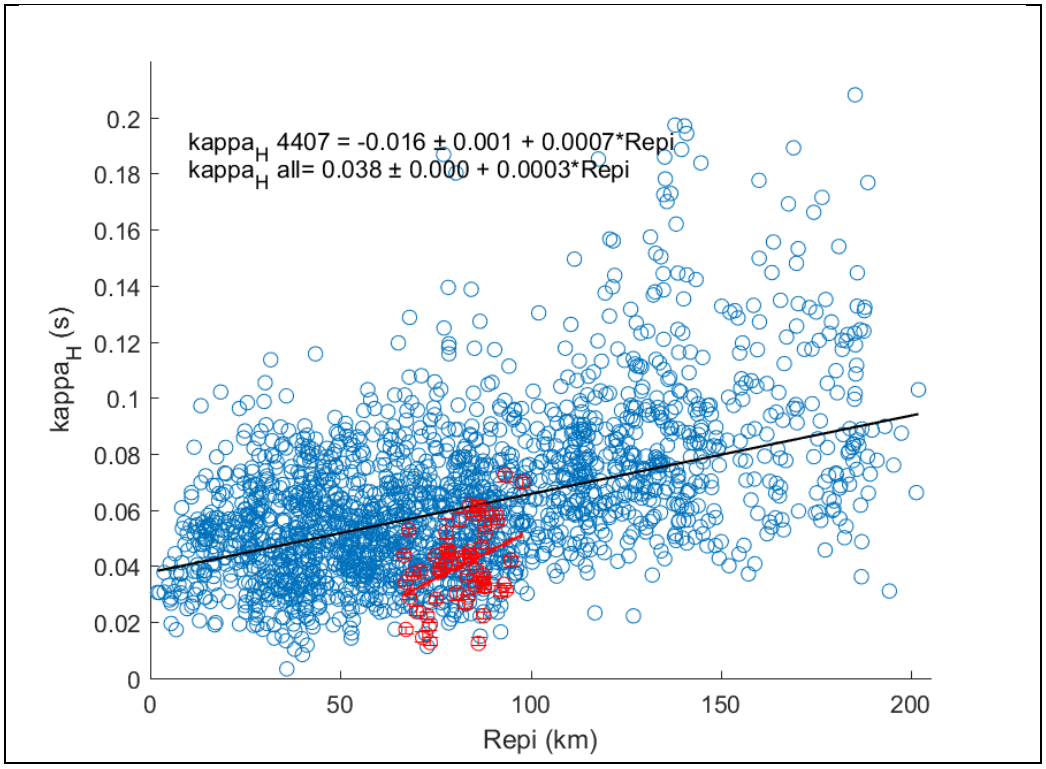


Figure 7.123: The unconstrained to overall κ_H vs R_{epi} fit for Stn4407.

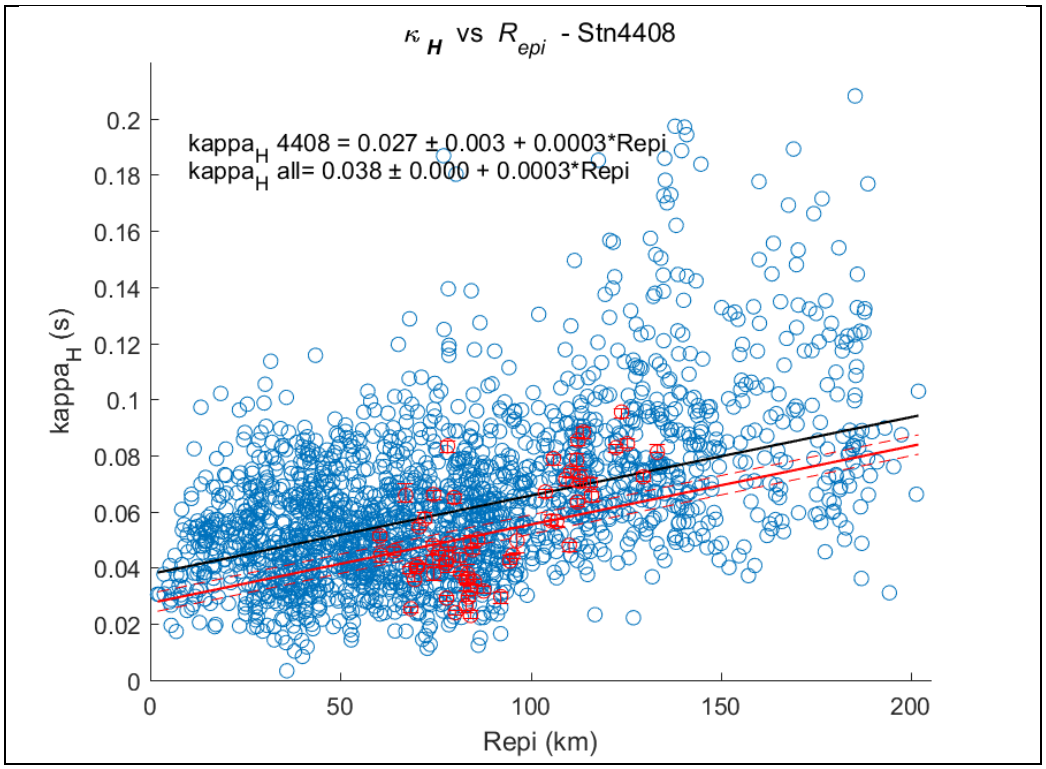


Figure 7.124: The constrained to overall κ_H vs R_{epi} fit for Stn4408.

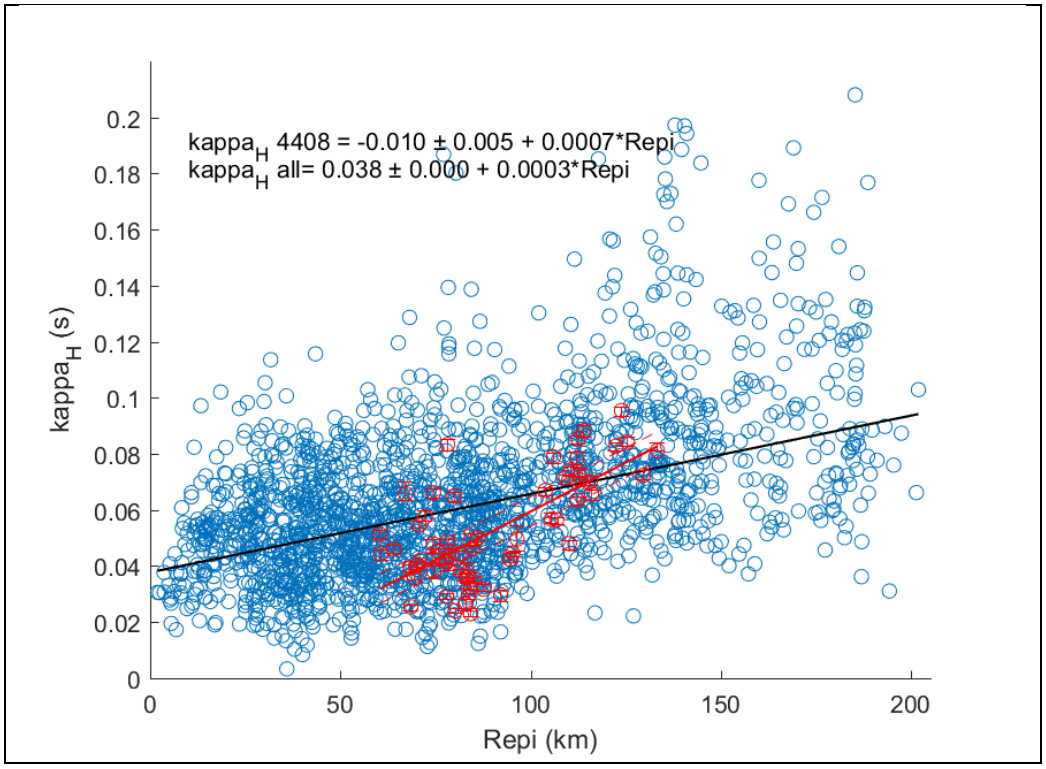


Figure 7.125: The unconstrained to overall κ_H vs R_{epi} fit for Stn4408.

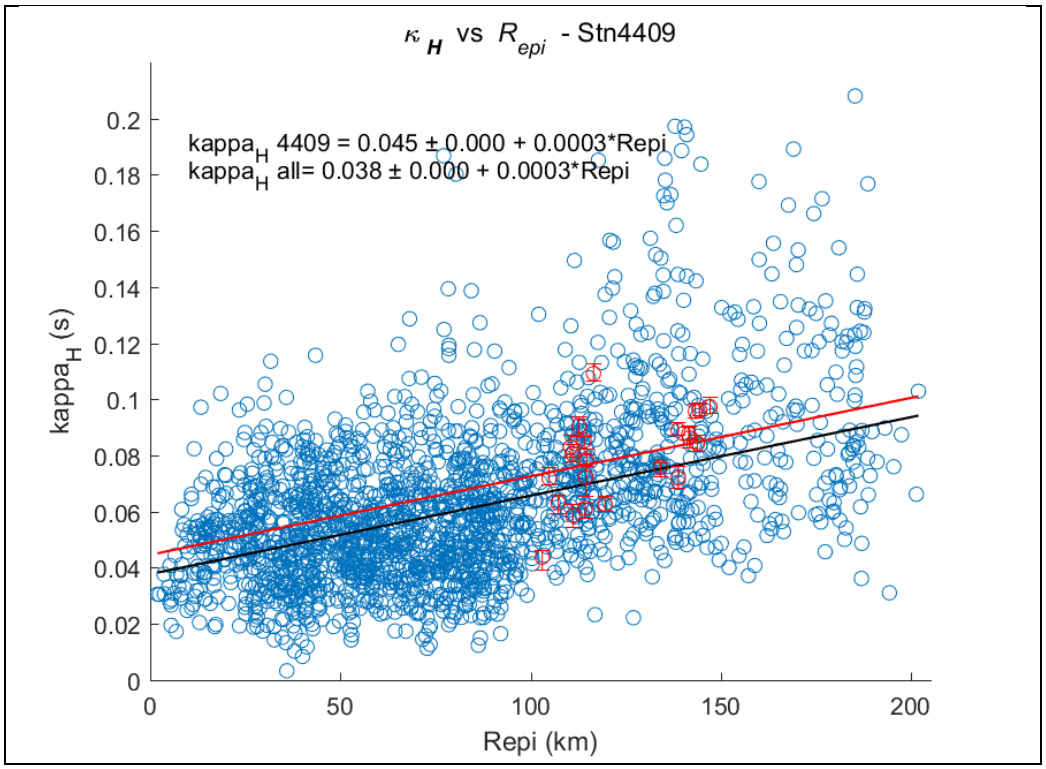


Figure 7.126: The constrained to overall κ_H vs R_{epi} fit for Stn4409.

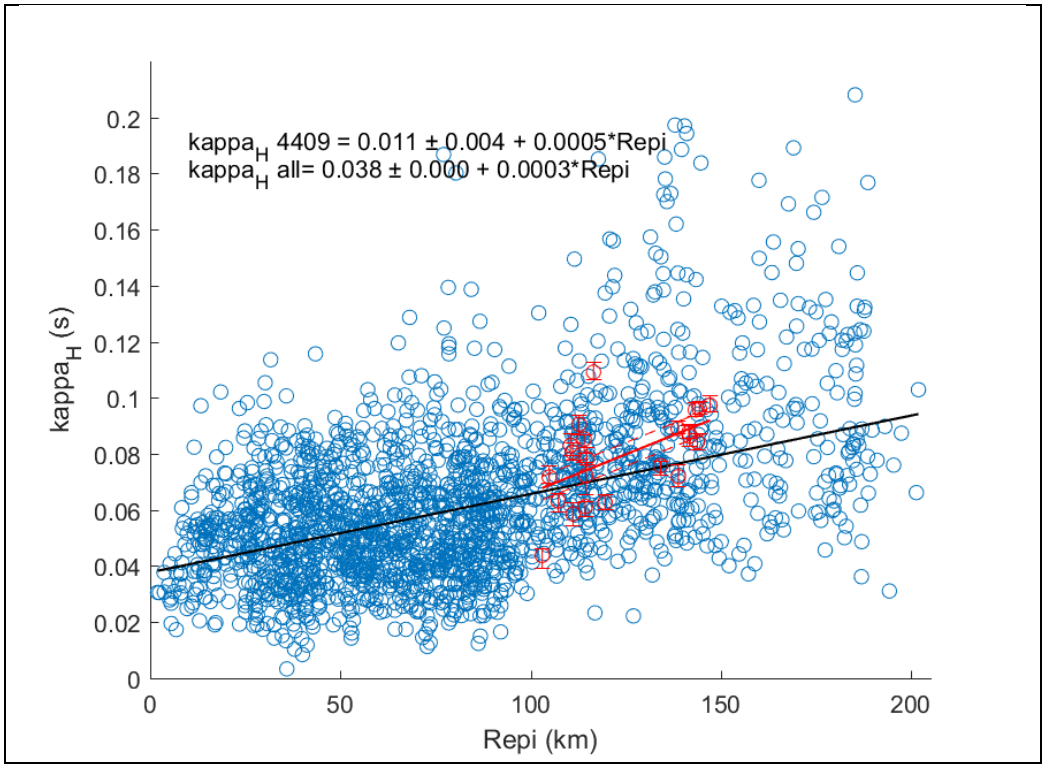


Figure 7.127: The unconstrained to overall κ_H vs R_{epi} fit for Stn4409.

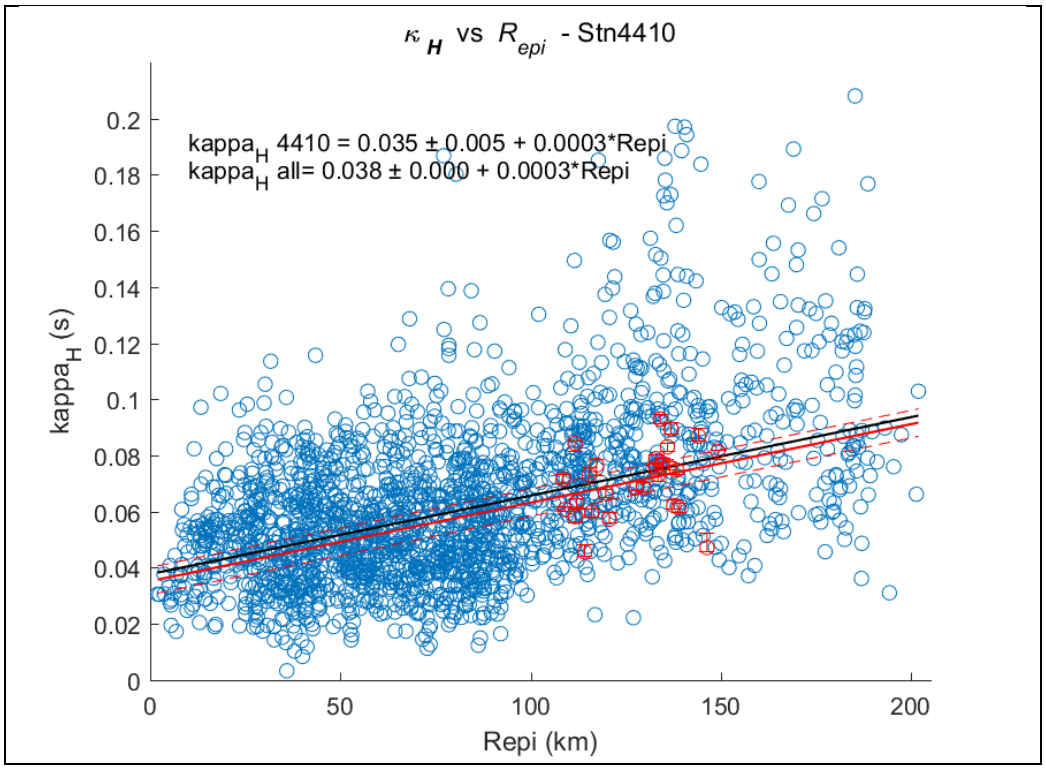


Figure 7.128: The constrained to overall κ_H vs R_{epi} fit for Stn4410.

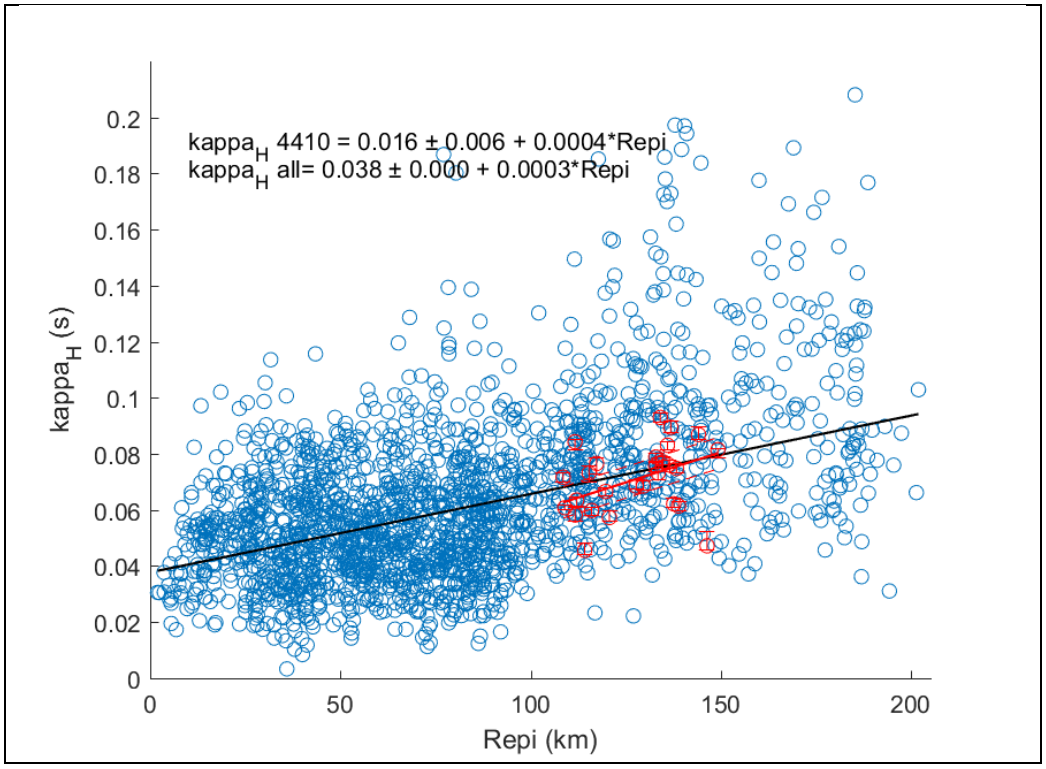


Figure 7.129: The unconstrained to overall κ_H vs R_{epi} fit for Stn4410.

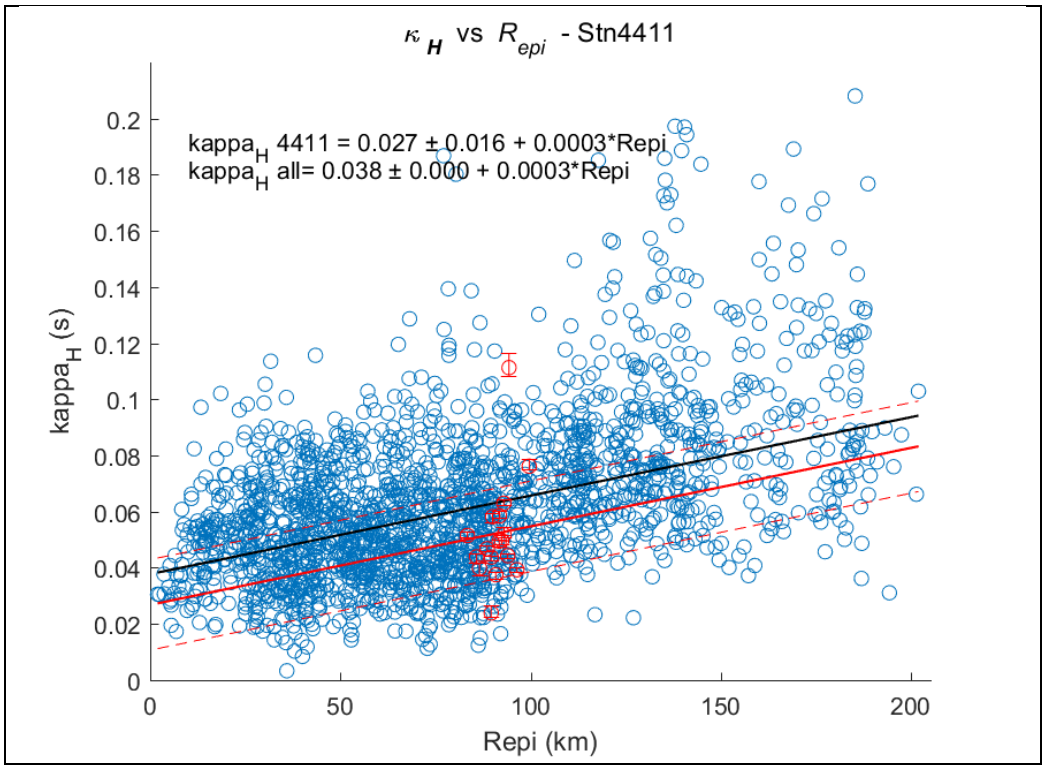


Figure 7.130: The constrained to overall κ_H vs R_{epi} fit for Stn4411.

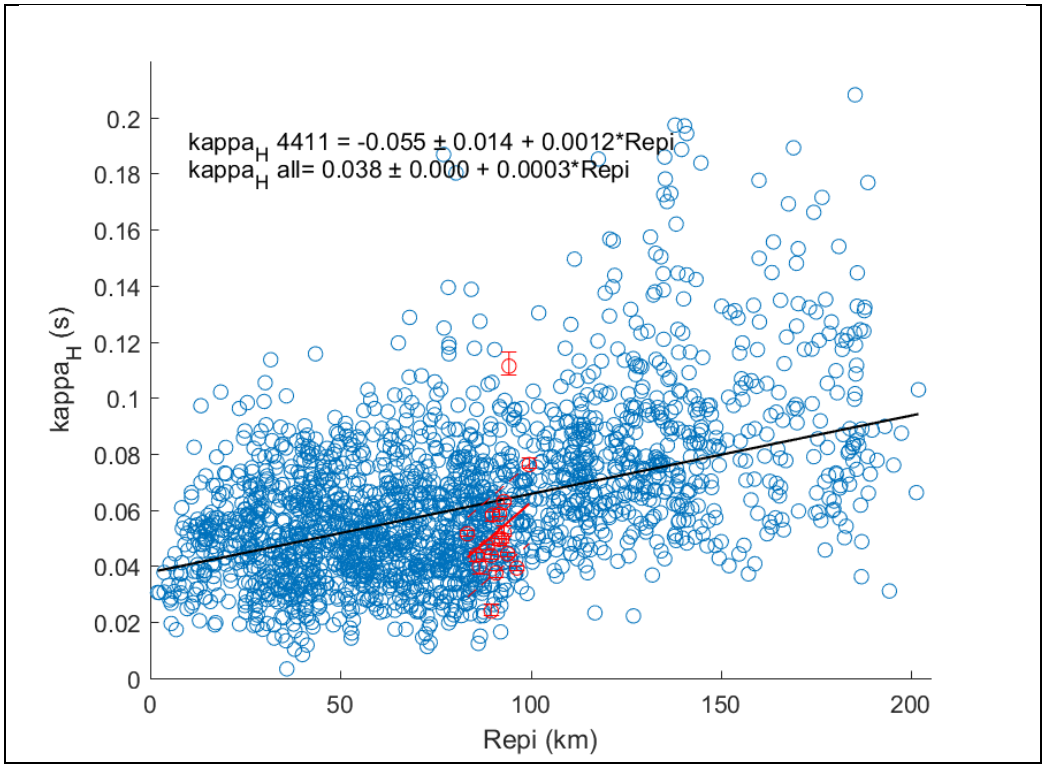


Figure 7.131: The unconstrained to overall κ_H vs R_{epi} fit for Stn4411.

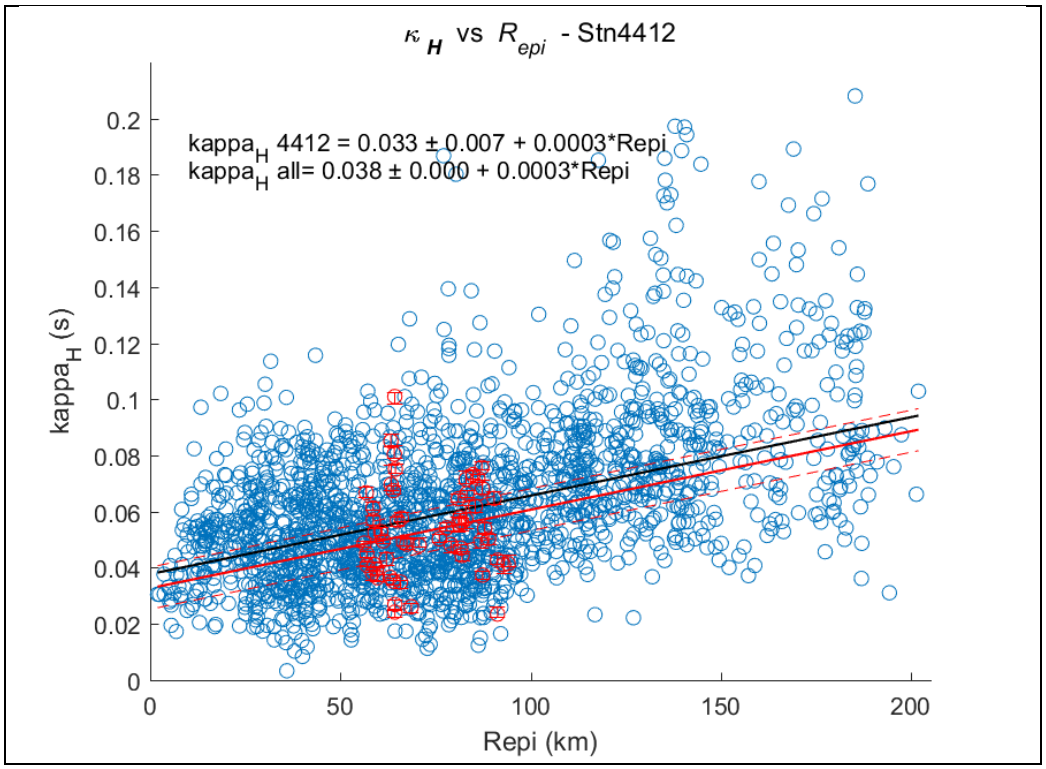


Figure 7.132: The constrained to overall κ_H vs R_{epi} fit for Stn4412.

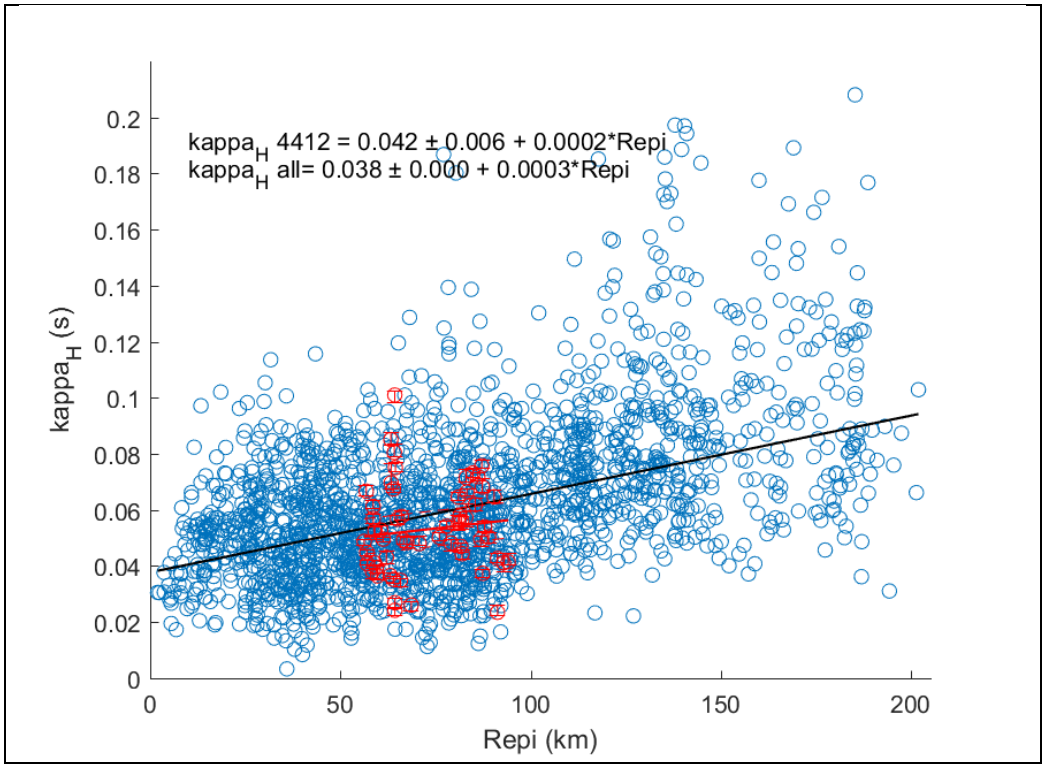


Figure 7.133: The unconstrained to overall κ_H vs R_{epi} fit for Stn4412.

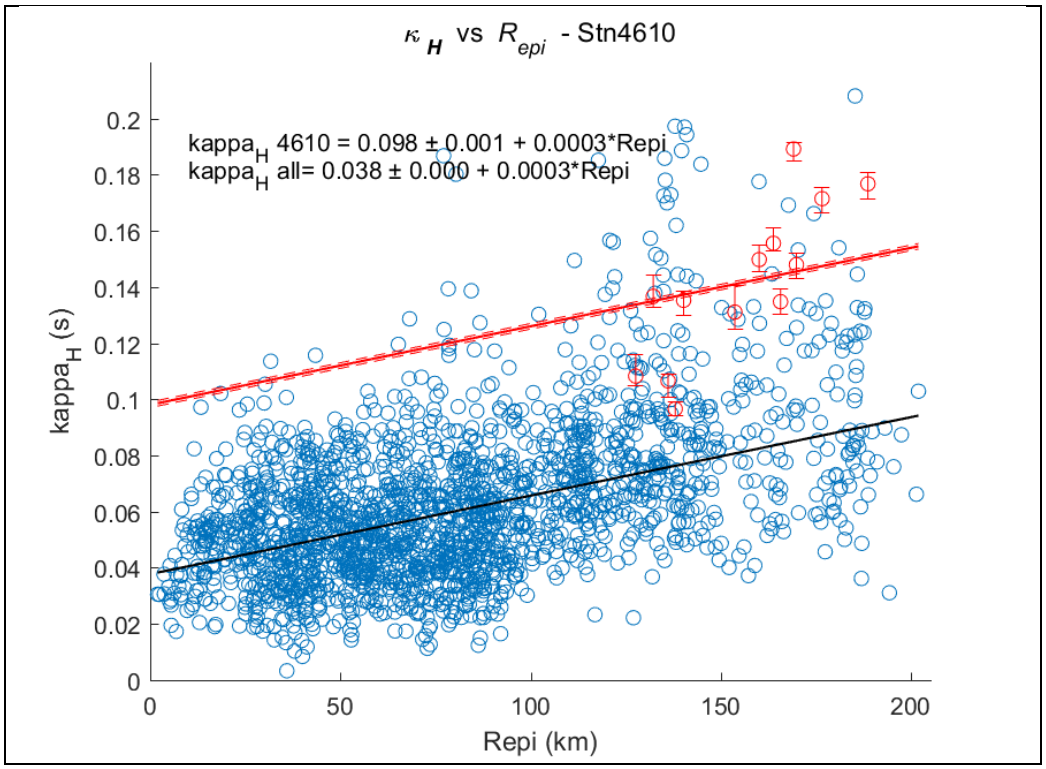


Figure 7.134: The constrained to overall κ_H vs R_{epi} fit for Stn4610.

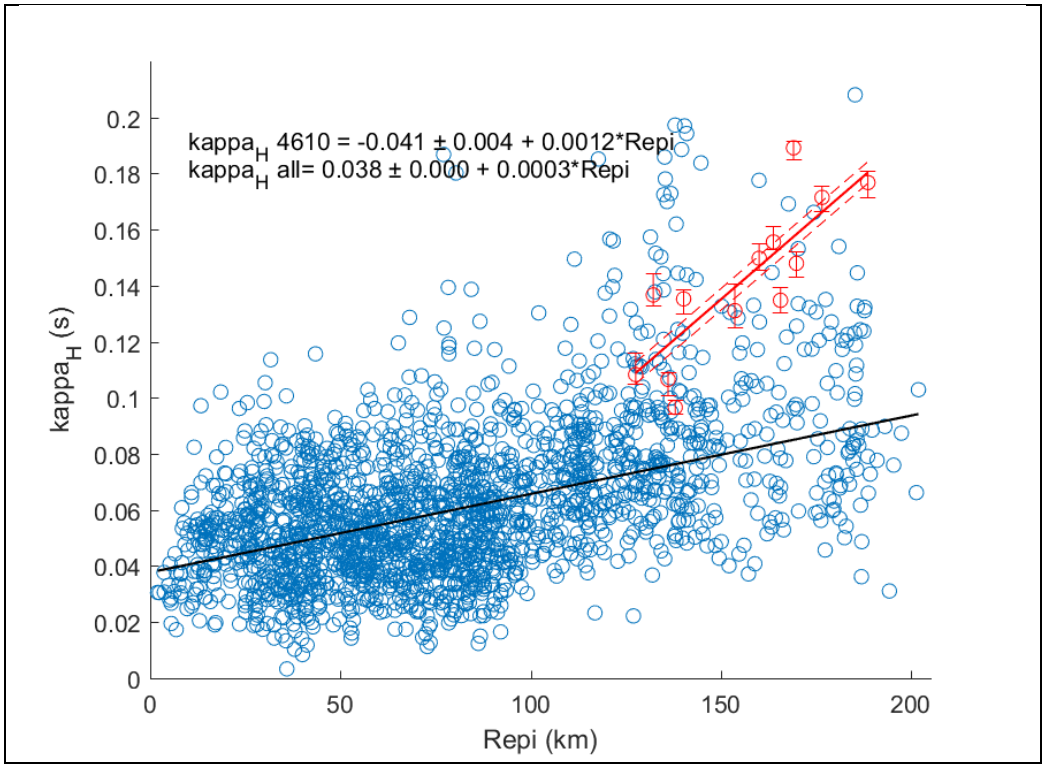


Figure 7.135: The unconstrained to overall κ_H vs R_{epi} fit for Stn4610.

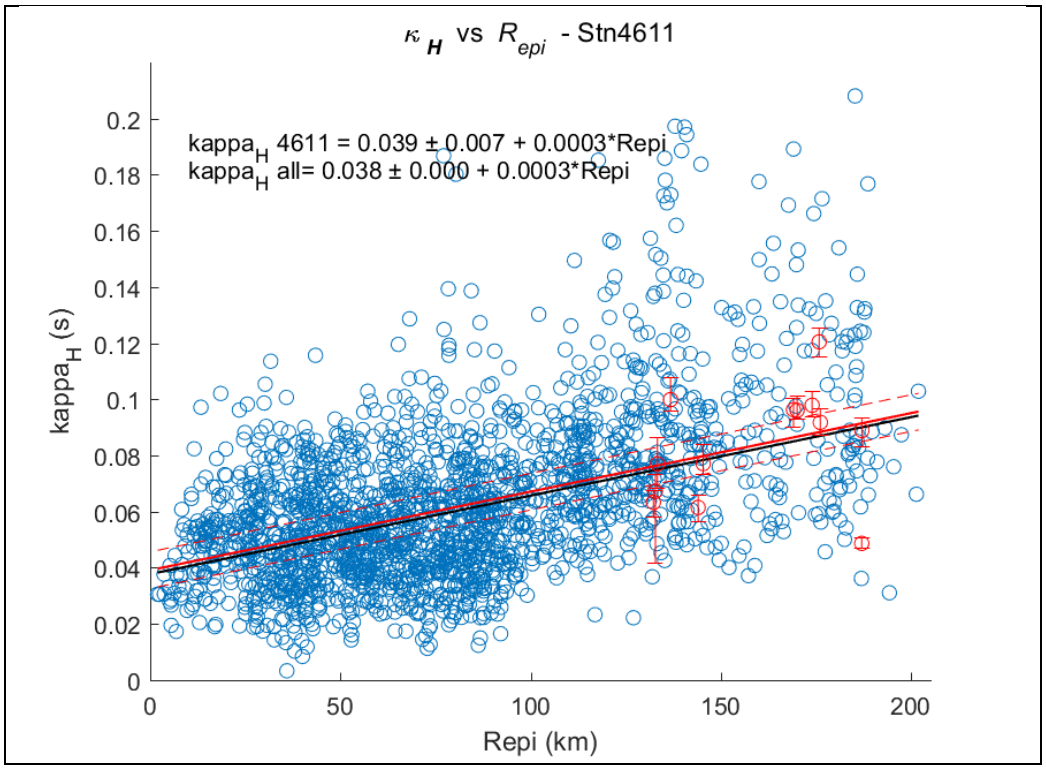


Figure 7.136: The constrained to overall κ_H vs R_{epi} fit for Stn4611.

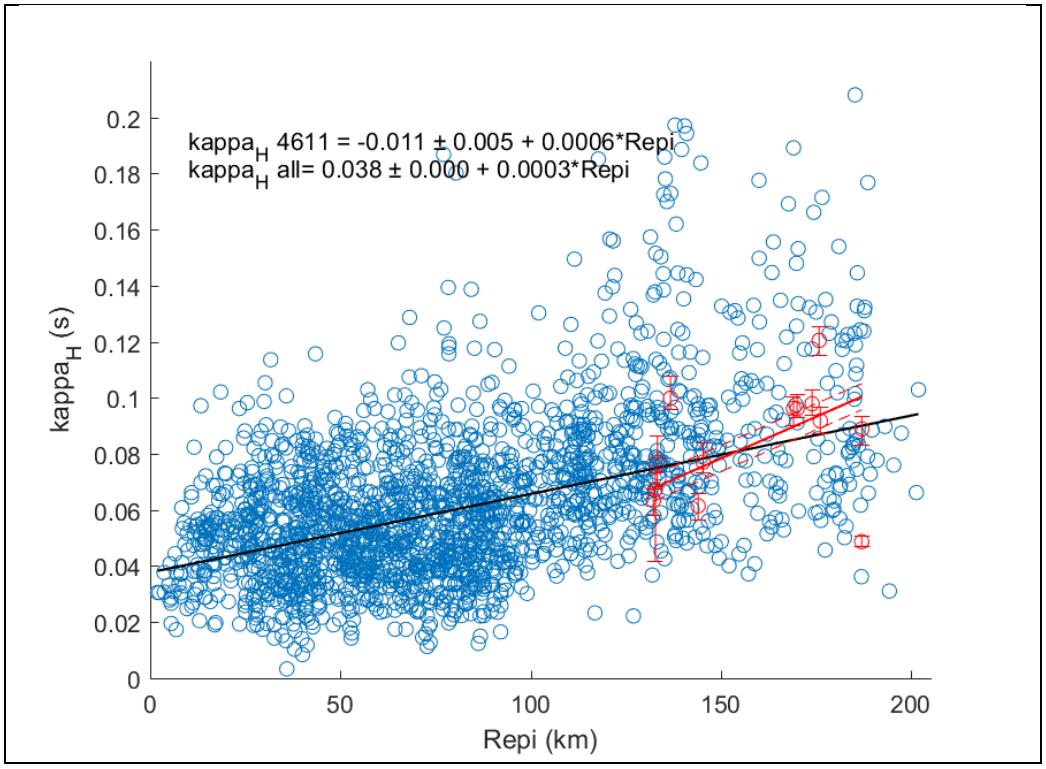


Figure 7.137: The unconstrained to overall κ_H vs R_{epi} fit for Stn4611.

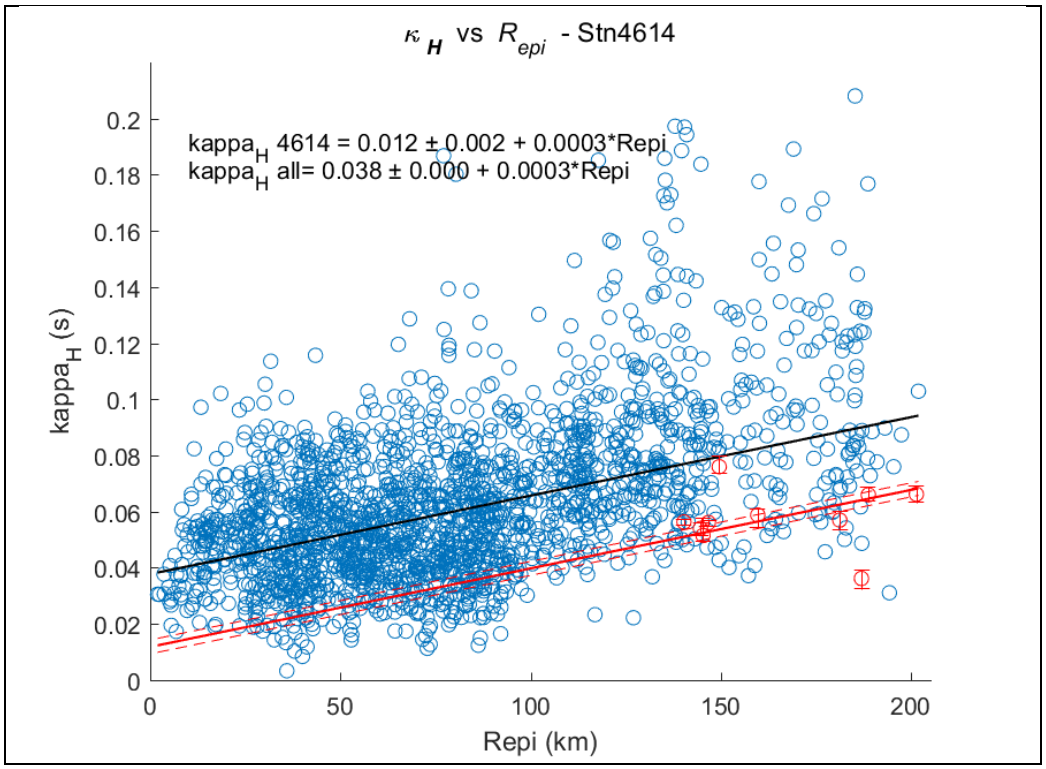


Figure 7.138: The constrained to overall κ_H vs R_{epi} fit for Stn4614.

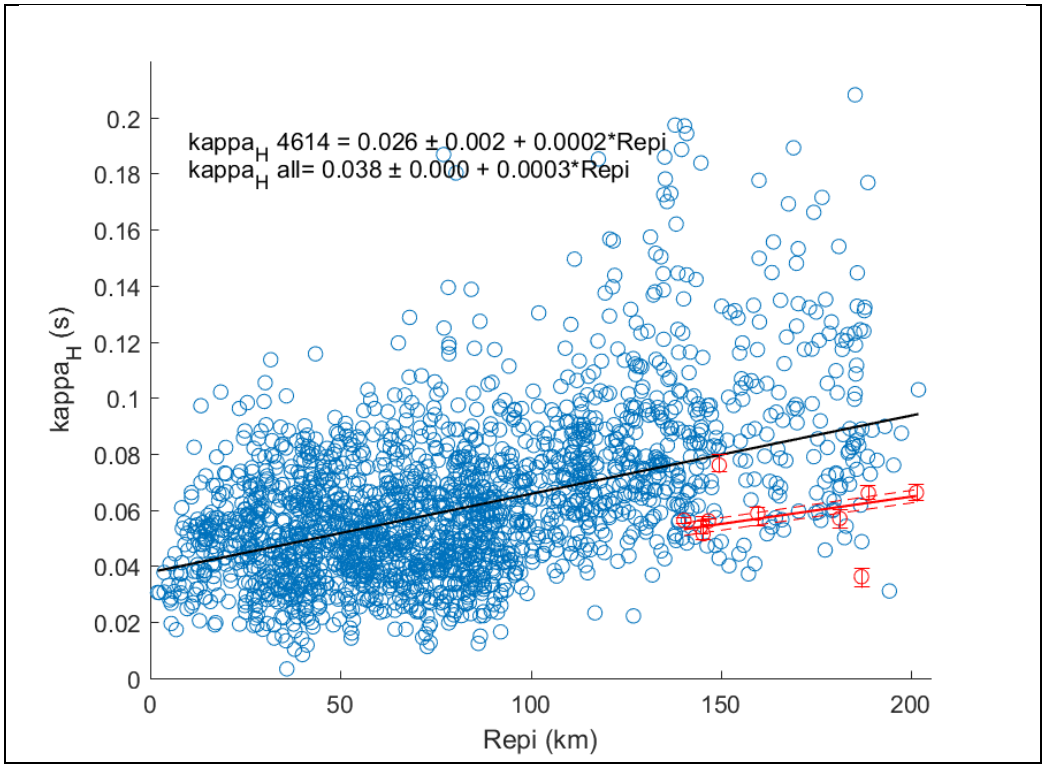


Figure 7.139: The unconstrained to overall κ_H vs R_{epi} fit for Stn4614.

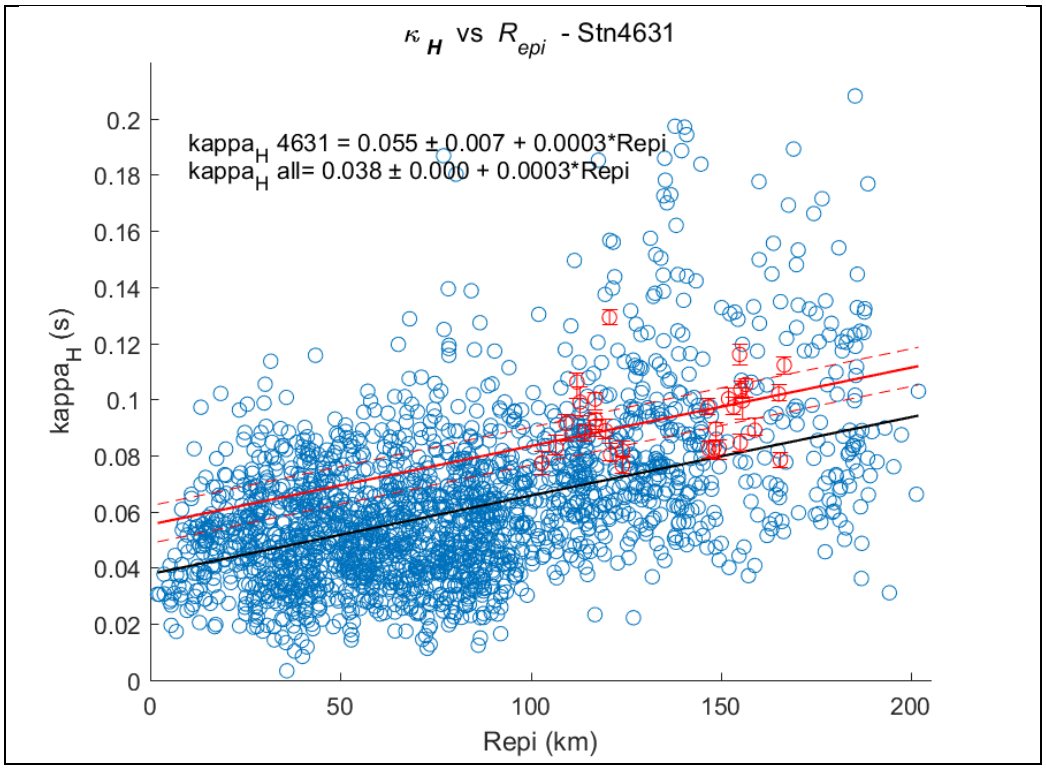


Figure 7.140: The constrained to overall κ_H vs R_{epi} fit for Stn4631.

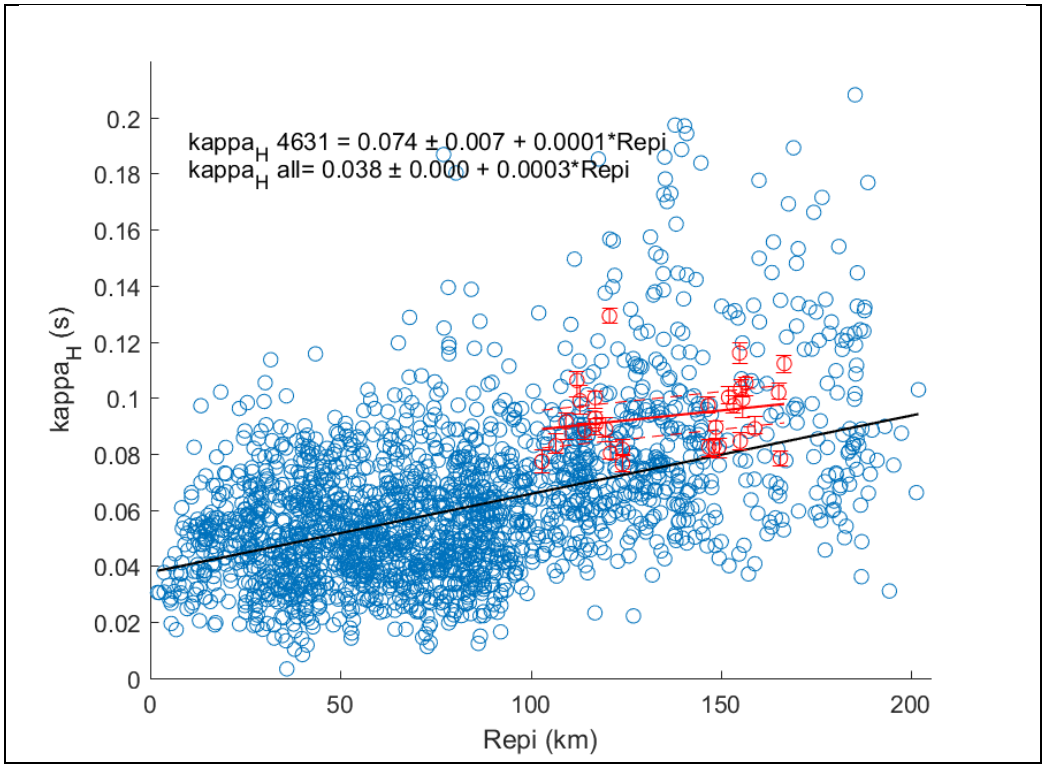


Figure 7.141: The unconstrained to overall κ_H vs R_{epi} fit for Stn4631.

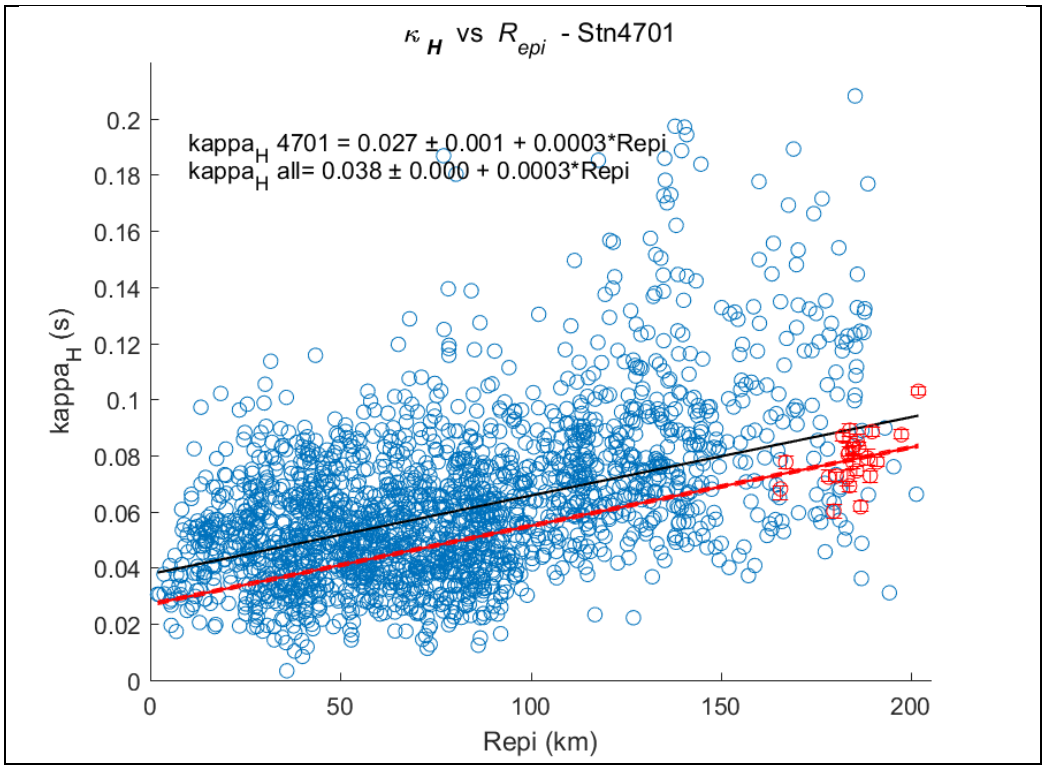


Figure 7.142: The constrained to overall κ_H vs R_{epi} fit for Stn4701.

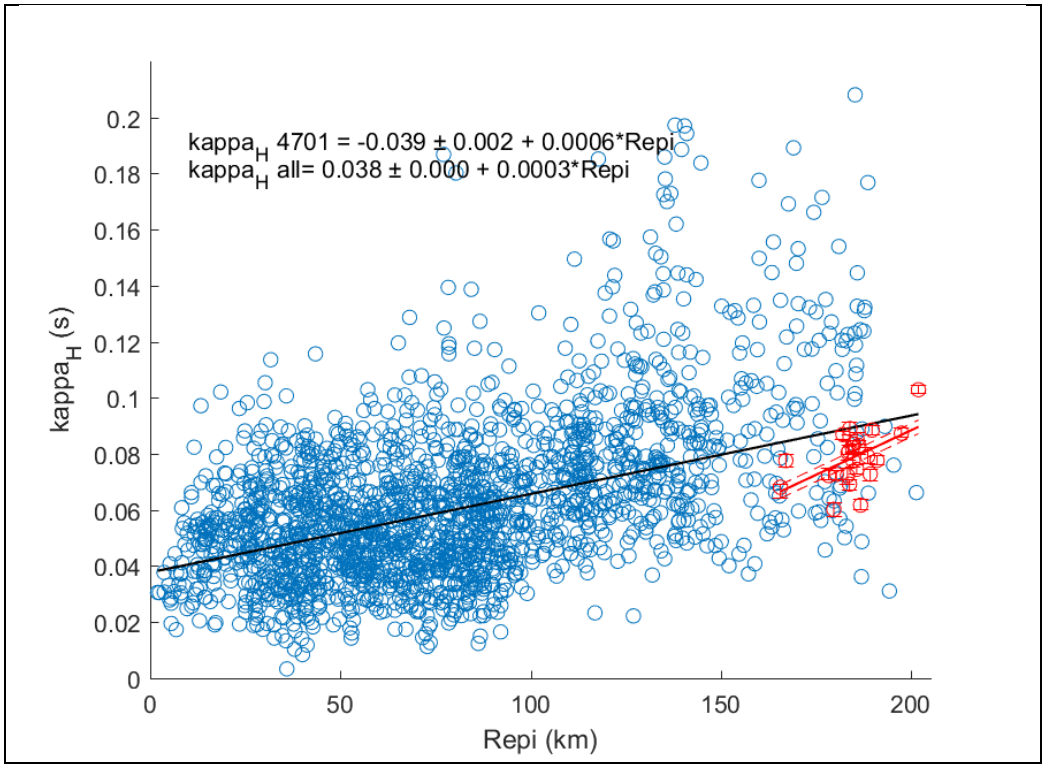


Figure 7.143: The unconstrained to overall κ_H vs R_{epi} fit for Stn4701.

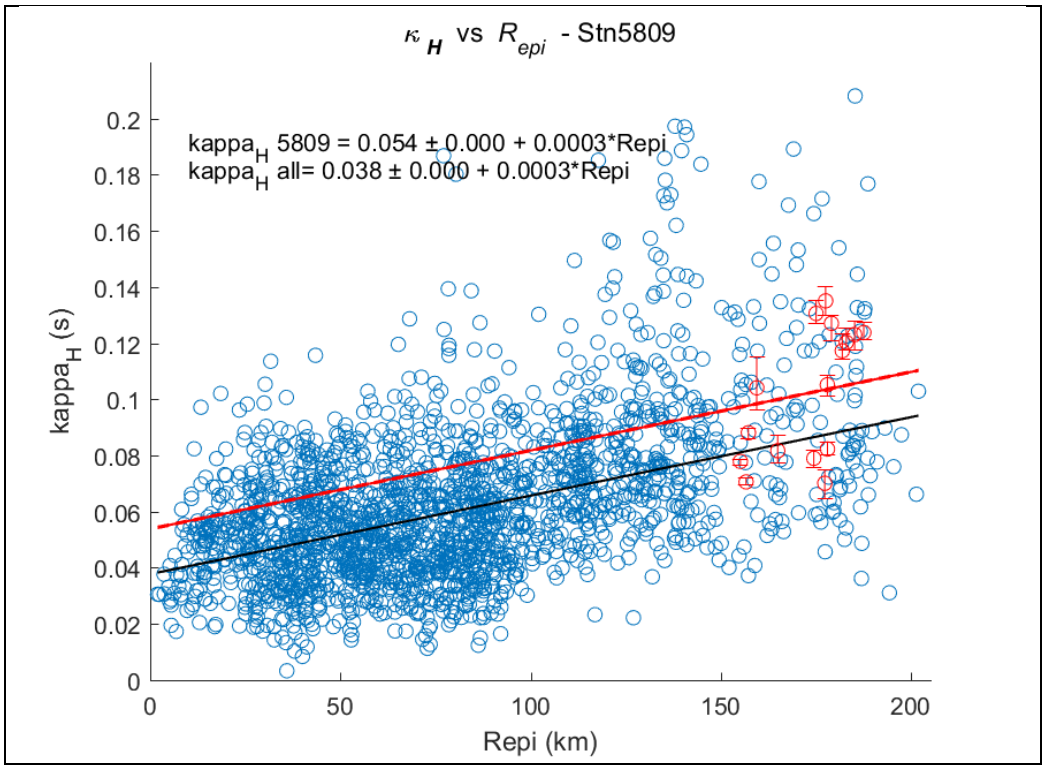


Figure 7.144: The constrained to overall κ_H vs R_{epi} fit for Stn5809.

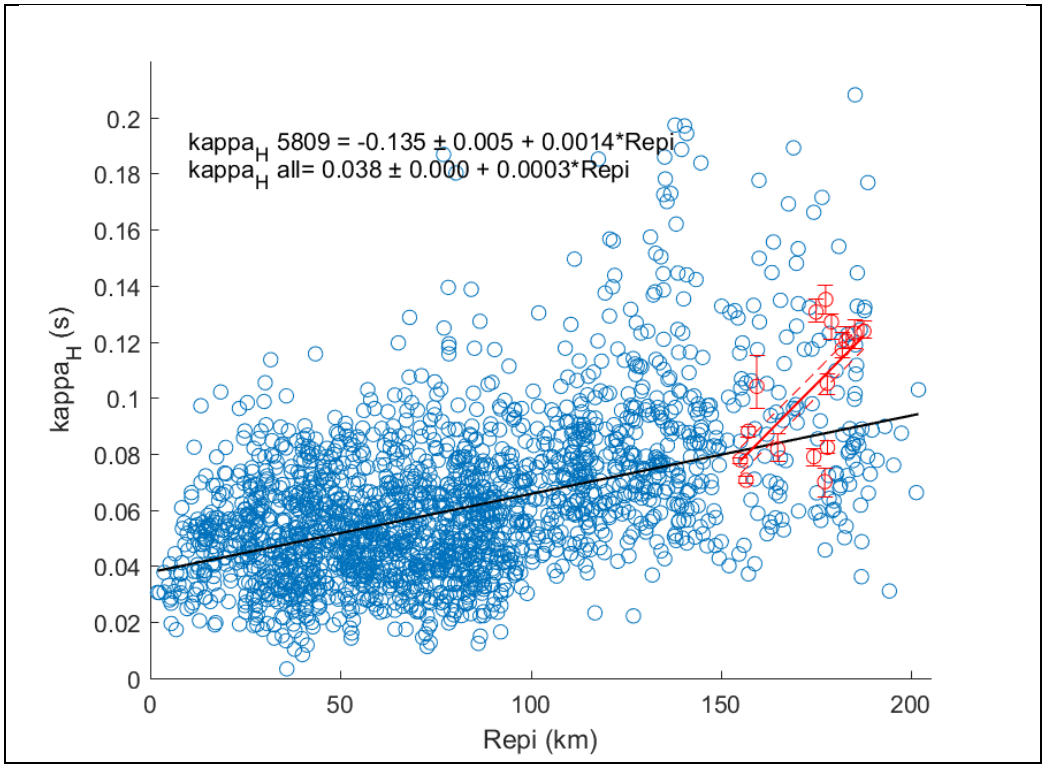


Figure 7.145: The unconstrained to overall κ_H vs R_{epi} fit for Stn5809.

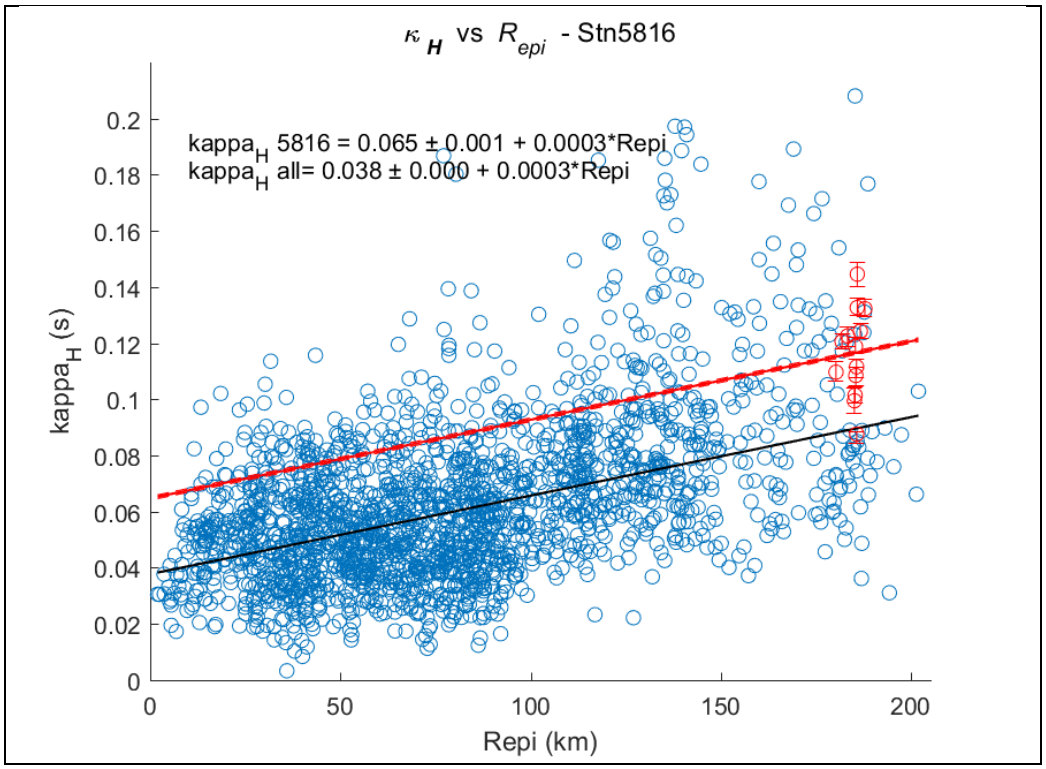


Figure 7.146: The constrained to overall κ_H vs R_{epi} fit for Stn5816.

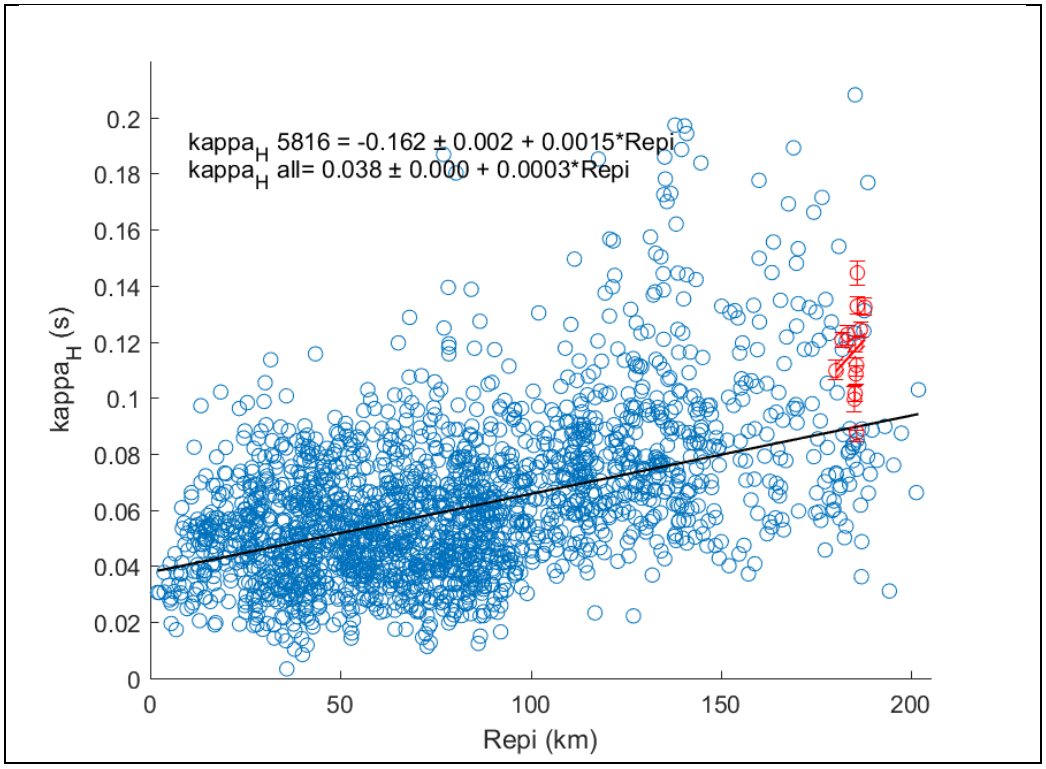


Figure 7.147: The unconstrained to overall κ_H vs R_{epi} fit for Stn5816.

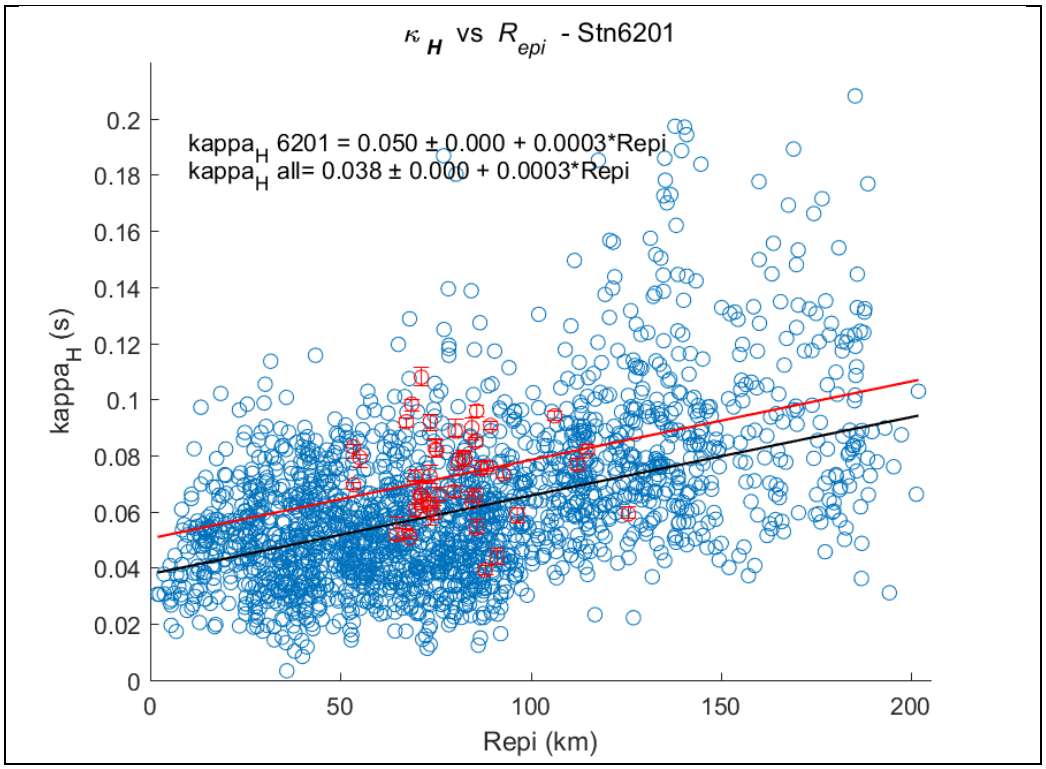


Figure 7.148: The constrained to overall κ_H vs R_{epi} fit for Stn6201.

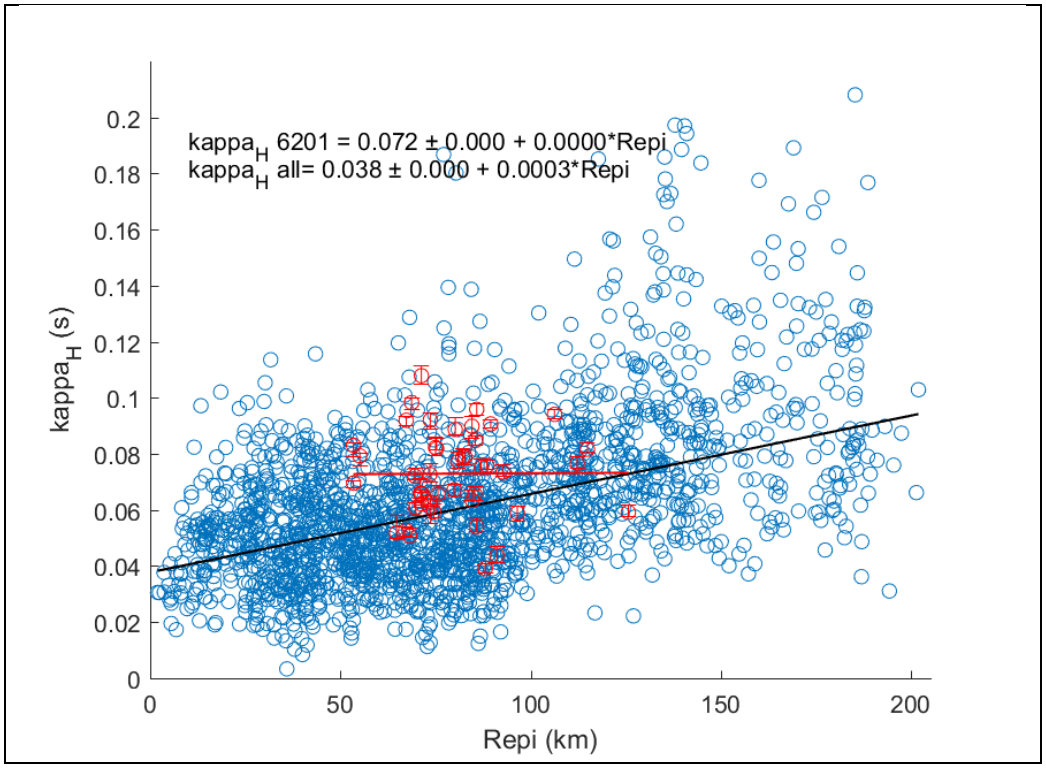


Figure 7.149: The unconstrained to overall κ_H vs R_{epi} fit for Stn6201.

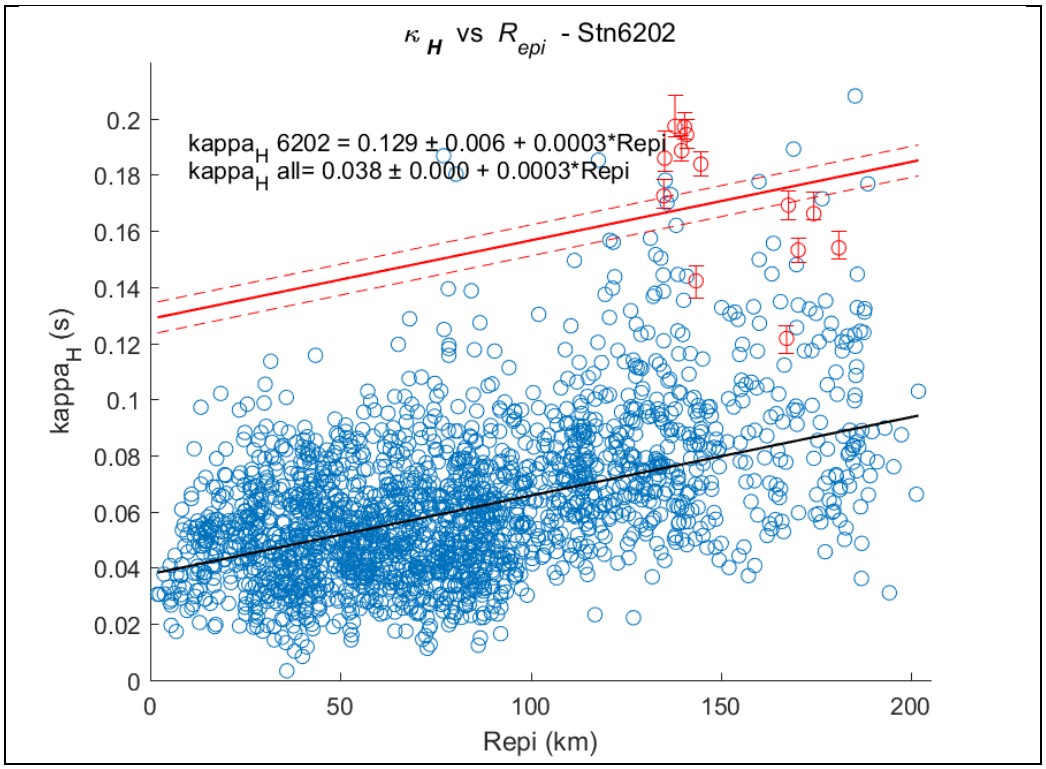


Figure 7.150: The constrained to overall κ_H vs R_{epi} fit for Stn6202.

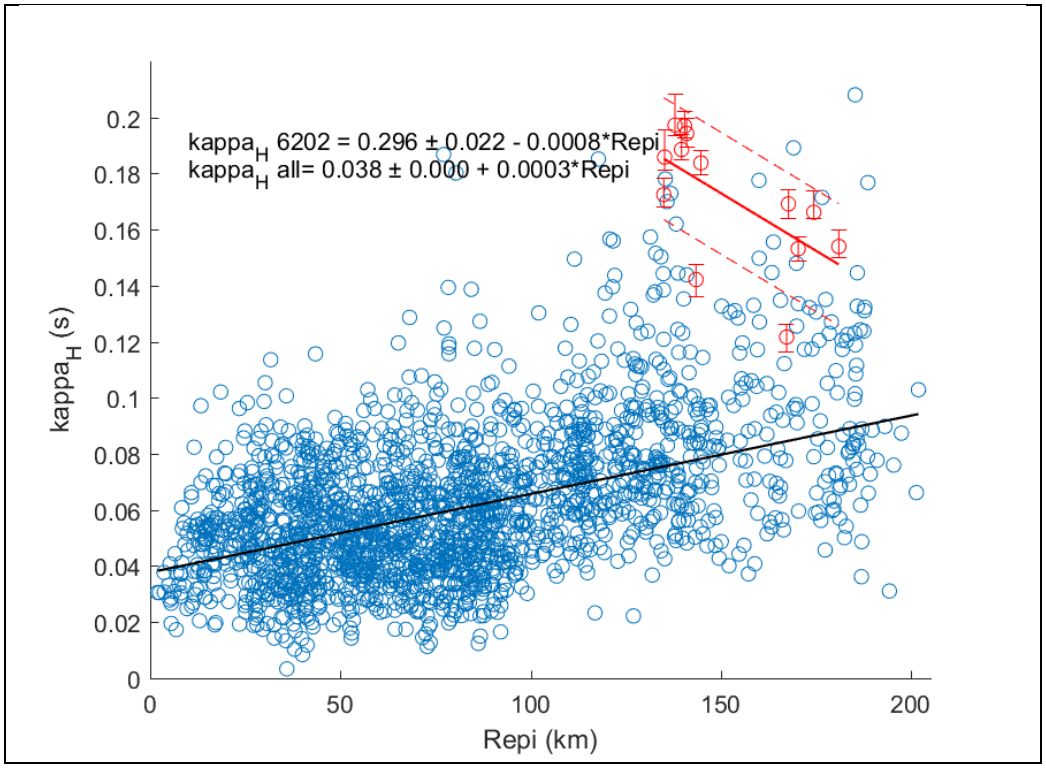


Figure 7.151: The unconstrained to overall κ_H vs R_{epi} fit for Stn6202.

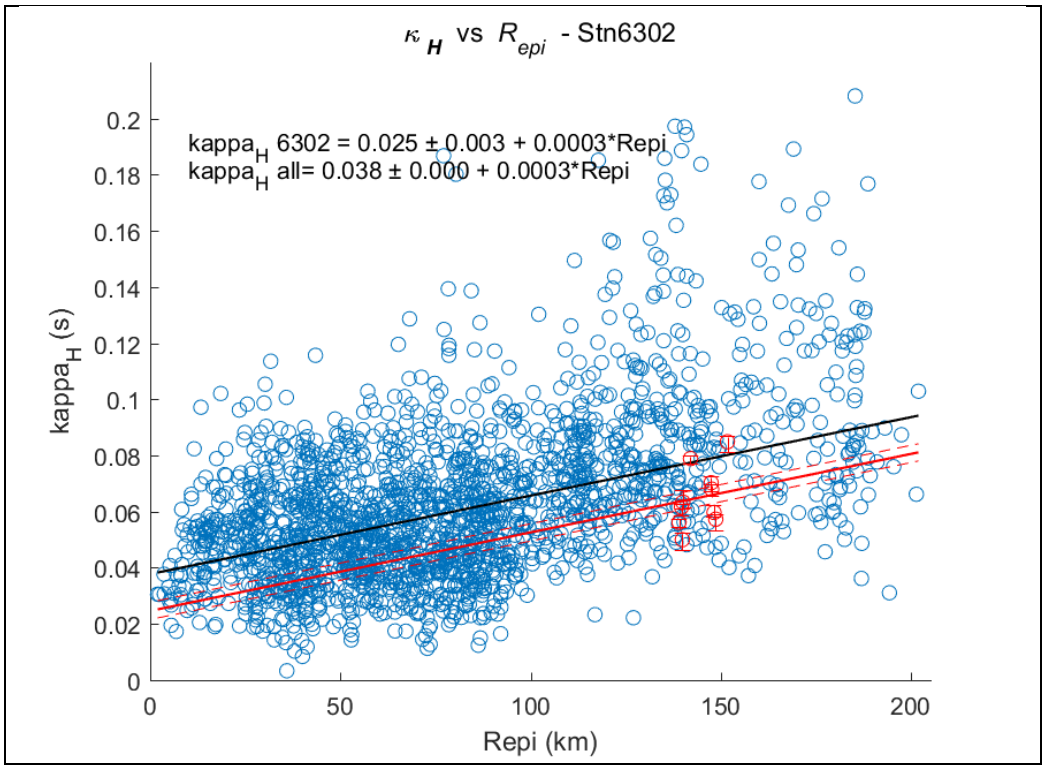


Figure 7.152: The constrained to overall κ_H vs R_{epi} fit for Stn6302.

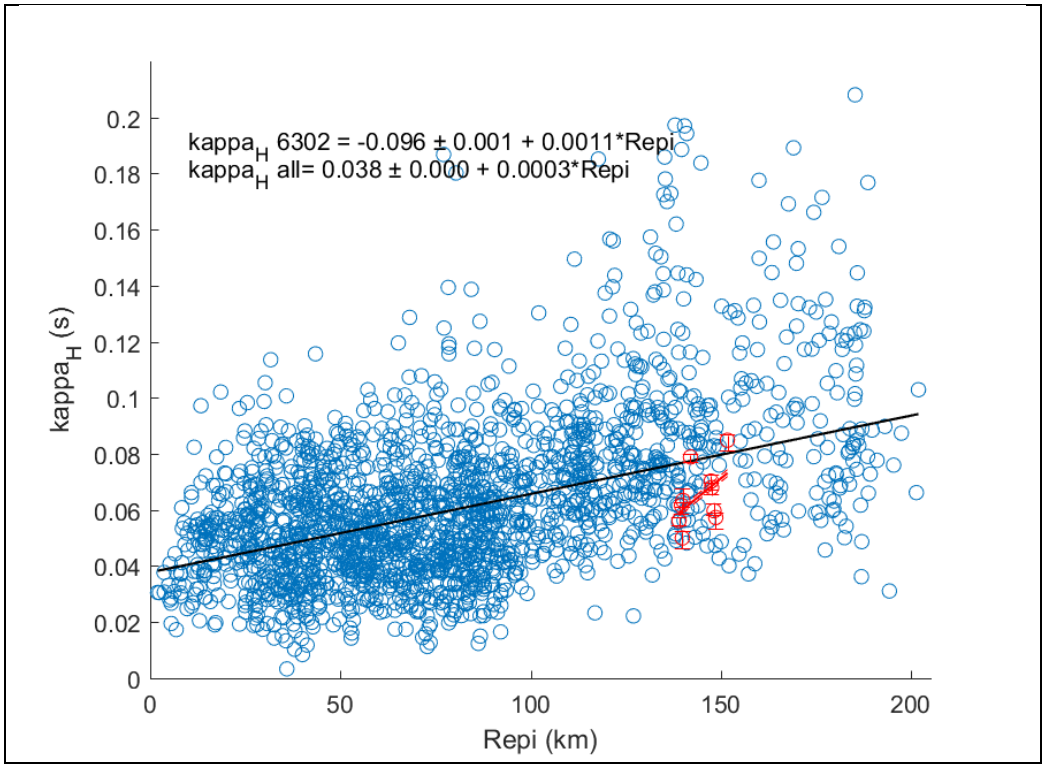


Figure 7.153: The unconstrained to overall κ_H vs R_{epi} fit for Stn6302.

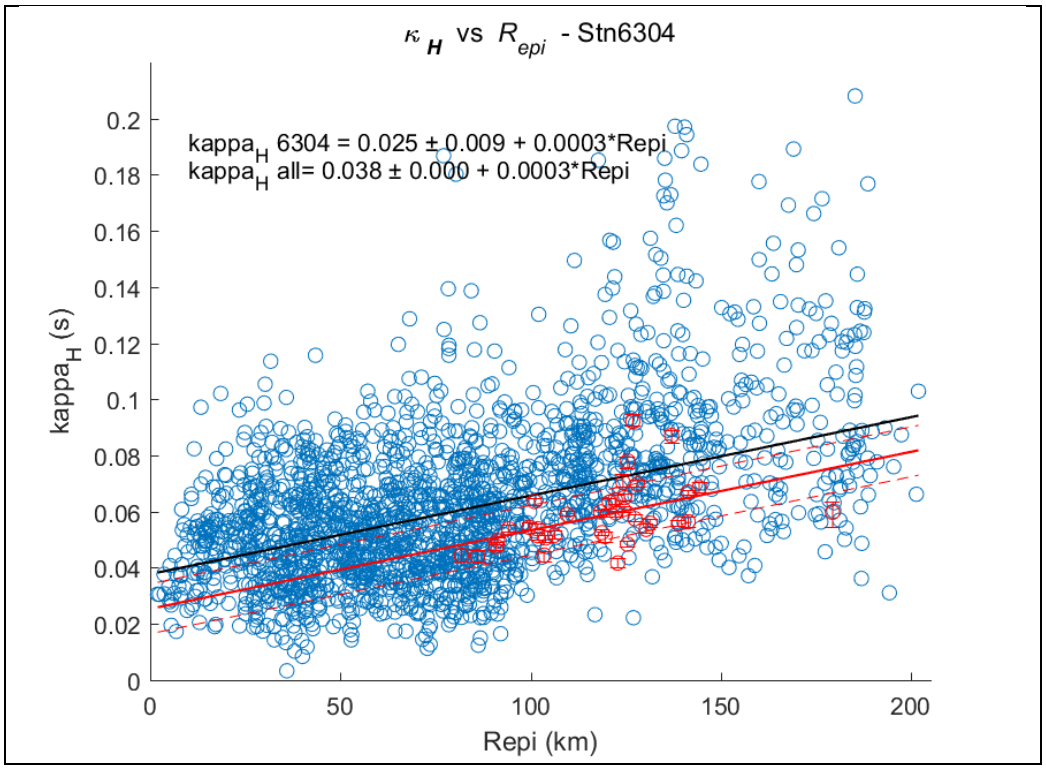


Figure 7.154: The constrained to overall κ_H vs R_{epi} fit for Stn6304.

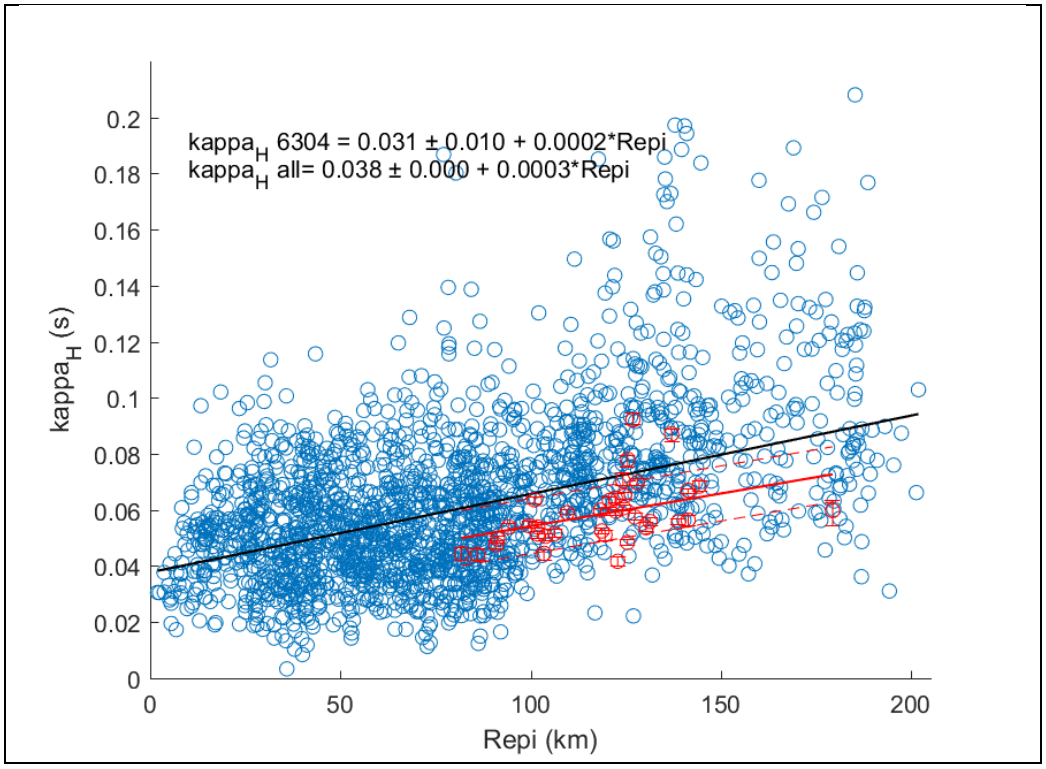


Figure 7.155: The unconstrained to overall κ_H vs R_{epi} fit for Stn6304.

The illustrated κ_0 estimations are also listed in Table 7.8. The values in parenthesis are indicating negative linear trend. Stn4605 is passive and Stn4610 is active at the same installation site.

Table 7.8: Station based κ_0 estimations with constrained and unconstrained fit. Constrained fit is favored in the current study.

Station Code	**κ_0 (s) constrained κ_H vs R_{epi} robust fit**	**κ_0 (s) unconstrained κ_H vs R_{epi} robust fit**
0201	0.031 ± 0.000	0.040 ± 0.001
0204	0.029 ± 0.003	0.037 ± 0.004
0205	0.030 ± 0.018	0.036 ± 0.020
0206	0.034 ± 0.007	-0.009 ± 0.000
0207	0.029 ± 0.005	0.029 ± 0.005
0208	0.050 ± 0.017	(0.109 ± 0.019)
0209	0.030 ± 0.009	0.054 ± 0.012
0212	0.027 ± 0.004	0.025 ± 0.004
0213	0.039 ± 0.009	0.031 ± 0.008
1201	0.107 ± 0.009	(0.152 ± 0.014)
1210	0.056 ± 0.007	0.081 ± 0.008
2101	0.029 ± 0.000	0.049 ± 0.000
2102	0.036 ± 0.002	0.030 ± 0.002
2104	0.060 ± 0.002	0.047 ± 0.001
2105	0.020 ± 0.011	0.002 ± 0.011
2106	0.023 ± 0.010	0.040 ± 0.009
2107	0.049 ± 0.002	(0.077 ± 0.008)
2301	0.038 ± 0.004	(0.052 ± 0.002)
2302	0.027 ± 0.020	0.032 ± 0.020
2304	0.048 ± 0.005	0.048 ± 0.005
2305	0.049 ± 0.002	0.061 ± 0.002
2306	0.059 ± 0.009	0.005 ± 0.002
2307	0.072 ± 0.028	0.036 ± 0.026

Table 7.8: Continuation. Station based κ_0 estimations with constrained and unconstrained fit. Constrained fit is favored in the current.

Station Code	**κ_0 (s) constrained κ_H vs R_{epi} robust fit**	**κ_0 (s) unconstrained κ_H vs R_{epi} robust fit**
2308	0.042 ± 0.000	0.034 ± 0.005
2309	0.033 ± 0.002	(0.053 ± 0.001)
2401	0.076 ± 0.011	(0.193 ± 0.002)
2404	0.056 ± 0.001	0.007 ± 0.001
2408	0.118 ± 0.003	(0.254 ± 0.001)
2409	0.046 ± 0.006	0.013 ± 0.004
2412	0.051 ± 0.000	0.080 ± 0.001
2414	0.085 ± 0.031	0.048 ± 0.029
2415	0.062 ± 0.001	(0.175 ± 0.002)
2710	0.013 ± 0.001	(0.058 ± 0.002)
2711	0.011 ± 0.005	-0.011 ± 0.007
4401	0.025 ± 0.012	0.033 ± 0.012
4404	0.060 ± 0.010	0.049 ± 0.018
4405	0.028 ± 0.003	-0.024 ± 0.003
4407	0.017 ± 0.000	-0.016 ± 0.001
4408	0.027 ± 0.003	-0.010 ± 0.005
4409	0.045 ± 0.000	0.011 ± 0.004
4410	0.035 ± 0.005	0.016 ± 0.006
4411	0.027 ± 0.016	-0.055 ± 0.014
4412	0.033 ± 0.007	0.042 ± 0.006
4605/4610	0.098 ± 0.001	-0.041 ± 0.004
4611	0.039 ± 0.007	-0.011 ± 0.005
4614	0.012 ± 0.002	0.026 ± 0.002
4631	0.055 ± 0.007	0.074 ± 0.007
4701	0.027 ± 0.001	-0.039 ± 0.002

Table 7.8: Continuation. Station based κ_0 estimations with constrained and unconstrained fit. Constrained fit is favored in the current.

Station Code	**κ_0 (s) constrained κ_H vs R_{epi} robust fit**	**κ_0 (s) unconstrained κ_H vs R_{epi} robust fit**
5809	0.054 ± 0.000	-0.135 ± 0.005
5816	0.065 ± 0.001	-0.162 ± 0.002
6201	0.050 ± 0.000	0.072 ± 0.000
6202	0.129 ± 0.006	(0.296 ± 0.022)
6302	0.025 ± 0.003	-0.096 ± 0.001
6304	0.025 ± 0.009	0.031 ± 0.010

Station 4404 at Pütürge, Malatya has V_{s30} = 1380 km/s and was evaluated for the hard rock cases also with the former AFAD database and is given under section "7.2. Hard Rock AFAD Stations in Turkey" of this PhD thesis. The database used to evaluate κ_0 when referred to that section could be seen that it includes all different source events from former AFAD dataset. Two different cases were evaluated for Stn4404 (Table 7.3), and the resulting κ_0 estimates can be summarized as the following:

- Case 1: κ_0 = 0.049 s with $3.5 \leq M_L \leq 5.5$ event recordings within 100 km from unconstrained κ_H vs R_{epi} fit.
- Case 2: κ_0 = 0.024 s with $3.5 \leq M_L \leq 4.2$ event recordings within 30 km from unconstrained κ_H vs R_{epi} fit.

However, under this section of the thesis herein, many inconsistencies are excluded in the methodology as explained throughout this PhD thesis and the findings are more likely to reflect better κ_0 estimates for near field stations, especially with the new, rich AFAD database. For far field stations, this cannot be said as it is clearly observed with both KOERI and AFAD database that the higher the magnitude of the event, the higher the κ_H values are, not only due to path attenuation but also the observed magnitude dependencies shown in Figure 7.47 and Figure 7.48 for AFAD and in Figure 7.14 and Figure 7.15 for KOERI stations. When only a single fault source

is taken into account, the far field stations no longer can capture low magnitude events from the selected seismic source (single fault source) and the dataset for these stations are no longer in full content in magnitude bins.

Stn4404, being a near filed station, has luckily recorded also high magnitude events and two above cases could be applied with new AFAD database with suggested methodology herein proposed. For Case 2 even a maximum R_{epi} could be set to 26 km with maximum event M_w = 6.8. The magnitude dependency is also checked only for this station for up to R_{epi} 100km and 26 km and is given in Figure 7.156 and Figure 7.157 respectively. In these figures orange trend represents $4.0 > M_w \geq 3.5$, green trend represents $4.5 > M_w \geq 4.0$, red trend represents $5.0 > M_w \geq 4.5$, blue trend represents $M_w \geq 5.0$, and black dashed line represents the overall fit.

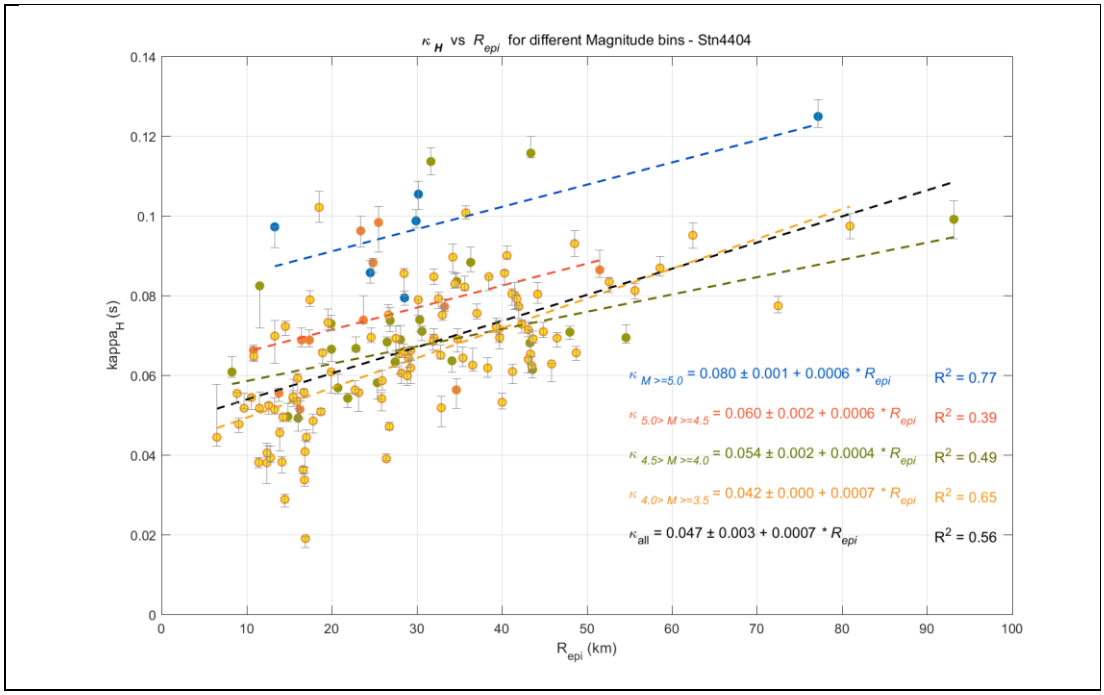


Figure 7.156: The horizontal event kappa, κ_H vs R_{epi} up to 100 km at different magnitude bins via robust multiple linear regression model for Stn4404 with V_{s30} = 1380 km/s.

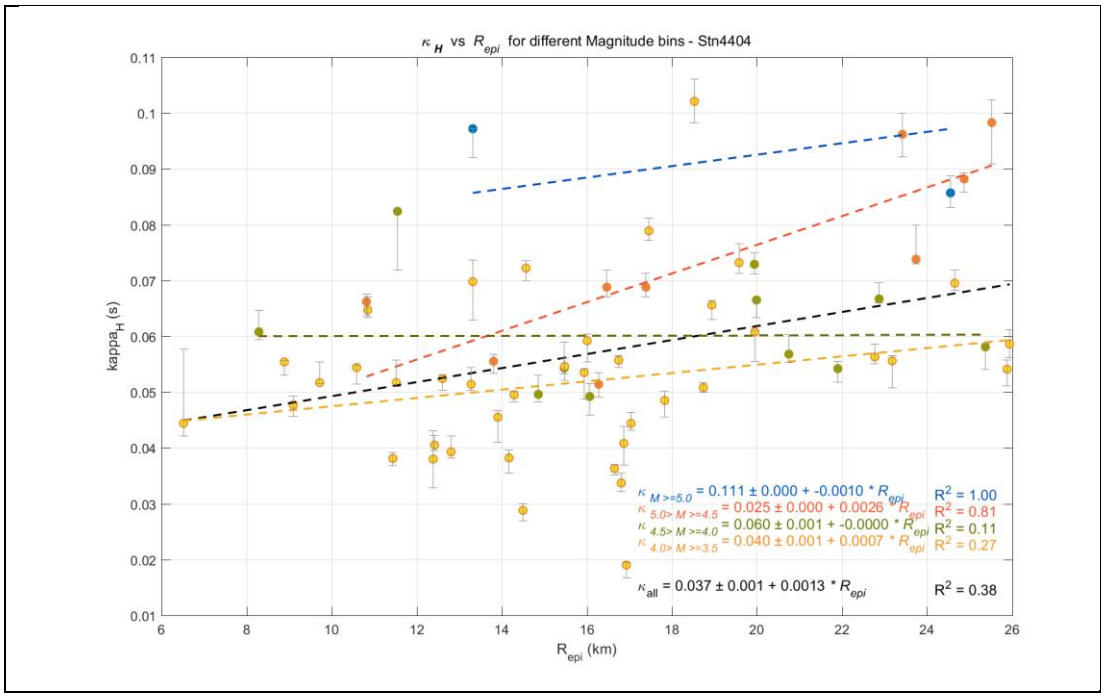


Figure 7.157: The horizontal event kappa, κ_H vs R_{epi} up to 26 km at different magnitude bins via robust multiple linear regression model for Stn4404 with V_{s30} = 1380 km/s.

Even though in Figure 7.157, the linear trends for different magnitude bins tend to represent different slopes, the findings show that the stronger the earthquake is, the higher the κ_H values are, where the influence of path attenuation should be minimum, even almost negligible for up to epicentral distance, R_{epi} of 26 km.

The κ_0 estimates can be summarized as following for Stn4404 with new AFAD database:

- Case 1: κ_0 = 0.047 ± 0.003 s with $3.5 \leq M_w \leq 6.8$ event recordings within 100 km from unconstrained κ_H vs R_{epi} fit.
- Case 2: κ_0 = 0.037 ± 0.001 s with $3.5 \leq M_w \leq 6.8$ event recordings within 26 km from unconstrained κ_H vs R_{epi} fit.
- Case 3: κ_0 = 0.060 ± 0.010 s with $3.5 \leq M_w \leq 6.8$ event recordings within 200 km from constrained κ_H vs R_{epi} fit (Table 7.8).

When compared with the previous findings, especially for Case 2 option, it is clearly seen that with low magnitude datasets, the results may give highly low κ_0

values, although in reality this could result with significantly higher κ_0 estimates when the station has records from near field with M_w > 5.0.

Stn4404, with V_{s30} = 1380 km/s also indicates that hard rock stations do not tend to give lower κ_0 values than the softer sites, meaning there is no soil type dependency as discussed under section "3.2. Soil Type Dependency and HVSR". In fact, the reason why for some regions the κ_0 values are lower could be the result of small magnitude datasets as well as the wide spread of the event data geospatially. Due to lack of data, and assuming there is no magnitude dependency could result with very low κ_0 estimates that does no longer represent the reality.

To make this point clearer, κ_0 versus V_{s30} is plotted where V_{s30} data is available in Figure 7.158 and Figure 7.159 from the new AFAD database for only Sivrice-Pütürge segment of EAF.

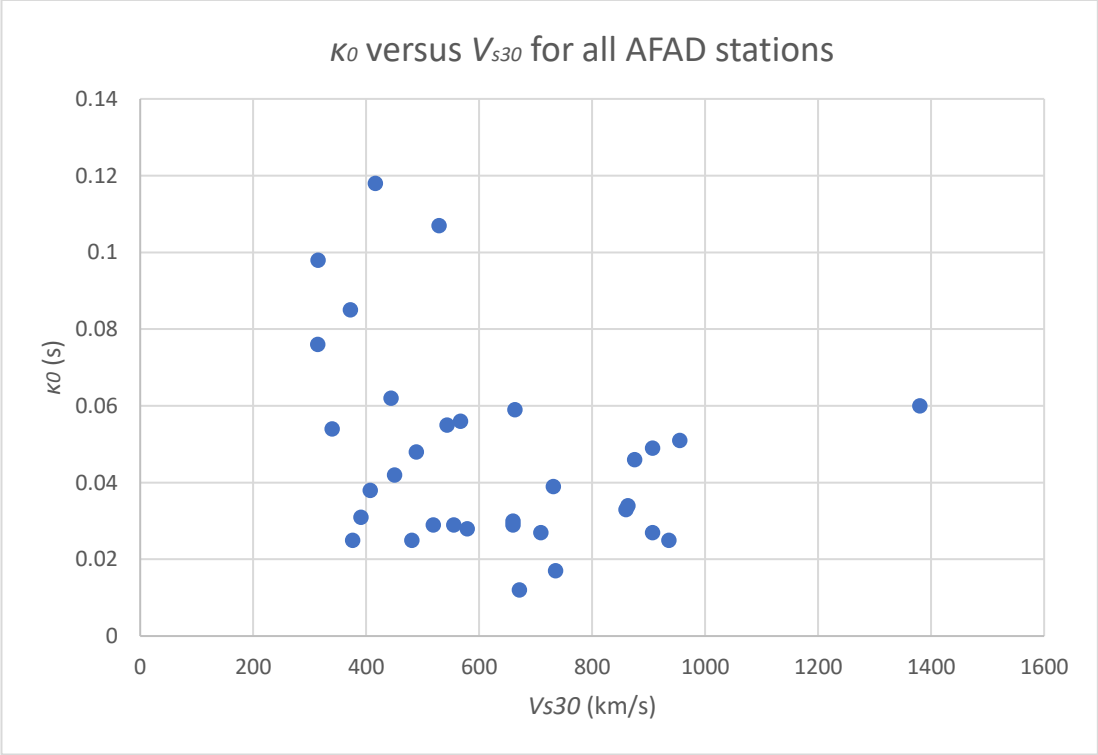


Figure 7.158. κ_0 versus V_{s30} from all AFAD stations that recorded events from Sivrice-Pütürge segment of EAF.

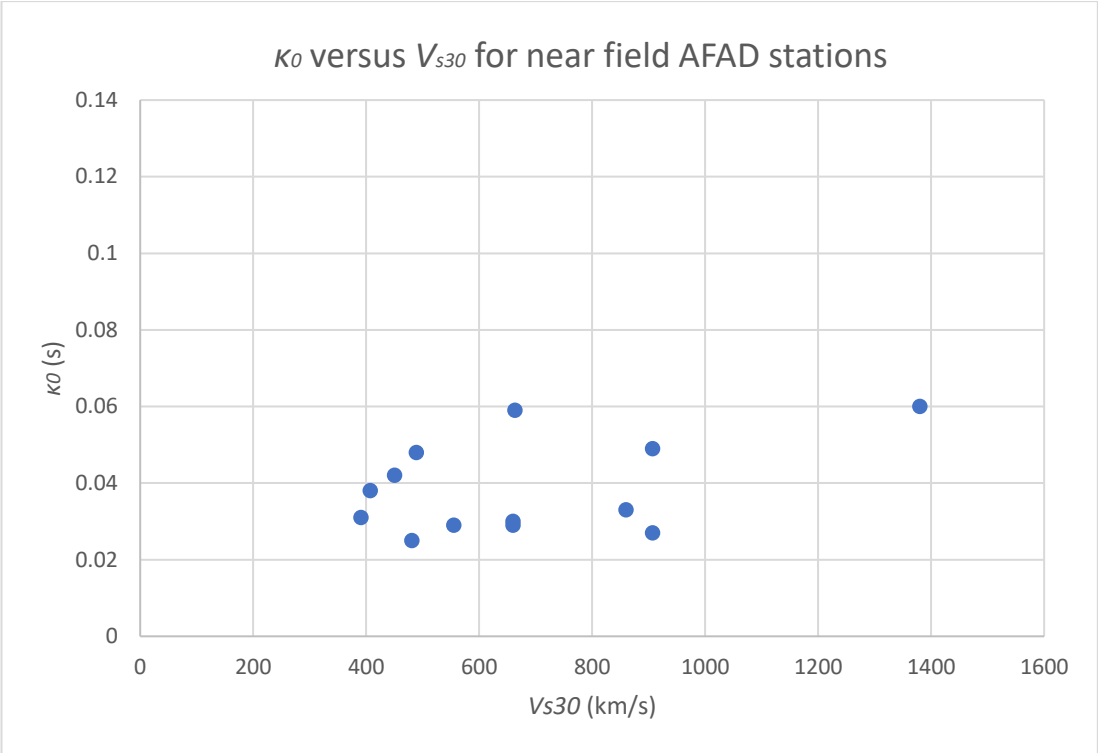


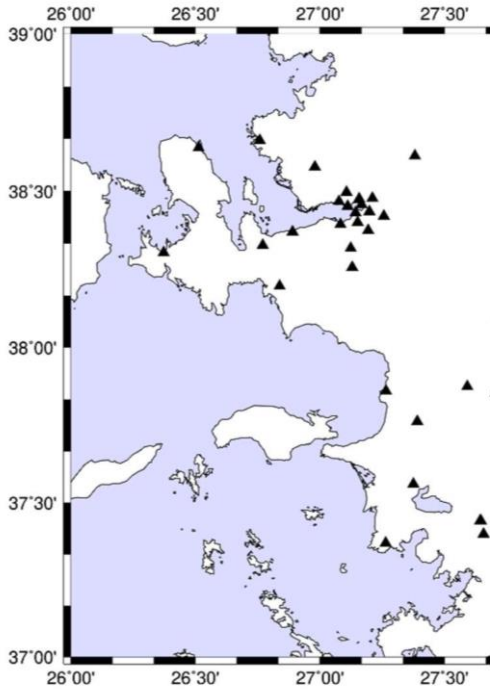
Figure 7.159. κ_0 versus V_{s30} from near field AFAD stations that recorded events from Sivrice-Pütürge segment of EAF.

It is clearly seen in Figure 7.158 that the scatter for V_{s30} < 600 km/s is higher than the rest of the resulting κ_0 estimates. When the far filed stations are eliminated from the dataset, then κ_0 estimate range shows no correlation between κ_0 and V_{s30} as seen in Figure 7.159.

7.4. Izmir Region

On October 30, 2020 a moment magnitude, M_w of 6.9 (KOERI) or 6.6 (AFAD) earthquake occurred in Aegean Sea, at the north of Samos Island and offshore Doğanbey - Izmir [GTU Report, 2020]. The Samos (İzmir-Seferihisar offshore) earthquake is noteworthy due to several different aspects, especially for the casualties (115 people) and significant structural damage observed in İzmir, Bayraklı that is located approximately 70 km away for the epicenter and the tsunami hitting the coastal area between Akarca and Sığacık towns of İzmir [METU Report, 2020].

The mainshock earthquake was recorded by 33 AFAD strong ground motion stations within 100 km distance from the epicenter (Figure 7.160). The records show variability in terms of azimuth, source-to-site distances and site classes.



METU Report, 2020

30 Ekim 2020 EGE DENİZİ, SEFERİHİSAR (İZMİR) AÇIKLARI DEPREMİNDE ÖLÇÜLEN BAZI İVME DEĞERLERİ (AFAD)

No	İstasyon Yeri	İstasyon Kodu	Mesafe (Km)	Ölçülen En Büyük İvme (PGA) Değerleri (gal=cm/sn^2)
1	Seferihisar	3536	34.75	**79.14**
2	Aydın-Kuşadası	0905	42.95	**180.79**
3	İzmir-Urla	3523	48.94	**80.32**
4	İzmir-Menderes	3533	51.38	**73.64**
5	İzmir-Güzelbahçe	3516	54.57	**48.36**
6	Aydın-Söke	0911	55.71	**66.66**
7	İzmir-Gaziemir	3538	56.67	**85.48**
8	İzmir-Çeşme	3528	58.23	**149.31**
11	İzmir-Buca-2	3512	65.76	**57.54**
12	İzmir-Konak	3518	68.36	**106.1**
13	İzmir-Karşıyaka	3519	69.23	**150.09**
14	İzmir-Karşıyaka-2	3521	69.58	**110.84**
15	İzmir-Bornova	3522	71.18	**73.72**
16	Aydın-Germencik	0921	71.56	70.85
17	Aydın-Didim	0918	71.86	38.19
18	İzmir-Bayraklı	3513	72.01	**106.28**
19	İzmir-Pınarbaşı	3511	72.61	41.29
20	İzmir-Bayraklı-2	3514	73.39	56.02
21	İzmir-Karşıyaka-3	3524	73.59	68.34
22	İzmir-Bornova-2	3520	75.78	58.55
23	İzmir-Menemen	3526	78.75	88.77
24	Aydın-İncirliova	0922	81.83	60.05
25	İzmir-Tire	3539	86.09	37.63
26	İzmir-Foça	3534	86.11	92.48
27	İzmir-Karaburun	3527	86.63	80.93
28	Muğla-Milas	4823	91.03	25.77
29	Muğla-Milas_2	4822	91.18	80.06
30	Muğla-Milas_3	4814	94.63	25.33
31	Manisa-Merkez	4501	96.31	40.01
32	Muğla-Milas_4	4817	102.44	16.45
33	Muğla-Bodrum	4809	111.64	9.31

GTU Report, 2020

Figure 7.160: Locations of the strong ground motion AFAD stations within 100 km epicentral distance.

Within 200 km, the mainshock was recorded with 72 AFAD stations. Their distribution and individual κ values for each directional component of the ground motion are given in Appendix B.

Stations 3513 and 3514 are both in Bayraklı region close to the structural failures and are located on soil (V_{s30} = 196 m/s) and rock (V_{s30} = 836 m/s) sites with site classes of D and B, respectively. At the station 3513, despite a low PGA level of 0.11 g, a clear long-period amplification is observed up to 1.5 s (Figure 7.161, [modified from GTU Report, 2020]).

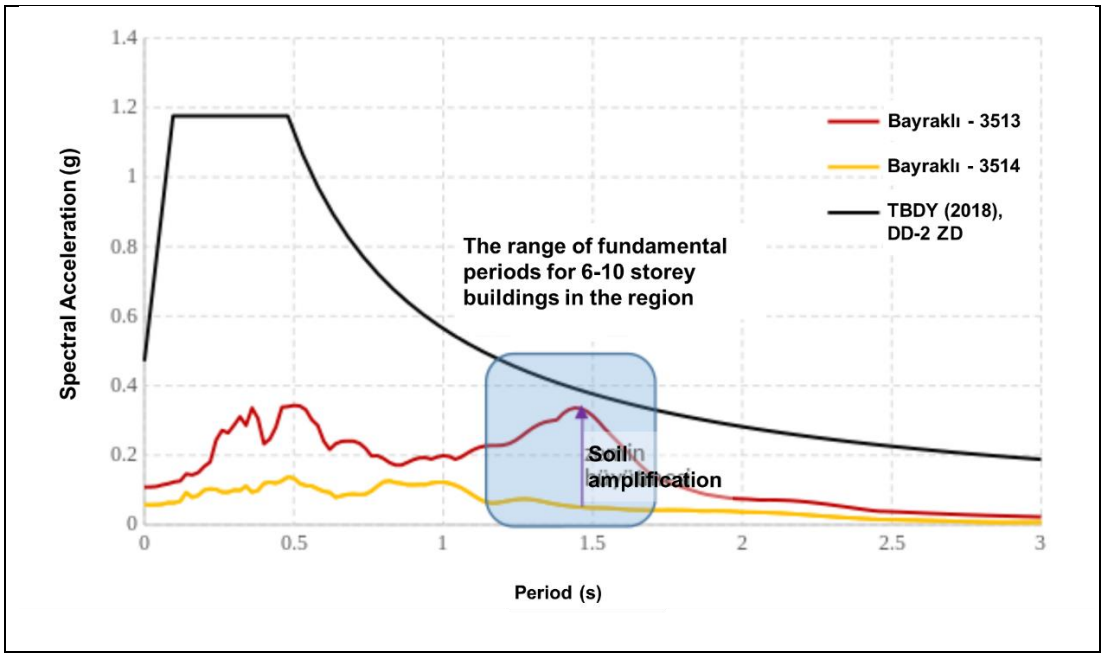


Figure 7.161: Pseudo Spectral Acceleration graphs for Bayrakli soil (Station 3513 with V_{s30} = 196 m/s) and rock (Station 3514 with V_{s30} = 836 m/s) stations with respect to 2018 Turkish Seismic Code Design Spectrum.

In METU Report [2020] it is noted that at the rock station in Bayraklı region, station 3514, no similar amplifications were observed. Overall, longer significant durations were computed at softer sites. The authors have made a PGA value comparison of the recorded data within 100 km epicentral distance against the ground motion prediction equation (GMPE) by Akkar et. al. [2014]. They observed that some PGA values recorded at the soil sites and soft soil sites are above the corresponding median amplitudes predicted with the GMPE for M_w = 6.6. They pointed out that the use of a larger M_w value as suggested by KOERI or USGS could yield closer values to the observed data peaks.

In this section of the PhD thesis, for Station 3514, the pseudo spectral acceleration of the mainshock was checked with NGA West-2 ground motion models of ASK14 [Abrahamson et. al., 2014], BSSA14 [Boore et. al., 2014], CB14 [Campbell and Bozorgnia, 2014], and CY14 [Chiou and Youngs, 2014]. Each of these 2014 GMMs are weighted with 0.25 in a logic tree, meaning they are calculated separately for the event and the weighted average of the natural logarithm of the spectral values are taken. The comparison of the mainshock and the mentioned weighted average GMM model for both M_w = 6.6 and M_w = 6.9 with their standard deviation is presented in Figure 7.162.

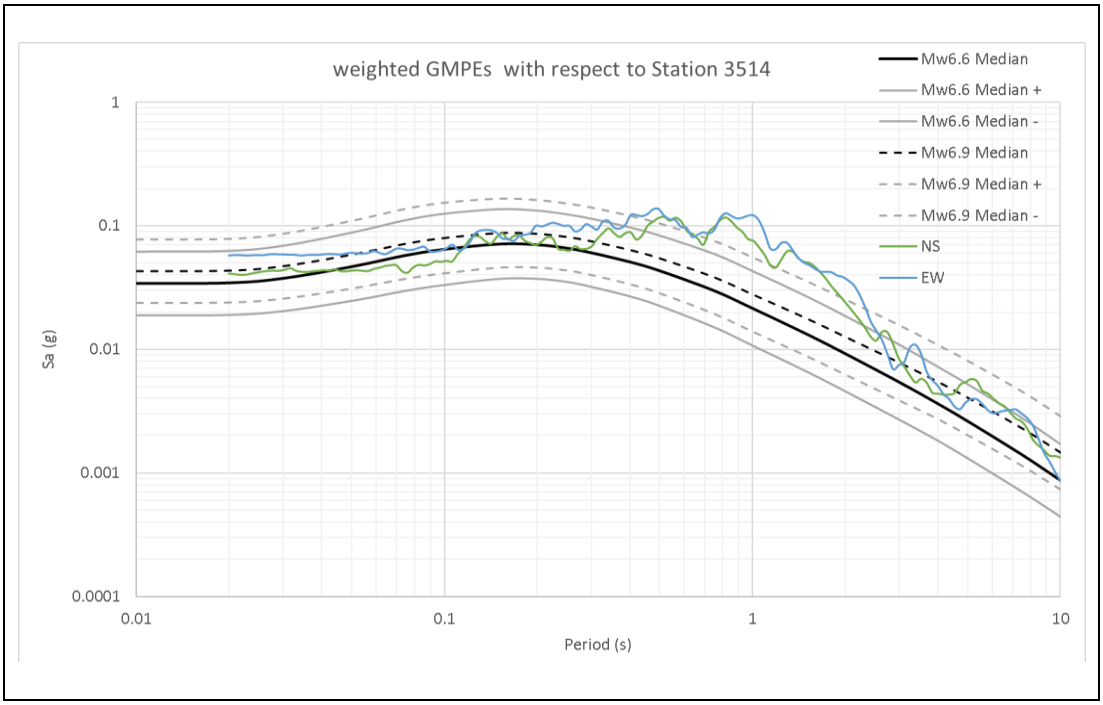


Figure 7.162: The weighted average 2014 GMPEs for M_w = 6.6 and M_w = 6.9 with respect to the mainshock recording of 30th October, 2020 Samos earthquake at Station 3514.

Although Station 3514 has V_{s30} = 836 m/s and is considered to be rock site, it is clearly seen from Figure 7.162 that not only the low period close to PGA but also the spectral acceleration values between natural periods T = 0.4 s and T = 2.5 s are underestimated for both M_w = 6.6 and M_w = 6.9.

In METU Report [2020], it is pointed out that the use of a larger M_w value as suggested by KOERI or USGS could yield closer values to the observed data peaks, and yet it is clearly seen in Figure 7.162 that on this rock site these new generation GMMs (former GMPEs or attenuation relationships) cannot represent expected spectral acceleration values especially between T = 0.4 s and T = 2.5 s. Either a regional GMM has to be developed (if there is enough data) or the existing GMMs need to be adjusted accordingly for Izmir region, where scientists studying the region believe there is not only "basin effect", but also the source mechanism that produces high energy at long periods [Cetin et. al., 2020]. κ correction to these GMMs might be one of the possible solutions for this issue.

During the computation phase, the "significant duration", "Arias intensity" [Arias, 1970], and "Housner intensity" [Housner, 1959] measures are calculated for

all data evaluated for κ calculations. These are checked with the values provided from METU Report [2020] for the mainshock values and can be seen in Table 7.9.

Housner Intensity (or response spectrum intensity) is defined as follows [Housner, 1959]:

$$SI(\xi) = \int_{0.1}^{2.5} PSV(T, \xi) dT \tag{7.8}$$

where *PSV* is the pseudo velocity response spectrum, *T* and ξ=5% are the structural natural period and damping, respectively. This parameter of seismic motion severity is related to the potential damage expected from the considered earthquake, since the majority of structures have a fundamental period of vibration in the range between 0.1 and 2.5 s.

Table 7.9: Comparison of significant duration, Arias intensity and Housner intensity values for 30th October, 2020 Samos earthquake recorded at Station 3514.

Station 3514	**METU Report [2020]**			**This study**		
	EW	**NS**	**UD**	**EW**	**NS**	**UD**
Significant Duration (s)	23.75	25.90	27.17	23.89	26.11	27.23
Arias Intensity (cm/s)	4.59	3.52	2.09	4.62	3.56	2.13
Housner Intensity (cm)	28.30	22.40	10.90	25.53	20.68	10.05

The slight differences between METU Report [2020] and this study values may come from the differences in signal process.

Here, it is important to point out that the vertical (UD) component significant duration of the event is longer than the two horizontal components. This could come from the basin effects as indicated before as many scientists suggested after 30th October, 2020 Samos earthquake, but it is also possible that this is due to having a normal fault rupture rather than strike slip rupture. There is vertical slip at the fault plane and this could cause vertical motions to differ from strike slip motion behavior.

To perform κ evaluations, the dataset formed from Samos region events was retrieved from new AFAD strong motion database for Station 3514 [Web 3]. The related events could be visualized in Figure 7.163.



Figure 7.163: Samos region events with $M \geq 3.5$ that are recorded at Station 3514.

Station 3514 was previously evaluated in terms of κ for all events recorded at this station up to November 2019 for the paper published 17th World Conference on Earthquake Engineering (17WCEE). In this published conference paper [Biro. et. al., 2020] an unconstrained κ_H vs R_{epi} fit for each hard rock AFAD station was applied. The reason for that was the lack of knowledge of a regional Q for each station to be corrected or to be constrained as a fit. Also, the newly developed f_x selection for this thesis was not yet developed and was not applied. A fixed $f_E - f_x$ value was taken for the linear κ fits (f_E = 2Hz to f_x = 20 Hz).

For events from new AFAD database between August 2019 until December 2020, the κ evaluations are made according the new procedure of Sivrice-Pütürge segment process and added to the previous study in Figure 7.164. The old database included all the events from all sources. It can be seen that the resulting κ_H values for Samos related events are higher than the overall κ_H values. We still have to keep in

mind that the overall κ_H values were evaluated with a fixed f_E – f_x of 2 – 20Hz respectively. Checking the new f_x values with newly developed selection procedure, it was seen that the fit could even be made up to 30 Hz and the minimum f_x selected was 18.66 Hz, so the pre-selected f_x value of 20 Hz for this station stayed to be applicable as well.

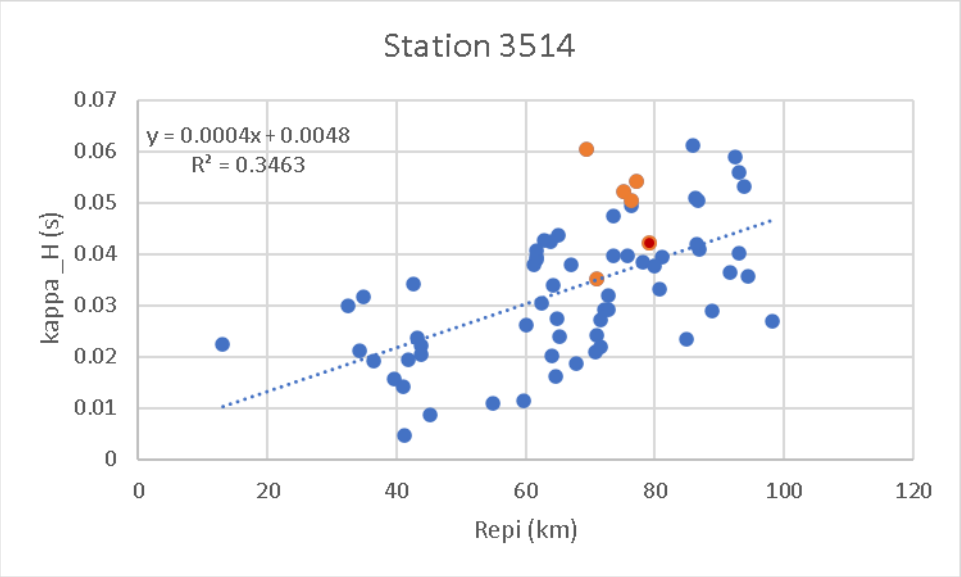


Figure 7.164: Event κ_H values evaluated for the events recorded at Station 3514.

The blue circles in Figure 7.164 indicate the events from former AFAD database until August 2019. The orange events and the red event (30th October, 2020 Samos mainshock) are from new AFAD database between August 2019 until December 2020. The unconstrained fit here is only applied to the former AFAD database events.

A trial to fit the κ_H vs R_{epi} constraining to the fit of former AFAD database and process related κ_H values is illustrated in Figure 7.165.

With the new AFAD database related κ_H values the overall κ_0 is now 0.006 s instead of 0.005 s (the new dataset gave higher κ_H values as shown in Figure 7.164) and the κ_0 value for the new dataset that consists of August 2019-December2020 Samos related events is 0.018 s (Figure 7.165).

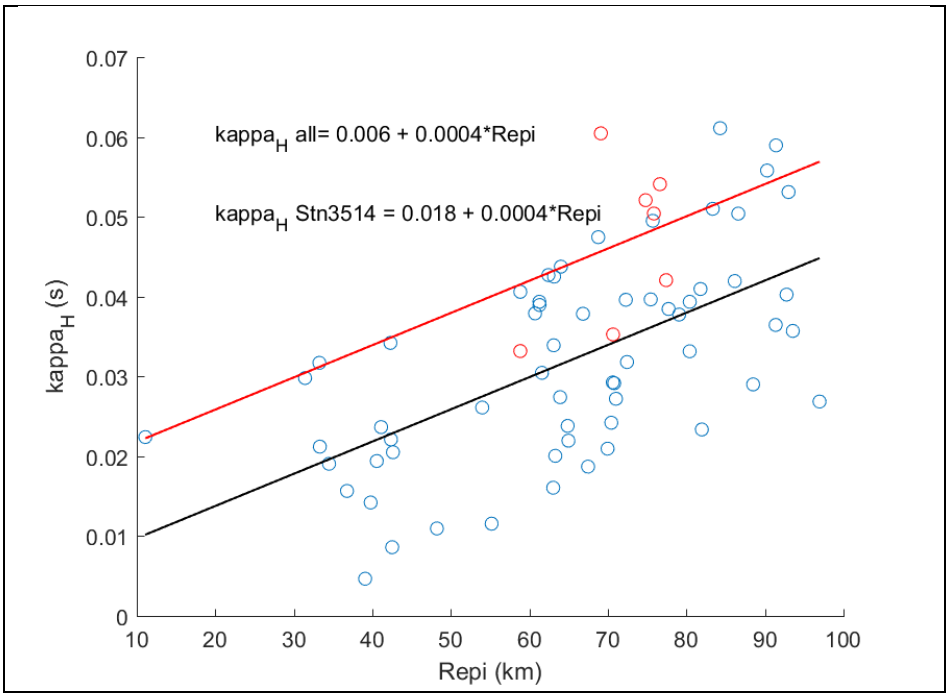


Figure 7.165: κ_0 value for the new dataset that consists of August 2019 – December 2020 Samos related events is 0.018 s when constrained with the overall κ_H values at Station 3514.

This approach, which is widely used worldwide, may not give a good fit for κ_0 values of overall events, and for this reason also for Samos related events. The reason is the need of a regional kappa evaluation before deciding the constrained Q correction. This could be really hard for Izmir region as there are many seismic sources and also different path properties for these sources between these stations. There may not be enough recorded events to investigate these different path and source relations. It is also questioned if it would make sense to evaluate κ_0 at Izmir stations at this point, as the R_{epi} for the Samos related events are approximately 70 km and for this reason these stations cannot be evaluated as near site stations. It is therefore crucial to gather a dataset from near field records for Izmir region, as well as a clear definition of the basin effect in this area.

However, from the κ evaluations a significant important result is obtained in terms of vertical κ values (κ_V). Very different from other regions, where approximately κ_H values could be even 2 times higher than κ_V, these events recorded at Station 3514, give higher vertical κ values than the horizontal. This could be also defined as basin effect or the normal faulting as mentioned before. The resulting kappa values for the selected events are in Table 7.10.

Table 7.10: the κ_H and κ_V values for the new dataset related Samos events at Station 3514.

Event	R_{epi} **(km)**	**Magnitude**	**Mag.Type**	κ_H **(s)**	κ_V **(s)**
'20190808083908'	58.84	4.8	M_w	0.033	0.037
'20201030115124'	77.41	6.6	M_w	0.042	0.049
'20201030151456'	75.85	5.1	M_w	0.050	0.053
'20201031052216'	76.62	3.8	M_w	0.054	0.051
'20201101070513'	70.65	4.5	M_L	0.035	0.043
'20201101125703'	74.80	4.2	M_L	0.052	0.054
'20201109203059'	69.10	4.2	M_w	0.061	0.047

As seen from the analyses of Station 3514 with V_{s30} = 836 m/s, and the Pseudo Spectral acceleration values are well under the 2018 Turkish Seismic Code Design Spectrum as illustrated in Figure 7.161 and yet PGA as well as between natural periods T = 0.4 s and T = 2.5 the spectral values are well above the newly generated GMMs (Figure 7.162). Unless a wide range of magnitude, distance with same path allocation records is available for Izmir region, the damage occurred in Izmir from Samos earthquake cannot be represented with the GMMs available. This also means that the hazard and risk calculations if applied with these new generation worldwide used GMMs, will not be able to represent the actual events occurring in the region. It is definitive that a profound κ_0 evaluation and a host-to-target conversion of these GMMs or a regional GMM development is necessary for Izmir region.

8. CONCLUSION

In Anderson and Hough [1984], the origin of κ evaluations, it is suggested and stated that "*the points at 25 Hz falling above the level consistent with exponential decay may result from the noise of the records*". During the course of κ evaluations, due to paucity of data in low seismic regions, this suggestion however is forgotten along the way.

As explained under sections "2. Kappa Studies and Evaluation Methodology" and "3. Uncertainty Reduction Trials" of this PhD thesis, especially the f_x selection of the signal FAS dominates the vast variability in κ estimates. Assumption of magnitude independency in κ_0 and R_{epi} correlations also provides false indications for station based κ_0 estimates and false correlation between κ_0 and V_{s30}. In sections "7.1 Van Region" and "7.3. Sivrice-Pütürge Segment of EAF", it is clearly seen that there is magnitude dependency in κ_0 and R_{epi} correlations. As explained in detail for hard rock AFAD station (V_{s30} = 1380 km/s) Stn4404 under section "7.3.2.2. κ Results", having a dataset of events up to 6.8M_w with maximum R_{epi} = 26 km proves that only looking at the low seismic data will provide low κ values, whereas the real case provides higher κ values. In low seismic regions therefore, there should be new relationships and or theoretical estimates for high magnitude event κ values by studying high seismic regions with high magnitude event records in near filed in the future.

AFAD results have clearly shown the necessity of a full cover of database. In the current time, even though the rich AFAD database is online, it is reachable only 10 records per hand selection as described before. If the database could be accessible fully, this would provide massive input for such evaluations which are critical for earthquake hazard and risk evaluations, simulations applicable for nonlinear structural analysis, soil structure interaction analysis and therefore, for earthquake sustainable cities.

REFERENCES

Abrahamson N., Silva W., (2008), "Summary of the Abrahamson and Silva NGA Ground-Motion Relations", Earthquake Spectra, 24(1), 67-97.

Abrahamson N.A., Silva W.J., Kamai R., (2013), "Update of the AS08 Ground Motion Prediction Equations Based on the NGA-West2 Data Set", PEER Report No. 2013/04, Pacific Earthquake Engineering Research Center, University of California, Berkeley. USA.

Abrahamson N.A., Silva W.J., Kamai R., (2014), "Summary of the ASK14 ground motion relation for active crustal regions", Earthquake Spectra, 30(3), 1025–1055.

Abrahamson N.A., Gülerce Z., (2020), "Regionalized Ground-Motion Models for Subduction Earthquakes Based on the NGA-SUB Database", PEER Report No. 2020/25, Pacific Earthquake Engineering Research Center, University of California, Berkeley. USA.

Aki K., (1987), "Magnitude-frequency relation for small earthquakes: A clue to the origin of f_{max} of large earthquakes", Journal of Geophysical Research, 92(B2), 1349–1355.

Akkar S., Sandıkkaya M.A., Bommer J.J., (2014), "Empirical ground-motion models for point-and extended-source crustal earthquake scenarios in Europe and the Middle East", Bulletin of Earthquake Engineering, 12(1), 359–387.

Ancheta T.D., Darragh R.B., Steward J.P., Seyhan E., Silva W.J., Chiou B.S.J., Wooddell K.E., Graves R.W., Kottke A.R., Boore D.M., Kishida T., Donahue J.L., (2013), "PEER NGA-West2 Database", PEER Report No: 2013/03, Pacific Earthquake Engineering Research, University of California, Berkeley, USA.

Anderson J., Hough S., (1984), "A model for the shape of the Fourier amplitude spectrum of acceleration at high frequencies", Bulletin of Seismological Society of America, 74 (5), 1969–1993.

Andrews D.J., (1986), "Objective determination of source parameters and similarity of earthquakes of different size", Earthquake Source Mechanics, 37, 259-267.

Anderson J.G., Humprey J.R., (1991), "A least squares method for objective determination of earthquake source parameters", Seismological Research Letters, 62(3-4), 201–209.

Arias A., (1970), "A measure of earthquake intensity" In: Hansen, RJ (ed.) Seismic Design for Nuclear Power Plants. Cambridge, MA: MIT Press, pp. 438–483.

Askan A., Sisman F.N., Pekcan O., (2014)," A regional near-surface high frequency spectral attenuation (kappa) model for northwestern Turkey", Soil Dynamics and Earthquake Engineering, 65, 113–25.

Bard P.Y., Bora S.S., Hollender F., Laurendeau A., Traversa P., (2018), "Are the standard V_{s30}-Kappa host-to-target adjustments the best way to get consistent hard-rock ground motion prediction?", Best Practices in Physics-based Fault Rupture Models for Seismic Hazard Assessment of Nuclear Installations: issues and challenges towards full Seismic Risk Analysis , CEA - AIEA, May 2018, Cadarache France. hal-01826648.

Biasi G.P., Smith K.D., (2001), "Site Effects for Seismic Monitoring Stations in the Vicinity of Yucca Mountain, Nevada", Report No.: MOL20011204.0045, A Report Prepared for the US DOE/University and Community College System of Nevada (UCCSN) Cooperative Agreement.

Biro Y., Renault P., (2012), "Importance and impact of host-to-target conversions for ground motion equations in PSHA", 15th World Conference of Earthquake Engineering, Paper No: 10928, Lisbon, Portugal, 24-28 September.

Biro Y., Siyahi B., Akbas B., (2019), "The spectral decay parameter κ (kappa) for the near site events in Van Region", 5th International Conference on Earthquake Engineering and Seismology, METU, Ankara, Turkey, 8-11 October.

Biro Y., Siyahi B., Akbas B., (2020), "The Spectral Decay Parameter κ (kappa) for the Near Site Events in Van Region", Turkish Journal of Earthquake Research, 2 (1), 1-13.

Biro Y., Siyahi B., Akbas B., (2021), "The spectral decay parameter κ (kappa) for hard rock strong ground motion stations in Turkey", 17th World Conference of Earthquake Engineering, Paper No: C002364, Sendai, Japan, 27 September-2 October.

Biro Y., Siyahi B., Akbas B., (2022), "Spectral decay parameter (κ) analysis for a single fault source and an automatic selection procedure for spectral flattening frequency (f_x)", Soil Dynamics and Earthquake Engineering, 153, 2022, 107122.

Boore D.M., Stewart J.P., Atkinson G.M., (2013), "NGA-West2 Equations for Predicting Response Spectral Accelerations for Shallow Crustal Earthquakes", PEER Report No. 2013/05, Pacific Earthquake Engineering Research Center, University of California, Berkeley. USA.

Boore D.M., Stewart J.P., Seyhan E., Atkinson G.M., (2014), "NGA-West2 equations for predicting PGA, PGV, and 5% damped PSA for shallow crustal earthquakes", Earthquake Spectra 30(3), 1057–1085.

Bora S.S., Scherbaum F., Kuehn N., Stafford P., (2016), "On the relationship between Fourier and Response spectra: Implications for the adjustment of empirical ground-motion prediction equations (GMPEs)", Bulletin of Seismological Society of America, 106(3), 1235–1253.

Bora S.S., Cotton F., Scherbaum F., Edwards B., Traversa P., (2017), "Stochastic source, path and site attenuation parameters and associated variables for shallow

crustal European earthquakes", Bulletin of Earthquake Engineering, 15(11), 4531–4561

Bozorgnia Y., Stewart J.P., (2020), "Data Resources for NGA-Subduction Project", PEER Report No: 2020/02, Pacific Earthquake Engineering Research, University of California, Berkeley, USA.

Brooks C., Douglas J., (2021), "Influence of the Site-Specific Component of Kappa on the Magnitude-Dependency of Within-Event Aleatory Variabilities in Ground-Motion Models", Seismological Research Letters, 92(1), 238–245.

Cabas A., Ji C., (2020), "Improving the Assessment of Site-specific Seismic Hazards Through the Lens of Novel Attenuation Models" USGS Final Report Award No: G19AP00058.

Campbell K.W., Youssef H.M.A., (2013), "NGA-West2 Campbell-Bozorgnia Ground Motion Model for the Horizontal Components of PGA, PGV, and 5%-Damped Elastic Pseudo-Acceleration Response Spectra for Periods Ranging from 0.01 to 10 sec", PEER Report No: 2013/06, Pacific Earthquake Engineering Research, University of California, Berkeley, USA.

Campbell K.W., Youssef H.M.A., Kim B., Kottke A.R. Rathje E. M., Silva W.J., Stewart J.P., (2014), "Reference-Rock Site Conditions for Central and Eastern North America: Part II – Attenuation (Kappa) Definition", PEER Report No: 2014/12, Pacific Earthquake Engineering Research, University of California, Berkeley, USA.

Campbell K.W., Bozorgnia Y., (2014), "NGA-West2 ground motion model for the average horizontal components of PGA, PGV, and 5% damped linear acceleration response spectra", Earthquake Spectra, 30(3), 1087–1115.

Cetin K.O., Mylonakis G., Sextos A., Stewart J.P., (2020), "Seismological and Engineering Effects of the M 7.0 Samos Island (Aegean Sea) Earthquake", Report GEER-069, Geotechnical Extreme Events Reconnaissance Association.

Chiou B. S.-J., Youngs R.R., (2013), "Update of the Chiou and Youngs NGA Ground Motion Model for Average Horizontal Component of Peak Ground Motion and Response Spectra", PEER Report No: 2013/07, Pacific Earthquake Engineering Research, University of California, Berkeley, USA.

Chiou B. S.-J., Youngs R.R., (2014), "Update of the Chiou and Youngs NGA model for the average horizontal component of peak ground motion and response spectra", Earthquake Spectra, 30(3), 1117–1153.

Cormier V. F. (1982), "The effect of attenuation on seismic body waves", Bulletin of Seismological Society of America, 72(6), 169–200.

Douglas J., Gehl P., Bonilla L.F., Gélis C., (2010), "A κ Model for Mainland France", Pure and Applied Geophysics, 167, 1303–1315.

Durukal E., Erdik M., Avci J., Yuzugullu O., Alpay Y., Avar B., Zulfikar C., Biro T., Mert A., (1998), "Analysis of strong motion data of the 1995 Dinar, Turkey earthquake", Soil Dynamics and Earthquake Engineering, 17, 557–578.

Durukal E., Catalyurekli Y., (2004), "Spectral Analysis of Source Parameters of the 1999 Kocaeli and Düzce Earthquake Aftershock Sequences", 13th World Conference of Earthquake Engineering, Paper No: 421, Vancouver, B.C., Canada, 1-6 August.

Edwards B., Fäh D., Giardini D., (2011), "Attenuation of seismic shear wave energy in Switzerland", Geophysical Journal International,185(2), 967–984.

Edwards B., Ktenidou O.J., Cotton F., Abrahamson N.A., Van Houtte C., Fäh D., (2015), "Epistemic uncertainty and limitations of the κ_0 model for near-surface attenuation at hard rock sites", Geophysical Journal International, 202(3), 1627–1645.

EPRI, (1993), "Guidelines for Determining Design Basis Ground Motions: Method and guidelines for estimating earthquake ground motion in eastern North America", Report No: EPRI TR-102293-V1, Electric Power Research Institute, Palo Alto, USA.

Gariel J.-C. and Campillo M., (1989), "The influence of the source on the high-frequency behavior of the near-field acceleration spectrum: A numerical study", Geophysical Research Letters, 16(4), 279–282.

Gregor N., Abrahamson N.A., Atkinson G.M., Boore D.M., Bozorgnia Y., Campbell K.W., Chiou B.S.-J., Idriss I.M., Kamai R., Seyhan E., Silva W., Stewart J.P., Youngs R., (2014), "Comparison of NGA-West2 GMPEs", Earthquake Spectra 30(3), 1179–1197.

Goulet C.A., Kishida T., Ancheta T.D., Cramer C.H., Darragh R.B., Silva W.J., Hashash Y.M.A., Harmon J., Parker G.A. Stewart J.P., Youngs R.R., (2021), "PEER NGA-East Database", Earthquake Spectra, 37(S1), 1331–1353.

GTU Report (2nd November, 2020), "30 Ekim 2020 14:51 (UTC 11:51) M_w = 6.9 Ege Denizi Depremi Bilgilendirme Notu", Deprem ve Yapı Mühendisliği Programı, İnşaat Mühendisliği Bölümü, Gebze Teknik Üniversitesi, Gebze/Kocaeli, Turkiye.

Idriss I.M., (2013), "NGA-West2 Model for Estimating Average Horizontal Values of Pseudo-Absolute Spectral Accelerations Generated by Crustal Earthquakes", PEER Report No: 2013/08, Pacific Earthquake Engineering Research, University of California, Berkeley, USA.

Idriss I.M., (2014), "An NGA-West2 empirical model for estimating the horizontal spectral values generated by shallow crustal earthquakes", Earthquake Spectra, 30(3), 1155–1177.

Ji C., Cabas A., Cotton F., Pilz M., Bindi D., (2020), "Within-Station Variability in Kappa: Evidence of Directionality Effects", Bulletin of Seismological Society of America ,110 (3), 1247–1259.

Ji. C, Cabas A., Bonilla L.F., Gelis C., (2021), "Effects of Nonlinear Soil Behavior on Kappa (κ): Observations from the KiK-Net Database", Bulletin of the Seismological Society of America, 111(4), 2138–2157.

Hollender F., Roumelioti Z., Maufroy E., Traversa P., Mariscal A., (2020), "Can We Trust High-Frequency Content in Stong-Motion Database Signals? Impact of Housing, Coupling, and Installation Depth of Seismic Sensors", Seismological Research Letters, 91(4), 2192–2205.

Hough S.E., Anderson J.G., (1988), "High frequency spectra observed at Azna, California: Implications for Q structure", Bulletin of Seismological Society of America, 78(2), 692–707.

Housner G.W., (1959), "Behavior of Structures During Earthquakes", Journal of the Engineering Mechanics Division, American Society of Civil Engineering, 85(4), 109–130.

Humprey J.R., Anderson J.G., (1992), "Shear wave attenuation and site response in Guerrero, Mexico", Bulletin of Seismological Society of America, 81(4), 1622–1645.

Husid P., (1967), "Gravity Effects on the Earthquake Response of Yielding Structures", PhD. thesis, California Institute of Technology, CA, USA, 1–153.

Kilb D., Biasi G., Anderson J., Brune J., Peng Z., Vernon F.L, (2012), "A Comparison of Spectral Parameter Kappa from Small and Moderate Earthquakes Using Southern California ANZA Seismic Network Data", Bulletin of Seismological Society of America, 102 (1), 284–300.

Konno K., Ohmachi T., (1998), "Ground motion characteristics estimated from spectral ratio between horizontal and vertical components of microtremor", Bulletin of Seismological Society of America, 88(1), 228–241.

Ktenidou O.J., Cotton F., Abrahamson N.A., Anderson J.G., (2014), "Taxonomy of κ: A Review of Definitions and Estimation Approaches Targeted to Applications", Seismological Research Letters, 85(1), 135–146.

Ktenidou O.J., Abrahamson N.A., Darragh R.B., Silva W.A., (2016a), "A Methodology for the Estimation of Kappa from Large Datasets: Example Application to Rock Sites in the NGA-East Database and Implications on Design Motions", PEER Report No: 2016/01, Pacific Earthquake Engineering Research, University of California, Berkeley, USA.

Ktenidou O.J., Abrahamson N.A., (2016b), "Empirical Estimation of High-Frequency Ground Motion on Hard Rock", Seismological Research Letters, 87(6), 1465–1478.

Ktenidou O.J., Silva W.A., Darragh R.B., Abrahamson N.A., Kishida T., (2017), "Squeezing Kappa (κ) Out of the Transportable Array: A Strategy for Using Bandlimited Data in Regions of Sparse Seismicity", Bulletin of Seismological Society of America, 107(1), 256–275.

Ktenidou O.J., Abrahamson N.A., Silva W.J., Darragh R.B., Kishida T., (2021), "The search for hard-rock kappa (k) in NGA-East: A semi-automated method for large, challenging datasets in stable continental regions", Earthquake Spectra, 37(S1), 1391–1419.

Kurtulmus T.O., Akyol N., (2015), "Separation of source, site and near-surface attenuation effects in western Turkey", Natural Hazards, 77, 1515–1532.

Laurendeau A., Cotton F., Ktenidou O.J., Bonilla L.F., Hollender F., (2013), "Rock and stiff-soil site amplification: Dependency on V_{s30} and kappa (κ_0)", Bulletin of Seismological Society of America, 103(6): 3131-3148.

Lermo J, Chavez-Garcia FJ., (1993), "Site effect evaluation using spectral ratios with only one station", Bulletin of Seismological Society of America, 83(5),1574–1594.

Li J., Zhou B., Rong M., Chen S., Zhou Y., (2020), "Estimation of Source Spectra, Attenuation, and Site Responses from Strong-Motion Data Recorded in the 2019 Changning Earthquake Sequence", Bulletin of Seismological Society of America, 110(2), 410–426,

McCann M.W., Shah H.C., (1979), "Determining Strong Motion Duration of Earthquakes", Bulletin of Seismological Society of America, 69(4), 1253–1265.

METU Report (November, 2020), "The Samos (Izmir- Seferihisar offshore) earthquake [30 October 2020 M_w = 6.6] field observations on seismic and structural damage.", Report No: METU/EERC 2020-03, Earthquake Engineering Research Center, Middle Eastern Technical University, Ankara, Turkey.

Nakamura Y., (1989), "A method for dynamic characteristics estimation of subsurface using microtremor on ground surface", Quarterly Report 30(1), RTRI (Railway Technical Research Institute), Japanese National Railways, Tokyo, Japan.

Nakamura Y., (2019), "What is the Nakamura method?", Seismological Research Letters, 90(4), 1437–1443.

Palmer S.M., Atkinson G.M., (2020), "The High-Frequency Decay Slope of Spectra (Kappa) for M ≥ 3.5 Earthquakes on Rock Sites in Eastern and Western Canada", Bulletin of Seismological Society of America, 110, 471–488.

Papageorgiou A.S., Aki K., (1983), "A specific barrier model for the quantitative description of inhomogeneous faulting and the prediction of strong ground motion: Part II. Applications of the model", Bulletin of Seismological Society of America, 73(4), 953–978.

Papageorgiou A.S., (1988), "On two characteristic frequencies of acceleration spectra: Patch corner frequency and fmax", Bulletin of Seismological Society of America, 78(2), 509–529.

Papageorgiou A.S., (2003), "The barrier model and strong ground motion", Pure and Applied Geophysics, 160, 603–634.

Perron V., Hollender F., Bard P.Y., Gélis C., Guyonnet-Benaize C., Hernandez B., Ktenidou O.J., (2017), "Robustness of Kappa (κ) Measurement in Low-to-Moderate Seismicity Areas: Insight from a Site-Specific Study in Provence, France", Bulletin of Seismological Society of America, 107(5), 256–275.

Ren Y., Wen R., Yamanaka H., Kashima T., (2013), "Site effects by generalized inversion technique using strong motion recordings of the 2008 Wenchuan earthquake", Earthquake Engineering and Engineering Vibration, 12, 165–184,

Silva W.J., Darragh R.B., (1995), "Engineering characterization of earthquake strong ground motion recorded at rock sites", Electric Power Research Institute, TR-102261, Palo Alto, CA.

Silva W.J., Abrahamson N. A., Toro G., Costantino C., (1997), "Description and validation of the stochastic ground motion model", Report Submitted to Brookhaven National Laboratory, Contract No. 770573, Associated Universities, Inc. Upton, NY.

Silva W.J., Darragh R.B., Gregor N., Martin G., Abrahamson N.A., Kircher C., (1998), "Reassessment of site coefficients and near-fault factors for building code provisions", Technical Report Program Element II: 98-HQGR-1010, Pacific Engineering and Analysis, El Cerrito, CA.

Stafford P.J., Rodriguez-Marek A., Edwards B., Kruiver P.P., Bommer J.J., (2017), "Scenario dependence of linear site-effect factors for short-period response spectral ordinates", Bulletin of Seismological Society of America, 107(6), 2859–2872.

Tanircan G., Dikmen S.U., (2018), "Variation of high frequency spectral attenuation (Kappa) in vertical arrays Soil Dynamics and Earthquake Engineering,113, 406–414.

Tsurugi M., Tanaka R., Kagawa T., Irikura K., (2020), "High-Frequency Spectral Decay Characteristics of Seismic Records of Inland Crustal Earthquakes in Japan: Evaluation of the f_{max} and κ Models", Bulletin of Seismological Society of America, 110(2), 452–470.

Web 1, (2020), https://www.sigma-2.net/pages/technical-programme/wp3-ground-motion/3-1-ground-motion-prediction-site-proxies-ref-gm-new-intensity-measures/action-3-1-1-ground-motion-high-frequency-attenuation-proxy-kappa-project.html, (accessed 17 June 2020).

Web 2, (2020), http://www.koeri.boun.edu.tr/sismo/zeqdb/indexeng.asp, (accessed 17/06/2020).

Web 3, (2021), http://tadas.afad.gov.tr, (accessed 17/03/2021).

Wen R., Ren Y., Shi D., (2011), "Improved HVSR site classification method for free-field strong motion stations validated with Wenchuan aftershock recordings", Earthquake Engineering and Engineering Vibration, 10(3), 325–337.

Wen J., Chen X., (2012), “Variations in fmax along the ruptured fault during the Mw 7.9 Wenchuan earthquake of 12 May 2008”, Bulletin of Seismological Society of America, 102(3), 991–998.

Zhu C., Cotton F., Pilz M., (2020), “Detecting Site Resonant Frequency Using HVSR: Fourier versus Response Spectrum and the First versus the Highest Peak Frequency”, Bulletin of Seismological Society of America, 110(2), 427–440,

BIOGRAPHY

Yeşim (ALPAY) BİRO graduated from Department of Civil Engineering in Yıldız Technical University. In June 1998, she got the certificate of Geological Risk Management Certificate Program (CERG), from Université de Genève, Geneva, Switzerland. She got her M.Sc. degree in Earthquake Engineering in February 1999 from Earthquake Engineering Department of Kandilli Observatory and Earthquake Research Institute (KOERI), Boğaziçi University.

She performed and participated in many earthquake hazard and risk related projects and studies during her career. Some of them can be listed as Istanbul Earthquake Masterplan, Izmir Earthquake Masterplan, Global Seismic Hazard Program, GSHAP project for the Aegean and the surrounding region, Bağcılar and Silivri Earthquake Masterplan, Turkey Emergency Flood and Earthquake Recovery (TEFER) Project (for DASK), Earthquake Hazard Analysis and Risk Assessment of Istanbul for Münich-RE, Baku-Ceyhan Oil Pipeline & its junction constructions, Istanbul Underground Metro System, Turkey Earthquake Model for RMS Inc., both in USA and UK, and Converium AG, Switzerland. She managed the EMME Project (Earthquake Model of the Middle East Region), for GEM (Global Earthquake Model), under the coordination of Prof. Domenico Giardini, ETHZ, Zürich, Switzerland and both managed and technically guided the hazard and structural analyses for nuclear power plants in Switzerland under the scope of PEGASOS Refinement Project in swissnuclear, ALPIQ.

APPENDICES

Appendix A: Publications within the Scope of Thesis Study

Biro Y., Siyahi B., Akbas B., (2019), "The spectral decay parameter κ (kappa) for the near site events in Van Region", 5th International Conference on Earthquake Engineering and Seismology, METU, Ankara, Turkey, 8-11 October.

Biro Y., Siyahi B., Akbas B., (2020), "The Spectral Decay Parameter κ (kappa) for the Near Site Events in Van Region", Turkish Journal of Earthquake Research, 2 (1), 1-13.

Biro Y., Siyahi B., Akbas B., (2021), "The spectral decay parameter κ (kappa) for hard rock strong ground motion stations in Turkey", 17th World Conference of Earthquake Engineering, Paper No: C002364, Sendai, Japan, 27 September-2 October.

Biro Y., Siyahi B., Akbas B., (2022), "Spectral decay parameter (κ) analysis for a single fault source and an automatic selection procedure for spectral flattening frequency (f_x)", Soil Dynamics and Earthquake Engineering (SDEE), 153, 2022, 107122.

Appendix B: October 30, 2020 M_w6.9 (KOERI) Samos Earthquake Main Event κ Estimations

The October 30, 2020 Samos earthquake was recorded by 72 AFAD strong ground motion stations that are located within 200 km and their distribution is given in Figure B1.1. The three directional component κ estimations are given for this mainshock for each station within 90 km in the following figures (FigureB1.2 – Figure B1.28)

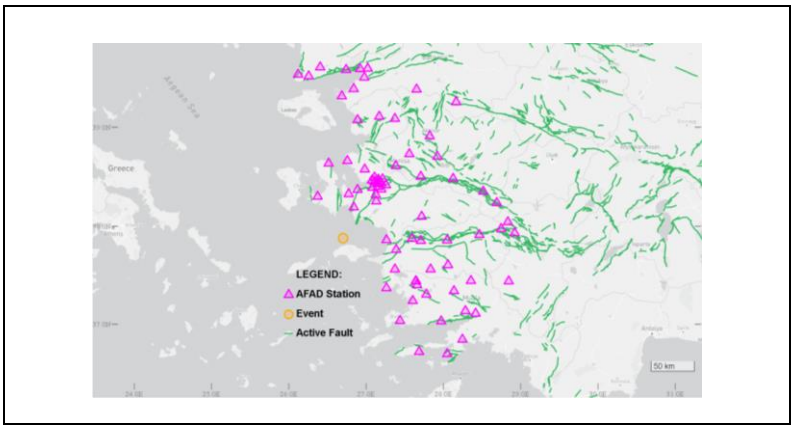


Figure B1.1: The distribution of AFAD stations within R_{epi} = 200 km.

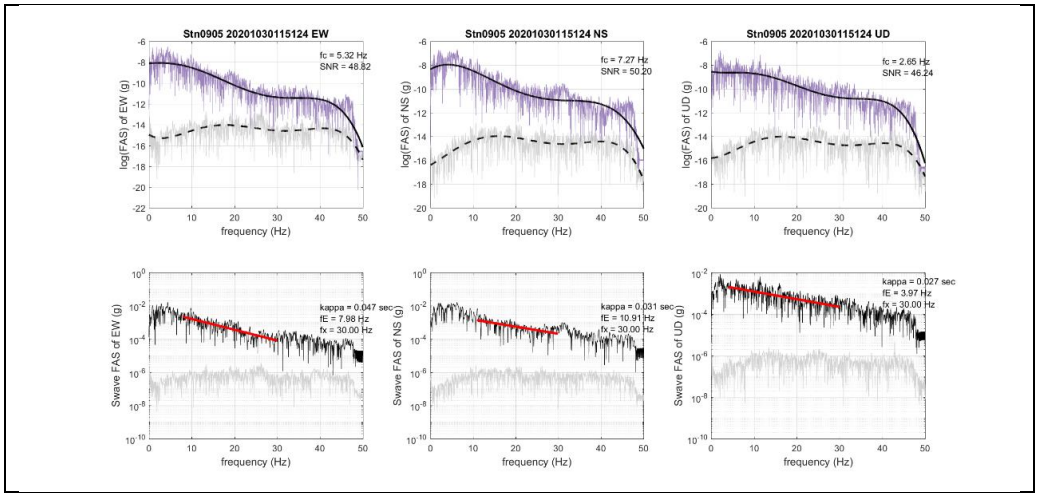


Figure B1.2: κ estimations for Stn0905. The mainshock occurred at 49 km R_{epi}.

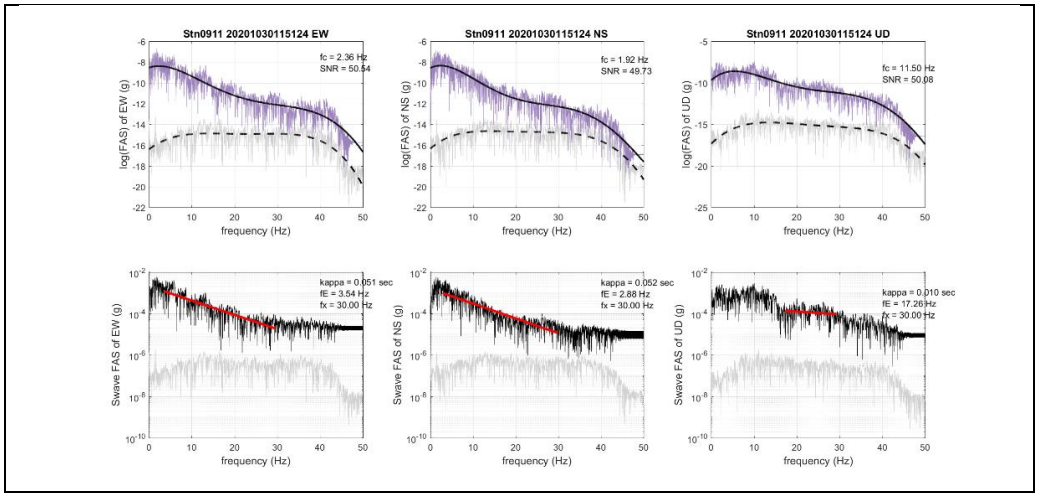


Figure B1.3: κ estimations for Stn0911. The mainshock occurred at 62 km R_{epi}.

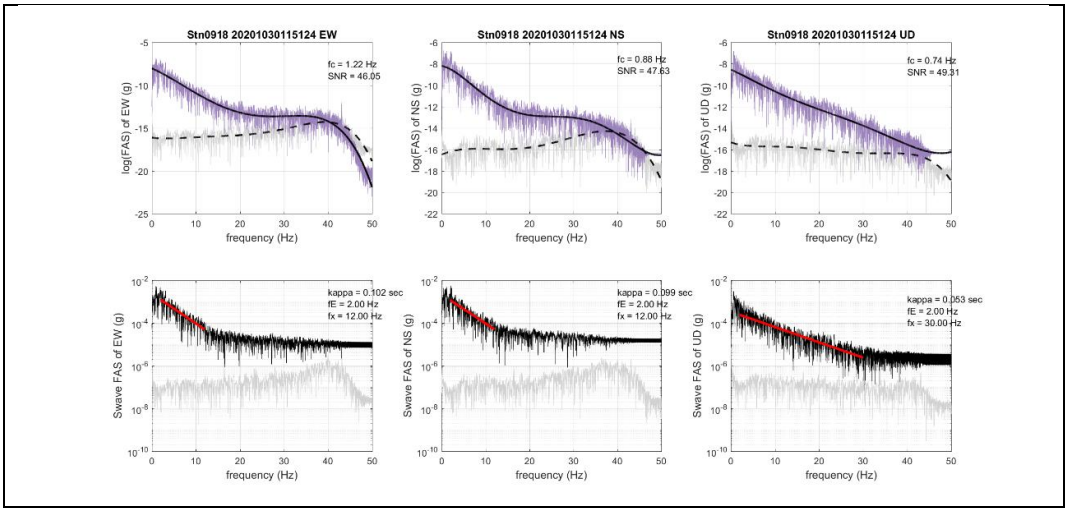


Figure B1.4: κ estimations for Stn0918. The mainshock occurred at 75 km R_{epi}.

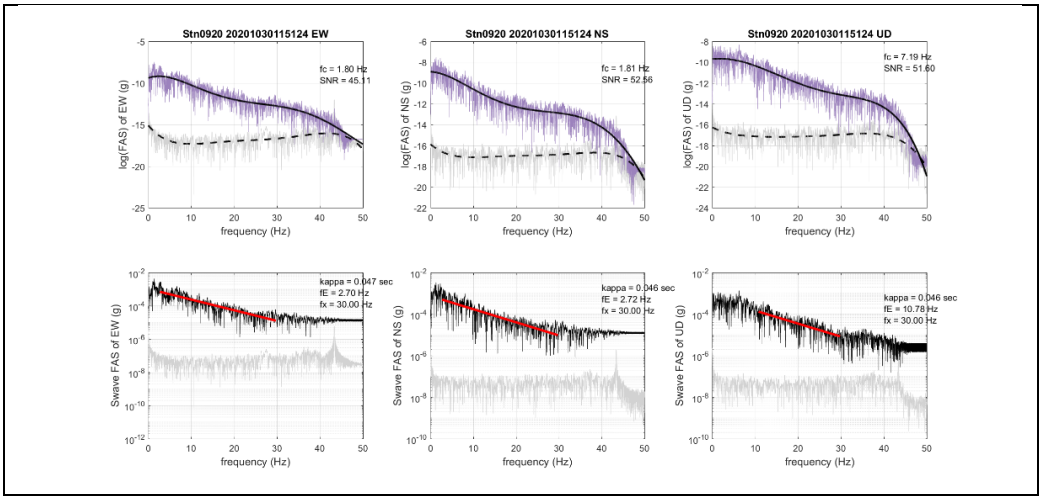


Figure B1.5: κ estimations for Stn0920. The mainshock occurred at 69 km R_{epi}.

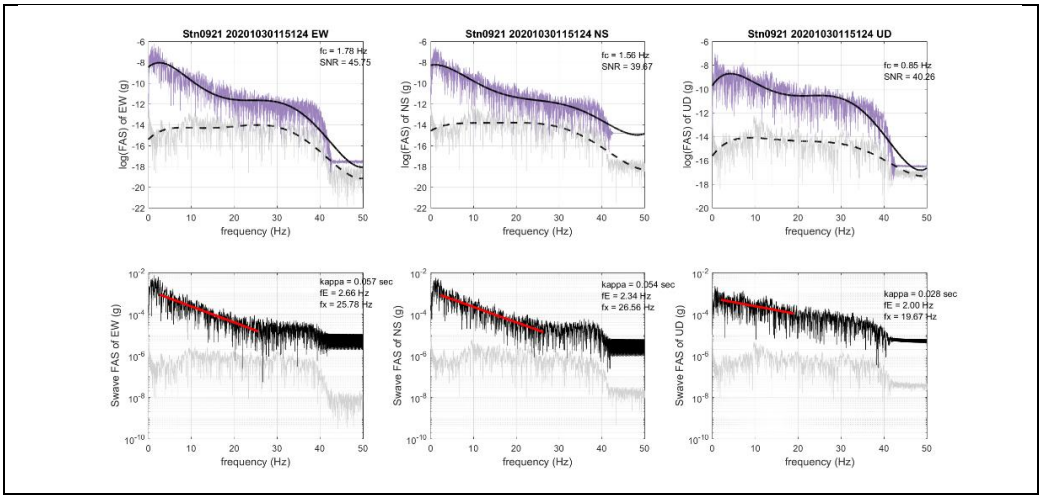


Figure B1.6: κ estimations for Stn0921. The mainshock occurred at 78 km R_{epi}.

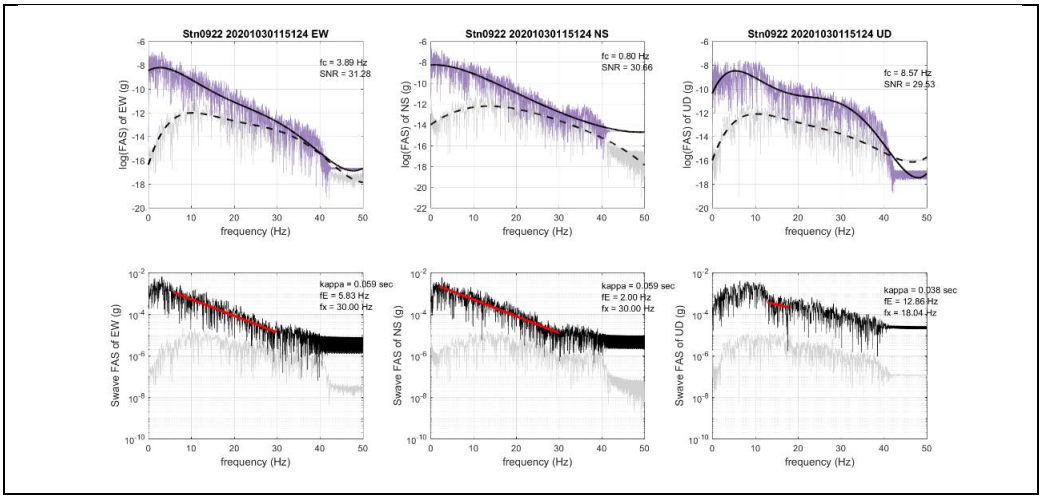


Figure B1.7: κ estimations for Stn0922. The mainshock occurred at 88 km R_{epi}.

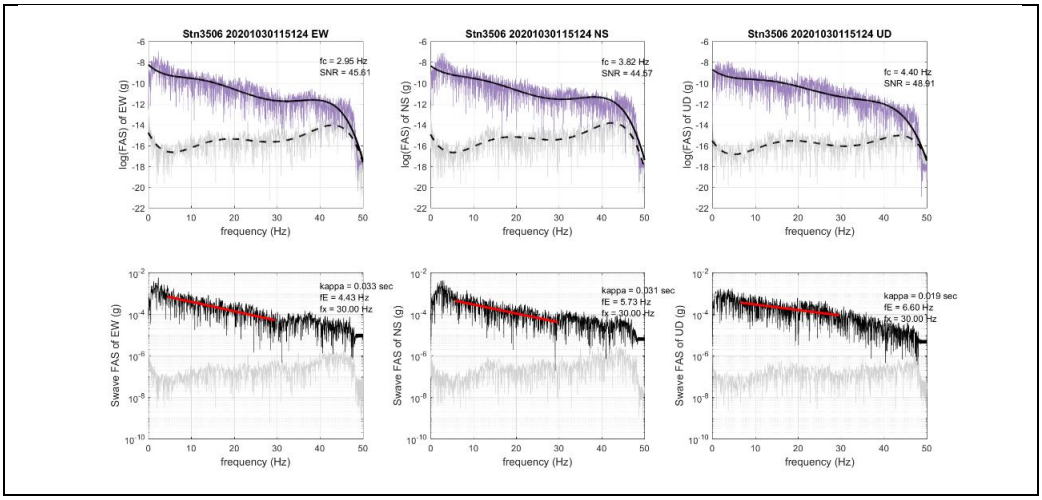


Figure B1.8: κ estimations for Stn3506. The mainshock occurred at 66 km R_{epi}.

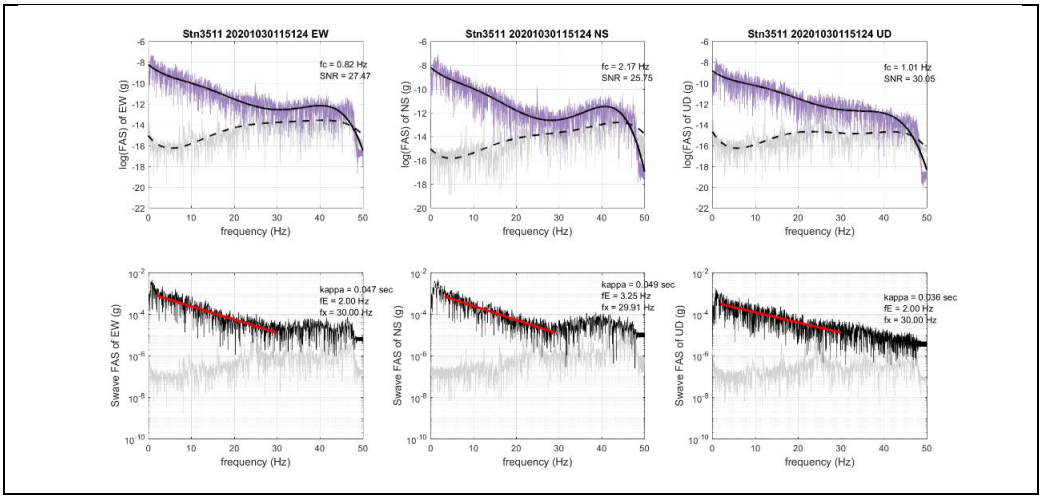


Figure B1.9: κ estimations for Stn3511. The mainshock occurred at 77 km R_{epi}.

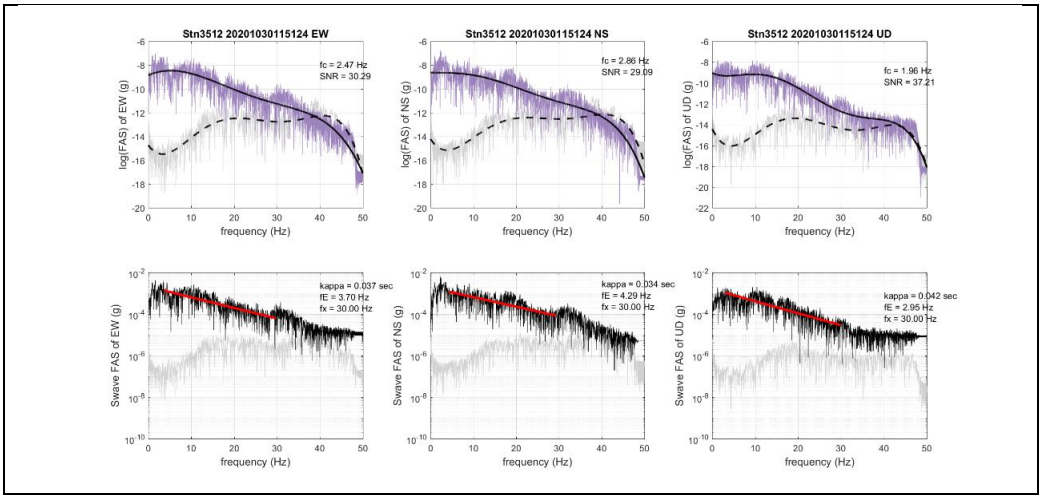


Figure B1.10: κ estimations for Stn3512. The mainshock occurred at 70 km R_{epi}.

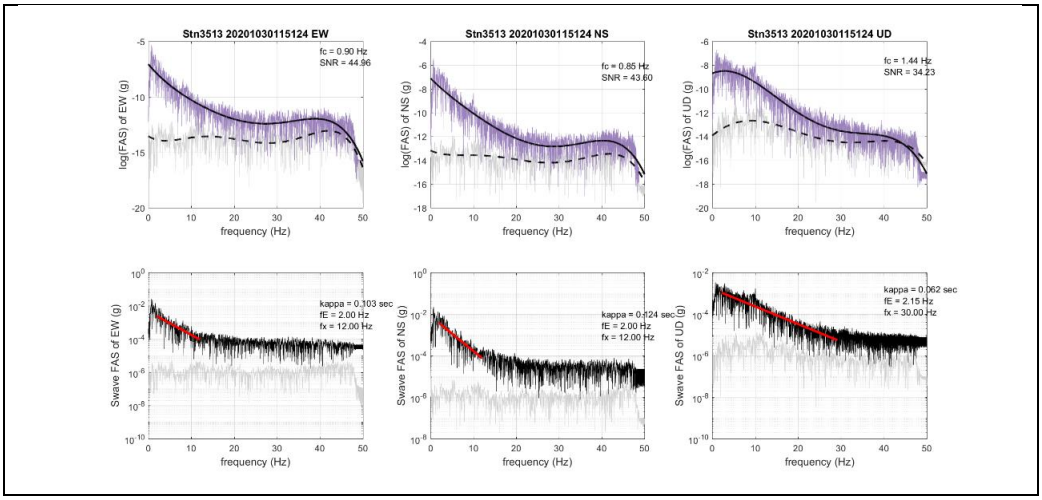


Figure B1.11: κ estimations for Stn3513. The mainshock occurred at 76 km R_{epi}.

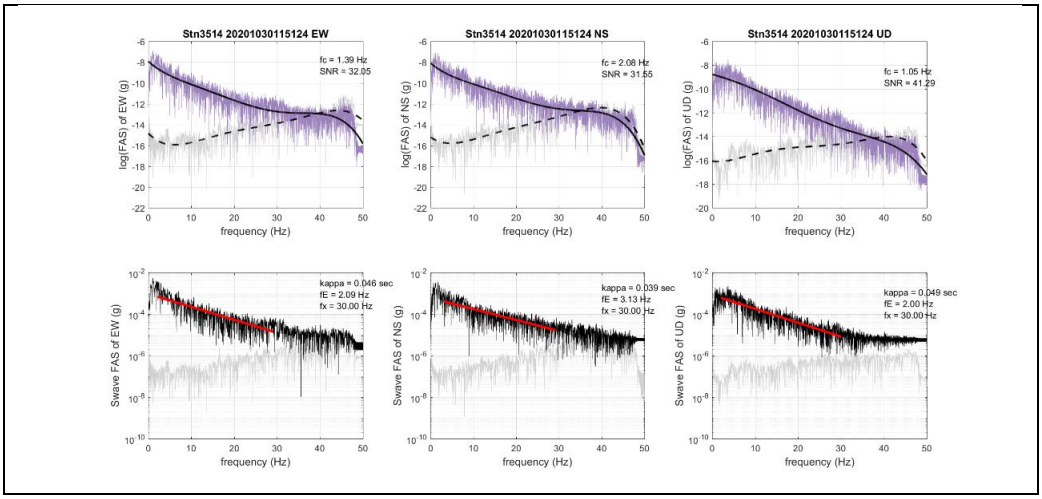


Figure B1.12: κ estimations for Stn3514. The mainshock occurred at 77 km R_{epi}.

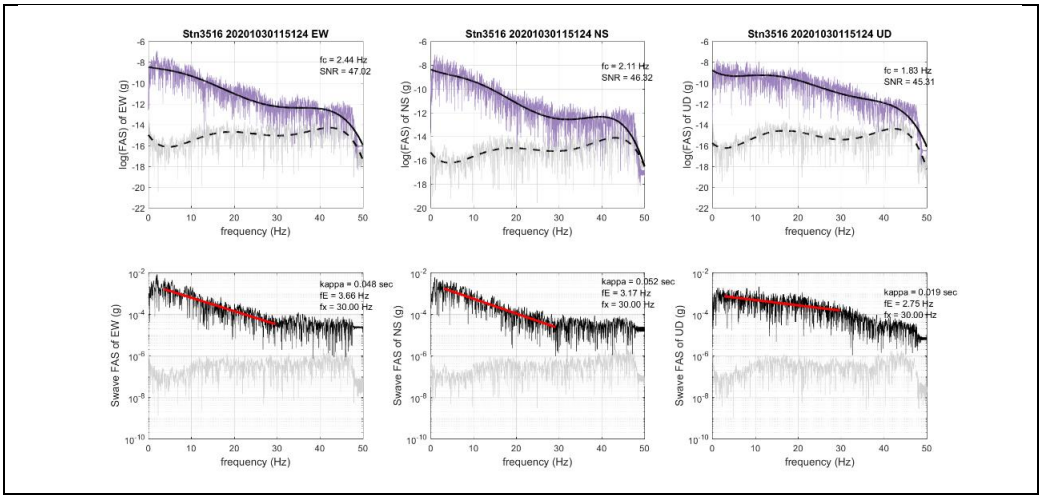


Figure B1.13: κ estimations for Stn3516. The mainshock occurred at 57 km R_{epi}.

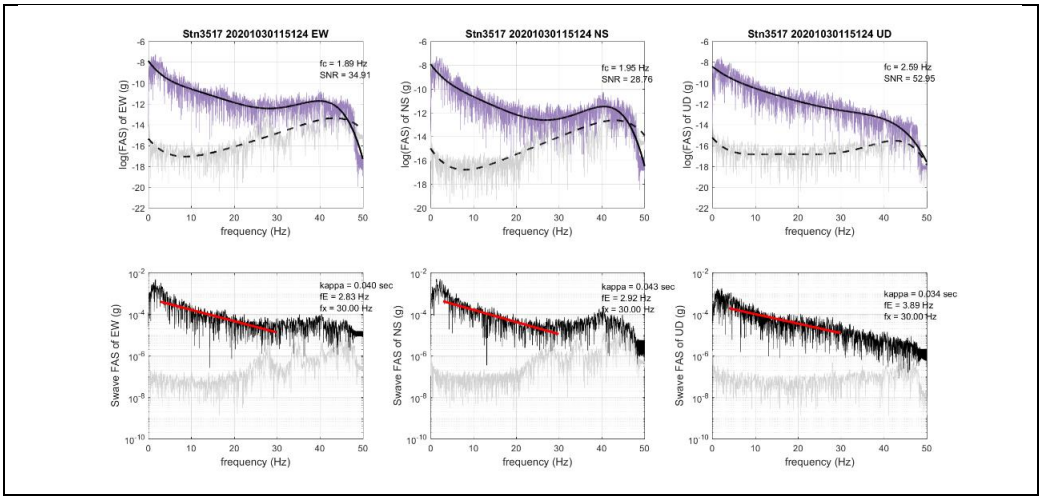


Figure B1.14: κ estimations for Stn3517. The mainshock occurred at 70 km R_{epi}.

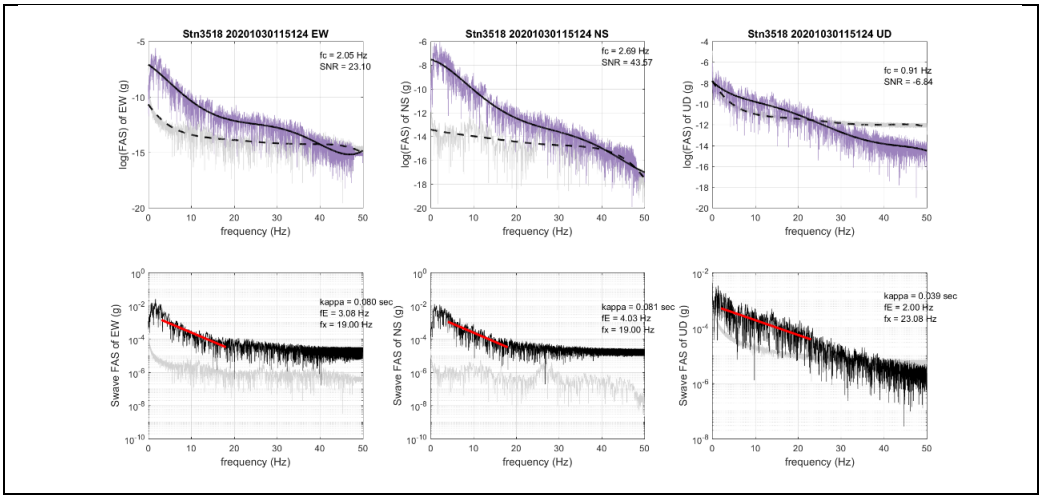


Figure B1.15: κ estimations for Stn3518. The mainshock occurred at 73 km R_{epi}.

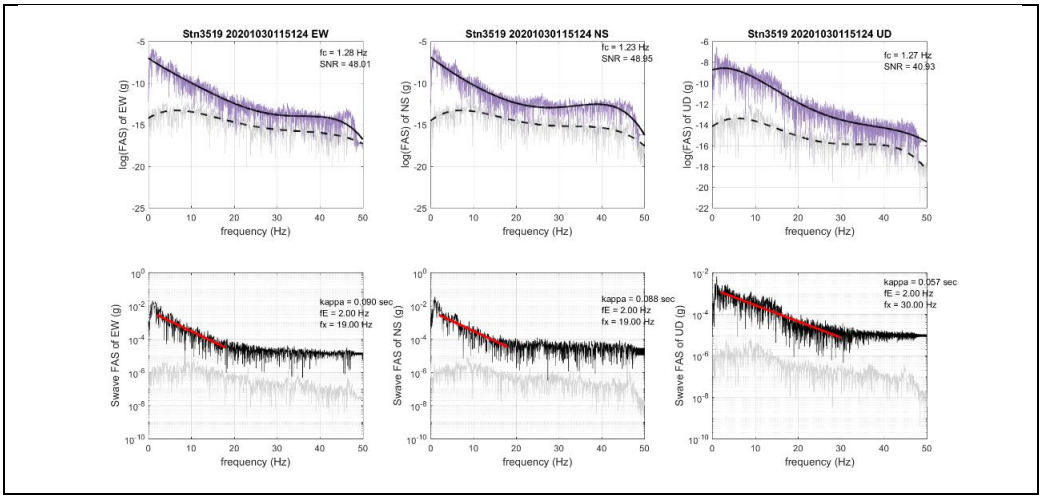


Figure B1.16: κ estimations for Stn3519. The mainshock occurred at 73 km R_{epi}.

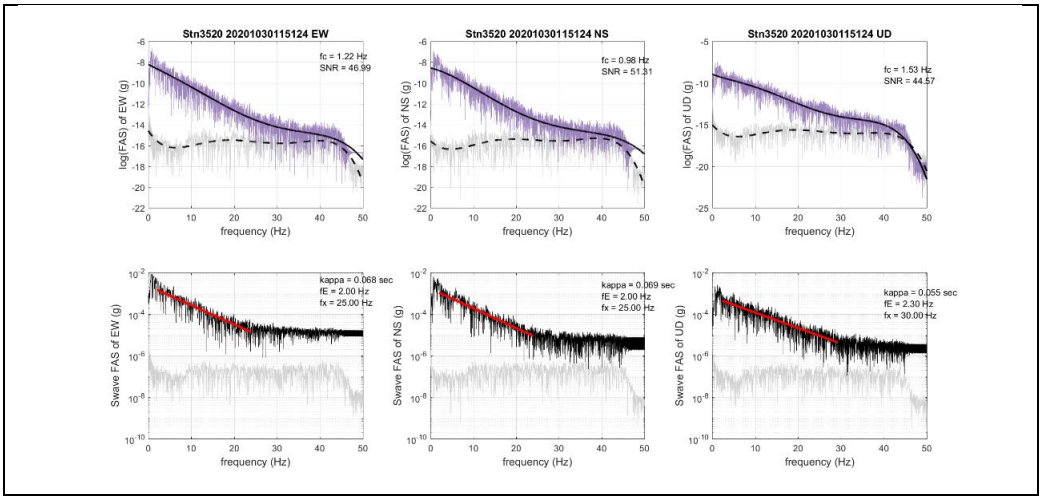


Figure B1.17: κ estimations for Stn3520. The mainshock occurred at 80 km R_{epi}.

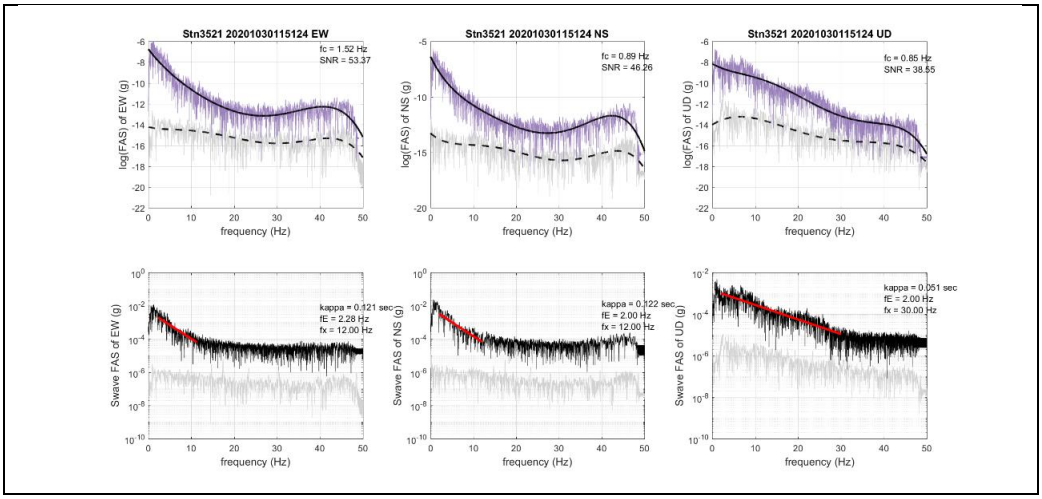


Figure B1.18: κ estimations for Stn3521. The mainshock occurred at 73 km R_{epi}.

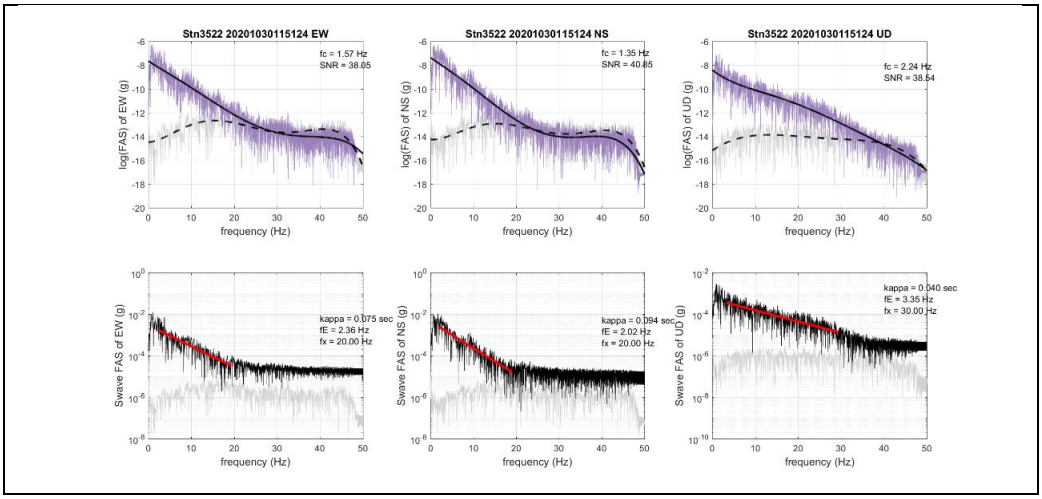


Figure B1.19: κ estimations for Stn3522. The mainshock occurred at 76 km R_{epi}.

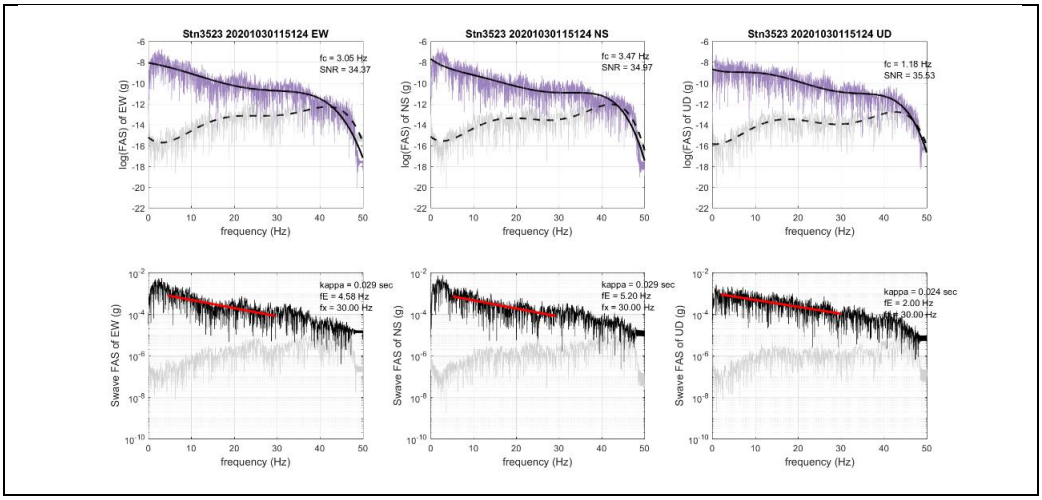


Figure B1.20: κ estimations for Stn3523. The mainshock occurred at 50 km R_{epi}.

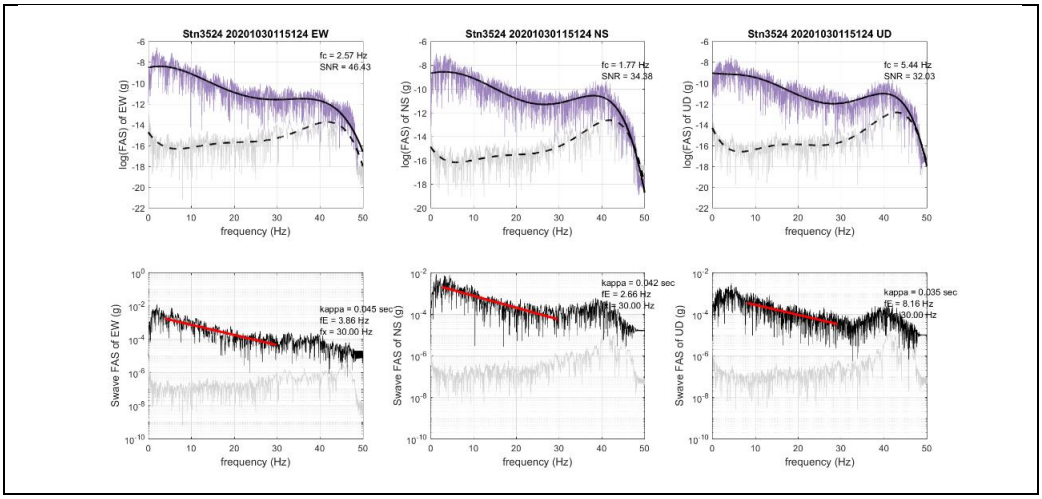


Figure B1.21: κ estimations for Stn3524. The mainshock occurred at 77 km R_{epi}.

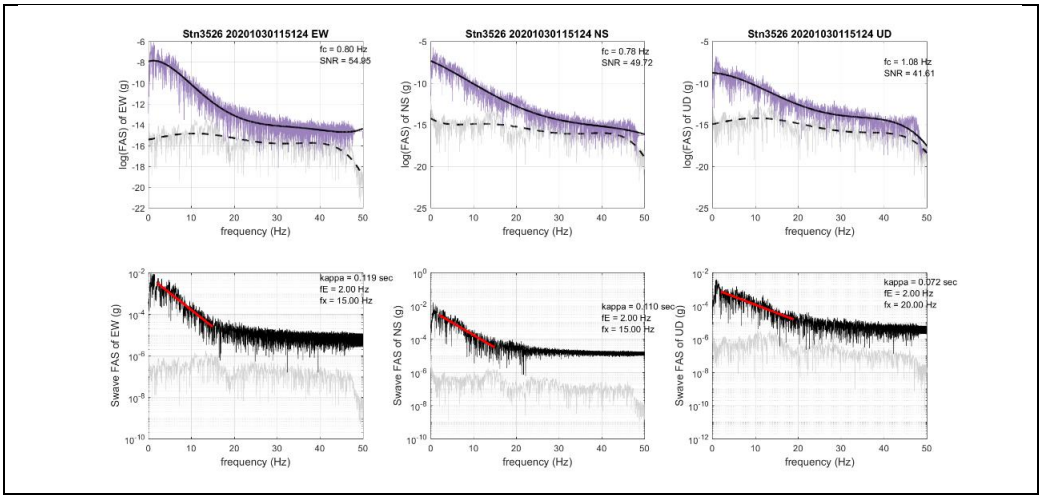


Figure B1.22: κ estimations for Stn3526. The mainshock occurred at 81 km R_{epi}.

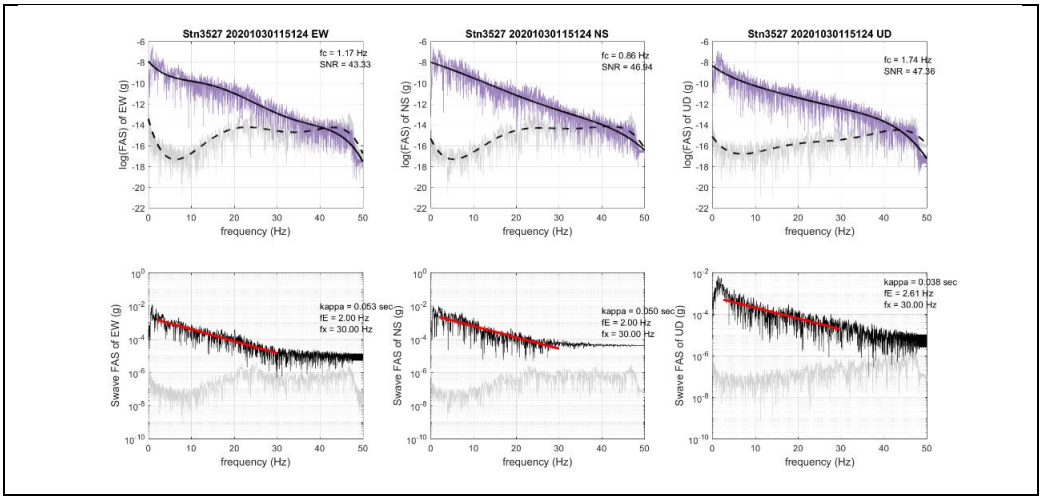


Figure B1.23: κ estimations for Stn3527. The mainshock occurred at 86 km R_{epi}.

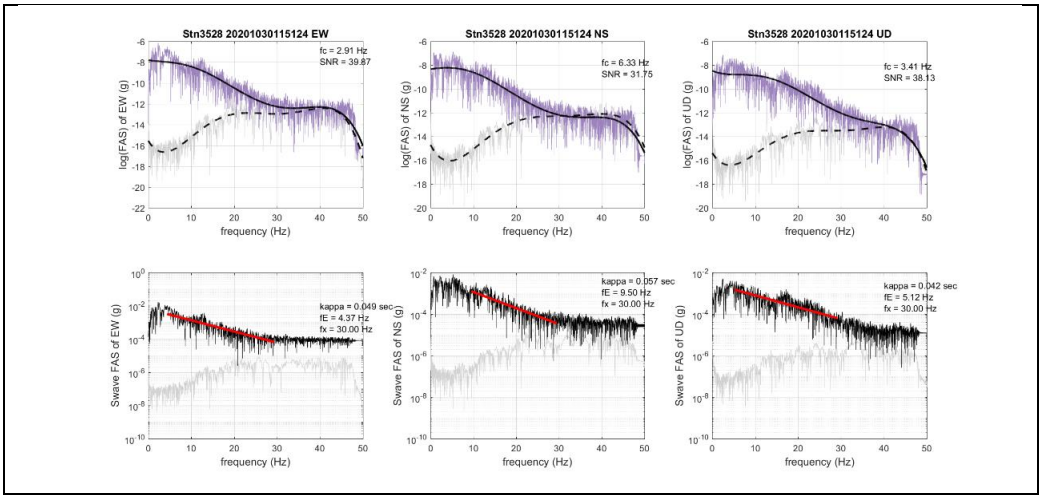


Figure B1.24: κ estimations for Stn3528. The mainshock occurred at 55 km R_{epi}.

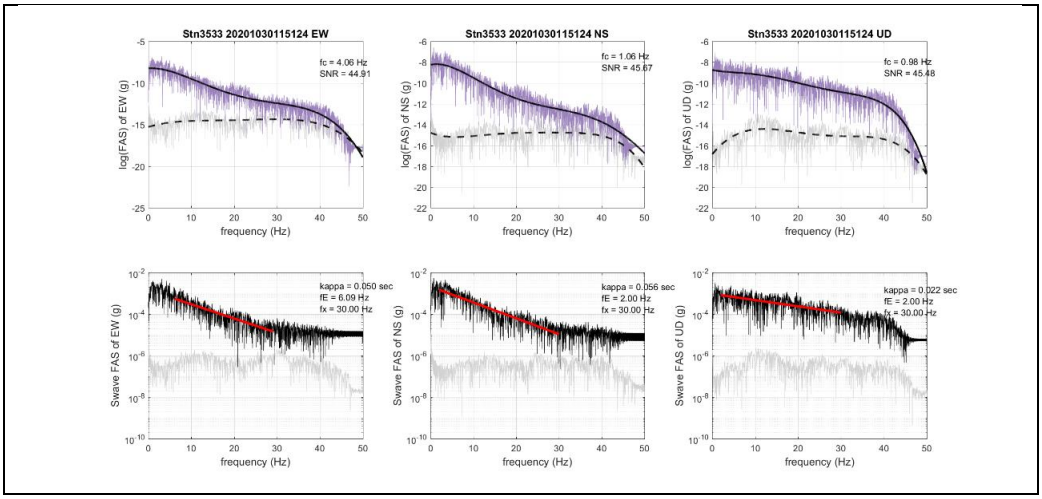


Figure B1.25: κ estimations for Stn3533. The mainshock occurred at 56 km R_{epi}.

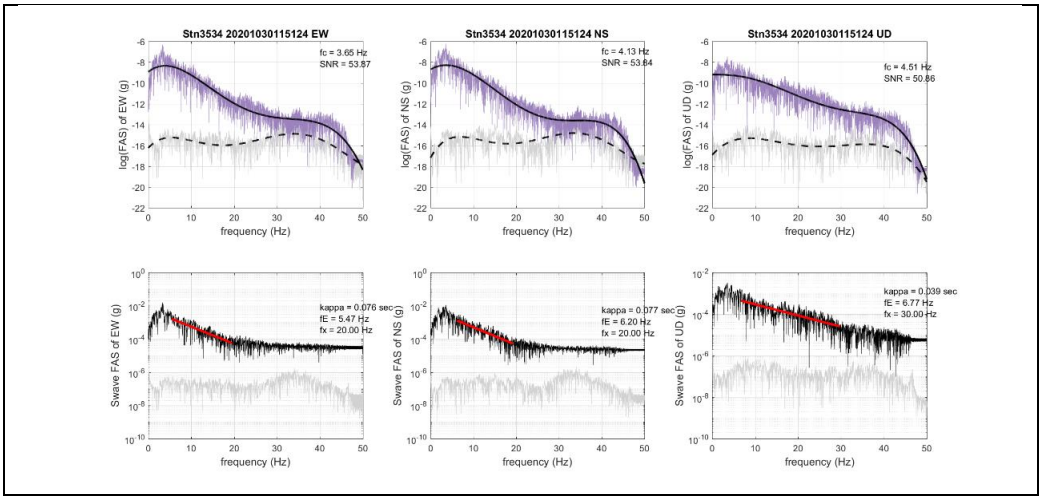


Figure B1.26: κ estimations for Stn3534. The mainshock occurred at 87 km R_{epi}.

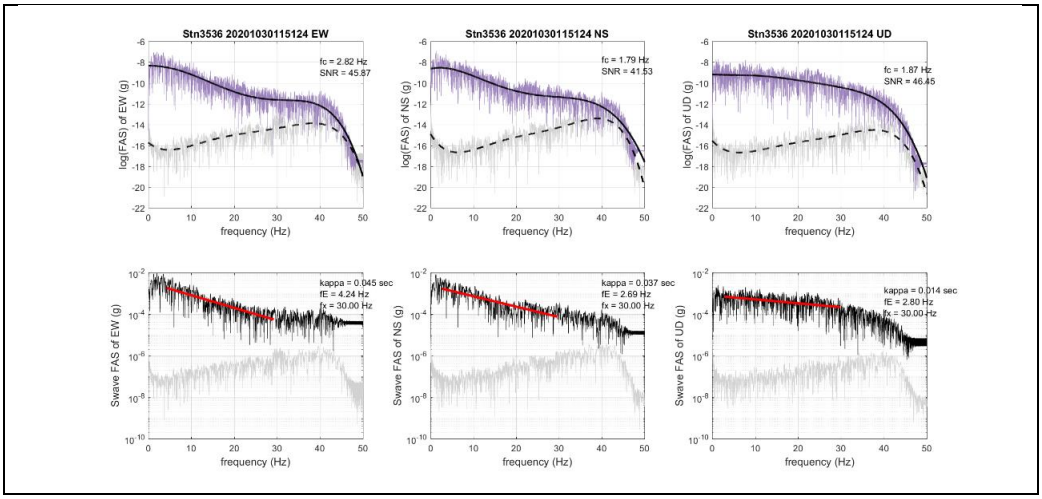


Figure B1.27: κ estimations for Stn3536. The mainshock occurred at 37 km R_{epi}.

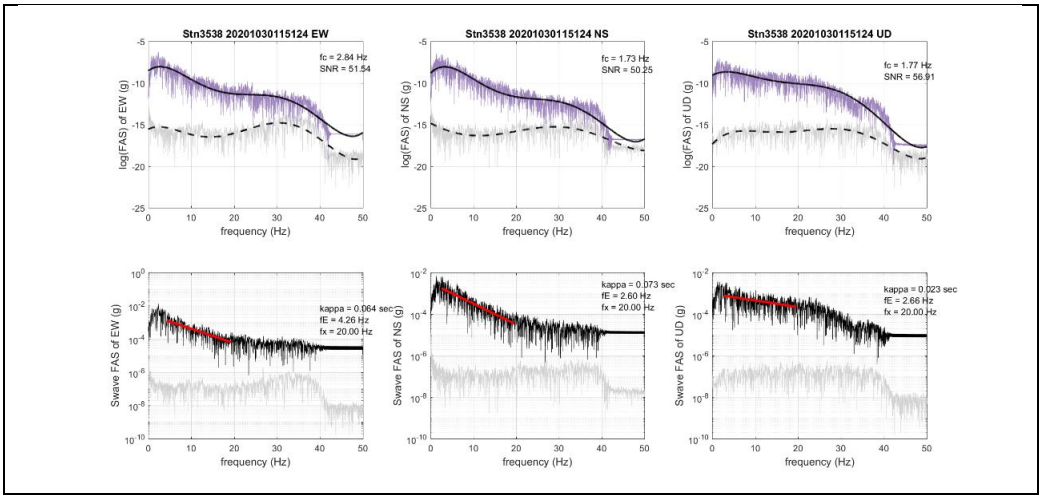


Figure B1.28: κ estimations for Stn3538. The mainshock occurred at 61 km R_{epi}.